ADVANCES IN COMPRESSION IGNITION NATURAL GAS – DIESEL DUAL FUEL ENGINES

EDITED BY: Hongsheng Guo, Hailin Li, Lino Guzzella and Masahiro Shioji
PUBLISHED IN: Frontiers in Mechanical Engineering

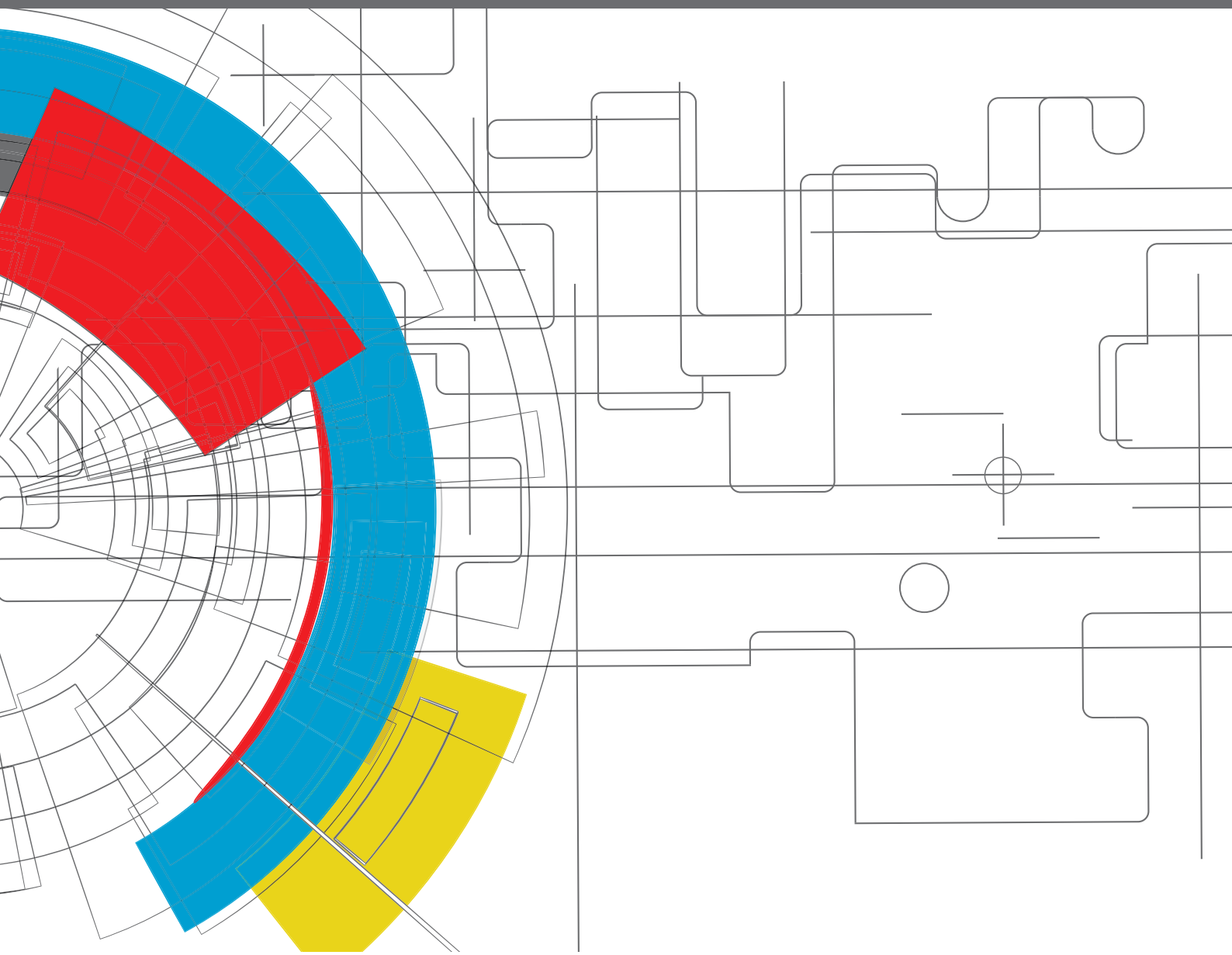

frontiers Research Topics

frontiers

ISSN 1664-8714
ISBN 978-2-88966-621-8
DOI 10.3389/978-2-88966-621-8

About Frontiers

Frontiers is more than just an open-access publisher of scholarly articles: it is a pioneering approach to the world of academia, radically improving the way scholarly research is managed. The grand vision of Frontiers is a world where all people have an equal opportunity to seek, share and generate knowledge. Frontiers provides immediate and permanent online open access to all its publications, but this alone is not enough to realize our grand goals.

Frontiers Journal Series

The Frontiers Journal Series is a multi-tier and interdisciplinary set of open-access, online journals, promising a paradigm shift from the current review, selection and dissemination processes in academic publishing. All Frontiers journals are driven by researchers for researchers; therefore, they constitute a service to the scholarly community. At the same time, the Frontiers Journal Series operates on a revolutionary invention, the tiered publishing system, initially addressing specific communities of scholars, and gradually climbing up to broader public understanding, thus serving the interests of the lay society, too.

Dedication to Quality

Each Frontiers article is a landmark of the highest quality, thanks to genuinely collaborative interactions between authors and review editors, who include some of the world's best academicians. Research must be certified by peers before entering a stream of knowledge that may eventually reach the public - and shape society; therefore, Frontiers only applies the most rigorous and unbiased reviews.
Frontiers revolutionizes research publishing by freely delivering the most outstanding research, evaluated with no bias from both the academic and social point of view. By applying the most advanced information technologies, Frontiers is catapulting scholarly publishing into a new generation.

What are Frontiers Research Topics?

Frontiers Research Topics are very popular trademarks of the Frontiers Journals Series: they are collections of at least ten articles, all centered on a particular subject. With their unique mix of varied contributions from Original Research to Review Articles, Frontiers Research Topics unify the most influential researchers, the latest key findings and historical advances in a hot research area! Find out more on how to host your own Frontiers Research Topic or contribute to one as an author by contacting the Frontiers Editorial Office: frontiersin.org/about/contact

ADVANCES IN COMPRESSION IGNITION NATURAL GAS – DIESEL DUAL FUEL ENGINES

Topic Editors:
Hongsheng Guo, National Research Council Canada (NRC-CNRC), Canada
Hailin Li, West Virginia University, United States
Lino Guzzella, ETH Zürich, Switzerland
Masahiro Shioji, Kyoto University, Japan

Citation: Guo, H., Li, H., Guzzella, L., Shioji, M., eds. (2021). Advances in Compression Ignition Natural Gas – Diesel Dual Fuel Engines. Lausanne: Frontiers Media SA. doi: 10.3389/978-2-88966-621-8

Table of Contents

frontiers in Mechanical Engineering

EDITORIAL
published: 15 February 2021
doi: 10.3389/fmech.2021.642187

Editorial: Advances in Compression Ignition Natural Gas–Diesel Dual-Fuel Engines

Hongsheng Guo[1]*, *Hailin Li*[2], *Lino Guzzella*[3] and *Masahiro Shioji*[4]

[1]National Research Council Canada, Ottawa, ON, Canada, [2]Department of Mechanical and Aerospace Engineering, West Virginia University, Morgantown, WV, United States, [3]Department of Mechanical and Process Engineering, ETH Zürich, Zurich, Switzerland, [4]Department of Energy Conversion Science, Kyoto University, Kyoto, Japan

Keywords: compression ignition engines, diesel engines, natural gas, greenhouse gas emissions, PM emissions

Editorial on the Research Topic

Advances in Compression Ignition Natural Gas–Diesel Dual-Fuel Engines

Natural gas (NG) has been recognized as a low-carbon clean fuel that generates about 20–30% less carbon dioxide (CO_2) and much less particulate matter (PM) emissions than diesel. Replacing diesel by NG in compression ignition diesel engines helps reduce CO_2 and PM emissions. Dual-fuel technology is an effective way to replace diesel by NG in diesel engines. However, there are some technical issues that are limiting the wide application of NG–diesel dual-fuel engines. These include the limited replacement ratio, efficiency deterioration, and especially the low combustion efficiency of NG due to the incomplete combustion of methane. Emissions of unburned methane are also an issue because of its very high global warming potential. This research topic gathers contributions that highlight the advantages/disadvantages and address the existing issues of NG–diesel dual-fuel engines.

The first article (Boretti) reviews the advantages and disadvantages of compression ignition dual-fuel engines compared to those of diesel engines. After a comprehensive literature review, the article indicates that dual-fuel engines allow for comparable or better performances of diesel-only internal combustion engines in terms of steady-state torque, power, and fuel conversion efficiency while dramatically improving the CO_2 and engine-out PM and NOx emissions. Further development of the fuel injection system for the second fuel may lead to novel dual-fuel engine designs with better performance.

The article by Yoshimoto et al. presents an investigation on trade-off improvements by combining exhaust gas recirculation (EGR) and supercharging in a dual-fuel engine using next-generation bio-alcohol–blended FAME as ignition fuel. Instead of conventional diesel, *Pongamia pinnata* methyl ester, which has potential to further reduce CO_2 emissions, was used in the investigation. The influence of the ignition fuel on engine performance, combustion characteristics, and emissions is examined and compared for dual-fuel and diesel operation by combining supercharging and EGR in the article.

The third article (Xu and Filipi) presents a quasi-dimensional multi-zone model of methane–diesel dual-fuel combustion. The model is further validated by experimental results. It provides a simplified but practical tool to predict and analyze the performance of dual-fuel engines.

The study by Ichihashi et al. also develops and validates a control model that is able to predict the combustion efficiency for compression ignition dual-fuel engines, and can be used to construct a controller that outputs the diesel injection condition to maximize the combustion efficiency of NG.

OPEN ACCESS

Edited by:
Apostolos Pesyridis, Alasala University, Saudi Arabia

Reviewed by:
Jose Ramon Serrano, Universitat Politècnica de València, Spain

***Correspondence:**
Hongsheng Guo
Hongsheng.guo@nrc-cnrc.gc.ca

Specialty section:
This article was submitted to Engine and Automotive Engineering, a section of the journal Frontiers in Mechanical Engineering

Received: *15 December 2020*
Accepted: *07 January 2021*
Published: *15 February 2021*

Citation:
Guo H, Li H, Guzzella L and Shioji M (2021) Editorial: Advances in Compression Ignition Natural Gas–Diesel Dual-Fuel Engines. Front. Mech. Eng 7:642187. doi: 10.3389/fmech.2021.642187

The model has the potential to be used to better control and optimize dual-fuel combustion in the real-world applications to improve methane slip, a key technical issue for NG–diesel dual-fuel engines.

An experimental and simulation study on NG–diesel dual-fuel combustion was conducted by Dimitriou et al. for three dual-fuel engines. Their results reveal that an advanced diesel injection timing could significantly reduce NOx formation and improve the engine's thermal efficiency, and hot EGR could contribute to simultaneous reduction of NOx and unburned hydrocarbons dominated by methane while increasing the thermal efficiency of the engine at low-load operation. However, they noted that a multiple pulse diesel injection strategy and intake boosting do not provide any benefits on emissions but increase unburned CH_4 emissions.

Yousefi et al. systematically investigated the effect of the variation of NG fraction on engine performance and the fundamental mechanisms behind the phenomena observed at different engine load conditions by a combination of experiments and numerical simulation. The results of the article indicate that the effect of NG fraction on engine and combustion performance, such as combustion phasing, thermal efficiency, and emissions, depends on engine load, suggesting that different strategies should be adopted to optimize the performance of a NG–diesel dual-fuel engine at different loads. Some strategies that are able to improve the dual-fuel engine performance at different loads are also investigated in this research.

Most previous studies on NG–diesel dual-fuel engines focused on low load conditions at which methane slip is a significant issue, while relatively not enough attention has been paid for high load conditions. Although methane slip is not significant for dual-fuel engines at high load conditions, there are some other issues that need to be addressed. One of these issues is injector tip overheating due to the decrease in diesel flow rate, since diesel also plays the role of coolant to reduce the injector tip temperature for diesel engines. Besides, the effect of NG on engine performance and emissions at high loads is different from that at low loads, as indicated in the article by Yousefi et al. The article by Dev et al. presents an investigation on the high load operation of a NG–diesel dual-fuel engine, including the injection tip temperature performance. Their results reveal that with increasing NG fraction at a given diesel injection timing or advancing diesel injection timing at a given NG fraction, injector tip temperature increases. In addition, combustion phasing is a very critical determinant of dual-fuel combustion performance at high engine loads. Being different from that at low load conditions, increasing NG fraction can advance combustion phasing and cause the combustion duration to decrease.

We hope readers can find from this Research Topic some useful references for better understanding the fundamental mechanisms of dual-fuel combustion and the future development and optimization of NG–diesel dual-fuel engines. Technologies that further decrease and eventually eliminate emissions of unburned methane, and optimize the combustion process at high load are necessary for the wide application of NG–diesel dual-fuel engines.

AUTHOR CONTRIBUTIONS

All authors listed have made a substantial, direct, and intellectual contribution to the work and approved it for publication.

Conflict of Interest: The authors declare that the research was conducted in the absence of any commercial or financial relationships that could be construed as a potential conflict of interest.

frontiers in Mechanical Engineering

REVIEW
published: 03 December 2019
doi: 10.3389/fmech.2019.00064

Advantages and Disadvantages of Diesel Single and Dual-Fuel Engines

Alberto Boretti [1,2]*

[1] Department of Mechanical Engineering, College of Engineering, Prince Mohammad Bin Fahd University, Al Khobar, Saudi Arabia, [2] Faculty of Applied Sciences, Ton Duc Thang University, Ho Chi Minh City, Vietnam

The pros and the cons of lean-burn, compression ignition (CI), direct injection (DI) internal combustion engines (ICE) are reviewed for transport applications. Fueling options considered include diesel only and dual-fuel applications with diesel and a gaseous fuel (CNG, LNG, and LPG). CIDI ICEs have higher fuel conversion efficiencies than stoichiometric, spark ignition (SI) ICEs, whether DI or port fuel injected (PFI). However, diesel-fueled CIDI ICEs have higher particulate matter (PM) and NOx engine-out emissions. The tail-pipe NOx emissions in real-world driving of diesel-powered vehicles have been, in the past, above the limits requested over the simplified cold start driving cycles used for certification. This issue has recently been resolved. The newest diesel-powered vehicles are now compliant with new laboratory test cycles and real-world-driving schedules and have no disadvantages in terms of criteria air pollutants compared to older diesel vehicles, while delivering improvements in fuel economy and CO_2 emissions. Dual-fuel CIDI ICEs offer the opportunity for enhanced environmental friendliness. Dual-fuel CIDI ICEs have lower engine-out NOx and PM emissions compared to diesel-only CIDI ICEs. The latest diesel-only vehicles and vehicles with dual-fuel ICEs deliver dramatic reductions in tail-pipe PM emissions compared to older diesel-only vehicles. Moreover, they deliver tail-pipe PM emissions well below the ambient conditions in most city areas that are highly polluted, thereby helping to clean the air. The diesel-fueled CIDI ICEs may be further improved to deliver better fuel economy and further reduced tail-pipe emissions. The dual-fuel CIDI ICE has more room for improvement to produce similar or better steady state and transient performance in terms of torque, power output and fuel conversion efficiency compared to diesel-fueled CIDI ICEs, while drastically reducing CO_2 and PM tail-pipe emissions, and improving NOx tail-pipe emissions. This is due to the ability to modulate the premixed and diffusion phases of combustion with a second fuel that is much easier to vaporize and is less prone to auto-ignition. Further development of the fuel injection system for the second fuel will lead to novel dual-fuel CIDI ICE designs with better performance.

Keywords: compression ignition diesel engines, dual fuel engines, natural gas, greenhouse gas emissions, particulate matter

OPEN ACCESS

Edited by:
Hongsheng Guo,
National Research Council Canada (NRC-CNRC), Canada

Reviewed by:
Stuart Neill,
National Research Council Canada (NRC-CNRC), Canada
Lorenzo Bartolucci,
University of Rome Tor Vergata, Italy

***Correspondence:**
Alberto Boretti
a.a.boretti@gmail.com

Specialty section:
This article was submitted to Engine and Automotive Engineering, a section of the journal Frontiers in Mechanical Engineering

Received: *27 August 2019*
Accepted: *14 November 2019*
Published: *03 December 2019*

Citation:
Boretti A (2019) Advantages and Disadvantages of Diesel Single and Dual-Fuel Engines. Front. Mech. Eng. 5:64. doi: 10.3389/fmech.2019.00064

INTRODUCTION

The lean-burn, compression ignition (CI), direct injection (DI), is the most efficient internal combustion engine (ICE) (Zhao, 2009; Mollenhauer and Tschöke, 2010). It produces engine-out emissions of nitrous oxides and particulate matter (PM) that need after treatment to match the extremely low limits set up for transport applications (Lloyd and Cackette, 2001; Burtscher, 2005; Maricq, 2007), despite air quality is not only influenced by the transport emissions but by many other sources. Combustion strategies alone (Khair and Majewski, 2006) were not enough to meet the emission threshold, and specific lean burn catalysts were needed especially for NOx additional to particulate filters in the exhaust. Despite their economic success, diesel engines were facing ever more stringent emission legislation worldwide (Knecht, 2008; Zhao, 2009) at the price of phasing out the technology targeting unrealistic minimal incremental improvements.

The diesel engine has pros and cons as everything. It has full and part load fuel conversion efficiencies exceeding those of stoichiometric, spark ignition (SI) ICEs, both DI and port fuel injected (PFI). CIDI ICEs have peak efficiencies about 50% and efficiencies above 40% over most of the speeds and loads. Opposite, SI ICEs have peak efficiencies in the mid 30%, and these efficiencies are dramatically reduced by reducing the load. CI ICEs deliver mechanical energy on demand at fuel conversion efficiencies that are also higher than the efficiencies of combustion fuel power plants producing electricity. According to EIA (2018), in 2017, across the United States, coal steam generators run with an average efficiency of 33.98%. Petroleum and natural gas steam generators run at about the same efficiency, 33.45 and 32.96%. Gas turbine generators run at a reduced efficiency of 25.29% with petroleum, and 30.53% with natural gas. The efficiency of internal combustion engine generators is larger than gas turbine and steam generators, at 33.12% with petroleum and 37.41% with natural gas. Only combined-cycle generators, not with petroleum, that have an efficiency of 34.78%, but with natural gas, that have an efficiency of 44.61%, surpass the internal combustion generators.

In the comparison of the electric mobility, CIDI ICEs still have advantages for transport applications is unchallenged (Boretti, 2018). However, the CIDI ICE is suffering from a bad reputation jeopardizing its potentials. Diesel CIDI ICEs have failed in the recent past to deliver the specific NOx emissions of cold start certification cycles during warmed-up real-world driving schedules that were strongly differing from the certification cycles (Boretti, 2017; Boretti and Lappas, 2019). This unfortunate occurrence has been played against the CIDI ICE to give the impression this engine is environmentally unfriendly for pollutant emissions where it is not.

The large NOx emissions of CIDI ICEs are the result of large in-cylinder production of NOx working in excess air lean of stoichiometry, coupled to the improper operation of the after treatment. The lean-burn catalyst of CIDI ICEs is less evolved than the three-way catalytic (TWC) converter of stoichiometric, SI ICEs (Heywood, 1988; Zhao, 2009; Mollenhauer and Tschöke, 2010; Reşitoglu et al., 2015). Additionally, the prolonged operation warmed-up was not considered (Boretti and Lappas, 2019). Also, some manufacturers adopting urea injection in the after-treatment decided to inject less urea that the necessary when not strictly requested by the emission certification. Similarly, some manufacturers also focused on drivability and fuel economy issues rather than emissions when not strictly asked, far from the operating conditions of concern for the emission certification. Thus, the failure to meet the NOx emissions over randomly selected conditions was not a fundamental flaw of the CIDI ICEs in general, but only of the specific products developed for what were the emission regulations and the market requirements of the specific time. Not considered by the detractors of the CIDI ICEs, as these engines are equipped with particle traps of almost perfect efficiency, circulation of vehicles fitted with these engines, in high polluted areas, is resulting in better tailpipe than intake conditions, for particulate, thus contributing to cleaning the air.

The present contribution supplies a fair review of the pros and cons of the lean burn, CIDI ICEs, that are much better than what is thought. As the ICE is certainly needed for more decades to come, further improvements of the lean burn, CIDI ICE will be beneficial to the economy and the environment. In addition to diesel CIDI ICEs, this work also considers dual-fuel engines diesel-LNG (Goudie et al., 2004; Osorio-Tejada et al., 2015; Laughlin and Burnham, 2016), diesel-CNG (Maji et al., 2008; Shah et al., 2011; Ryu, 2013) or diesel-LPG (Jian et al., 2001; Ashok et al., 2015). The operation with a small amount of diesel and a much larger (in energy term) amount of a much lighter hydrocarbon fuel, with a reduced carbon to hydrogen content, permits to further reduce the PM engine-out emissions, as well as the CO_2 emissions, and being liberated from the PM-NOx trade-off that afflict the diesel-only injection strategies, also reduce the engine-out emissions of NOx. Development tendencies for dual fuel CIDI ICEs are also reviewed.

The utilization of biodiesel to produce low carbon diesel fuels using a single-fuel approach is certainly another option to reduce CO_2 emissions. While this opportunity does not impact on the pollutant emission, production of biofuels, in general, is increasing, but not at the expected rate (IEA, 2019), and the food vs. fuel issue (Ayre, 2007; Kingsbury, 2007; Inderwildi and King, 2009) may also weight negatively in a world with a projected imminent water and food crisis (United Nations, 2019). Additionally, the advantages of biofuels over LCA are a long-standing, controversial debate in the literature (McKone et al., 2011).

There is the opportunity of methane emissions from dual-fuel natural gas–diesel engines (Camuzeaux et al., 2015). As methane is a potent GHG, this aspect should be taken into due consideration when targeting GHG emissions reduction. There is not only the potential for methane leaks from the vehicles incorporating dual-fuel diesel-LNG engines. There are also methane emissions from oil and gas production. Additional to the methane emissions from natural gas production, there are the electricity emissions associated with the operation of the LNG facility. While LNG (and CNG) will certainly still give advantages vs. diesel, this advantage may be less than what could be inferred from the C-H ratio of the fuel. There is certainly an issue to reduce the methane emissions associated

with the production, transportation, and liquefaction of natural gas (Ravikumar, 2018).

Finally, while natural gas fumigation for dual-fuel diesel engines has been used widely, as it is much simpler and it can be accomplished through low tech conversions, and thus most vehicles utilize this approach, diesel engines converted to diesel and fumigated natural gas suffer from significant fuel conversion efficiency degradation vs. the original diesel, both full load and part load, and reduced power and torque density. If the natural gas is mixed (fumigated) with the intake air before induction to the cylinder, and diesel fuel is used as an ignition source, the amount of natural gas introduced is limited by the opportunity of knock of the premixed mixture. Furthermore, the load is typically controlled by throttling the intake as in conventional gasoline engines rather than by the quantity of fuel injected as in the diesel engine. As the goal is to provide equal or better performances (power, torque, transient operation) and emissions of the latest diesel with a dual fuel design, this dual-fuel design must adopt the direct injection of the diesel and the gaseous fuel.

THE GENESIS OF THE BAD REPUTATION OF THE DIESEL

The bad reputation of the diesel, and more in general of the internal combustion engine (ICE), is the result of actions by the California Air Resources Board (CARB), as well as of the US Environmental Protection Agency (EPA) (Parker, 2019), with "*Diesel-gate*" only one step of a ploy.

Back in the days, the hydrogen economy was the more likely future model for transportation, better than every other alternative considering the intermittency of wind and solar energy production (Crabtree et al., 2004; Muradov and Veziroglu, 2005; Marbán and Valdés-Solís, 2007). Vehicles were supposed to use ICEs powered by renewable hydrogen (H_2-ICEs), with everything but dramatic changes needed in the engine technology, but efforts mostly devoted to storage and distribution. About the same days, it was also popular the idea of a methanol economy, where the methanol produced by using the renewable hydrogen and the CO_2 captured in coal-fired power plants was a direct replacement of traditional gasoline fuel (Olah, 2004, 2005). The H_2-ICE become history after the CARB deliberated the BMW Hydrogen 7, the first vehicle powered by an ICE was delivered to the market, did not qualify as a zero (CO_2) emission vehicle. In 2005 BMW proposed the Hydrogen 7 car as a zero-emissions vehicle. Burning hydrogen, at the tailpipe there was mostly water vapor and absolutely no CO_2 emission, but the US EPA did not agree with the zero-emission of CO_2 (Nica, 2016). The US EPA said that the vehicle still had an ICE, with the opportunity that oil used for lubrication could have ended up within the cylinder, thus producing CO_2. The fact that the total oil consumption was a negligible 0.04 L of oil every 1,000 km was not considered. Because of the unofficial deliberation, BMW dropped the hydrogen ICE research. All the other Original Equipment Manufacturers stopped their R&D afterward.

Regarding the negative attitude of CARB and US EPA toward the ICE in general, in 2011 BMW proposed as a concept car the battery-electric i3 with the opportunity of a range extender (Ramsbrock et al., 2013; Scott and Burton, 2013). The range extender was a small gasoline ICE powering a generator to recharge the battery. By introducing the range extender, it was possible to increase the range of the car and reduce the cost, weight, and volume of the battery pack, which is a major issue for the economy and the environment. With production only planned to start in 2013, the CARB at once rushed to set up rules to prevent the optimization of this concept, issuing in 2012 (CARB, 2012) an overlong regulation prescribing a range extender must only be used to reach the nearest recharging point. In between the other requirements, the CARB requested, from a range extender vehicle, a rated all-electric range of at least 75 miles, a range less than, or equal to, battery range from the auxiliary power unit, and finally, that the auxiliary power unit must not be capable of switching on until the battery charge was depleted. As a result, of all these limitations, BMW struggled to make the range extender competitive, and ultimately, they recently dropped the production of the i3 with range extender (Autocar, 2018).

These two events help to explain the 2015 "*diesel-gate*" and the subsequent "*diesel-phobia*." The diesel engine was popular (for passenger cars) mostly in Europe, and the EU was promoting diesel vehicles to tackle the issues of climate change. At the time, it was clear that a premature move toward electric mobility could have translated into an economic and environmental disaster. Thus, the Volkswagen group was targeted by the "*diesel gate*" scandal. Diesel ICEs were providing low CO_2 emissions, competitive with battery electric vehicles in life cycle analyses while emitting less than the prescribed pollutants over the tests prescribed at the time. Passenger cars were tested for compliance with emission rules over a prescribed cycle, in a laboratory, under repeatable conditions with the correct equipment. The International Council on Clean Transportation (ICCT), organized some casual driving on the road of different diesel vehicles, and measurements of pollutants with PEMs. They found that vehicles optimized to produce low specific (per km) CO_2 and pollutant emissions in certain conditions, were not able to ensure the same specific emissions under every other condition, as it was logic to expect. The EPA issued a notice of violation against Volkswagen then resulting in a huge fine in the following court actions. "*Diesel-gate*" has cost so far to VW more than 29 billion $, in fines, compensation, and buybacks, mainly in the United States (phys.org, 2018). Part of the Volkswagen billion $ ended up supporting the battery electric vehicle mobility, funding the electric vehicle recharging infrastructure in the United States by selected suppliers (O'Boyle, 2018). "*Diesel-gate*" has then been used to determine the end of the ICE-based mobility (Raftery, 2018; Taylor, 2018).

The alleged excess emission of NOx by vehicles equipped with CIDI diesel ICEs that started with "*diesel gate,*" is still popular, despite untrue (Chossière et al., 2018) claims that diesel vehicles caused 2,700 premature mortalities in 2015 only across Europe, because of their "*excess*" NOx emissions. This work is not objective in analyzing the emissions of the diesel engine. It is incorrect to claim that diesel vehicles in the EU emit much more NOx on the road than the regulatory limits. As

previously written, the emission rules regulated the pollutant emissions in the specific laboratory test conditions, and not in every other possible condition. It is unreasonable to expect a specific fuel economy and emissions of regulated pollutants and carbon dioxide that are independent of the specific test. To have an "*excess*" emission, first there is a need for a limit for the specific application, and then the measure of the "*excess*" under the specific condition. The claim of premature mortalities caused by excess NOx emissions from diesel vehicles is based on an overrated differential emission of NOx, assuming much worse than actual emissions, and comparing this emission to an improbable near-zero-emission reference situation. The claim is also based on an overrated attribution of the number of mortalities to this differential emission. These two assumptions are not supported by proven data.

As the more recent diesel vehicles have replaced even more polluting vehicles, the only possible objective statement that can be made about the emissions of old and new diesel vehicles in Europe, based on unquestionable evidence, is only based on the emission complaint rules of the time of their registrations. As the emission rules have been made increasingly restrictive, albeit, as only verified over the laboratory certification test, as shown in **Table 1**, it is incorrect to assume CIDI diesel ICEs emit more NOx than before. While Euro 6 compliant diesel passenger vehicles were required to emit less than 0.08 g/km of NOx when covering the NEDC in the laboratory test, Euro 5 to 3 compliant diesel vehicles were otherwise permitted to emit 0.18, 0.25 and 0.50 g/km on the same test, and Euro 1 and 2 compliant diesel vehicles had to verify only an emission threshold of 0.7-0.9 and 0.97 g/km on the same test. There are no measurements that prove old diesel vehicles, that were compliant with prior Euro rules, were more environmentally friendly, under every pollutant criterion, including NOx, during real-world driving than the latest diesel vehicles. Furthermore, the emission performances usually deteriorate with age, and lack of maintenance can make things even worse. This makes the claim of Chossière et al. (2018) inconsistent.

ADVANTAGES AND DISADVANTAGES OF THE LEAN-BURN CIDI ENGINE

The major advantage of the lean burn, CIDI ICE is the fuel conversion efficiency, which is much higher than in stoichiometric, SI ICEs, both full loads, and more than that, part load (Heywood, 1988; Zhao, 2009; Mollenhauer and Tschöke, 2010). While passenger vehicles with a lean burn, CIDI ICE fueled with diesel have fuel peak fuel conversion efficiencies of about 45%, the peak efficiency of passenger vehicles with stoichiometric, SI ICEs fueled with gasoline is only about 35%. Reducing the load by the quantity of fuel injected, the fuel conversion efficiency of the lean burn, CIDI ICE is high over most of the load range. Conversely, by reducing the load throttling the intake, the fuel conversion efficiency of the stoichiometric, SI ICE dramatically deteriorates when reducing the load. This gives the opportunity to passenger vehicles equipped with a lean burn, CIDI ICE to consume much less fuel, and therefore emit much less CO_2, during driving cycles (Schipper et al., 2002; Zervas et al., 2006; Johnson, 2009; Zhao, 2009; Mollenhauer and Tschöke, 2010; Boretti, 2017, 2018; Boretti and Lappas, 2019).

The lean-burn after treatment in general (CIDI diesel ICEs innately run lean, apart from cases of extreme uses of exhaust gas recirculation, EGR) is however much less efficient than the stoichiometric after treatment by TWC converters of SI gasoline ICEs (Lloyd and Cackette, 2001; Burtscher, 2005; Maricq, 2007). Hence, emissions of regulated pollutants, in particular, NOx, over duty cycles that largely deviate from the certification cycles, being much longer and needing the engine to run to a significant extent fully warmed up, are much larger in lean-burn ICEs rather than stoichiometric ICEs. Additionally, lean-burn, CIDI ICEs have particulate, a common downfall, even to a reduced extent, of directly injected engines, including SI DI ICEs. PM originates when the injected fluid still liquid interacts with the flame thus producing soot. Soot is formed in the fuel-rich regions of the combustion chamber (Hiroyasu and Kadota, 1976; Smith, 1981; Neeft et al., 1997). Lean burn, CIDI ICEs thus need particle traps (Neeft et al., 1996; Saracco et al., 2000; Ambrogio et al., 2001; Mohr et al., 2006). This is, however, also an opportunity, as circulation in areas with background particulate may produce better air quality at the tailpipe than the intake. An added downfall of lean-burn, CIDI ICEs, these engines, typically turbocharged, are more expensive. The dual-fuel operation with LPG, CNG, or LNG, does not introduce any disadvantage in terms of regulated pollutants or CO_2, but only advantages.

Fuel Conversion Efficiency

Without targeting the waste heat recovery (WHR), diesel CIDI ICEs have proven their ability to achieve peak fuel conversion efficiencies about 50% while supplying extremely high brake mean effective pressures in endurance racing (Boretti and Ordys, 2018). Thanks to high pressure, high atomization, high flow rate, and fast-actuating injectors, multiple injection strategies allow controlled combustion processes occurring in the bulk of the combustion chamber, for the best trade-off between pressure work, pressure build-up, and peak pressure.

While waste heat recovery systems (WHR) may certainly improve the steady-state fuel conversion efficiency of diesel engines (Teng et al., 2007, 2011; Teng and Regner, 2009; Park et al., 2011; Wang et al., 2014; Yu et al., 2016; Shi et al., 2018), cold start transients are the Achille's heel of traditional WHRs. Additionally, WHRs add weight, thermal inertia, packaging issues, and complexity. Innovative concepts for WHR, utilizing the coolant circuit as the pre-heater of a modified "*turbo steamer*" (Freymann et al., 2008, 2012) without any need of a double circuit, require significant research and development efforts.

The results achieved in endurance racing by Audi (Audi, 2014), in less than a decade of developments, are important. 2006 to 2008, Audi adopted the V12 TDI in the Audi R10 TDI. The 5.5 L engine delivered 1,100 Nm of torque. At rated speed, the very quiet-running twin-turbo produced roughly 480 kW. In 2009 and 2010, Audi moved to the V10 TDI in the Audi R15 TDI. It was shorter and lighter than the twelve-cylinder. The 5.5 L of displacement were spread across two fewer cylinders. The engine had roughly 440 kW and more than 1,050 Nm of torque. Top

TABLE 1 | European Union emission standards for passenger vehicles (category M) of positive (gasoline) and compression (diesel) design.

Stage	Date	CO	HC+NOx	HC	NOx	PM	PN
				g/km			*#/km*
Positive Ignition (Gasoline)							
Euro 1	Jan-92	2.72	0.97				
Euro 2	Jan-96	2.2	0.5				
Euro 3	Jan-00	2.3	0.35	0.2	0.15		
Euro 4	Jan-05	1	0.18	0.1	0.08		
Euro 5	Jan-09	1	0.16	0.1	0.06	0.005	
Euro 6	Jan-14	1	0.16	0.1	0.06	0.005	$6{\cdot}10^{11}$
Compression-Ignition (Diesel)							
Euro 1	Jan-92	2.72	0.97			0.14	
Euro 2, IDI	Jan-96	1	0.7			0.08	
Euro 2, DI	Jan-96	1	0.9			0.1	
Euro 3	Jan-00	0.64	0.56		0.5	0.05	
Euro 4	Jan-05	0.5	0.3		0.25	0.025	
Euro 5a	Jan-09	0.5	0.23		0.18	0.005	
Euro 5b	Jan-11	0.5	0.23		0.18	0.005	$6{\cdot}10^{11}$
Euro 6	Jan-14	0.5	0.17		0.08	0.005	$6{\cdot}10^{11}$

IDI indirect (pre-chamber) injection. DI direct t injection.

BMEP were exceeding 24 bars. Then, 2011 to 2013, Audi moved to the V6 TDI in the Audi R18 TDI, R18 ultra and R18 e-Tron Quattro. Downsizing of the engine brought to a displacement of 3.7 L. The lightweight and compact V6 TDI produced over 397 kW and more than 900 Nm of torque. The common-rail system generated up to 2,600 bars of pressure. Top BMEP were exceeding 30 bars.

When the focus was placed more on fuel economy, in 2014, the V6 TDI in the Audi R18 e-Tron Quattro was powered by a redesigned V6 TDI with displacement increased to 4.0 L. Maximum power was 395 kW and maximum torque was more than 800 Nm. The injection pressure was more than 2,800 bars. Fuel consumption decreased by more than 25% compared with the 3.7-liter engine. Latest (2016) power outputs from the 4-liter engine were 410 kW, corresponding to 870 Nm of torque at the maximum speed of 4,500 rpm. This translated into 27.3 bar BMEP in the maximum speed / maximum power operating point. The latest engines had a limited fuel flow rate, that for a 6 MJ energy recovery system (ERS) for braking, the maximum fuel flow rate was 71.4 kg/h. For a diesel fuel of 43.4 MJ/kg Lower Heating Value (LHV), the fuel flow power was 860.8 kW. The maximum power was thus obtained with a peak power brake efficiency $\eta = 0.475$, which is much larger than the peak efficiency of many production high-speed diesel engines, that may run, up to a peak efficiency $\eta = 0.45$ at lower engine speeds.

From computations, the maximum torque, as well as the maximum brake efficiency, were obtained at speeds <4,500 rpm, which is a technological limit of the diffusion combustion (Boretti and Ordys, 2018). Due to the constant time needed for the fuel to vaporize and mix with air, the diffusion combustion phase has a duration in terms of crank angle degrees that increases with the engine speed. Thus, at speeds above 4,500 rpm, the length of the combustion phase usually becomes excessive and much better power is obtained at lower speeds. Peak torque was highly likely more than 916 Nm, corresponding to 29 bar BMEP. Peak fuel conversion efficiency was highly likely approaching $\eta = 0.50$. Further developments for racing were within easy reach, at the time the activity was stopped in the aftermath of "*diesel-gate*." Higher injection pressures, and more advanced turbocharging such as the contemporary F1 e-turbo, or super turbocharging (Boretti and Castelletto, 2018; Boretti and Ordys, 2018), could have been beneficial to normal production diesel engines for passenger cars.

Laboratory Test Emissions

The past emission certification, that was carried out by the original equipment manufacturers (OEM) and not independently tested, was flawed by inaccuracies in the tests, and inadequacy of the certification cycle (Boretti, 2017; Boretti and Lappas, 2019). The short, highly stylized new European driving cycle (NEDC), was extremely far from the real-world-driving conditions experienced by European commuters. As the OEM were forced for more than two decades to focus their RandD to produce engines compliant and fuel-efficient during this cycle, having the aggravation of the cold start, other possible uses were not regulated and left of the discretion of the OEM. Inaccuracies (and discretion) in the way the tests were handled produced many inconsistencies, starting from large spreading of carbon dioxide (CO_2) emissions for the consumption of theoretically the same liter of fuel (Boretti and Lappas, 2019). The new Worldwide harmonized Light Vehicles' Test Cycle (WLTC), that has recently replaced the NEDC, because of "*diesel gate*" (Chossière et al., 2018), is better, being a little bit longer. However, it still involves

driving conditions different from those experienced during peak hours in congested areas (Boretti and Lappas, 2019).

For a historical perspective, emission rules have been made tougher and tougher year after year, but only declared to be measured during the prescribed laboratory tests. **Table 1** presents the European Union (EU) emission standards for passenger vehicles (category M) of positive (gasoline) and compression (diesel) ignition design. Unburned hydrocarbons (HC)+NOx was prescribed for gasoline and diesel only in Euro 1 and 2 standards. Emissions were tested over the NEDC by using a chassis dynamometer laboratory procedure. What was requested to the OEM over the years, was to produce vehicles emitting less than the regulated pollutant over the specific certification cycle during the laboratory tests. Real-world driving was an immaterial concept, not translated in any specific legislative requirement. The reduction of the emission limits for NOx and PM in Euro 5 and 6 resulted in dramatically increased costs of the after treatment, and in an increased, rather than reduced, fuel consumption, with sometimes also issues of drivability. Once more it is important to understand the trade-off between fuel economy and pollutant emissions and realize that excessive requests under one criterion may translate in the impossibility to meet the other criteria.

Real World Driving Emissions

Only recently, the European Union (EU) has introduced Real Driving Emissions (RDE) tests. On-the-road vehicle emissions are now measured by using portable emission analyzers (PEMs). The RDE test must last 90–120 min and include one urban (<60 km/h), one rural (60–90 km/h) and one motorway (>90 km/h) segment, of equal weight, covering a distance of at least 16 km. RDE emission limits then use conformity factors to relate to the chassis dynamometer laboratory test. For what concerns NOx, the conformity factor is 2.1 since September 2017 for new models and since September 2019 for all new vehicles. Other conformity factors are still to be defined. While the RDE test is still not representative of real-world driving in congested areas, it is non-accurate, subjective, non-reproducible, and not yet determinant (Boretti and Lappas, 2019), it is certainly a step forward.

Australian real-world driving emissions data of pre-new rules vehicles are proposed by ABMARC (ABMARC, 2017). The report prepared for the Australian Automobile Association presents the emissions and fuel consumption test results from 30 different passenger and light commercial vehicles, measured with PEMS on Australian roads. Most of the vehicles were compliant with Euro 4, 5, and 6 standards, while 1 of them was compliant with Euro 2 standards. The real-world fuel consumption of the tested vehicles, compared to the certification cycle results, was on average 23% higher, 21% higher for diesel vehicles, from 4% below to 59% above, and 24% higher for petrol vehicles, from 3% below to 55% above. One LPG vehicle had a real-world fuel consumption 27% higher than the certification cycle result. One plug-in hybrid vehicle had a real-world fuel consumption 166% higher than the certification cycle result with a full state of charge, and 337% higher when tested with a low state of charge. Fuel consumption figures for vehicles with diesel particulate filters include the application of a correction factor to account for filter regeneration.

The discrepancies between the laboratory tests and real-world driving were thus different not only for vehicles fitted with CIDI diesel ICEs, but also for vehicles with SI gasoline ICEs, and traditional as well as hybrid powertrains. However, the major difference was the NOx emissions of the CIDI diesel ICEs. In the latest EURO rules, vehicles were requested to meet increasingly stringent emission standards of regulated pollutants, while also reducing CO_2 emissions. As these requirements were conflicting and difficult to meet, the discrepancy between the real-world fuel consumption and the certification cycle results increases with the standard. The Euro 6 compliant vehicles had the highest discrepancy between the real world and certification cycle results.

Regarding emissions, 13 vehicles exceeded the NOx specific emission prescribed for the certification cycle. Of these 13 vehicles, 11 were diesel vehicles. Only 1 of 12 diesel vehicles delivered a NOx specific emission within the limit of the certification cycle. Five petrol vehicles exceeded the CO limit of the certification cycle. Only 1 diesel vehicle exceeded the PM limit of the certification cycle. On average, diesel vehicles' NOx and PM emissions were 24 and 26 times higher than that of petrol vehicles, while diesel vehicles' CO emissions were 10 times lower than that of petrol vehicles. The diesel vehicles exceeded the NOx limit of the certification cycle by 370%, while the petrol vehicles emitted 43% of the NOx limit of the certification cycle. The petrol vehicles emitted 95% of the CO limit of the certification cycle. The diesel vehicles emitted 20% of the CO limit of the certification cycle. For what concerns PM, the diesel vehicles emitted 43% of the PM limit of the certification cycle, and the 2-petrol gasoline direct injection (GDI) vehicles emitted 26% of the PM limit of the certification cycle. For what concerns the NOx emissions of lean-burn CI engines, the measured results were better than what was claimed during "*diesel gate,*" or it is claimed in works such as (Chossière et al., 2018).

New rules have been introduced since "*diesel gate,*" and CIDI diesel engines have been improved. European real-world driving emissions data of post-new rules vehicles are proposed by ACEA (2018a). In a properly conducted experimental campaign, under repeatable conditions, with adequate equipment, and applying the scientific method, the European Automobile Manufacturers' Association (ACEA), has recently shown that all the 270 diesel vehicles tested were below the emission limits of the newly defined real-world driving (RDE) tests, both total and urban. None of the vehicles was above the NOx specific emission of 165 mg/km that is now prescribed (ACEA, 2018a), **Figure 1**. The detailed type-approval results for the 270 RDE-compliant diesel vehicle types are available in ACEA (2018b). The RDE results for individual vehicles can be found at (ACEA, 2018c).

The new data released by the ACEA supply unambiguous evidence that the latest-generation diesel vehicles emit low pollutant emissions on the road and are fuel-efficient. The tests were performed in real-driving conditions by the drivers of the various national type-approval authorities. The 270 new types of diesel cars certified against the latest Euro 6d-TEMP standard were introduced on the European market over the previous year. All these diesel cars performed very well below the NOx threshold

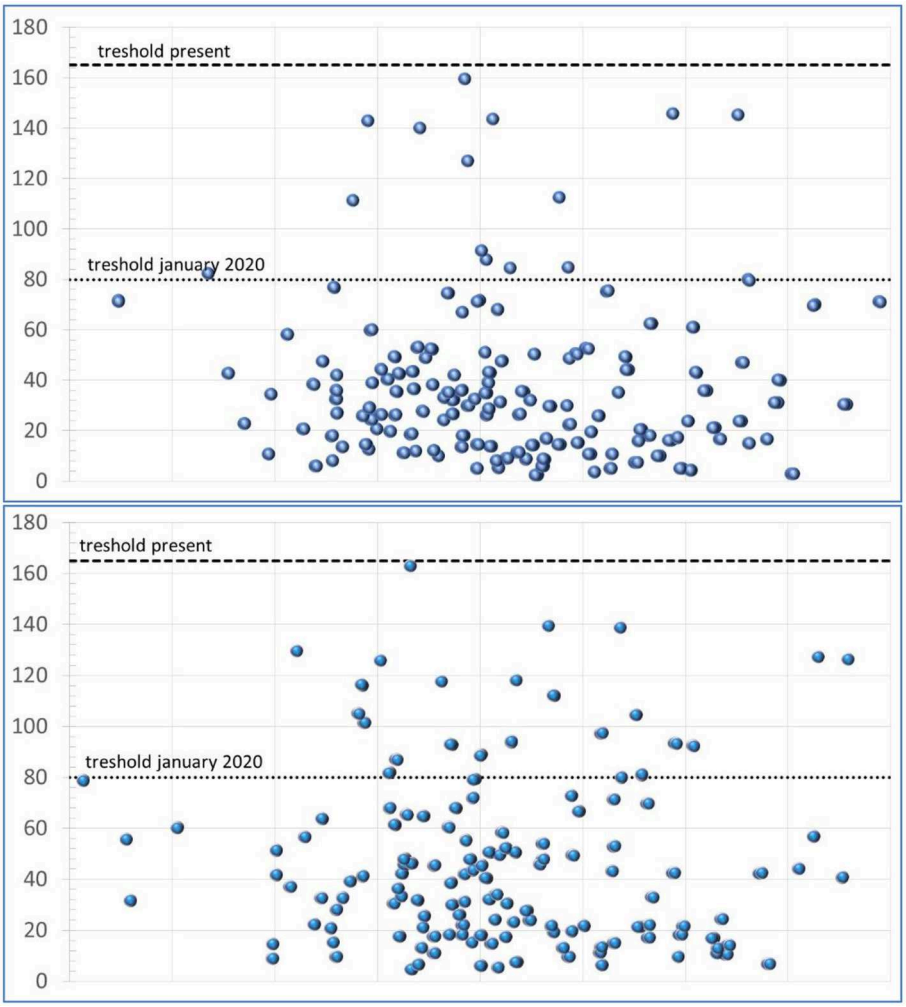

FIGURE 1 | Real-world driving emissions of NOx of diesel vehicles. NOx total (mg/km) vs. PM total (#/km). Top total RDE. Bottom urban RDE. Data digitized from www.acea.be/uploads/press_releases_files/RDE-compliant_diesels_November_2018.pdf.

of the RDE test, which now applies to all new car types since September 2017. Most of these vehicles have NOx emissions well below the stricter threshold that will be mandatory from January 2020. The RDE test ensures that pollutant emission levels measured during the new WLTP laboratory test are confirmed on the road. Every car tested stands for a "*family*" of similar cars of differing variants. This activity proves that the diesel vehicles now available on the market are low-emitting in any reasonable condition. The German automobile club (ADAC) recently estimated that there were 1,206 different RDE-compliant cars available on 30 October 2018, both gasoline and diesel (ADAC, 2018a). Hence, CIDI diesel ICEs do not deserve the bad reputation they got because of the "*diesel gate,*" that is a political more than a technological issue.

Modern diesel vehicles, supported by fleet renewal policies and combined with alternative powertrains, may play a strong role in helping cities to move toward compliance with air quality targets while improving fuel efficiency and reducing CO_2 emissions in the short and medium-term. Recent on-road testing by the ADAC (2018b) found that the latest diesel vehicles emit 85% less NOx on average than Euro 5 cars, with the best-performing RDE-compliant Euro 6 diesel vehicles emitting as much as 95–99% less NOx than Euro 5 vehicles. Every car tested emit less than the limits for every regulated pollutant. These cars also supply an exceptional fuel economy. Additionally, there is the opportunity to produce even less CO_2, and less regulated pollutant, moving to dual-fuel diesel-LNG, CNG, or LPG.

PM BENEFITS OF DIESEL VEHICLES

Diesel engines are not targeted because of their PM contribution by the transportation sector to the overall air quality. However, as the air quality is poor in many parts of the world, and diesel particulate filters can help to improve the air quality, the PM argument may actually be played in favor of the diesel-based

mobility, also against alternatives such as the electric mobility. While it is incorrect to claim that the more recent diesel vehicles emit "*excess*" NOx and make worse the air quality, the more recent diesel vehicles contribute to cleaning the air of polluted areas, for example of PM. From **Table 1**, old diesel vehicles were produced compliant with much less restrictive PM rules. Air pollutants are emitted from many natural and anthropogenic sources, the latter including the burning of fossil fuels in power generation, industry, households, transport, industrial processes, solvent uses, agriculture, and waste treatment. Hence, to have vehicles with tailpipe PM emissions potentially lower than in the intake is an opportunity to clean up the air.

Environmental tobacco smoke (ETS) causes fine PM indoor pollution exceeding the outdoor limits of vehicles. Data comparing PM emission from ETS and a Euro 3 diesel vehicle show indoor PM concentrations up to 10-fold those emitted from the idling Euro 3 diesel vehicle (Invernizzi et al., 2004). PM limits have been drastically improved in Euro 4, 5, and 6, 10 times to be precise. The World Health Organization (WHO) study (Martuzzi et al., 2006) shows a significant health impact of PM_{10} on urban populations of 13 large Italian cities, assessed in 8,220 deaths a year, attributable to PM_{10} concentrations above 20 μg/m. This is 9% of the mortality for all causes (excluding accidents) in the population over 30 years of age. These levels of PM_{10} are not the result of the circulation of the latest, clean diesel vehicles.

The performances of diesel particulate filters (DPF) are relatively complex (Fiebig et al., 2014). The latest DPF technologies are more effective on larger sizes while less effective, or even negative, on the smaller nanometric sizes. Monitoring is often limited to PM_{10}–particles of 10-micrometer diameter—or $PM_{2.5}$–particles of 2.5-micrometer diameter. DPF can capture from 30% to more than 95% of the micrometric PM (Barone et al., 2010). With optimal DPF, PM emissions may be decreased to 0.001 g/km or less (Fiebig et al., 2014), down 5 times from the present 0.005 of Euro 6. While this mass measure does not pay justice to pollution by sub-micrometric and nanometric particles, there is no present control of this type of pollutant from any source.

If new diesel vehicles do not emit more NOx than older diesel vehicles, they certainly emit much less PM, with possibly in some circumstances, the ability to clean the air of the PM produced by other sources, that are not adequately targeted by the policymakers. The case of Hong Kong, that is not the worse on Earth, is reported in Haas (2017). In addition to local emissions from various sources, including passenger vehicles, there is Hong Kong a significant amount of pollutants brought from mainland China. While data of pollutants in China is limited, it is well-known that Hong Kong is facing serious health issues linked to air pollution mostly imported from the mainland. Hong Kong's air pollution is not as bad as it is in China, or India, where the toxic cloud dubbed "*airpocalypse*" often covers substantial portions of these countries, but it is still one good example of more latest diesel vehicles replacing on the road older vehicles making a positive impact.

Of the many types of aerosol particles circulated in the atmosphere, one of the most damaging is $PM_{2.5}$. Many areas of China and India have levels of $PM_{2.5}$ and PM_{10} much larger than the WHO guidelines, **Figure 2**. The WHO guidelines (annual

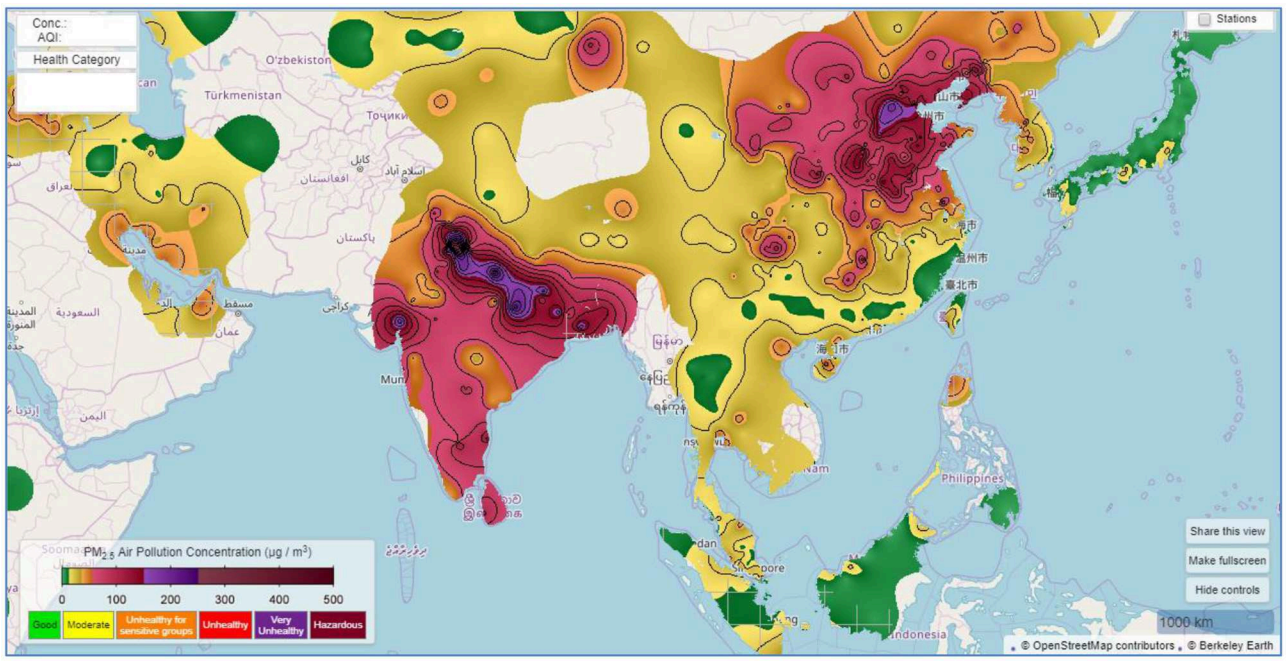

FIGURE 2 | Nearly real-time $PM_{2.5}$ map for Asia during Autumn 2018. Only the areas covered by stations are shown. Image from Berkeley Earth, www.berkeleyearth.org.

mean) are $PM_{2.5}$ of 10 $\mu g/m^3$ and PM_{10} of 20 $\mu g/m^3$. Across the world, the mean ambient air pollution ranges from <10 to over 100 $\mu g/m^3$ for $PM_{2.5}$, and from <10, to over 200 $\mu g/m^3$, for PM_{10}. There are widespread cases of poor air quality not limited to China and India. However, China's south coast industrial heartland is one of the areas with the worse pollution, like Beijing and Delhi. While Beijing's "*airpocalypse*" is being clamped down on by drastic measures, mostly targeting the use of coal, but also limiting the circulation of any vehicle (South China Morning Post, 2018), Delhi's "*airpocalypse*" is reaching a new dramatic high, also thanks to "*stubble burning*" from neighborhoods (Indiatimes, 2018).

The air quality in Hong Kong is everything but excellent (Haas, 2017). Levels of pollutants have exceeded the WHO standards for over 15 years. At peaks, they have reached more than five times the acceptable levels. Emissions from vehicles and ships are some of the largest local contributors to pollution. Power plants also have their role, being reliant almost entirely on fossil fuels, mostly coal. However, about 60-70% of the PM comes from mainland China. This flux is extremely relevant especially in winter when the imported PM is about 77% of the total. Asthma and bronchial infections have rocketed in recent years. In Hong Kong alone, there were more than 1,600 actuals, not hypothetical as those of Chossière et al. (2018), premature deaths in 2016 only because of air pollution (Haas, 2017).

In addition to improved fuel standards and expansion of the use of electric vehicles, significant uptake of recent diesel vehicles equipped with particle traps may further contribute to the improved air quality of a city that still falls short of any WHO guideline. Regarding the opportunity to use electric vehicles, recharged by combustible fuel power plants, the EV may actually contribute to PM pollution. According to Hodan and Barnard (2004), the largest source of $PM_{2.5}$ from anthropogenic sources are from tire and road surface wear. As the electric vehicles are heavier and have more instant torque than ICE based cars, they produce a lot more $PM_{2.5}$. Hence, more EV will make Hong Kong even dirtier of PM, as they produce $PM_{2.5}$ and they cannot burn the PM produced by other sources, like a CIDI diesel ICE fitted with a particle trap.

As shown in **Figure 1** and **Table 1**, vehicles fitted with the latest CI engines do not produce excess NOx, and from **Figures 2**, **3**, there are many areas of the world with PM concentrations in the air much larger than what can be found at the tailpipe of vehicles fitted with the latest CIDI diesel engines, **Table 1**, and NO_2 concentrations also quite large. The dual-fuel operation with LNG, CNG or LPG, with an otherwise unchanged vehicle that keeps the particulate filter, may contribute even more to the cleaning of the ambient air from particulate.

ADVANTAGES OF DUAL-FUEL DIESEL-LNG/LPG/CNG

Current Technology

Diesel-LNG (Goudie et al., 2004; Osorio-Tejada et al., 2015; Laughlin and Burnham, 2016), diesel-CNG (Maji et al., 2008; Shah et al., 2011; Ryu, 2013) or diesel-LPG (Jian et al., 2001; Ashok et al., 2015) engines supply like diesel fuel conversion efficiency and power density, while improving the emissions, for both regulated pollutants (PM, NOx) and CO_2. LNG can be used for heavy-duty trucks, due to the cryogenic storage. LPG (and CNG) may be preferred in passenger cars and light-duty vehicle applications.

Diesel engines still generate significant amounts of carbon dioxide (CO_2) and engine-out emissions of particulate matter (PM), because of the diffusion combustion of the heavy hydrocarbon, high C/H ratio, liquid diesel fuel. Nitrogen oxides (NOx) engine-out emissions are also intrinsic to the lean-burn operation in excess air (Heywood, 1988). Both PM and NOx can be reduced through the after-treatment, albeit diesel combustion strategies are often determined for the best NOx-PM trade-off.

The use of a reduced carbon content gaseous fuel such as natural gas, that is mostly methane CH_4, in liquid form as LNG, or gas form as CNG, or liquified petroleum gas (LPG), that is mostly propane C_3H_8, has intuitive major advantages in CO_2 emissions vs. the diesel, of variable composition but roughly $C_{13.5}H_{23.6}$. Being vaporization much easier, there are also advantages for engine-out PM emissions, and thus indirectly also of engine-out NOx emissions, vs. the diesel (Kathuria, 2004; Chelani and Devotta, 2007; Yeh, 2007; Engerer and Horn, 2010; Lin et al., 2010; Kumar et al., 2011).

LNG, CNG, and LPG have smaller carbon-to-hydrogen ratios. Hence, much less CO_2 is emitted to produce the same output with about the same fuel conversion efficiency. CNG is injected gas. LNG is also gas in normal conditions. LPG is liquid in normal conditions, but it vaporizes much quicker than the diesel. This practically reduces to zero the PM emissions (apart from those originating from the pilot diesel). As LNG, CNG and LPG are high octane low cetane fuels, they are difficult to use alone in a compression ignition engine. The issue is solved with the dual fuel operation (westport.com, 2019a,b). A small amount of diesel fuel produces the ignition. The LNG, CNG or LPG injected prior or after the diesel injection ignition may then burn premixed or diffusion. The first combustion phase produces a rapid pressure build-up. The rate of combustion of the second phase is determined by the injection rate of the LNG, CNG, or LPG, is targeting pressure maintenance during the first part of the expansion stroke.

One major issue with the use of LNG or CNG is the specific volume of the fuel, as the density of the gas is low at normal conditions. This creates problems for the injection system, that needs injectors with much larger cross-sectional areas of the diesel, and makes much more difficult the fast actuation, multiple injection capabilities, proper of the latest diesel injectors. This is also a problem for the storage, as the volume of fuel needed for a given amount of energy onboard the vehicle is much larger than the diesel. LNG has a better volumetric density, but it needs a cryogenic system to keep the temperature low. CNG has a smaller volumetric density and additionally needs pressurized tanks.

The Westport HPDI system for diesel and CNG/LNG is a technology very well-proven by decades (Li et al., 1999; westport.com, 2015). In the beginning, HPDI was a simple main injection of natural gas following the pilot/pre-diesel injection. Recently, HPDI is evolving toward more complex strategies,

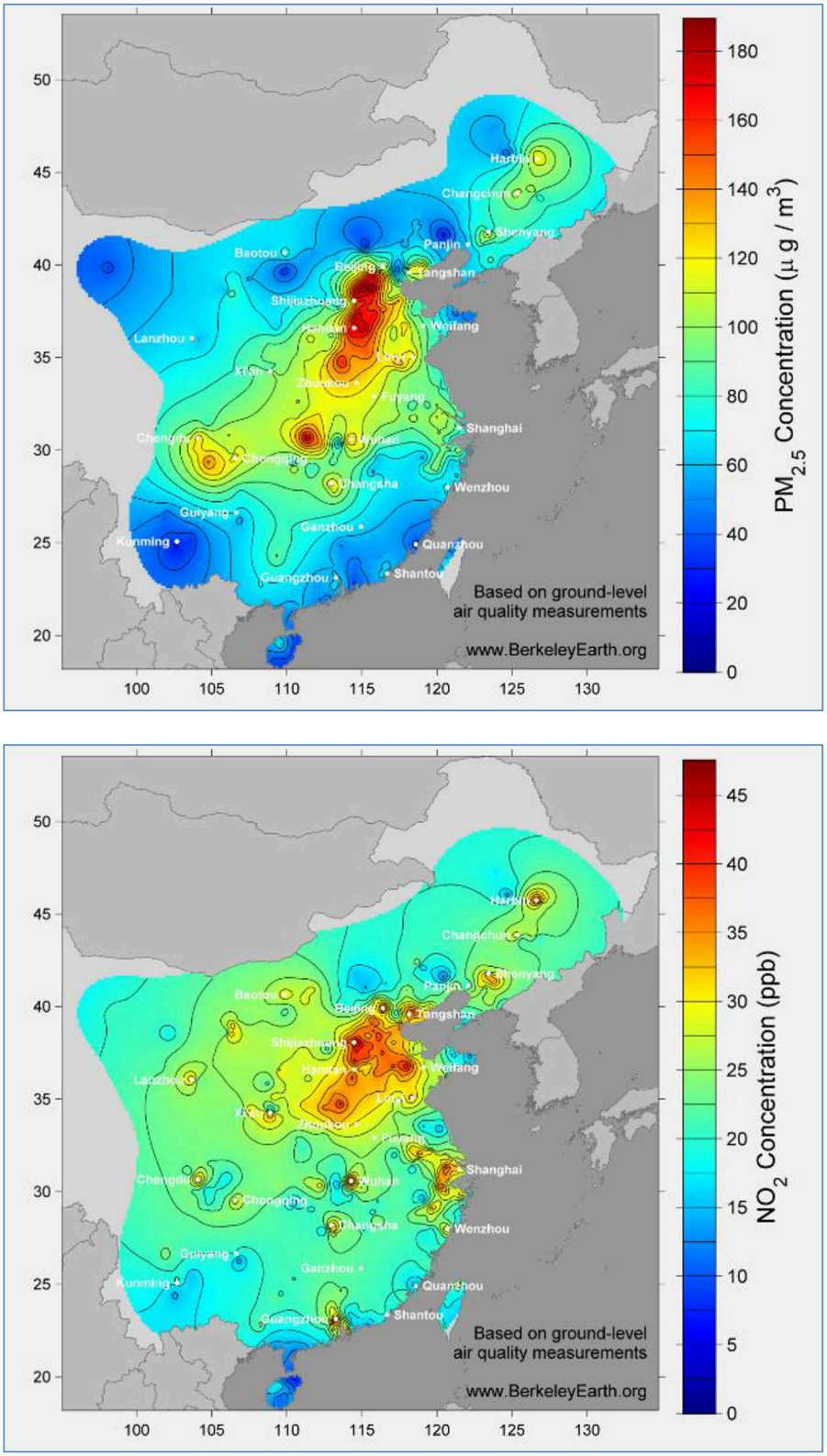

FIGURE 3 | Average monthly concentrations for China during January 2015 of $PM_{2.5}$, top, and NO_2, bottom. Images from Berkeley Earth, www.berkeleyearth.org.

modulating premixed and diffusion combustion of the natural gas, as suggested by Boretti (2013).

Traditional HPDI in heavy-duty ICEs allows a natural gas ICE to keep diesel-like performance while deriving most of its power from natural gas. A small diesel pilot injection (5–10% of the fuel energy) is used to ignite the directly injected gas jet. The natural gas burns in a mixing-controlled, diffusion, combustion mode (Li et al., 1999; westport.com, 2015).

Future Technology

Several works describe the development trends in HPDI technology. McTaggart-Cowan et al. (2015) report on 600 bar dual fuel injectors for the LNG. The LNG combustion event is limited by the injection pressure, which dictates the rate of mixing and combustion. Significant efficiency improvements and PM reductions are achieved at high loads, and especially at higher speeds, by increasing the injection pressure from the traditional 300 bar to the latest 600 bar. Combustion is an injection rate limited. McTaggart-Cowan et al. (2015) report efficiency benefits of higher pressures about 3%, added to PM reductions of 40–60%.

Different nozzle shapes were considered by Mabson et al. (2016). A "*paired-hole nozzles*" injector was designed to reduce PM formation by increasing air entrainment due to jet interaction. CO and PM emissions were opposite 3–10 times higher with the paired hole nozzles. The paired hole nozzle produced larger soot aggregates and larger numbers of particles.

Mumford et al. report improvements of Westport HPDI 2.0, (Mumford et al., 2017). HPDI 2.0 delivers better performances and emissions vs. the first generation HPDI as well as the baseline diesel only. Mumford et al. (2017) also discuss the potential and challenges of higher injection pressures.

Diffusion-controlled and partially premixed combustion strategies are considered by Florea et al. (2016) by using the Westport HPDI. The partially premixed combustion, called DI_2 shows promise, improving engine efficiency of more than 2 efficiency points, compared to the diffusion-controlled combustion strategy. Modulation of the two combustion phases, potentially more rewarding, is not investigated in the work.

The DI_2 combustion mode is also studied in Neely et al. (2017). The natural gas is injected during the compression stroke prior to the diesel injection ignition. This partially premixed combustion of the natural gas is shown to improve both the thermal and the combustion efficiencies over traditional fumigated dual-fuel combustion mode. The partially premixed combustion of the natural gas also supplies thermal efficiency improvement over the baseline diffusion-controlled combustion where the natural gas injection occurs after the diesel ignition injection.

The effect of injection strategies on the emissions and engine performances from an HPDI engine is studied by Faghani et al. (2017a,b). They investigate the effect of late post-injection (LPI), as well as slightly premixed combustion (SPC) on emission and engine performance. With SPC, the diesel injection is delayed. High load SPC operation reduces over 90% the PM with a 2% improvement in fuel efficiency with the almost same level of NOx. SPC has however large cycle-to-cycle variation and excessive rate of pressure build-up. PM does not increase for SPC with higher EGR level, higher global oxygen-based equivalence ratio (EQR) or higher pilot mass, which normally increases PM in mixing-controlled HPDI combustion. LPI, a post-injection of 10–25% of the total fuel occurring after the main combustion event, results in significant PM reductions with only small effects on other emissions and engine performance. The main PM reduction from LPI is due to the reduced amount of fuel in the first injection. The second injection makes an insignificant net contribution to the total PM.

The Westport HPDI dual fuel diesel-LNG injector is producing excellent results. However, there is a fundamental downfall of this approach. It does not offer the same performance of a latest-generation diesel-only injector, in both flow rate, speed of actuation, and atomization of the diesel. Thus, it may be preferable to couple to one latest generation diesel-only injector, with a dedicated injector for the second fuel, to deliver better injection performances for the diesel as well as the second fuel. Higher injection pressures and faster actuation are drivers of improved combustion patterns.

Dual fuel diesel-hydrogen CIDI ICEs featuring this possibility of two direct injectors per cylinder were studied for example in (Boretti, 2011b,c). One injector was used for the diesel, and one for the hydrogen. A modeled diesel engine converted to dual fuel diesel-hydrogen following this approach was shown to deliver full load efficiencies up to 40–45%, and reduced penalties in efficiencies reducing the load working slightly better than the baseline diesel in every operating point. While the use of two injectors per cylinder does not pose an issue for new engines, it is difficult to introduce two injectors when retrofitting existing diesel engines. Dedicated direct injectors for LNG, LPG, or CNG, need to be further evolved for the specific application.

The use of two dedicated injectors, rather than one dual fuel injector, of higher injection pressure, faster actuation, and complete independence of the individual fuels' injection, allows much more flexibility in injection shaping. The dual-fuel operation is typically characterized by pilot/pre-diesel injections, followed by the main second fuel injection. Preferably, the second fuel has not to be all injected after the diesel injection ignition. It may be injected before, or at the same time as the diesel, or after the diesel, not only in a single injection but in multiple injections. Thus, the second fuel may burn partially premixed and partially diffusion.

Different combustion modes are possible. "*Controlled*" HCCI is one of these modes. In controlled HCCI, the second fuel is injected first, and the diesel injection ignition occurs prior to the expected start of the HCCI autoignition (Boretti, 2011a,b). HCCI has no advantage, in terms of fuel conversion efficiency, vs. the bulk combustion in the center of the chamber surrounded by a cushion of air. Homogeneous combustion always suffers from larger heat losses at the walls and incomplete combustion for the quenching of the flame. HCCI also does not produce a peak pressure during the expansion stroke, delivering peak pressure exactly at top dead center. However, HCCI may have advantages for engine-out emissions, as it is an extremely low-temperature process, and it is the combustion event much closer to the theoretically best isochoric combustion of pressure cycle analyses.

The most interesting modes are premixed, diffusion or modulated premixed and diffusion in the center of the chamber. In premixed, but stratified combustion, the second fuel is injected at the center of the chamber and burned by the diesel injection before filling homogeneously all the chamber. In diffusion combustion, the second fuel is injected at the center of the chamber, after the diesel injection ignition has created suitable conditions for the next combustion to progress diffusion-controlled, and there it burns. There is the scope for pre- injections of the second fuel, as well as contemporary, or post-injections of the second fuel, with reference to the diesel pilot/pre-injection ignition, to be carefully shaped for producing the best fuel conversion efficiency, within constraints of engine-out emissions, pressure build-up rate, and peak pressure.

THE ELECTRIC MOBILITY ALTERNATIVE IS STILL PREMATURE

The environmental friendliness and economy of the diesel-based mobility fact is not recognized by many countries, that have otherwise deliberated toward a premature move to the electric mobility, without having addressed first the many issue of electric vehicles, i.e., the high economic and environmental costs to build, run and dispose of the cars, the limited performances of these heavy vehicles due to the still inadequate battery technologies, the lack of a recharging infrastructure only feed by renewable energy.

Nominally to address global warming, more than air pollution, Britain, France, and China have deliberated the end of the ICE-based mobility by 2040. However, the IEA data (IEA, 2018), shows that the production of electricity geothermal, solar, wind, tide, wave, and the ocean was still about 1% of the total in 2015, with the total primary energy supply (TPES) that is largely exceeding the electricity production. With the solar and wind share of the TPES still small, it does not make any sense to propose only electric vehicles, even forgetting the other key issues embedded in the electric mobility quest.

Presently, the CO_2 emission life cycle analyses (LCA), do not show a clear advantage of electric vs. ICE-based mobility (Boretti, 2018). The LCA case for electric mobility critically depends on how the electricity is generated, that without an enormous increment of the energy storage, more than the simple increase of the registered capacity of wind and solar, needs back up by fossil fuels. Since the 1990s, there have been advancements, but not yet the breakthroughs needed, in battery technologies. It is still too expensive, economically, and environmentally, to produce, use and dispose of electric vehicles, with the added challenge of the materials needed to produce the batteries that are at a greater risk of depletion than the fossil fuels (Boretti, 2018). Additionally, these materials are unethically mined in very few places.

Amnesty International (Onstad, 2019) recently pointed out as the electric vehicle (EV) industry is selling itself as environmentally friendly but is producing many of its batteries using fossil fuels and unethically sourced minerals tainted by human rights abuses. It is unlikely that there are enough raw materials to meet the dramatic demand expected for lithium-ion batteries of electric vehicles, and grid-connected battery systems for storing intermittent wind and solar renewable energy electricity (Jaffe, 2017). Furthermore, without any clear path considered for recycling, and the negative past (and present) examples of recycling by industrialized countries at the expense of environmental damage in developing countries (Minter, 2016), the electric mobility may translate in considerable damage to the economy and the environment.

While the electric mobility may certainly solve some of the issues of air pollution-related to transport, it is unlikely it may occur soon, it does not address the pollution from other sources, and it is not yet that friendly, in the big picture, where everything is included. Consumption of combustion fuels is still dramatically increasing, and there are very few examples of technological opportunities to convert the chemical energy of the fuels into mechanical or electrical power with a better fuel energy conversion efficiency, and reduced pollutant emissions, of the CIDI diesel ICEs. There will be enormous costs, also in terms of GHG emissions, to switch to electric mobility in the transportation sector.

DISCUSSION AND CONCLUSIONS

Although the ICCT, US EPA, and CARB depict diesel vehicles as being bad for the environment, the latest real-world driving tests conducted by ACEA show that this is incorrect. Modern diesel vehicles have relatively low CO_2 and pollutant emissions, including NOx, and PM. As they are, the circulation of diesel vehicles in highly polluted areas may improve the quality of the air that is polluted by other sources, not only older diesel vehicles.

CIDI diesel ICEs can be made better, much more environmentally friendly, thanks to the further developments in the injection system as well as the after-treatment. CIDI ICEs may also be improved by simply adopting dual-fuel designs, with LPG, CNG, or LNG the second fuel. These alternative fuels allow the same, or better, performances of the diesel-only ICE, for what concerns steady-state torque, power, and fuel conversion efficiency, and transients, while dramatically improving the CO_2 emissions, as well as the PM and NOx engine-out emissions.

In addition to the better C-H ratio for what concerns the CO_2 emission, the advantages of the dual-fuel CIDI ICEs with LNG, CNG, or LPG also originate from the opportunity of modulating premixed and diffusion phases of combustion injecting the second fuel, that is much easier to vaporize, and less prone to auto-ignition, prior, contemporary or after the pre/pilot diesel. Also relevant especially with LNG is the cooling effect due to the cryogenic injection. Further developments in the injection system are the area of major concern for the development of these novels CIDI dual-fuel ICEs.

The advantages of CIDI ICEs, diesel or dual-fuel vs. every other alternative solution for transport applications, are presently not acknowledged by any policymaker. The European carmakers have already stopped their research and development plans for their ICEs to focus only on electric cars. Considering the unresolved issues embedded in electric mobility, this may prove shortly to be wrong for the economy and the environment. The use of more recent diesel vehicles, and dual fuel diesel-alternative fuels vehicles, may

only save lives, not cause mortalities, improving air quality, while limiting the depletion of natural resources and the emission of CO_2 without requiring unaffordable efforts and dramatic changes.

AUTHOR CONTRIBUTIONS

The author confirms being the sole contributor of this work and has approved it for publication.

REFERENCES

ABMARC (2017). *Real-World Driving. Fuel Efficiency and Emissions Testing*. Available online at: www.aaa.asn.au/storage/2017-abmarc-aaa-rde-report-executive-summary-first-17.pdf

ACEA (2018a). *Diesel: New Data Proves That Modern Diesel Cars Emit Low Pollutant Emissions on the Road*. Available online at: www.acea.be/press-releases/article/diesel-new-data-proves-that-modern-diesel-cars-emit-low-pollutant-emissions

ACEA (2018c). *RDE Results for Individual Vehicles*. Available online at: www.acea.be/publications/article/access-to-euro-6-rde-monitoring-data

ACEA (European Automobile Manufacturers' Association) (2018b). *The Type-Approval Results for the 270 RDE-Compliant Diesel Vehicle Types*. Available online at: www.acea.be/uploads/press_releases_files/RDE-compliant_diesels_November_2018.pdf

ADAC (2018a). *Overview of RDE-Compliant Cars Available on the Market*. Available online at: www.adac.de/infotestrat/umwelt-und-innovation/abgas/modelle_mit_euro_6d_temp/

ADAC (2018b) *Ecotest, Moderne Diesel Sind Sehr Sauber*. Available online at: www.presse.adac.de/meldungen/adac-ev/technik/euro6-d-temp-diesel-sind-sehr-sauber.html

Ambrogio, M., Saracco, G., and Specchia, V. (2001). Combining filtration and catalytic combustion in particulate traps for diesel exhaust treatment. *Chem. Eng. Sci.* 56, 1613–1621. doi: 10.1016/S0009-2509(00)00389-4

Ashok, B., Ashok, S. D., and Kumar, C. R. (2015). LPG diesel dual fuel engine–A critical review. *Alexand. Eng. J.* 54, 105–126. doi: 10.1016/j.aej.2015.03.002

Audi (2014). *The Racing Engines*. Available online at: www.audi-mediacenter.com/en/the-audi-tdi-tech-workshop-2014-3039/the-racing-engines-3109

Autocar (2018). *BMW to Cease Production of the i3 Range Extender*. Available online at: www.autocar.co.uk/car-news/new-cars/bmw-cease-production-i3-range-extender

Ayre, M. (2007). *Will Biofuel Leave the Poor Hungry*?. Available online at: news.bbc.co.uk/1/hi/business/7026105.stm

Barone, T. L., Storey, J. M., and Domingo, N. (2010). An analysis of field-aged diesel particulate filter performance: particle emissions before, during, and after regeneration. *J. Air Waste Manage. Assoc.* 60, 968–976. doi: 10.3155/1047-3289.60.8.968

Boretti, A. (2011a). Diesel-like and HCCI-like operation of a truck engine converted to hydrogen. *Int. J. Hydr. Energy* 36, 15382–15391. doi: 10.1016/j.ijhydene.2011.09.005

Boretti, A. (2011b). Advances in hydrogen compression ignition internal combustion engines. *Int. J. Hydr. Energy* 36, 12601–12606. doi: 10.1016/j.ijhydene.2011.06.148

Boretti, A. (2011c). Advantages of the direct injection of both diesel and hydrogen in dual fuel H2ICE. *Int. J. Hydr. Energy* 36, 9312–9317. doi: 10.1016/j.ijhydene.2011.05.037

Boretti, A. (2013). Latest concepts for combustion and waste heat recovery systems being considered for hydrogen engines. *Int. J. Hydr. Energy* 38, 3802–3807. doi: 10.1016/j.ijhydene.2013.01.112

Boretti, A. (2017). *The Future of the Internal Combustion Engine After "Diesel-Gate*. Warrendale, PA: SAE Technical Paper 2017-28-1933. doi: 10.4271/2017-28-1933

Boretti, A. (2018). *Life Cycle Analysis Comparison of Electric and Internal Combustion Engine Based Mobility*. Warrendale, PA: SAE Technical Paper 2018-28-0037. doi: 10.4271/2018-28-0037

Boretti, A., and Castelletto, S. (2018). "Super-turbo-charged direct injection jet ignition gasoline engine," in *Proceedings of the FISITA World Automotive Conference, 2–5 OCTOBER 2018* (Chennai).

Boretti, A., and Lappas, P. (2019). Complex independent laboratory tests to signify fuel economy and emissions under real world driving. *Adv. Technol. Innovat.* 4, 59–72.

Boretti, A., and Ordys, A. (2018). *Super-Turbocharging the Dual Fuel Diesel Injection Ignition Engine*. SAE Technical Paper 2018-28-0036. doi: 10.4271/2018-28-0036

Burtscher, H. (2005). Physical characterization of particulate emissions from diesel engines: a review. *J. Aerosol. Sci.* 36, 896–932. doi: 10.1016/j.jaerosci.2004.12.001

Camuzeaux, J. R., Alvarez, R. A., Brooks, S. A., Browne, J. B., and Sterner, T. (2015). Influence of methane emissions and vehicle efficiency on the climate implications of heavy-duty natural gas trucks. *Environ. Sci. Technol.* 49, 6402–6410. doi: 10.1021/acs.est.5b00412

CARB (2012). *Final Statement of Reasons For Rulemaking Including Summary of Comments and Agency Responses. 2012 Amendments to the Zero Emission Vehicle Regulations*. Available online at: www.arb.ca.gov/regact/2012/zev2012/zevfsor.pdf

Chelani, A. B., and Devotta, S. (2007). Air quality assessment in Delhi: before and after CNG as fuel. *Environ. Monit. Assess.* 125, 257–263. doi: 10.1007/s10661-006-9517-x

Chossière, G. P., Malina, R., Allroggen, F., Eastham, S. D., Speth, R. L., and Barrett, S. R. (2018). Country-and manufacturer-level attribution of air quality impacts due to excess NOx emissions from diesel passenger vehicles in Europe. *Atmos. Environ.* 189, 89–97. doi: 10.1016/j.atmosenv.2018.06.047

Crabtree, G. W., Dresselhaus, M. S., and Buchanan, M. V. (2004). The hydrogen economy. *Phys. Today* 57, 39–44. doi: 10.1063/1.1878333

EIA (2018). *Table 8.2. Average Tested Heat Rates by Prime Mover and Energy Source, 2007 – 2017*. Available online at: www.eia.gov/electricity/annual/html/epa_08_02.html

Engerer, H., and Horn, M. (2010). Natural gas vehicles: an option for Europe. *Energy Policy* 38, 1017–1029. doi: 10.1016/j.enpol.2009.10.054

Faghani, E., Kheirkhah, P., Mabson, C., McTaggart-Cowan, G., et al. (2017a). *Effect of Injection Strategies on Emissions from a Pilot-Ignited Direct-Injection Natural-Gas Engine- Part I: Late Post Injection*. Warrendale, PA: SAE Paper 2017-01-0774. doi: 10.4271/2017-01-0774

Faghani, E., Kheirkhah, P., Mabson, C., McTaggart-Cowan, G., et al. (2017b). *Effect of Injection Strategies on Emissions from a Pilot-Ignited Direct-Injection Natural-Gas Engine- Part II: Slightly Premixed Combustion*. Warrendale, PA: SAE Technical Paper 2017-01-0763. doi: 10.4271/2017-01-0763

Fiebig, M., Wiartalla, A., Holderbaum, B., and Kiesow, S. (2014). Particulate emissions from diesel engines: correlation between engine technology and emissions. *J. Occup. Med. Toxicol.* 9:6. doi: 10.1186/1745-6673-9-6

Florea, R., Neely, G., Abidin, Z., and Miwa, J. (2016). *Efficiency and Emissions Characteristics of Partially Premixed Dual-Fuel Combustion by Co-Direct Injection of NG and Diesel Fuel (DI2)*. Warrendale, PA: SAE Paper 2016-01-0779. doi: 10.4271/2016-01-0779

Freymann, R., Ringler, J., Seifert, M., and Horst, T. (2012). The second generation turbosteamer. *MTZ Worldwide* 73, 18–23. doi: 10.1365/s38313-012-0138-1

Freymann, R., Strobl, W., and Obieglo, A. (2008). The turbosteamer: a system introducing the principle of cogeneration in automotive applications. *MTZ Worldwide* 69, 20–27. doi: 10.1007/BF03226909

Goudie, D., Dunn, M., Munshi, S. R., Lyford-Pike, E., Wright, J., Duggal, V., et al. (2004). *Development of a Compression Ignition Heavy Duty Pilot-Ignited Natural Gas Fuelled Engine for Low NOx Emissions (No. 2004-01-2954)*. Warrendale, PA: SAE Technical Paper. doi: 10.4271/2004-01-2954

Haas, B. (2017). *Where the Wind Blows: How China's Dirty Air Becomes Hong Kong's Problem*. Available online at: www.theguardian.com/cities/2017/feb/16/hong-kong-death-trap-dirty-air-pollution-china

Heywood, J. B. (1988). "Combustion in compression-ignition engines," in *Internal Combustion Engine Fundamentals* (New York, NY:McGraw-Hill), 522–562.

Hiroyasu, H., and Kadota, T. (1976). Models for combustion and formation of nitric oxide and soot in direct injection diesel engines. *SAE Trans.* 85, 513–526. doi: 10.4271/760129

Hodan, W. M., and Barnard, W. R. (2004). *Evaluating the Contribution of PM2. 5 Precursor Gases and Re-entrained Road Emissions to Mobile Source PM2. 5 Particulate Matter Emissions*. Research Triangle Park, NC: MACTEC Federal Programs. Available online at: www3.epa.gov/ttnchie1/conference/ei13/mobile/hodan.pdf

IEA (2018). *IEA World Energy Balances 2018*. Available online at: webstore.iea.org/world-energy-balances-2018

IEA (2019). *Transport Biofuels*. Available online at: www.iea.org/tcep/transport/biofuels/

Inderwildi, O. R., and King, D. A. (2009). Quo vadis biofuels? *Energy Environ. Sci.* 2, 343–346. doi: 10.1039/b822951c

Indiatimes (2018). *Construction Activities Banned Till November 12 To Save Delhi From 'Airpocalypse'. But Is It Enough?* Available online at: www.indiatimes.com/news/india/construction-activities-banned-till-november-12-to-save-delhi-from-airpocalypse-but-is-it-enough-356413.html

Invernizzi, G., Ruprecht, A., Mazza, R., Rossetti, E., Sasco, A., Nardini, S., et al. (2004). Particulate matter from tobacco versus diesel car exhaust: an educational perspective. *Tobacco Control* 13, 219–221. doi: 10.1136/tc.2003.005975

Jaffe, S. (2017). Vulnerable links in the lithium-ion battery supply chain. *Joule* 1, 225–228. doi: 10.1016/j.joule.2017.09.021

Jian, D., Xiaohong, G., Gesheng, L., and Xintang, Z. (2001). *Study on Diesel-LPG Dual Fuel Engines (No. 2001-01-3679)*. Warrendale, PA: SAE Technical Paper. doi: 10.4271/2001-01-3679

Johnson, T. V. (2009). Review of diesel emissions and control. *Int. J. Eng. Res.* 10, 275–285. doi: 10.1243/14680874JER04009

Kathuria, V. (2004). Impact of CNG on vehicular pollution in Delhi: a note. *Transport. Res. Part D.* 9, 409–417. doi: 10.1016/j.trd.2004.05.003

Khair, M. K., and Majewski, W. A. (2006). *Diesel Emissions and their Control (Vol. 303)*. Warrendale, PA: SAE Technical Paper. doi: 10.4271/R-303

Kingsbury, K. (2007). *After the Oil Crisis, a Food Crisis?* Available online at: www.time.com/time/business/article/0,8599,1684910,00.html?iid$=$sphere-inline-sidebar

Knecht, W. (2008). Diesel engine development in view of reduced emission standards. *Energy* 33, 264–271. doi: 10.1016/j.energy.2007.10.003

Kumar, S., Kwon, H. T., Choi, K. H., Lim, W., Cho, J. H., Tak, K., et al. (2011). LNG: an eco-friendly cryogenic fuel for sustainable development. *Appl. Energy* 88, 4264–4273. doi: 10.1016/j.apenergy.2011.06.035

Laughlin, M., and Burnham, A. (2016). *Case Study: Natural Gas Regional Transport Trucks (No. DOE/CHO-AC02-06CH11357-1603)*. Argonne, IL; Columbia, MD: Energetics; Argonne National Laboratory.

Li, G., Ouellette, P., Dumitrescu, S., and Hill, P. G. (1999). *Optimization Study of Pilot-Ignited Natural Gas Direct-Injection in Diesel Engines*. Warrendale, PA: SAE Paper 1999-01-3556. doi: 10.4271/1999-01-3556

Lin, W., Zhang, N., and Gu, A. (2010). LNG (liquefied natural gas): a necessary part in China's future energy infrastructure. *Energy* 35, 4383–4391. doi: 10.1016/j.energy.2009.04.036

Lloyd, A. C., and Cackette, T. A. (2001). Diesel engines: environmental impact and control. *J. Air Waste Manage. Assoc.* 51, 809–847. doi: 10.1080/10473289.2001.10464315

Mabson, C., Faghani, E., Kheirkhah, P., Kirchen, P., et al. (2016). *Combustion and Emissions of Paired-Nozzle Jets in a Pilot-Ignited Direct-Injection Natural Gas Engine*. Warrendale, PA: SAE Paper 2016-01-0807. doi: 10.4271/2016-01-0807

Maji, S., Pal, A., and Arora, B. B. (2008). *Use of CNG and Diesel in CI Engines in Dual Fuel Mode (No. 2008-28-0072)*. Warrendale, PA: SAE Technical Paper. doi: 10.4271/2008-28-0072

Marbán, G., and Valdés-Solís, T. (2007). Towards the hydrogen economy? *Int. J. Hydr. Energy* 32, 1625–1637. doi: 10.1016/j.ijhydene.2006.12.017

Maricq, M. M. (2007). Chemical characterization of particulate emissions from diesel engines: a review. *J. Aerosol. Sci.* 38, 1079–1118. doi: 10.1016/j.jaerosci.2007.08.001

Martuzzi, M., Mitis, F., Iavarone, I., and Serinelli, M. (2006). *Health Impact of PM10 and Ozone in 13 Italian Cities*. WHO Regional Office for Europe.

McKone, T. E., Nazaroff, W. W., Berck, P., Auffhammer, M., Lipman, T., Torn, M. S., et al. (2011). Grand challenges for life-cycle assessment of biofuels. *Environ. Sci. Technol.* 45, 1751–1756. doi: 10.1021/es103579c

McTaggart-Cowan, G., Mann, K., Huang, J., Singh, A., et al. (2015). Direct injection of natural gas at up to 600 bar in a pilot-ignited heavy-duty engine. *SAE Int. J. Eng.* 8, 981–996. doi: 10.4271/2015-01-0865

Minter, A. (2016). *The Burning Truth Behind an E-Waste Dump in Africa*. SMITHSONIAN.COM. Available online at: www.smithsonianmag.com/science-nature/burning-truth-behind-e-waste-dump-africa-180957597/

Mohr, M., Forss, A. M., and Lehmann, U. (2006). Particle emissions from diesel passenger cars equipped with a particle trap in comparison to other technologies. *Environ. Sci. Technol.* 40, 2375–2383. doi: 10.1021/es051440z

Mollenhauer, K., and Tschöke, H. (eds.). (2010). *Handbook of Diesel Engines, Vol. 1*. Berlin: Springer. doi: 10.1007/978-3-540-89083-6

Mumford, D., Goudie, D., and Saunders, J. (2017). *Potential and Challenges of HPDI*. Warrendale, PA: SAE Paper 2017-01-1928. doi: 10.4271/2017-01-1928

Muradov, N. Z., and Veziroglu, T. N. (2005). From hydrocarbon to hydrogen–carbon to hydrogen economy. *Int. J. Hydr. Energy* 30, 225–237. doi: 10.1016/j.ijhydene.2004.03.033

Neeft, J. P., Makkee, M., and Moulijn, J. A. (1996). Diesel particulate emission control. *Fuel Process. Technol.* 47, 1–69. doi: 10.1016/0378-3820(96)01002-8

Neeft, J. P., Nijhuis, T. X., Smakman, E., Makkee, M., and Moulijn, J. A. (1997). Kinetics of the oxidation of diesel soot. *Fuel* 76, 1129–1136. doi: 10.1016/S0016-2361(97)00119-1

Neely, G., Florea, R., Miwa, J., and Abidin, Z. (2017). *Efficiency and Emissions Characteristics of Partially Premixed Dual-Fuel Combustion by Co-Direct Injection of NG and Diesel Fuel (DI2) - Part 2*. Warrendale, PA: SAE Paper 2017-01-0766. doi: 10.4271/2017-01-0766

Nica, G. (2016). *Why Did BMW Really Stop Making the Hydrogen 7 Model*? Available online at: www.bmwblog.com/2016/08/17/bmw-stop-making-hydrogen-7-model/

O'Boyle, M. (2018). *How Volkswagen's Dieselgate Billions Are Helping to Jump-Start EV Charging*. Available online at: www.energypost.eu/are-electric-vehicle-charging-corridors-the-best-way-to-spend-volkswagens-dieselgate-billions/

Olah, G. A. (2004). After oil and gas: methanol economy. *Catal. Lett.* 93, 1–2. doi: 10.1023/B:CATL.0000017043.93210.9c

Olah, G. A. (2005). Beyond oil and gas: the methanol economy. *Angew. Chem. Int. Edn.* 44, 2636–2639. doi: 10.1002/anie.200462121

Onstad, E. (2019). *Amnesty Faults Electric Vehicle Batteries as Carbon Intensive*. Available online at: www.uk.mobile.reuters.com/article/amp/idUKKCN1R200B

Osorio-Tejada, J., Llera, E., and Scarpellini, S. (2015). LNG: an alternative fuel for road freight transport in Europe. *WIT Trans. Built Environ.* 168, 235–246. doi: 10.2495/SD150211

Park, T., Teng, H., Hunter, G. L., van der Velde, B., and Klaver, J. (2011). *A Rankine Cycle System for Recovering Waste Heat from Hd Diesel Engines-Experimental Results (No. 2011-01-1337)*. Warrendale, PA: SAE Technical Paper. doi: 10.4271/2011-01-1337

Parker, A. (2019). *Some Examples the War Against the Internal Combustion Engine by CARB and US EPA is not Based on Real Scientific Evidence*. Available online at: www.wattsupwiththat.com/2019/03/22/the-war-against-the-internal-combustion-engine-by-carb-and-us-epa-is-not-based-on-real-scientific-evidence-examples/

phys.org (2018). *Five things to know about VW's 'dieselgate' scandal*. Available online at: www.phys.org/news/2018-06-vw-dieselgate-scandal.html#jCp

Raftery, T. (2018). *Seven Reasons Why The Internal Combustion Engine Is A Dead Man Walking [Updated]*. Available online at: www.forbes.com/sites/sap/2018/09/06/seven-reasons-why-the-internal-combustion-engine-is-a-dead-man-walking-updated/#1284409e603f

Ramsbrock, J., Vilimek, R., and Weber, J. (2013). "Exploring electric driving pleasure–the BMW EV pilot projects," in *International Conference on Human-Computer Interaction* (Berlin; Heidelberg: Springer), 621–630. doi: 10.1007/978-3-642-39262-7_70

Ravikumar, A. P. (2018). *How to Make the Liquefied Natural Gas Industry More Sustainable*. Available online at: www.phys.org/news/2018-11-liquefied-natural-gas-industry-sustainable.html

Reşitoglu, I. A., Altinişik, K., and Keskin, A. (2015). The pollutant emissions from diesel-engine vehicles and exhaust aftertreatment systems. *Clean Technol. Environm. Policy* 17, 15–27. doi: 10.1007/s10098-014-0793-9

Ryu, K. (2013). Effects of pilot injection timing on the combustion and emissions characteristics in a diesel engine using biodiesel–CNG dual fuel. *Appl. Energy* 111, 721–730. doi: 10.1016/j.apenergy.2013.05.046

Saracco, G., Russo, N., Ambrogio, M., Badini, C., and Specchia, V. (2000). Diesel particulate abatement via catalytic traps. *Catal. Today*, 60, 33–41. doi: 10.1016/S0920-5861(00)00314-X

Schipper, L., Marie-Lilliu, C., and Fulton, L. (2002). Diesels in Europe: analysis of characteristics, usage patterns, energy savings and Co2 emission implications. *J. Transp. Econ. Policy* 36, 305–340.

Scott, P., and Burton, M. (2013). *The New BMW i3. Hg. v. BMW AG*. Available online at: www.asymcar.com/graphics/14/i3/bmwi3b.pdf

Shah, A., Thipse, S. S., Tyagi, A., Rairikar, S. D., Kavthekar, K. P., Marathe, N. V., et al. (2011). *Literature Review and Simulation of Dual Fuel Diesel-CNG Engines (No. 2011-26-0001)*. Warrendale, PA: SAE Technical Paper. doi: 10.4271/2011-26-0001

Shi, L., Shu, G., Tian, H., and Deng, S. (2018). A review of modified Organic Rankine cycles (ORCs) for internal combustion engine waste heat recovery (ICE-WHR). *Renew. Sustain. Energy Rev.* 92, 95–110. doi: 10.1016/j.rser.2018.04.023

Smith, O. I. (1981). Fundamentals of soot formation in flames with application to diesel engine particulate emissions. *Prog. Energy Combust. Sci.* 7, 275–291. doi: 10.1016/0360-1285(81)90002-2

South China Morning Post (2018). *'Airpocalypse' Over? Beijing Breathes Easier as Clean Air Drive Pays Off, US Embassy Smog Readings Suggest*. Available online at: www.scmp.com/news/china/policies-politics/article/2160444/beijings-clean-air-drive-paying-swift-recovery

Taylor, E. (2018). *Volkswagen Says Last Generation of Combustion Engines to be Launched in 2026*. Available online at: www.reuters.com/article/us-volkswagen-emissions-combustion/volkswagen-says-last-generation-of-combustion-engines-to-be-launched-in-2026-idUSKBN1O32O6

Teng, H., Klaver, J., Park, T., Hunter, G. L., and van der Velde, B. (2011). A *Rankine Cycle System for Recovering Waste Heat from HD Diesel Engines-WHR System Development (No. 2011-01-0311)*. Warrendale, PA: SAE Technical Paper. doi: 10.4271/2011-01-0311

Teng, H., and Regner, G. (2009). *Improving Fuel Economy for HD Diesel Engines with WHR Rankine Cycle Driven by EGR Cooler Heat Rejection (No. 2009-01-2913)*. Warrendale, PA: SAE Technical Paper. doi: 10.4271/2009-01-2913

Teng, H., Regner, G., and Cowland, C. (2007). *Waste Heat Recovery of Heavy-Duty Diesel Engines by Organic Rankine Cycle Part I: Hybrid Energy System of Diesel and Rankine Engines (No. 2007-01-0537)*. Warrendale, PA: SAE Technical Paper. doi: 10.4271/2007-01-0537

United Nations (2019). *World Water Development Report 2019*. Available online at: www.unwater.org/publications/world-water-development-report-2019/

Wang, T., Zhang, Y., Zhang, J., Peng, Z., and Shu, G. (2014). Comparisons of system benefits and thermo-economics for exhaust energy recovery applied on a heavy-duty diesel engine and a light-duty vehicle gasoline engine. *Energy Conv. Manage.* 84, 97–107. doi: 10.1016/j.enconman.2014.04.022

westport.com (2015). *Westport HPDI 2.0 on Track for Commercial Production*. Available online at: www.westport.com/news/2015/westport-hpdi-2.0-on-track-for-commercial-production

westport.com (2019a). *1st Gen. Westport HPDI Technology*. Available online at: www.westport.com/old-pages/combustion/hpdi/integration

westport.com (2019b). *Westport^{TM} HPDI 2.0*. Available online at: www.westport.com/is/core-technologies/hpdi-2

Yeh, S. (2007). An empirical analysis on the adoption of alternative fuel vehicles: the case of natural gas vehicles. *Energy Policy* 35, 5865–5875. doi: 10.1016/j.enpol.2007.06.012

Yu, G., Shu, G., Tian, H., Huo, Y., and Zhu, W. (2016). Experimental investigations on a cascaded steam-/organic-Rankine-cycle (RC/ORC) system for waste heat recovery (WHR) from diesel engine. *Energy Conv. Manage.* 129, 43–51. doi: 10.1016/j.enconman.2016.10.010

Zervas, E., Poulopoulos, S., and Philippopoulos, C. (2006). CO_2 emissions change from the introduction of diesel passenger cars: case of Greece. *Energy* 31, 2915–2925. doi: 10.1016/j.energy.2005.11.005

Zhao, H. (ed.). (2009). *Advanced Direct Injection Combustion Engine Technologies and Development: Diesel Engines*. Cambridge: Woodhead Publishing.

Conflict of Interest: The author declares that the research was conducted in the absence of any commercial or financial relationships that could be construed as a potential conflict of interest.

frontiers in Mechanical Engineering

ORIGINAL RESEARCH
published: 16 July 2020
doi: 10.3389/fmech.2020.00046

Quasi-Dimensional Multi-Zone Modeling of Methane-Diesel Dual-Fuel Combustion

Shuonan Xu and Zoran Filipi*

CU-ICAR, Automotive Engineering Department, Clemson University, Greenville, SC, United States

Strict CO_2 emission and fuel economy regulations are motivating the developers of internal combustion engines to consider alternative fuels. Dual-fuel NG diesel engines are attractive due to minimal design changes, ability to maintain high compression ratio of the diesel baseline, and elimination of driver's range anxiety. A typical overarching goal is to maximize the substitution ratio, but the higher complexity of the dual-fuel engine comes with challenges, such as the knock limit at high load, combustion instability at low load and methane slip. Development of dual-fuel engine and its control strategies can benefit from predictive simulations, capable of providing deep insights into combustion and emission formation. They can dramatically lower the time and cost for explorations of design and optimizing engine control strategies. Even when experimental data is available, the simulation can provide useful additional insight by predicting value of parameters that are not easy to measure from experimental setup. This paper presents development of a Quasi-D multi-zone combustion model of a heavy-duty dual-fuel engine. The approach marries the best features of the multi-zonal diesel spray model with the turbulent flame entrainment model for the premixed charge of NG and air/EGR. The diesel combustion model developed in this study is based on the framework proposed by Hiroyasu (1985) with several improvements in its sub-models. Regarding the combustion of the premixed charge, a new way of modeling the flame front area during NG flame propagation is proposed. The NG flame is assumed to initiate from the outer boundary of diesel spray and propagates into the space in the direction perpendicular to the diesel spray envelope. The algorithm incorporates geometrical information of all spatial constraints and it can provide a universal solution for various piston or cylinder head designs. The diesel and NG combustion models run concurrently to arrive at a complete prediction of the heat release history of both fuels, based on detailed information about the evolution of diesel spray, ignition and flame propagation of NG-air mixture.

Keywords: dual-fuel, methane, diesel, quasi-D, modeling, combustion

OPEN ACCESS

Edited by:
Hailin Li,
West Virginia University, United States

Reviewed by:
Adam Dempsey,
Marquette University, United States
John Nuszkowski,
University of North Florida, United States
Jinlong Liu,
Purdue University, United States

****Correspondence:***
Shuonan Xu
shuonax@clemson.edu

Specialty section:
This article was submitted to Engine and Automotive Engineering, a section of the journal Frontiers in Mechanical Engineering

Received: *04 February 2020*
Accepted: *02 June 2020*
Published: *16 July 2020*

Citation:
Xu S and Filipi Z (2020) Quasi-Dimensional Multi-Zone Modeling of Methane-Diesel Dual-Fuel Combustion. Front. Mech. Eng. 6:46. doi: 10.3389/fmech.2020.00046

INTRODUCTION

Advancements in extraction technologies have greatly increased NG reserve in recent years and kept its price very low. In the transportation sector, there is a strong economic drive to utilize more of this low carbon gaseous fuel. In heavy-duty (HD) markets, diesel engines have been playing a dominating role due to their high thermal efficiency. According to 2020 Annual Energy Outlook

published by EIA, in highway transportation sector, the annual amount of fuel consumed by HD trucks accounts for 26.3% of total fuel used in 2020. The prediction of this percentage for 2050 is 31.2%. The CO_2 emission potential of NG is less than liquid hydrocarbon fuels; therefore, due to the high miles traveled by HD trucks, converting base diesel to NG only or dual-fuel mode would quickly increase the utilization of NG in transportation, as well as reduce the CO_2 emission. NG is a relatively clean fuel due to its main constituent being Methane. Since Methane does not contain carbon-carbon bonds, its combustion is soot-free (Korakianitis and Namasivayam, 2011). All of these facts place NG as a top choice for alternative fuel.

Majority of HD NG engines today are spark ignited (SI) engines converted from diesel platforms. Those engines operate at near stoichiometric charge in order to use three-way catalysts for mitigating emissions. To avoid knock, compression ratio (CR) is generally lowered to typical level for an SI engine. The major drawbacks of this type of NG engine are: (i) SI NG engine operates solely on NG and relies heavily on NG re-fueling facilities, and (ii) efficiency is compromised due to reduced CR and stoichiometric mixture. Dual-fuel engine on the other hand, is converted from a diesel platform with minimal changes of hardware. In a typical dual-fuel engine setup, NG is injected into the intake runner through port fuel injection. This is often referred to as fumigation. The NG mixes with air and exhaust gas recirculation (EGR) as it is being inducted into the cylinder. A small amount of diesel spray is used as ignition source toward the end of compression. Multiple ignition sources generated from combustion of diesel fuel allow NG to burn in very lean conditions. Both the high compression ratio and lean-operation are retained, and its thermal efficiency is superior compared to its SI counterpart (Krishnan et al., 2002).

A dual fuel engine can run either diesel-only mode or diesel-NG dual fuel mode; therefore, the driver's range anxiety is eliminated in regions with sparse NG infrastructure. Of course, conversions to NG come with their own challenges. The storage of NG is one, since NG is a gaseous fuel, and even when compressed to high pressure NG has significantly lower energy density by volume compared to diesel fuel. In addition, fueling stations and infrastructure for natural gas are far from fully developed in US. The leakage of NG to atmosphere also poses significant environmental risk, since NG has much higher greenhouse effect than that of CO_2.

Karim et al. pioneered early research studies of dual-fuel engines (Karim et al., 1966; Karim and Khan, 1968; Karim, 1987; Karim and Liu, 1992; Liu and Karim, 1997, 1998). Poor combustion stability at low loads and knocking at high loads were the two major issues identified. At lower loads, the lean NG-air mixture creates a challenge for the flame to propagate, while under high load, the high compression ratio of a diesel engine elevates the risk of end-gas knock. Methane slip is another common issue associated with dual fuel engines. Poor combustion stability at low loads leads to incomplete combustion and allows part of unburned NG to escape to environment. In more recent studies, Krishnan et al. proposed a new mode of dual-fuel combustion, where an early pilot injection of diesel fuel serve solely as ignition source, while vast majority of heat release comes from combustion of NG fuel (Krishnan et al., 2004, 2009; Srinivasan et al., 2006a,b; Krishnan and Srinivasan, 2010). In that case, the ignition timing is governed by chemical kinetics, and since the diesel is injected early the pre-ignition period is extended thus promoting better mixing. The presence of rich diesel pockets is significantly reduced and consequently soot emission is negligible. Better mixing between diesel and NG-air mixture also helps ignition of NG, and NOx emissions are generally lower too.

Though experimental study is the most trusted method for validating concepts and providing insight into the combustion process, it is also the most expensive and lengthy, particularly is multiple design variants have to be explored. Additionally, experimental data does not always reveal the underlying mechanisms of the observed phenomenon and information such as instant in-cylinder gas temperature or composition. Simulation studies on the other hand, generate insights into the combustion characteristics much faster and allow efficient screening of design options or investigations of control strategies. In particular, predictive simulation of the dual-fuel combustion process would be invaluable for detailed characterization of diesel-NG injection strategies.

Generally, 3-D simulations provide detailed spatial resolution of the combustion process, but come with the heavy computational cost. Previous work by Reitz and Krishnan's group (Zhang et al., 2003; Singh et al., 2004, 2006) focused on dual-fuel concepts and produced valuable insights of the in-cylinder process. However, compared to Quasi-D or 0-D modeling approaches, 3-D simulation requires one or more orders of magnitude higher computational effort. On the other end of the spectrum, a 0-D combustion model, such as a Wiebe function representation of the heat release, requires little computing effort, but provides no information about the details of spatially-resolved phenomena such as mixing or flame propagation. Previously published literature (Liu and Karim, 1997; Abd Alla et al., 2000; Karim, 2003; Xu et al., 2014, 2017a) have established 0-D models that separate the heat release contributions of each fuel, but in a prescriptive manner. In summary, the fidelity and predictiveness of a 0-D model is very limited. In comparison, Quasi-D modeling approaches provide a compromise between model fidelity and computing efficiency. Quasi-D multi-zone models of dual-fuel combustion have been studied in the literature (Papagiannakis et al., 2005, 2007; Johnson et al., 2012; Walther et al., 2012). In the previous research efforts to develop a Quasi-D model for a dual-fuel engine, Papagiannakis et al. (2005) proposed to incorporate turbulent flame propagation modeling approach to represent the combustion of NG. The NG flame was assumed to propagate from the outer boundary of a diesel spray, which was approximated as a conical shape. However, the discussion of the combustion of diesel fuel was limited. Krishnan and Srinivasan (2010) on the other hand, has incorporated detailed discussion of the diesel spray and combustion modeling, where a diesel spray was divided into multiple packets that were treated individually. However, the author assumed NG to propagate as individual spherical flames from each ignition site that do not interact with each other.

The modeling approach proposed in this paper marries the best features of the two approaches described above, i.e., the multi-zonal spray model of the diesel mixing and combustion and the turbulent flame entrainment model of the premixed NG combustion. In particular, the diesel spray and combustion behavior are modeled by dividing the injected diesel fuel into multiple packets, and tracking the break-up, evaporation, air entrainment and ignition in each packet. The combustion of NG is modeled as two simultaneous processes, i.e., the turbulent flame entrainment, which is highly dependent on spatial considerations and the turbulent flow field, and the burn up of NG-air charge in the finite reaction zone defined by the flame area and its thickness. The two combustion models run concurrently to arrive at a complete prediction of the dual-fuel combustion process, where heat release histories of both fuels are dependent on parameters such as the injection timing and rate, spray targeting, air motion, combustion chamber shape and NG-air ratio. The diesel combustion model developed in this work is based on the framework proposed by Hiroyasu and Kadota (1976) and Hiroyasu (1985) with several improvements done with sub-models (Xu et al., 2017b). The NG combustion predictions are based on a new way of modeling the flame front area and flame propagation. We assume that the flame is initiated from the outer boundary of diesel spray and propagates outward perpendicular to the spray boundary. As the flame evolves, it starts to interact with spatial constraints, e.g., combustion chamber walls or the adjacent flame. The algorithm incorporates geometrical information of all spatial constraints and it is capable of providing a universal solution for various piston or cylinder head designs. The paper includes experimental validation and ends with conclusions.

MATERIALS AND METHODS

Approach to Dual-Fuel Combustion Modeling: Combining the Multi-Zonal Diesel Spray and Combustion Model With the NG-Air Mixture Ignition and Flame Propagation Scheme

The combustion mode in a typical modern diesel is a mixing-controlled process (Dec, 1997). After being injected with the high pressure and thus high velocity, the fuel evaporates while surrounding air entrains and mixes with it. Autoignition then occurs as soon as the induction period elapses at any location in the chamber, and the burning starts. In contrast, the conventional SI engine combustion is governed by the turbulent flame propagation, and the modelers typically divide the cylinder space into two zones: unburned and burned. This approach, combined with the flame entrainment model that takes into account the instantaneous flame area, can be categorized as the Quasi-Dimensional model, since it takes into consideration the interaction of the spherical flame with the walls. To achieve a similar level of prediction accuracy in case of the mixing-controlled combustion, the fuel injection and spray development processes have to be represented with multiple zones and sub-models of the key phenomena, such as break-up, evaporation, air entrainment, autoignition, and emission formation.

Hiroyasu et al. laid the foundation of such a multi-zone Quasi-D diesel combustion modeling approach, where a diesel spray is divided into individual packets as the fuel enters the chambers (Hiroyasu, 1985). A general description of this modeling methodology is given in **Figure 1** (Xu et al., 2017b). In the direction perpendicular to the spray, the spray is defined as multiple slices, as shown in **Figures 1A,B**. Along YZ directions, the mass of the fuel is further allocated into each packet, where the distribution of mass is assumed to be uniform. Each packet in the spray is defined as P(i,j), as shown in **Figure 1C**. In this convention, i depicts packet index in X axis, while j depicts the index in Z axis. In real-world, the penetration depth at the center of the spray is longer than its periphery. This effect is considered as shown in **Figure 1D**. Transfer of mass or heat is not allowed in between packets.

Figure 2 gives an illustration of dual-fuel combustion process. Given the nature of the two fuels, e.g., diesel and Natural Gas, and the type of mixture preparation, it is clear that the two combustion modes progress in a sequence until the ignition of the premixed NG-air charge, followed by the simultaneous mixing controlled burning of diesel and flame propagation through the surrounding premixed charge. The conceptual representation of the diesel spray used here is adopted from the seminal work by Dec (1997). **Figure 2**(1–6) gives a time-lapse illustration of the combustion process from start of injection (SOI) of diesel to the end of combustion. Stage (1) shows the initial development of diesel spray right after the fuel is injected into the NG-air mixture. After a short ignition delay period, diesel fuel auto ignites and initiates the premixed combustion of diesel vapor that was able to mix with air up to that point. As soon as the local temperature increases significantly enough, the NG-air mixture surrounding the diesel spray is also ignited (Karim, 2003). As the combustion progresses to stage (3), the combustion mode of diesel transfers from premixed burning to mixing controlled burning, with evidence of a head vortex formation, surrounded by the diffusion flame. Meanwhile, a NG flame front forms around the diesel spray as multiple flame kernels merge together and propagate into the unburned NG-air mixture. At stage (4), diesel fuel continues to burn in the mixing-controlled mode and soot cloud forms in the center of the head vortex, while NG flame continues to propagate into the end gas zone. Due to the heat released from diesel and NG combustion, the NG-air mixture in the end gas zone is subject to high temperature and pressure, thus there is a chance for an auto-ignition in the late stages of the process (Liu and Karim, 1998), especially at higher loads. At stage (5), diesel combustion mode remains governed by the mixing-controlled burning until all diesel fuel is consumed. As NG flame continue to propagate, the flame fronts formed from each individual spray interact with neighboring ones and merge together. In the final stage (6), diesel fuel is already consumed and most of the soot is oxidized due to high temperatures and oxygen available in the lean products of NG combustion. Lastly, the flame propagation of NG terminates as the flame front reaches the wall. Due to the lower laminar flame speed of lean NG-air mixture, there is a chance that a small portion of NG in the

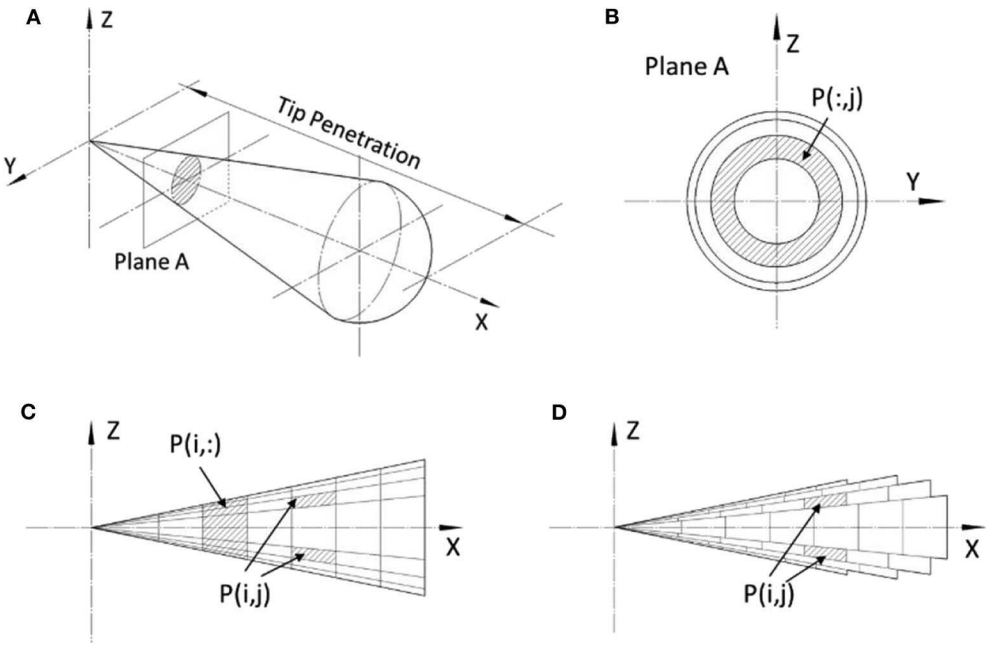

FIGURE 1 | (A-D) Spatial illustration of diesel spray combustion modeling scheme.

end gas zone remains unburned at exhaust valve opening (EVO), especially at low load conditions. The ability of the model to predict that is critical for enabling studies aimed at prevention of the methane slip.

Figure 3 shows the simulation flow-chart. The process shown in this figure is executed at each crank-angle from the start of diesel fuel injection, until the completion of the combustion process, i.e., termination of all heat-release pathways. The output drives the thermodynamic simulation and produces crank-angle resolved heat release and pressure trace. The cycle simulation is initiated at intake valve closing (IVC) and is terminated at EVO. Since both intake and exhaust valves are shut, the in-cylinder mass stays unchanged, i.e., the work presented here was focused on the closed-cycle simulation. The gas composition in the cylinder at onset of simulation is either premixed NG-air or NG-air-EGR mixture. During compression, thermodynamics model updates in cylinder pressure and temperature by solving the first law equations and considering heat transfer. The temperature information is subsequently used for ignition delay prediction. Starting from SOI, the diesel spray tip penetration sub-model, air-NG entrainment sub-model, and diesel droplet evaporation sub-models are triggered to update spray variables. In this work, NG is allowed to entrain into the packets together with air before the start of combustion (SOC). The NG entrainment is terminated after SOC since the burning mode of NG is transformed into turbulent flame propagation. After the ignition is detected, it triggers the sub-models for calculating heat release from diesel and NG in each packet. The NG entrained into the packets during the ignition delay period is consumed quickly after SOC while the diesel continues to burn thanks to the remaining oxygen in the lean charge.

In each packet, three modes of diesel heat release are being considered simultaneously, namely the air entrainment controlled, fuel evaporation controlled and reaction rate controlled (Xu et al., 2017b). As the heat released from diesel fuel ignites its surrounding NG-air mixture, the combustion of NG becomes self-sustaining and the flame propagates into the end gas zone similar to that in a SI engine. The total heat release of dual-fuel combustion is the sum of heat released by both fuels. In this work, the NG fuel used in experiment is mostly methane (95%). A detailed list of constituents of the NG fuel is provided in **Table 1**. The above-mentioned sub-models will be discussed in detail in latter sections.

Modeling of Diesel Spray and Combustion

Spray Tip Penetration Model

The spray tip penetration correlation used in this work is developed based on widely adopted Hiroyasu's work (Hiroyasu and Kadota, 1976; Hiroyasu, 1980, 1985). However, the model was updated to capture the recent development of diesel injectors characterized by much higher injection pressure and smaller hole diameters compared to the original Hiroyasu's experiments. In other words, new correlation for spray break-up time was developed and validated with the experimental data from Xu et al. (2017b). Equation (1) shows the new correlation used to represent the time between SOI and breakup of the fuel jet:

$$t_b = 38.57\left(\frac{\rho_a}{\rho_0}\right)^{0.15}\frac{\rho_l d_0}{\sqrt{2\rho_a \Delta P}} \quad (1)$$

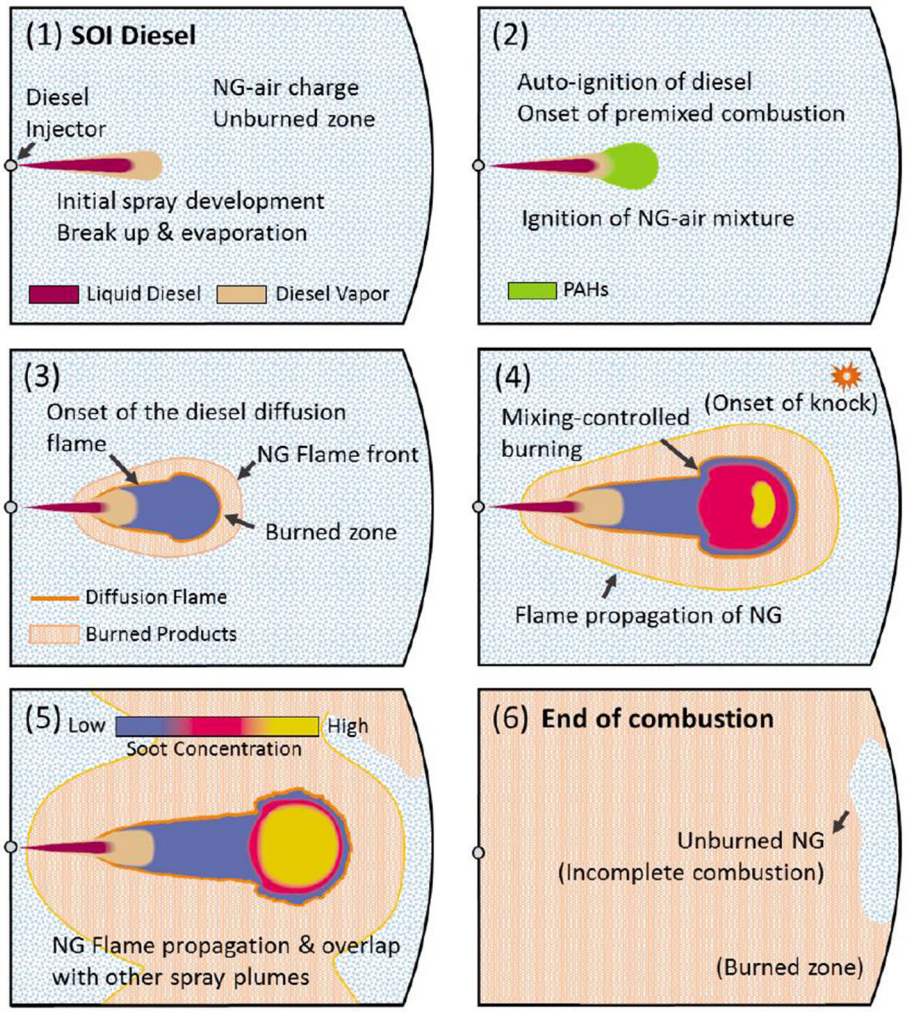

FIGURE 2 | A time-lapse illustration of dual-fuel combustion process. Conceptual spray evolution images are from the seminal paper by Dec (1997), SAE 970873.

where ρ_a is in-cylinder gas density, ρ_0 is reference density of air at SATP, ρ_l is the density of liquid fuel, d_0 is injector hole diameter and ΔP is the pressure difference between injection pressure and in-cylinder pressure. Before t_b is reached, spray tip penetration S is a linear function of time after injection t, given in Equation (2). After breakup of the spray, the tip penetration is represented as a function of $\sqrt{t}$, given in Equation (3).

$$S = 0.70\left(\frac{\rho_a}{\rho_0}\right)^{-0.25}\sqrt{\frac{2\Delta P}{\rho_l}}t, \quad 0<t<t_b \tag{2}$$

$$S = 4.347\left(\frac{\rho_a}{\rho_0}\right)^{-0.175}\left(\frac{2\Delta P}{\rho_a}\right)^{0.25}\sqrt{d_0 t}, \quad t_b \leq t \tag{3}$$

The centerline of a spray has highest penetration depth. The penetration depth gradually reduces as the locations move toward the periphery. Equations (4)–(5) represent penetration depth at the periphery. In the radial direction, E_x is defined as a weighting factor, where x_s is a non-dimensional parameter representing the distance from centerline of the spray. E_x reaches its maximum at the centerline of the spray, where x_s is zero. At the periphery of the spray, x_s becomes 1 and E_x reaches its minimum of 0.5. The breakup time at periphery region t_{bx} and penetration depth at periphery S_x are defined as a function of E_x.

$$E_x = 0.5\sqrt{1-x_s} + 0.5 \tag{4}$$

$$t_{bx} = E_x t_b, \; S_x = \sqrt{E_x}S \tag{5}$$

Air-NG Entrainment Model

The air entrainment rate is estimated based on the findings of Hiroyasu (1980). As shown in Equation (6), the entrainment rate is calculated based on the injection velocity v_0 defined in Equation (7), in-packet fuel mass m_{f0}, density of fuel ρ_l, density of air ρ_a, weighting factor E_x, breakup time coefficient α_b, air mass entrained m_a and the diameter of

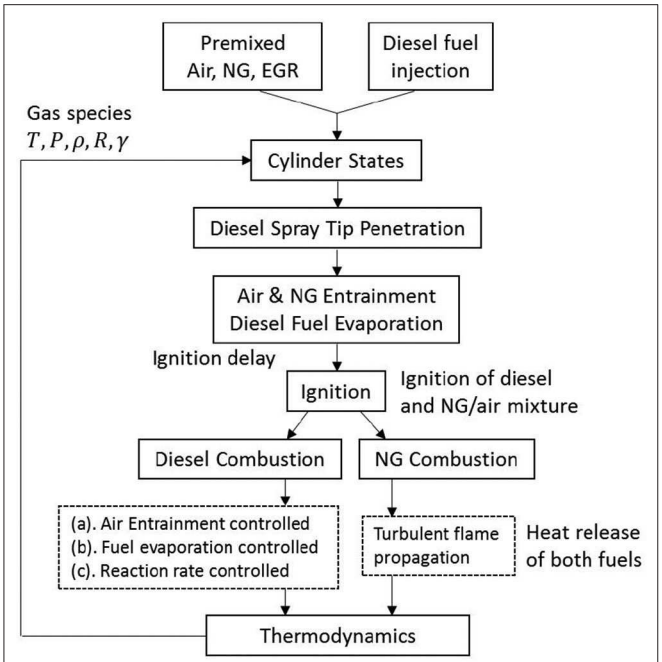

FIGURE 3 | A schematic description of computing process in the dual-fuel combustion model.

TABLE 1 | Test Engine and natural gas specifications.

Engine specifications	
Engine type	**Diesel/Dual-fuel 4-stroke**
Configuration	In-line 6-cylinder
Air intake	Turbocharged, intercooled
Fuel type	Diesel D2, Natural gas
Diesel Injector type	9-hole Unit injector
Firing order	1-5-3-6-2-4
Displacement	15L
Bore	137 mm
Stroke	169 mm
Connecting rod length	222 mm
Compression ratio	17:1
Rated power/rpm	405kW@2000rpm
Composition of natural gas	
Component	**Mole fraction (%)**
Methane	95.0
Ethane	3.2
Nitrogen	1.0
Carbon Dioxide	0.5
Propane	0.2
iso—Butane	0.03
Oxygen	0.02
iso—Pentane	0.01

nozzle hole d_0. In each calculation step, the ordinary differential equation (ODE) is integrated to update information of air mass entrainment.

$$\frac{dm_a}{dt} = \frac{2m_{f0}^2 v_0^2}{\sqrt{v_0}\left(\frac{\rho_l}{\rho_a}\right)^{1/4}\sqrt{\alpha_b E_x d_0}\left(m_a + m_{f0}\right)} \tag{6}$$

$$v_0 = 0.70\left(\frac{\rho_a}{\rho_0}\right)^{-0.25}\sqrt{\frac{2\Delta P}{\rho_l}} \tag{7}$$

At diesel only conditions, only air and EGR are entrained into the spray, while at dual-fuel conditions, the entrained mass also includes NG. Entrained NG mass can be derived from the mass fraction of NG in the premixed NG-air mixture at IVC x_{NG}, as given in Equation (8), where $\dot{m}_{NG}$ is the NG entrainment rate into the packet. The mass entrainment rate into the diesel spray is zero after the SOC. In this work, it is assumed that once ignition starts, the NG in the unburned zone (outside the outer boundary of diesel spray) is only consumed by flame propagation. This assumption is based on the observation that flame propagation speed of natural gas is faster than the diesel spray tip penetration. Even in a situation when the diesel spray penetration speed is relatively high, the buildup of the multi-zonal spray in the direction perpendicular to the injector hole axis is relatively low, and definitely lower that the outward propagation of the flame through the NG-air mixture. This assumption is captured with the equation below:

$$\dot{m}_{NG} = \begin{cases} x_{NG}\dot{m}_a; & t \le SOC \\ 0; & t > SOC \end{cases} \tag{8}$$

Fuel Evaporation Model

After the breakup period, the spray consists of miniature droplets. The droplet diameter plays a significant role in the evaporation process. While the actual droplets may have somewhat irregular shape, the Sauter Mean Diameter (SMD) was introduced by Hiroyasu et al. to define the diesel droplet diameter in a consistent manner (Hiroyasu and Kadota, 1976). The representation of SMD is defined in Equations (9–11), where d_0 represents diameter of nozzle hole, μ_l represents diesel fuel viscosity, μ_a represents air viscosity, *We* is Weber number and *Re* is Reynolds number. D_{32} is SMD, where LS and HS in the Equations (9) and (10) refer to low injection velocity (pressure) and high injection velocity (pressure), respectively (Hiroyasu et al., 1989).

$$\frac{D_{32}^{LS}}{d_0} = 4.12\ Re^{0.12}\ We^{-0.75}\left(\frac{\mu_l}{\mu_a}\right)^{0.54}\left(\frac{\rho_l}{\rho_a}\right)^{0.18} \tag{9}$$

$$\frac{D_{32}^{HS}}{d_0} = 0.38\ Re^{0.25}\ We^{-0.32}\left(\frac{\mu_l}{\mu_a}\right)^{0.37}\left(\frac{\rho_l}{\rho_a}\right)^{-0.47} \tag{10}$$

$$\frac{D_{32}}{d_0} = \max\left[\frac{D_{32}^{LS}}{d_0}\ \frac{D_{32}^{HS}}{d_0}\right] \tag{11}$$

The diameter of a fuel droplet can be updated through the ODE given in Equation (12), where D_l is droplet diameter, ρ_l is the density of liquid fuel and m_l is the mass of liquid fuel droplet. The initial diameter of the fuel droplet D_{l0} is obtained from the SMD given in Equation (11). The detailed calculation scheme to

obtain evaporation rate of a droplet dm_l/dt can be found in the work by Kadota and Hiroyasu (1976).

$$\frac{dD_l}{dt} = \frac{2}{\pi D_l^2 \rho_l}\left(\frac{dm_l}{dt} - \frac{\pi D_l^3}{6}\frac{d\rho_l}{dt}\right) \tag{12}$$

the mass of fuel vapor in a packet m_{fg} is represented in Equation (13), where N represents fuel droplets number, as defined in Equation (14), m_{f0} represents initial fuel mass in this packet, ρ_{l0} is initial density and D_{l0} is initial diameter of the droplet.

$$m_{fg} = \frac{\pi}{6}\left(\rho_{l0} D_{l0}^3 - \rho_l D_l^3\right) N \tag{13}$$

$$N = \frac{m_{f0}}{\frac{4}{3}\pi\left(\frac{D_{32}}{2}\right)^3 \rho_{l0}} \tag{14}$$

Ignition Delay Model

The ignition delay period in a dual-fuel engine is defined as the duration between SOI and SOC of the diesel fuel. Many correlations for predicting ignition delay in a diesel engine exist in the literature. Those include the Arrhenius-function based correlations (Wolfer, 1938; Kadota et al., 1976; Watson et al., 1980; Kobori et al., 2000; Assanis et al., 2003) and chemical kinetics based models (Halstead et al., 1977; Sazhina et al., 1999). In above mentioned methods, the Arrhenius-function based correlation proposed by Assanis et al., as given in Equation (15), has been proven to have good ignition delay prediction performance (Assanis et al., 2003).

$$\tau_{ID} = 2.4\phi^{-0.2} P^{-1.02} exp\left(\frac{E_a}{R_u T}\right) \tag{15}$$

where τ_{ID} is ignition delay in *ms*, ϕ is the equivalence fuel-air ratio, P and T are the cylinder pressure and temperature at SOI in bar and K and E_a/R_u is constant 2100 for diesel fuel (Watson et al., 1980). The same correlation has been modified to predict the ignition delay of a dual-fuel engine and was validated to yield satisfying results (Xu et al., 2017b).

Here we apply two definitions of equivalence ratio. The total fuel-oxygen ratio relative to stoichiometric is defined in Equation (16), where fuel masses of both diesel and NG are considered.

$$\phi_{total} = \frac{m_{fuel}/m_{O_2}}{\left(m_{fuel}/m_{O_2}\right)_{st}} \tag{16}$$

In the equation above, ϕ_{total} represents total equivalence ratio, m_{fuel} represents total fuel mass, m_{O_2} represents mass of oxygen and $\left(m_{fuel}/m_{O_2}\right)_{st}$ is represents stoich fuel-oxygen ratio:

$$\left(\frac{m_{fuel}}{m_{O_2}}\right)_{st} = \frac{m_D + m_{NG}}{3.045 m_D + 3.612 m_{NG}} \tag{17}$$

where m_D represents diesel fuel mass and m_{NG} represents NG fuel mass. Constant 3.045 is stoich oxygen-diesel ratio and constant 3.612 is stoich oxygen-NG ratio. To represent specific equivalence ratio of diesel fuel, a pseudo diesel equivalence ratio is defined:

$$\phi_{pD} = \frac{m_D/m_{O_2}}{0.328} \tag{18}$$

where 0.328 is stoich diesel-oxygen ratio. It is assumed that diesel fuel has access to all oxygen in the cylinder. To define ignition delay in dual-fuel combustion, the correlation defined in Equation (15) is applied. Pseudo diesel equivalence ratio ϕ_{pD} defined in Equation (18) is used in this correlation:

$$\tau_{ID} = 2.4{\phi_{pD}}^{-0.2} P^{-1.02} exp\left(\frac{E_a}{R_u T}\right) \tag{19}$$

Heat Release Model

It is assumed that only diesel vapor and NG react with surrounding air, while liquid fuel is not involved in combustion. The mass of fuel burned, including both diesel and NG in the individual packets or zones is determined by the mass of diesel vapor, NG and air and chemical reaction rates of both fuels. Equations (20) and (21) represent determination of the mass of fuel burned in each calculation step, where ϕ is the total equivalence ratio in the packet where both fuels are included; AFR_{stoich} is the stoichiometric air fuel ratio obtained from m_a, m_{fg} and m_{NG}, which are the mass of air, diesel vapor and NG, respectively; $\dot{m}_{chemD}$ and $\dot{m}_{chemNG}$ are chemical reaction rates of diesel-air and NG-air mixtures, respectively; Δm_D and Δm_{NG} are the mass of diesel and NG burned in a packet in each calculation step.

$$\Delta m_D = \begin{cases} m_a m_{fg}/(m_{fg} + m_{NG})/AFR_{stoich}; & \phi > 1 \\ m_{fg}; & \phi < 1 \\ \dot{m}_{chemD}\Delta t; & \Delta m_D > \Delta m_{chemD} \end{cases} \tag{20}$$

$$\Delta m_{NG} = \begin{cases} m_a m_{NG}/(m_D + m_{NG}/)AFR_{stoich}; & \phi > 1 \\ m_{NG}; & \phi < 1 \\ \dot{m}_{chemNG}\Delta t; & \Delta m_{NG} > \Delta m_{chemNG} \end{cases} \tag{21}$$

When the fuel/air mixture is rich ($\phi > 1$), the burned fuel mass Δm_D and Δm_{NG} are determined by the available air mass, AFR_{stoich} and the weighting between the mass of diesel vapor and NG. On the other hand, when the fuel/air mixture is lean, Δm_D and Δm_{NG} is determined by the fuel vapor mass m_{fg} and NG mass m_{NG}, respectively. When the burned fuel mass at each step calculated from the first two criteria is smaller than the chemical reaction rate limit $\dot{m}_{chemD}$ or $\dot{m}_{chemNG}$, the first two criteria determine the burn rate. On the contrary, when the mass fuel burned is greater than chemical reaction rate limit, the third criterion determines the burn rate. The chemical reaction rates of diesel-oxygen and NG-oxygen mixtures can be determined from the following formulas (Westbrook and Dryer, 1981):

$$\dot{m}_{chemD} = A_d\, exp\left(\frac{-E_a}{RT}\right)[C_{12}H_{26}]^{0.25}[O_2]^{1.5} V_{pac} \cdot M_D$$

$$\dot{m}_{chemNG} = A_{NG}\, exp\left(\frac{-E_a}{RT}\right)[CH_4]^{-0.3}[O_2]^{1.3} V_{pac} \cdot M_{NG} \tag{22}$$

where $C_{12}H_{26}$ is used to approximate the chemical composition of diesel (*n*-dodecane) and CH_4 is used to approximate NG,

$\dot{m}_{chemD}$ and $\dot{m}_{chemNG}$ are the chemical reaction rates of diesel and NG in *g/s*, respectively; A_d and A_{NG} are adjustable constants for diesel and NG, which are assumed as 2.5×10^{10} and 8.3×10^5, respectively; E_a is activation energy, being 30 *kcal/mol*, R is universal gas constant, T is gas temperature in the packet in K, V_{pac} is packet volume in cm^3, M_D and M_{NG} are the molecular weights of diesel and NG in g/mol and $[C_{12}H_{26}]$, $[CH_4]$, $[O_2]$ denote the concentration of diesel vapor, NG and oxygen in mol/cm^3.

With the aforementioned method to determine mass of fuel burned in each calculation step, the total heat release rate from the combustion of fuel $\dot{Q}_{fuel}$ is given in Equation (23), where LHV_D and LHV_{NG} are the lower heating values of diesel and NG and n_{pac} is the total number of packets.

$$\dot{Q}_{fuel} = \sum_{i=1}^{n_{pac}} \left(\frac{LHV_{NG} \cdot \Delta m_{NG} + LHV_D \cdot \Delta m_D}{\Delta t} \right) \tag{23}$$

Modeling of the Premixed NG-Air Combustion

As have been shown in **Figure 2**, the combustion of NG is initiated from the burning of the diesel-air mixture described in section Modeling of Diesel Spray and Combustion. The rest of NG-air mixture is then consumed through turbulent flame propagation. In this work, the burning of NG is divided into two stages: (1) combustion of NG entrained into the diesel spray before SOC and (2) self-sustaining combustion of NG-air mixture in the form of flame propagation.

The flame propagation of NG-air mixture is assumed to initiate from the outer boundary of diesel sprays. As shown in **Figure 4A**, the flame front propagates into space in the direction perpendicular to the outer boundary of a diesel spray (Papagiannakis et al., 2005). For the simplicity of numerical calculation, the outer boundary of a diesel spray is approximated as a conical shape with a hemisphere attached to the bottom of the cone. Once flame propagation is initiated, the flame front is assumed to travel with the same velocity in all directions until reaching other constrains such as cylinder wall, piston or the flame fronts initiated from surrounding sprays.

Turbulent Flame Propagation Model

In this work, the combustion of NG is modeled based on the turbulent flame propagation model widely used in 0-D, 1-D simulation of SI engines. In this modeling scheme, the in-cylinder space is divided into two zones: burned and unburned. However, in the context of a dual-fuel engine, a simple two-zone assumption is not sufficient since two fuels are burning in two different modes simultaneously. In this work, a multi-zone diesel spray-combustion model is running in parallel with the NG turbulent flame propagation model thus the definition of zones and boundaries had to be addressed carefully. This is presented in detail in section Flame Geometry Model.

Since the combustion of NG occurs after SOC of diesel, part of the in-cylinder charge has already entrained into the diesel spray and should not be included in the modeling of NG flame propagation. After the ignition of NG, it is assumed that only unburned NG-air mixture is entrained by the flame, while all the diesel vapor and burned products from the combustion of diesel are retained in the packets and are not participating the NG flame propagation.

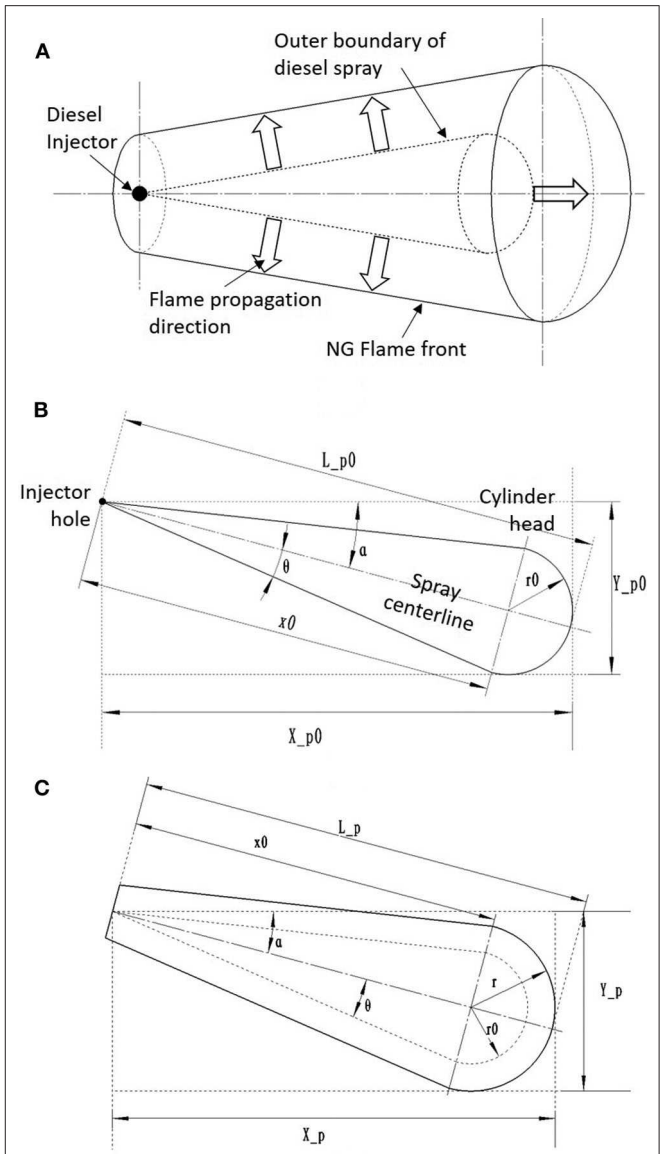

FIGURE 4 | (A) Spatial illustration of NG flame initiation and propagation relative to a diesel spray. **(B)** Geometrical definitions of a diesel spray at SOC. **(C)** Geometrical definitions of a free-evolving NG flame front.

According to the modeling approach proposed by Tabaczynski et al. (1977), the rate of mass entrained into the reaction zone is represented as:

$$\frac{dm_e}{dt} = \rho_u A_f \left(S_L + u' \right) \tag{24}$$

where m_e is the mass entrained into the reaction zone, ρ_u is unburned gas density, A_f is the surface area of flame front, S_L is laminar flame speed and u' is turbulent intensity. The calculation of A_f, S_L and u' will be discussed in detail in latter sections.

Once unburned gas is entrained into the reaction zone, the NG-air mixture burns with a rate proportional to the unburned mass in the entrainment front. The rate of mass burned can be obtained as:

$$\frac{dm_b}{dt} = \frac{m_e - m_b}{\tau} \tag{25}$$

where m_b is the burned mass and τ is the characteristic burning time. The characteristic burning time is defined as the time it takes to traverse the length of the Taylor microscale λ with laminar flame speed S_L (Tabaczynski et al., 1977):

$$\tau = \frac{\lambda}{S_L} \tag{26}$$

The laminar flame speed of NG-air mixture S_L can be obtained as (Heywood, 1988):

$$S_L = S_{L0}\left(\frac{T_u}{T_0}\right)^{\alpha_0}\left(\frac{p}{p_0}\right)^{\beta_0}\left(1 - 2.06\sim x_b^{0.77}\right) \tag{27}$$

where S_{L0}, α_0, β_0 are constants for a given fuel and equivalence ratio, $T_0 = 298K$ and $p_0 = 1atm$ are reference temperature and pressure, T_u is unburned gas temperature, p is cylinder pressure and $\tilde{x}_b$ is the mole fraction of burned gas diluent. In this work, $\tilde{x}_b$ represents the burned gas fraction in the NG-air mixture in the unburned zone. In the simulations performed in this study, this variable is set to zero, since the test points did not have external EGR, and the engine has negligible amount of internal residual at the operating conditions tested. In a situation where external EGR is used or a high cam overlap is present, the mole fraction of burned gas will need to be considered. The three constants S_{L0}, α and β for NG are defined as given in Equations (28) and (29) (Hernandez et al., 2005), where $B_m = 0.49m/s$, $B_\phi = -0.59m/s$, $\phi_m = 1.39$ and ϕ is equivalence ratio.

$$S_{L0} = B_m + B_\phi\,(\phi - \phi_m)^2 \tag{28}$$

$$\begin{aligned}\alpha &= 0.68\phi^2 - 1.7 + 3.18\\ \beta &= -0.52\phi^2 + 1.18\phi - 1.08\end{aligned} \tag{29}$$

The Taylor Microscale λ used in Equation (26) is the spacing of turbulent Kolmogorov vortices in the reaction zone, as conceptualized by Poulos and Heywood (1983). It can be tracked as a function of integral length scale L and turbulence intensity u':

$$\frac{\lambda}{L} = \left(\frac{15}{A}\right)^{0.5}\left(\frac{u'L}{\nu}\right)^{-0.5} \tag{30}$$

where $A = 1$ for perfect isotropy and ν is kinematic viscosity. The kinematic viscosity of unburned gas can be obtained from the correlation given in Equation (31), where T_u and ρ_u are unburned gas temperature and density.

$$\nu = 3.3 \times 10^{-7}\frac{T_u^{0.7}}{\rho_u} \tag{31}$$

Before SOC, the integral length scale L used in Equation (30) can be represented as the instantaneous height of the combustion chamber, based on the assumption that a smallest dimension will constrain to the size of large eddies. Therefore, L can be expressed as a function of cylinder volume V and bore size B–see Equation (32). The calculation of integral length scale after combustion will be discussed in the latter section.

$$L = \frac{4V}{\pi B^2} \tag{32}$$

The turbulence intensity u' before SOC is determined from the turbulent energy cascade model, also known as the $k - \varepsilon$ model (Poulos and Heywood, 1983). In this model, mean kinetic energy K is converted to kinetic turbulent energy k, and kinetic turbulent energy is then converted to heat via viscous dissipation on the Kolmogorov scale. The mean kinetic energy and kinetic turbulent energy are defined as given in Equations (33) and (34), where m is the mass in the cylinder and U is mean flow velocity.

$$K = \frac{1}{2}mU^2 \tag{33}$$

$$k = \frac{3}{2}mu'^2 \tag{34}$$

The change rate of mean kinetic energy and kinetic turbulent energy $\dot{K}$, $\dot{k}$ are given as:

$$\frac{dK}{dt} = \frac{1}{2}\dot{m}_i v_i^2 - P_t - K\frac{\dot{m}_e}{m} \tag{35}$$

$$\frac{dk}{dt} = P_t - m\varepsilon - k\frac{\dot{m}_e}{m} \tag{36}$$

where $\dot{m}_i$ and $\dot{m}_e$ are the mass flow rate into and out of the cylinder, v_i is velocity of flow into the cylinder, P_t and ε are the production and dissipation rate of turbulent kinetic energy, respectively. Since the cycle simulation starts at IVC and end at EVO, no mass transfer exists between cylinder and ambient during the simulation span, thus the terms with valve mass flow rates $\dot{m}_i$ and $\dot{m}_e$ are zero. The production and dissipation term for turbulent kinetic energy P_t, ε are defined as given in Equations (37) and (38), where c_β is an adjustable constant.

$$P_t = 0.3307c_\beta\left(\frac{K}{L}\right)\left(\frac{k}{m}\right)^{0.5} \tag{37}$$

$$\varepsilon = \frac{u'^3}{L} = \frac{(2k/3m)^{1.5}}{L} \tag{38}$$

During the combustion, the turbulence intensity and integral length scale are governed by the conservation of angular momentum of large eddies (Poulos and Heywood, 1983):

$$\frac{L}{L_0} = \left(\frac{\rho_{u0}}{\rho_u}\right)^{1/3} \qquad \frac{u'}{u_0'} = \left(\frac{\rho_u}{\rho_{u0}}\right)^{1/3} \tag{39}$$

where L_0, u'_0 and ρ_{u0} are integral length scale, turbulence intensity and unburned gas density at SOC.

Flame Geometry Model

The flame front area A_f appeared in Equation (24) is defined as the surface area of the leading edge of the flame. Flame front area governs the mass entrainment rate into the reaction zone. In conventional SI engines, it is generally accepted that the flame front initiates from the location of spark and propagates into the space with a spherical shape. In a dual-fuel engine, the ignition of diesel generates multiple ignition sites for the surrounding NG-air mixture. Those ignition sites then form a unit flame front which travels in a direction perpendicular to the outer boundary of diesel spray. Under this circumstance, the flame front can no longer be considered as spherical. Instead, a more sophisticated flame front model which has the fidelity to predict the evolution of the flame surface area as it propagates from the ignition sites in diesel-fuel packets is needed. The flame fronts formed around the glowing diesel sprays will eventually interact with each other, and the geometric constraints established by the combustion chamber boundaries.

In this work, a new flame geometry model is developed to predict the flame front area of NG-air flame. A detailed model is proposed to establish flame kernels and subsequently track the evolution of the flame front. The in-cylinder space is divided into a number of slices equal to the number of diesel injector holes. It is assumed that diesel sprays injected from each injector hole are identical and uniformity is assumed among all slices, thus the flame geometry model only needs to be applied to one slice.

Initial conditions for flame initiation

The NG flame front is assumed to originate from the outer boundary of a diesel spray, thus the geometry of diesel spray at SOC determines the initial conditions of NG combustion. It is assumed that combustion of NG in a dual-fuel engine initiates from multiple ignition sites surrounding the diesel spray, based on Karim and Liu (1992), and that initial flame kernels merge together to form a uniform front. **Figure 4B** gives geometrical definition of a diesel spray at SOC viewing from the side. The shape of the diesel spray is approximated by a combination of a cone and a hemisphere, which agrees well with optical studies of diesel sprays (Dec, 1997).

The spray tip penetration at SOC is represented as L_{p0}, which can be obtained from the spray penetration model given in Equations (2) and (3). The spray angle θ is obtained from the correlation developed by Hiroyasu (1980):

$$2\theta = 0.05\left(\frac{\rho_a \Delta P d_0^2}{\mu_a^2}\right)^{1/4} \tag{40}$$

where ρ_a, μ_a are density and dynamic viscosity of in-cylinder gas at SOI, ΔP is the pressure difference between the injector and ambient and d_0 is the injector hole diameter. The angle between the spray centerline and cylinder head is represented as α. The height of the cone x_0 and the diameter of the hemisphere r_0 can be obtained as:

$$x_0 = \frac{L_{p0}}{1+\tan\theta} \qquad r_0 = x_0 \tan\theta \tag{41}$$

Free evolving flame front

Once the flame front is formed, it propagates freely into the space in the direction perpendicular to the diesel spray outer boundary. In case that there are no constrains to the propagation, the geometry of flame front is represented in **Figure 4C**. For this free evolving flame front, it is assumed that the velocity of flame is identical at every location. At any moment of flame propagation, the distance between the injector hole and the furthest location of flame front relative to injector L_p is defined as:

$$L_p = L_{p0} + \int (u' + S_L)dt \tag{42}$$

where L_{p0} is obtained from initial conditions and $\int (u' + S_L)dt$ is the distance of flame front traveled after SOC. At any moment, this distance traveled is identical at every location of the flame front. With L_p known, the radius of the hemisphere flame front r is defined as the difference between L_p and initial height of the cone x_0:

$$r = L_p - x_0 \tag{43}$$

The furthest distance between flame front and the injector hole in the direction perpendicular and parallel to the cylinder head X_p and Y_p are defined as:

$$X_p = x_0 \cos\alpha + r \qquad Y_p = x_0 \sin\alpha + r \tag{44}$$

Interaction with constrains

In real-world conditions, the NG-air flame initiated from the diesel spray will not always propagate freely into the space. Instead, the flame front constantly interacts with surrounding constrains, including cylinder head, wall, piston and other flame fronts from surrounding sprays. All these constrains need to be taken into consideration in the calculation of flame front surface area. To realize this, geometrical information about the combustion chamber is needed, including the piston bowl shape. **Figure 5A** shows the shape of the bowl-in-piston design used in the experiments. A detailed modeling of piston top geometry requires full definition of boundaries and significantly increases computational burden. Instead, its geometry can be approximated with the shape shown in **Figure 5B**, where the piston bowl is further bounded by the two surfaces parallel to cylinder head and wall, which are depicted as dashed lines. This approximation is for the convenience of solving the geometrical interactions between the flame front and piston bowl, and provides sufficient accuracy for the flame propagation simulation.

To solve the interaction between flame front and cylinder head, wall and piston top, the cylinder space is divided into 9 identical slices as shown in **Figure 5C** (for a 9-hole injector). The geometries defined in **Figure 5C** set the basic framework of the flame geometry model. Each slice is approximated as a triangular prism, where O1-O2-O3 defines plane B, representing the cylinder head; O1-O4-O10-O9 defines plane A, a vertical slice coplanar to the spray centerline; O5-O6-O8-O7 defines plane C, a slice perpendicular to spray centerline. The shaded

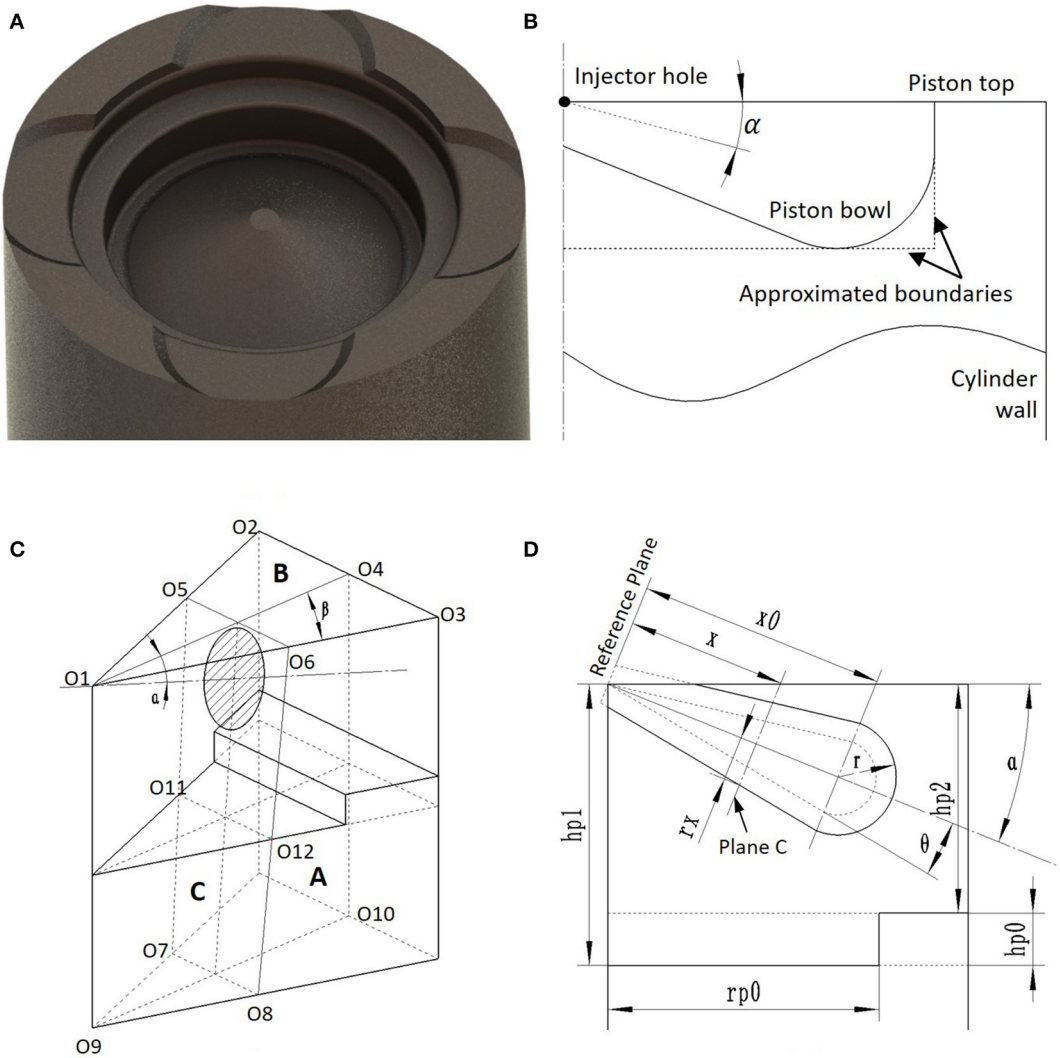

FIGURE 5 | (A) Geometry of the piston from the engine used in this work. **(B)** Approximation of the piston geometry on a 2-D plane. **(C)** 3-D illustration of geometrical framework of the flame geometry model. **(D)** Further illustration of geometrical framework in a 2-D plane.

area on plane C is the projection of the enflamed area, where the outer boundary of shaded area is the projection of flame front. The numerical scheme to arrive at the total flame front surface area is to calculate the projection of flame front on plane C and integrate them along the spray centerline. O5-O6-O8-O7 is the constraint for the flame front projection on plane C, where O5-O6 defines cylinder head, O11-O12 defines piston top, and O5-O7, O6-O8 defines the surrounding slices. When the projected flame front on plane C is within the constrains, the flame front is not touching any of the boundaries; however, when the projected flame front intersects with any of the constrains, the part outside of the boundaries is "cut-off" and is excluded from the calculation of the total flame front area. During the solving process, the position of the piston constantly changes as it moves toward or away from the TDC; thus, the plane C needs to be considered at every possible location. The geometrical definitions shown in this figure apply for all conditions and remain consistent in the latter sections of the paper.

The Plane A defined in **Figure 5C** can be further illustrated in **Figure 5D**. Here a reference plane is defined as a plane perpendicular to the spray centerline and is coplanar to the injector. The distance between the reference plane and Plane C is defined as x and the radius of projected free evolving flame front is defined as r_x. The distance between the piston top and cylinder head is defined as h_{p2}. The distance between piston top and the approximated plane of the piston bowl is defined as h_{p0}, while the distance between cylinder head and piston bowl plane is h_{p1}.

The radius of projected free evolving flame front r_x can be obtained through Equation (45). Three scenarios are considered based on the distance x between reference plane and Plane C. When x is smaller than x_0, it is assumed that the flame front travels in the direction parallel to the reference plane. Since the flame front has the same propagation speed at any location, the

distance traveled by the flame front in this scenario is the same as the location where the flame evolves as a hemisphere, which is $r - r_0$ at any instant. When x is greater than x_0 and smaller than the furthest location of flame front relative to the reference plane, radius r_x is obtained as the radius of the slice of the hemisphere. When x is greater than $x_0 + r$, r_x is zero.

$$r_x = \begin{cases} x\tan\theta + r - r_0; & 0 < x \le x_0 \\ \sqrt{r^2 - (x - x_0)^2}; & x_0 < x \le x_0 + r \\ 0; & x > x_0 + r \end{cases} \quad (45)$$

The distance between piston top and cylinder head h_{p2} and the distance between the piston bowl plane and cylinder head h_{p1} can be obtained according to Equation (46), where V_{cyl} is the instantaneous volume of the cylinder, while R_{cyl} is the radius of the cylinder which equals to Bore/2. In this work, cylinder volume is calculated by assuming the piston top is flat, thus the piston bowl volume is neglected when obtaining h_{p2}.

$$h_{p2} = \frac{V_{cyl}}{\pi R_{cyl}^2}; \qquad h_{p1} = h_{p2} + h_{p0} \quad (46)$$

Figure 6A defines a two-dimensional coordinate system for plane A. The X-axis is coplanar to the cylinder head while Y axis is coaxial to the centerline of the cylinder. The point where X and Y axes cross is defined as the origin. The Plane C is extended in both directions to intersect with every possible plane. The intersection lines in the 3-D space are reduced to points A, B, C, D, E and O in this 2-D plane, where point A stays on line $Y = -h_{p1}$, point B stays on line $Y = -h_{p2}$, point C stays on line $Y = 0$, point D stays on line $X = R_{cyl}$ and point O is the intersection point between line DE and spray centerline. The geometrical positions of these points enable a universal analytical solution of the flame front area. With the coordinate system defined, the functions of constraints and coordinates of intersection points can be easily obtained. The function representing the line on Plane C, which is line DE, can be defined as:

$$Y = \frac{1}{tan\,\alpha}X - \frac{x}{sin\,\alpha} \quad (47)$$

The coordinates of points A, B, C, D, E, and O can be obtained by solving the combined equations of line DE and other

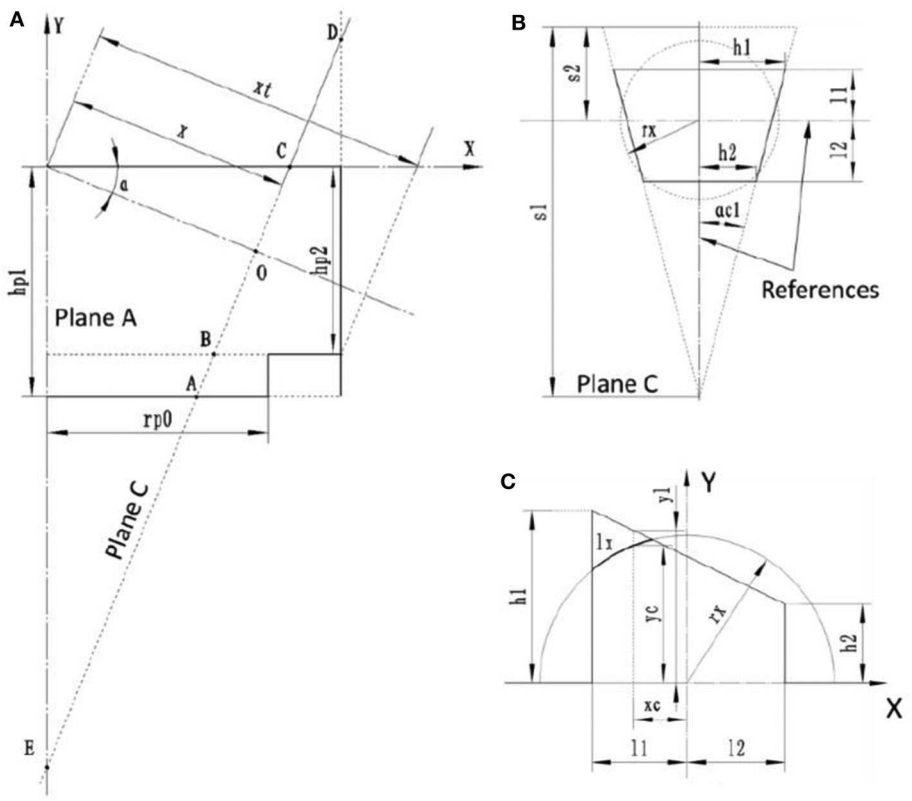

FIGURE 6 | (A) Coordinate system developed for plane A. **(B)** Geometrical definition of Plane C. **(C)** Coordinate system developed for Plane C.

constraining lines:

$$A: \left[tan\alpha \left(\frac{x}{sin\,\alpha} - h_{p1} \right), -h_{p1} \right]$$
$$B: \left[tan\alpha \left(\frac{x}{sin\,\alpha} - h_{p2} \right), -h_{p2} \right]$$
$$C: \left[\frac{x}{cos\,\alpha}, 0 \right]$$
$$D: \left[R_{cyl}, \frac{R_{cyl}}{tan\,\alpha} - \frac{x}{sin\,\alpha} \right]$$
$$E: \left[0, -\frac{x}{sin\,\alpha} \right]$$
$$O: [x\,cos\,\alpha, -x\,sin\,\alpha\,]$$

The piston bowl is approximated as a flat surface with a function of $Y = -h_{p1}$ for the convenience of numerical calculation. To obtain the solution of total flame front area, Plane C needs to be taken at every possible location. In the coordinate system defined above, Plane C is allowed to move between $x = 0$ and $x = x_t$. The furthest location x_t is defined as:

$$x_t = \left(h_{p2}\,tan\,\alpha + R_{cyl} \right)\,cos\,\alpha \tag{48}$$

Figure 6B gives the geometrical definition of Plane C viewed from the origin of the spray and perpendicular to Plane C. As shown in **Figure 5C**, each slice of cylinder volume is assumed as a triangular prism, thus the intersection between the slice and the Plane C always results in a triangle, shown as the dashed outline in **Figure 6B**, where the lowest point corresponds to the point E shown in **Figure 6A**. The top line of the triangle corresponds to the cylinder head, the lower solid line corresponds to piston top, and the remaining two lines represent the boundary between the slice and the adjacent slices. The dashed circle defines the projection of the flame front on this plane, while the solid lines shown in this figure with a trapezoidal shape represent the constraints of the flame front. When the projection of the flame front is beyond the trapezoidal constraints, it is considered to be cut-off by the boundaries. In the Plane C, the projected flame front within the constraints is defined as the *effective flame front*, while the total length of the effective flame front is defined as the *effective flame length*.

With the geometrical definition shown in **Figure 6B**, the geometrical information of the trapezoidal constraints can be easily obtained. Here the two reference lines are defined, both intersecting with the center of projected flame front, but one being parallel and another perpendicular to the cylinder head. The distances between the two horizontal lines and the horizontal reference are defined as l_1 and l_2. The two lengths which further defines the position of trapezoidal constraints in relative to the vertical references are h_1 and h_2, respectively. The numerical representation of l_1 can be summarized as:

$$l_1 = \begin{cases} |CO|\,; & Y_D \geq Y_C \\ |DO|\,; & Y_O \leq Y_D < Y_C \\ -|DO|\,; & Y_D < Y_O \end{cases} \tag{49}$$

where |CO| and |DO| are the lengths of lines CO and DO defined in Plane A, which can be obtained from the coordinates of each points given above. Y_C, Y_D and Y_O are the Y coordinates of points C, D and O. Similarly, l_2 can also be summarized as:

$$l_2 = \begin{cases} |OE|\,; & X_A \leq 0 \\ |OB|\,; & X_B \geq r_{p0} \wedge Y_O \geq Y_B \\ -|OB|\,; & X_B \geq r_{p0} \wedge Y_O < Y_B \\ |OA|\,; & X_A > 0 \wedge X_B < r_{p0} \wedge Y_O \geq Y_A \\ -|OA|\,; & X_A > 0 \wedge X_B < r_{p0} \wedge Y_O < Y_A \end{cases} \tag{50}$$

where X_i represents the X coordinates of each points defined in Plane A. In the above definition of l_1 and l_2, when the number becomes negative, the location of the constraints is on the opposite side of the reference line shown in **Figure 6B**. The height of the triangular boundary, defined as s_1 in **Figure 6B**, can be obtained as:

$$s_1 = \frac{x}{sin\,\alpha\,cos\,\alpha} \tag{51}$$

Similarly, the distance between the cylinder head and the lateral reference line s_2 can be represented as:

$$s_2 = x\,tan\,\alpha \tag{52}$$

The angle which determines the shape of the triangular boundary, define as α_{c1} in **Figure 6B**, can be obtained as:

$$\alpha_{c1} = arctan\,(sin\,\alpha\,tan\,\beta) \tag{53}$$

where β is the same as defined in **Figure 5C**, determined by the number of injector holes. The position of trapezoidal constraints relative to the vertical references are h_1 and h_2 can be obtained as:

$$h_1 = \left(l_1 + s_1 - s_2 \right)\,tan\,\alpha_{c1} \qquad h_2 = \left(s_1 - s_2 - l_2 \right)\,tan\,\alpha_{c1} \tag{54}$$

Solving the flame front area

As mentioned in previous section, the total length of effective flame front in Plane C is defined as the effective flame length. This section presents the analytical method for determining this length. Once this length is found in each Plane C, it can be integrated along the spray centerline to arrive the total flame surface area. For ease of numerical calculation, the right half of **Figure 6B** is tilted counterclockwise for 90 and is represented as shown in **Figure 6C**, where the effective flame length is represented as l_x. Since the geometry shown in **Figure 6B** is symmetrical with respect to the vertical reference line, the actual total effective flame length in this 2-D plane is twice of the effective flame length shown in **Figure 6C**, which is $2l_x$.

In the geometry defined in **Figure 6C**, when the projected flame front is beneath the constraints, the length of this flame front is considered as effective flame length and vice versa. To

arrive a universal numerical solution, another coordinate system is defined. In this figure, a 2-D coordinate system is defined where X and Y axes are marked. The relative geometrical position of projected flame front and constraints are evaluated along the X axis from $X = -r_x$ to $X = r_x$. At each point on both the projected flame front and constraints which satisfies $X = x_c$, the Y coordinates are defined as $Y = y_c$ and $Y = y_l$. By evaluating y_c and y_l at each x_c, the total length of l_x is obtained by discrete integration.

When $X = x_c$ is satisfied, y_l can be determined by the geometry of the constraints. Here the Y coordinates of constraints when $x_c < -l_1$ or $x_c > l_2$ are set to zero to ensure the effective flame length is always zero at these conditions. The numerical solution of y_l is given as:

$$y_l = \begin{cases} 0; & x_c \le -l_1 \\ -\frac{(x_c - l_2)(h_1 - h_2)}{l_1 + l_2} + h_2; & -l_1 < x_c \le l_2 \\ 0; & x_c > l_2 \end{cases} \quad (55)$$

Similarly, y_c can be determined using the geometry of the projected flame front. The numerical solution of y_c is given as:

$$y_c = \begin{cases} 0; & x_c \le -r_x \\ \sqrt{r_x^2 - x_c^2}; & -r_x < x_c \le r_x \\ 0; & x_c > r_x \end{cases} \quad (56)$$

With the information of y_l and y_c, the discrete segment of effective flame length dl_x can be obtained by evaluating the geometrical relationship between projected flame front and constraints at each location. The dl_x can be represented as a function of the coordinate of the X axis $dl_x = f(x_c)$. By integrating dl_x alone the X axis, the total effective flame length l_x can be obtained as:

$$l_x = \int_{-r_x}^{r_x} f(x_c) dx_c \quad (57)$$

The discrete segment of effective flame length $dl_x = f(x_c)$ can be determined from the geometrical information of the projected flame front and the relative relation between y_l and y_c. When y_c is greater than y_l, the projected flame surface is outside the constraints, indicating the flame is being "cut-off" by constraints, thus dl_x is 0. On the contrary, when the projected flame front is within the constraints, the effective flame length is obtained by solving along the projected flame front. The numerical solution of $f(x_c)$ is summarized as:

$$f(x_c) = \begin{cases} \frac{2r_x}{\sqrt{r_x^2 - x_c^2}}; & y_l \ge y_c \\ 0; & y_l < y_c \end{cases} \quad (58)$$

Figure 7A gives an example of effective flame length calculation and its relation to the relative geometry between projected flame front and constraints. The constrains are illustrated with the thick black line, where the left vertical represents the cylinder head surface, the top line is the boundary of the slice and the right vertical line is the piston top. In this figure, the geometry of flame is fixed and x is the only varying parameter. Recall that x represents the distance between the injector tip and Plane C. The relative geometry between constraints and projected flame front is also shown. It can be observed that effective flame length increases with x due to the center of projected flame front moving away from the cylinder head and surrounding flame front, the two major constraints when Plane C is in the proximity of the injector. When x is small, flame front is significantly constrained by cylinder head, since the center point of diesel spray is close to the cylinder head. Same applies to constraint imposed by the adjacent flame fronts. As x increases, the effective flame length continues to increase, until it reaches its maximum value at x = 50 mm, where no constraint is applied to the flame front any more. The flame is at a free propagating state in this situation. As x continue to increase, the effective flame length then starts to decrease due to Plane C entering the hemisphere region of the flame and the radius of the projected flame surface r_x starts to decrease.

Figure 7B shows an example of computed effective flame length l_x as a function of distance between Plane C and injector x and the evolving status of the flame front $r - r_0$. In this condition the piston position is fixed and $r - r_0$ is the only varying parameter. **Figure 4C** have shown the definition of $r - r_0$. As the flame front evolves into space, the interaction between flame front and constraints including cylinder head, piston and surrounding flame fronts varies and the details are captured by the model.

Once the effective flame surface length l_x is evaluated at each Plane C, the total flame surface area A can be obtained by integrating l_x along the spray axis:

$$A = \int_0^{x_t} 2 l_x ds \quad (59)$$

where x_t represents the furthest location of Plane C relative to injector as defined in Equation (48). The ds is represented as a function of the Plane C location x. For conditions when Plane C is in the cone region ($x \le x_0$) or hemisphere region ($x > x_0$), ds is represented as:

$$ds = \begin{cases} \frac{r}{\cos\theta} dx; & x \le x_0 \\ \frac{r}{r_x} dx; & x > x_0 \end{cases} \quad (60)$$

Figure 8 gives a flow chart of the iterative computing process for obtaining the flame front area. Two loops comprise this scheme: main loop and the sub-loop. The main loop updates the integrated flame area A while the sub loop updates the solution of the effective flame surface length l_x at each main loop iteration. The main loop starts by assuming that the distance between Plane C and injector x is 0 and ends when Plane C reaches its maximum distance $x = x_t$. Inside the main loop, coordinates of A, B, C, D, E, O defined in **Figure 6A** are calculated and are used to derive the length of OA, OB, OC, OD, OE. The l_1 and l_2 defined in **Figure 6C** are subsequently obtained using

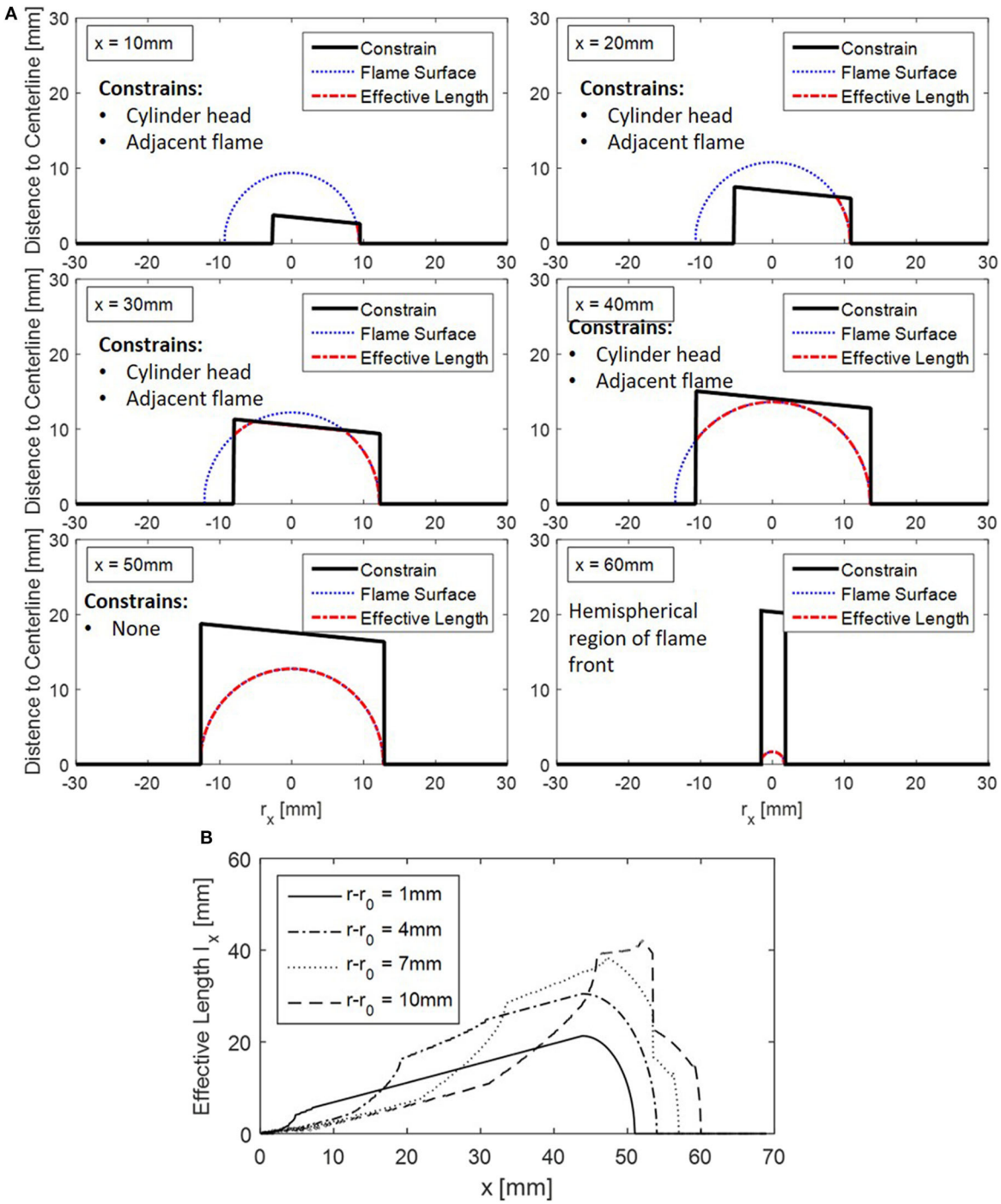

FIGURE 7 | (A) An example of effective flame length calculation. **(B)** An example of computed effective flame length l_x as a function of x and r-r_0.

Equations (49) and (50). The sub loop starts here by assuming the x_c defined in **Figure 6C** is at its boundary condition $x_c = -r_x$ and ends when x_c reaches another boundary $x_c = r_x$. Inside the sub loop, y_l and y_c defined in **Figure 6C** are calculated according to Equations (55) and (56). The quantitative relation between y_l and y_c is evaluated and the discrete segment of effective flame length $dl_x = f(x_c)$ is determined by Equation (58). The $f(x_c)$ is integrated in each iteration of the sub loop and a solution of l_x is reached when x_c reaches boundary condition $x_c = r_x$. The calculation then exits the sub loop and returns to the main loop, where l_x is integrated in each iteration of the main loop following Equation (59). The final value of flame surface area A is obtained when Plane C reaches its terminal position $x = x_t$.

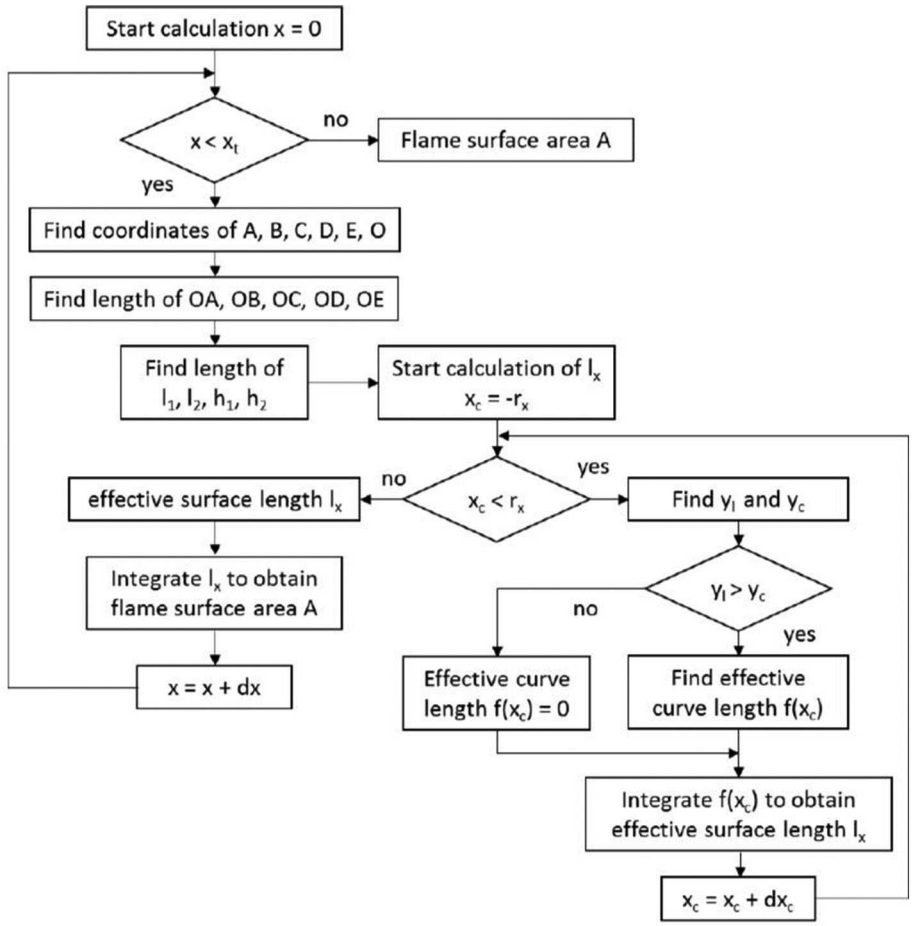

FIGURE 8 | Schematic description of the computing process of flame front area.

Initial formation of NG flame front

The flame front area calculation scheme assumes the flame initiates from the outer boundary of diesel spray, causing a step change of flame surface area at start of NG combustion. However, according to the work of Karim and Liu (1992), the combustion of NG in a dual-fuel engine initiates from multiple ignition sites surrounding the diesel spray. Instead of a step change from 0 to an initial value determined by surface area of spray, the evolving of flame front area at onset of NG combustion should be a continuous process. In this work, a method is proposed to approximate the multi-site ignition of NG-air mixture. The proposed approach assumes that ignition sites distribute evenly around the outer boundary of diesel spray and these sites ignite simultaneously at SOC. Upon ignition, individual flame fronts start to form at each site and propagate freely into the space. The flame is not allowed to travel into the diesel spray thus the flame fronts are approximated as hemispheres.

Figure 9A shows the geometrical assumption made at onset of NG combustion. The figure is showing a segment from the surface area of a diesel spray. The dots are representing the ignition sites, distributed evenly in the surface. The circle around each ignition site represents the flame front evolved from the original kernel. The radius of the hemispherical flame front is defined as r while the distance between adjacent ignition sites is defined as d. The spacing variable d is arbitrarily determined by the user. The scale of this parameter determines the slope of initial heat release after NG has been ignited. In this work, d of 5 mm yields a good agreement with the experimental heat release, and that is generally the simplest way to calibrate it. Insight from optical diagnostics work would be another possibility. The process of the flame growth during the initial stage of NG combustion is divided into three phases: free evolving, interacting and merging. The free evolving phase includes the flame propagation from the ignition site ($r = 0$) to the point where flame fronts start to interact with each other ($r = d/2$). The flame propagation then enters the interaction stage as flame fronts start interacting and partially merging with surrounding flames. When the individual flame propagates all the way to the ignition site of the adjacent flame ($r = d$), it is assumed that the elemental flame fronts have merged into a uniform flame front and the calculation switches according to the scheme discussed in previous sections.

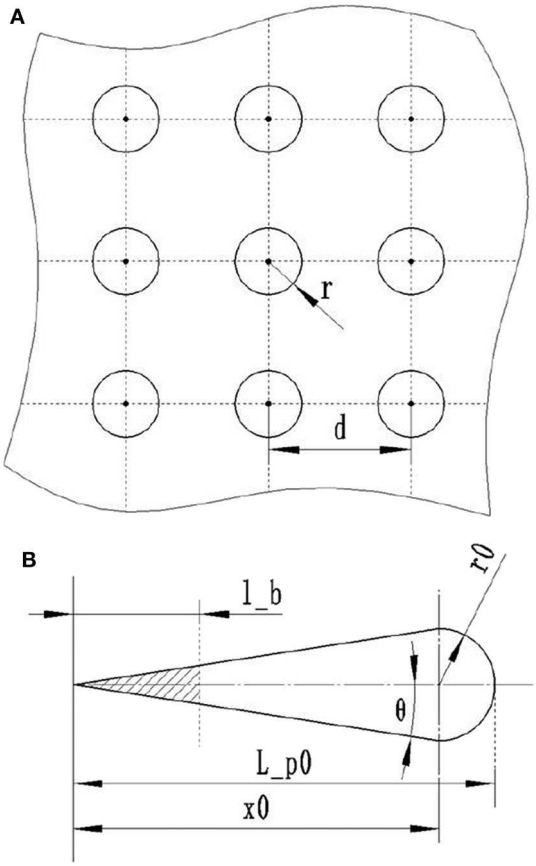

FIGURE 9 | (A) Geometrical assumptions made at initial stage of NG combustion. **(B)** A 2-D illustration of the approximated diesel spray form at SOC.

To obtain a numerical solution of total flame front area, the surface area of igniting diesel spray needs to be known. **Figure 9B** gives a 2-D illustration of approximated diesel spray at SOC. Since diesel spray travels a certain distance before it breaks up into droplets, the entire surface area shown in this figure does not contribute to the ignition of the surrounding NG. Rather, it is assumed that the shaded area in this figure does not produce ignition sites.

In the geometry defined in **Figure 9B**, the diesel spray breakup length l_b can be obtained from Equation (3) by setting $t = t_b$. The definition of other parameters is the same as defined in **Figure 4C**. The igniting diesel spray surface area is arrived as:

$$A_{ini} = 2\pi {r_0}^2 + \pi r_0 \sqrt{x_0^2 + {r_0}^2} - \pi l_b \tan\theta \sqrt{l_b^2 + (l_b \tan\theta)^2} \quad (61)$$

Based on the assumption that the NG ignition sites distribute evenly along the diesel spray igniting surface, the number of ignition sites from a diesel spray is approximated as:

$$N_{ign} = A_{ini}/d^2 \quad (62)$$

The surface area of each flame front initiated from individual ignition site A_0 can be determined as a non-continuous functions of flame radius r:

$$A_0 = \begin{cases} 2\pi r^2; & 0 < r \le \frac{d}{2} \\ 2\pi r^2 - 2\int_{d/2}^{r} 2\pi r dx; & \frac{d}{2} < r \le \frac{\sqrt{2}}{2} d \\ 2\int_0^{d/2} 2r \arcsin\frac{d}{2r_x} dx; & \frac{\sqrt{2}}{2} d < r < d \end{cases} \quad (63)$$

The total flame surface area during the initial stage of NG combustion can be obtained as:

$$A = A_0 N \quad (64)$$

Once the flame radius of individual flame front r reaches the merging point $r = d$, it is assumed that all individual flames merge as a uniform flame front and the calculation of flame front area follows the iterative scheme given in **Figure 8**.

Thermodynamics Model

The thermodynamic model updates the temperature, pressure, composition and gas properties of in each packet. Mass is only allowed to transfer from ambient to packet zone and heat transfer is not allowed in both directions. The in-cylinder pressure is uniform across the combustion chamber space, but obviously varies with crank-angle.

Equation (65) gives the ODE for updating cylinder pressure. Instead of being a constant, the heat capacity ratio γ is constantly updated as a function of gas composition and temperature.

$$\dot{P} = \frac{\gamma - 1}{V} \dot{Q}_{total} - \frac{\gamma}{V} P \dot{V} \quad (65)$$

The $\dot{Q}_{total}$ is total heat input, calculated from the difference between the heat release from combustion $\dot{Q}_{fuel}$ and heat transfer loss $\dot{Q}_{ht}$:

$$\dot{Q}_{total} = \dot{Q}_{fuel} - \dot{Q}_{ht} \quad (66)$$

The heat transfer to the wall is estimated using bulk in-cylinder temperature. Here convective heat transfer is the only form of heat transfer considered. Radiative heat transfer is excluded due to dual-fuel combustion's low production of soot. convective heat transfer rate $\dot{Q}_c$ is estimated based on Woschni correlation (Woschni, 1967), as represented in Equation (67). A_{wall} represents the area of wall available for heat transfer, including cylinder head, piston top and cylinder liner surfaces in contact with the gas. T_{wall} represents wall temperature, T represents bulk gas temperature and h_c is Woschni convective transfer coefficient. The assumed wall temperatures for the cylinder liner, piston top and cylinder head are 400K, 550K, and 550k, respectively.

$$\dot{Q}_c = h_c \sum A_{wall} (T - T_{wall}) \quad (67)$$

The Woschni convective heat transfer coefficient h_c is given in Equation (68), where T represents bulk gas temperature, P

represents cylinder pressure, and w is characteristic velocity. Equation (69) gives definition of characteristic velocity w, where C_1, C_2 are constants, S_p represents mean piston velocity P_r, T_r, V_r represents reference cylinder pressure, temperature and volume at IVC and P_m represents motored cylinder pressure. For compression stroke, $C_1 = 2.28$ and $C_2 = 0$, for combustion and expansion, $C_1 = 2.28$ and $C_2 = 3.24 \times 10^{-3}$.

$$h_c = 3.26\, Bore^{-0.2} P^{0.8} T^{-0.55} w^{0.8} \tag{68}$$

$$w = C_1 S_p + C_2 \frac{V T_r}{P_r V_r} (P - P_m) \tag{69}$$

Accuracy of gas temperature estimation is essential to the model. The temperature serves as input of various sub-models including ignition delay model, evaporation model, and temperature dependent emission models. The temperature estimation scheme used in this work is based on the formulation of the Conservation of Energy equation that relies on the energy derivatives expressed in terms of enthalpy and its partial derivatives proposed by Assanis and Heywood (1986). Therefore, the ordinary differential equation for temperature is:

$$\dot{T} = \frac{B'}{A'} \left[\frac{\dot{m}}{m} \left(1 - \frac{h}{B'} \right) - \frac{\dot{V}}{V} - \frac{C'}{B'} \dot{\phi} + \frac{1}{B' m} \left(\sum_j \dot{m}_j h_j + \dot{Q}_w \right) \right] \tag{70}$$

where:

$$\begin{cases} A' = \frac{\partial h}{\partial T} + \frac{\frac{\partial \rho}{\partial T}}{\frac{\partial \rho}{\partial P}} \left(\frac{1}{\rho} - \frac{\partial h}{\partial P} \right) \\ B' = \frac{1 - \rho (\partial h / \partial P)}{\partial \rho / \partial P} \\ C' = \frac{\partial h}{\partial \phi} + \frac{\partial P / \partial \phi}{\partial \rho / \partial p} \left(\frac{1}{\rho} - \frac{\partial h}{\partial P} \right) \end{cases} \tag{71}$$

In the above two equations, m represents the mass in the control volume. When Equation (70) is solved to calculate bulk cylinder temperature during compression and combustion, m is a constant as no mass transfer occurs when intake and exhaust valves are shut. When using this equation to estimate the temperature in a packet, mass transfer will need to be taken in to account. In Equation (70), V represents control volume, h represents specific enthalpy of gas in the control volume, ϕ represents equivalence ratio, $\sum_j \dot{m}_j h_j$ represents total enthalpy transfer rate and $\dot{Q}_w$ represents heat transfer rate into the control volume.

Gas Composition and Property

To achieve an accurate thermodynamics model, a sub-model for updating gas property is also included in this work. This model tracks and updates intake gas species, fuel composition and burned gas composition. The gas species being tracked are O_2, N_2, CO_2, H_2O and diesel fuel vapor. The initial gas composition and fuel-oxygen reactions are used to track the concentration of O_2, CO_2 and H_2O. Equations (72) and (73) gives representation of gas property for O_2, N_2, CO_2, H_2O. The constants α_1 to α_6 are given in the NASA reference (Gordon and McBride, 1976).

$$\frac{c_p}{R} = \alpha_1 + \alpha_2 T + \alpha_3 T^2 + \alpha_4 T^3 + \alpha_5 T^4 \tag{72}$$

$$\frac{h}{RT} = \alpha_1 + \frac{\alpha_2}{2} T + \frac{\alpha_3}{3} T^2 + \frac{\alpha_4}{4} T^3 + \frac{\alpha_5}{5} T^4 + \alpha_6 \frac{1}{T} \tag{73}$$

For diesel vapor and NG, the gas properties are calculated based on Heywood (1988):

$$\frac{c_p}{R} = \alpha_1{}' + \alpha_2{}' T + \alpha_3{}' T^2 + \alpha_4{}' T^3 + \alpha_5{}' \frac{1}{T^2} \tag{74}$$

$$\frac{h}{RT} = \alpha_1{}' + \frac{\alpha_2{}'}{2} T + \frac{\alpha_3{}'}{3} T^2 + \frac{\alpha_4{}'}{4} T^3 - \alpha_5{}' \frac{1}{T^2} + \alpha_6{}' \frac{1}{T} \tag{75}$$

where α_1' to α_6' are coefficients for diesel vapor. Specific heat capacity c_p is in unit of $J \cdot kg^{-1} K^{-1}$; specific enthalpy h is in J/kg and specific gas constant R is in $J \cdot kg^{-1} K^{-1}$. The specific gas constant R is derived from compositions in the control volume and heat capacity ratio γ is calculated as a function of R and c_p:

$$\gamma = \frac{c_p}{c_p - R} \tag{76}$$

Substituting the Equations (72–75) into Equation (71), Equation (71) leads to:

$$A' = c_p - \frac{p}{\rho T}, \quad B' = RT, \quad C' = 0 \tag{77}$$

Finally, substituting Equation (77) into Equation (70) enables expressing the temperature of the control volume in the form given in Equation (78), where γ, h and h_j are derived from the gas property model discussed above.

$$\dot{T} = T(\gamma - 1) \left[\frac{\dot{m}}{m} - \frac{\dot{m} h}{pV} - \frac{\dot{V}}{V} + \frac{1}{pV} \left(\sum_j \dot{m}_j h_j + \dot{Q}_w \right) \right] \tag{78}$$

Experimental Setup

The inline-six dual-fuel engine was mounted in the class 8 HD truck and the experimental investigation has been conducted on a chassis dynamometer. The baseline was established with the standard Cummins ISX 550 diesel engine. The engine was subsequently equipped with a prototype NG port fuel injection system to achieve dual-fuel operation. The NG fumigator in located downstream the compressor and upstream of the manifold, as shown in **Figure 10**. To meet NG flow requirement, three Clean Air Power NGV solenoids with injection pressure rated at 125 psi were installed on a custom designed manifold. Engine specifications and composition of NG used in the experiment are given in **Table 1**.

Regarding the direct injection of diesel, an overhead camshaft actuates an injector rocker that pushes injector plunger to generate high pressure, and an Integrated Fuel System Module controls the process. The diesel injectors used in the experimental engine are 9-hole unit-injectors with 0.186 mm nozzle holes and

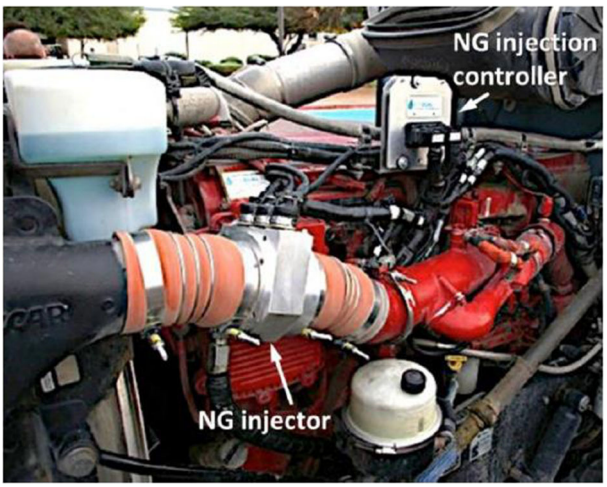

FIGURE 10 | NG injector location of the engine used in experiments.

maximum injection pressure of 2,200 bar. The injection pressure is a function of engine speed. In case of dual-fuel operation, the proprietary prototype system intercepts the signal from the control unit and alters the fuel metering according to the desired NG substitution rate.

Knock resistant GH15DK piezoelectric pressure transducers were installed in cylinders 5 and 6. MICROIFEM piezoelectric amplifiers was used within AVL IndiSmart data acquisition to amplify cylinder pressure signals. Additional signals were sampled by National Instruments CompactDAQ with 9205 and 9213 series modules. AVL KMA Mobile was used to measure diesel fuel flow, while FOX FT2 inline flowmeters were used to measure NG flow and air flow. A PicoTurn rotational speed sensor was used to measure turbo shaft speed. For comprehensive data acquisition, manifold pressure sensor, air temperature sensor and oxygen sensors, were also mounted on the engine. Fuel quantity in the timing chamber as well as in the injection chamber were quantified by voltages sent from Electronic Control Unit to injection solenoids.

Engine speed load sweeps for both diesel only (i.e., baseline) and duel fuel modes were conducted on a chassis dynamometer by controlling the road-load and keeping the transmission in pre-selected gear. The SOI information were difficult to obtain through otherwise commonly used hall-effect sensor, due to the peculiarities of the unit-injector design. Instead, a method based on heat release analysis was developed to extract SOI information. Smoothing of the rate of heat release profile is achieved using FFT method. The point where the downward slope originates is considered to be SOI (Xu et al., 2017b). Finally, measured cylinder pressure data was processed to derive apparent heat release rate (AHRR) using the expression given in Equation (79) (Heywood, 1988):

$$\dot{Q} = \frac{\gamma}{\gamma - 1} P\dot{V} + \frac{1}{\gamma - 1} V\dot{P} \tag{79}$$

Derivation of Diesel Fuel Injection Profile

Due to limited access to measurement of injection pressure and injection rate, a simplified correlation is developed in this work to generate fuel injection rate information as model input. To describe the profile of fuel injection rate, an injection rate shaping array A_s is introduced as a governing parameter. The shaping array A_s defines the history of injection rate during the injection event. An assumption is made that A_s remains constant for all injection conditions. With inclusion of shaping array A_s, the injection rate can be expressed as:

$$\dot{m_{inj}} = \frac{A_s m_{inj}}{\Delta t \cdot \sum_{i=1}^{n} A_s[i]} \tag{80}$$

where m_{inj} is total injected diesel mass and Δt is a time constant determined by the injection duration. A symmetric injection profile with gradual increase and decrease of injection rate at the beginning and ending stages of injection is used to approximate the injection characteristics of a unit injector. **Figure 11A** provides an example of approximated injection rate. A_s is fixed as constant for all cases while injected mass and injection duration is varying. For a given A_s, when injected mass and injection duration are known, a complete profile of fuel injection rate can be obtained.

In the experiment setup used in this work, the total injected mass m_{inj} is known while injection duration is unknown. However, a correlation between injected mass and injection duration in crank angle can be obtained. The injection duration is derived from injected mass and a full profile of fuel injection rate by applying Equation (80). The experimental data of diesel only operations is used to develop this correlation. To obtain a consistent detection of end of injection (EOI), the Quasi-D combustion model for diesel only condition is used to infer the injection duration. The performance of the Quasi-D diesel combustion model has been validated in previous work (Xu et al., 2017b). For each operating condition, an initial guess of EOI corresponds to peak heat release rate derived from cylinder pressure data. The EOI is subsequently manually tuned to arrive a best fitting of the heat release profile.

Figure 11B gives an example for the derivation of EOI at 1,400 rpm. Four engine load conditions are used where injected fuel mass per cycle varied from 95 to 225 mg. Good agreements between model predictions and experimentally derived heat release rates are achieved.

The same method was applied to other engine speeds. A correlation between injection duration and injected mass is subsequently derived through linear regression. **Figure 11C** shows the correlation for injection duration as a function of injected mass. A clear linear relationship was observed with $R^2 = 0.974$. Therefore, correlation between injection duration in crank angle degree CA_{inj} and injected mass m_{inj} shown in Equation (85) can be used with confidence across a wide operating range:

$$CA_{inj} = 0.124 m_{inj} + 4.815 \tag{81}$$

where CA_{inj} is in deg and m_{inj} is in mg. Once the injected mass per cycle is known, the injection duration can be obtained from this correlation, and a full profile of mass injection rate can be estimated as well. This approach also applies for dual-fuel operation conditions.

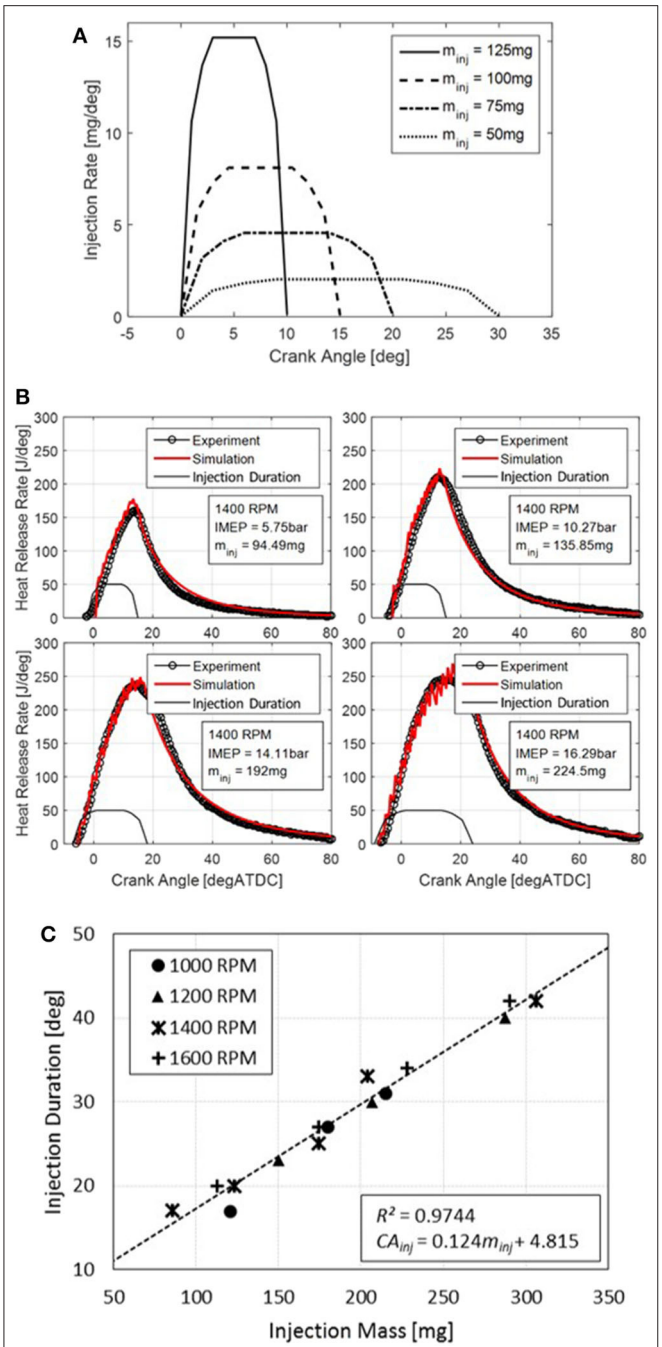

FIGURE 11 | (A) An example of the approximated injection rate model with fixed shaping array and varying injection quantity and duration. **(B)** Derivation of EOI by matching the experimentally derived heat release profiles using the diesel only combustion model. **(C)** Linear regression between diesel injection duration and injected mass.

RESULTS

Model Validation With Experimental Data

The dual-fuel simulation's initial parameters:

- Number of packets in X direction: 20
- Number of packets in Y direction: 5
- Mass fraction of residuals in the unburned zone: 0
- Distance between neighboring ignition sites: 5 mm
- Step size: 0.5 deg CA

The major calibration parameters of this Quasi-D combustion model are (1) Distance between neighboring ignition sites d, (2) Air entrainment rate, and (3) Turbulence intensity expressions.

The Quasi-D combustion model is validated with experimental data for both diesel-only and dual-fuel conditions. At diesel only condition, the model inputs associated with NG are set to zero and only the diesel spray-combustion model is activated. **Figure 12** gives the validation results of diesel only operation conditions where heat release and cylinder pressure are used for validation. Two engine speeds and four load conditions are tested. It is shown that the model agrees well with experimental data at various engine operating conditions. Though at higher loads the model is losing some details of heat release rate around its peak, the cylinder pressure prediction still agrees well with experimental data. It is observed that the predicted heat release profile is showing slight oscillations. This is due to the limited number of packets used in the simulation that leads to discrete "steps" when calculating cumulative heat release. A "smoother" predicted heat release profile can be achieved by increasing the number of packets used in the simulation. However, this would bring the cost of elevated computational power.

Figure 13 shows the validation results for dual-fuel operating conditions. Two examples are given where engine speeds are both 1,200 rpm but engine load and NG substitution ratio is different. The percentages of NG in energy content are 65.6 and 31.8%, respectively. **Figures 13A,B** show the comparison between predicted and experimentally obtained cylinder pressure and heat release rate, while **Figures 13C,D** show the predicted heat release rates contributed from the diesel and NG, respectively. The injection rate profile derived from the correlation developed in the previous section is also shown as reference. Although the heat release profile of these two operating conditions are alike, the contributions from combustion of NG and diesel fuel are quite different because the substitution rate in the case A-B was 65.6%, and for C-D 31.8%. It is shown in **Figures 13C,D** that the proposed diesel injection duration correlation generates reasonable injection profiles under dual-fuel conditions. The turbulent flame propagation model and diesel spray combustion model work simultaneously to output the energy released by both fuels. Overall, the newly developed dual-fuel model agrees very well with experimental data in terms of both heat release rate and cylinder pressure.

Figure 14A shows the prediction of NG flame front surface area of the same engine operation conditions shown in **Figure 13**. The flame surface area A_{flame} and traveled distance R_{flame} are normalized with the Bore^2 and Bore, respectively. The traveled distance R_{flame} is the same as $r - r_0$ in the geometry illustrated in **Figure 4C**. It is shown that the flame front surface area model captures the details of the flame evolving history in its initiation, free-evolving and constraint cut-off stages. The difference between the two operating conditions is mainly due to the penetration depth of the diesel spray at SOC. For the

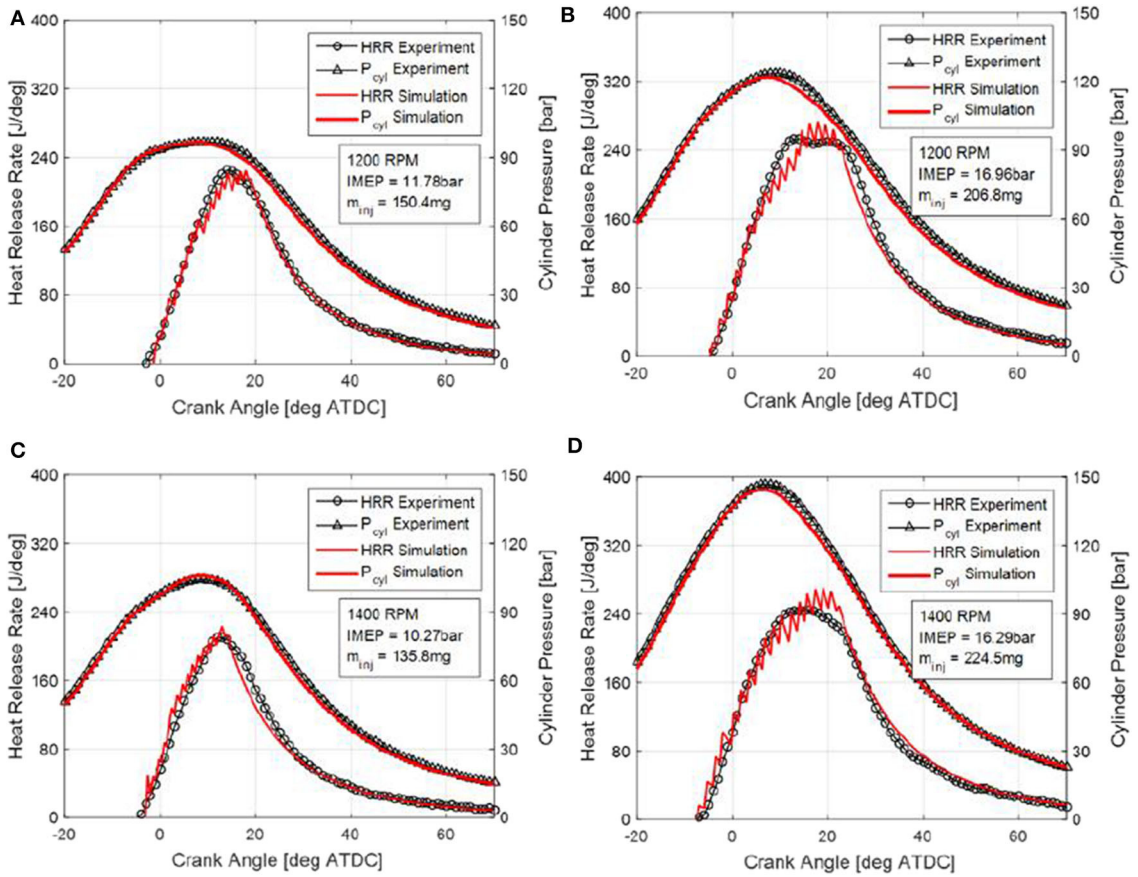

FIGURE 12 | (A–D) Validation results of heat release profile and cylinder pressure at diesel only operation conditions.

higher load case (IMEP = 19.8 bar), the ignition delay is shorter, resulting a shorter penetration, hence a smaller surface area to initiate the combustion of NG-air mixture. In the early free-evolving stage, the normalized flame surface area of the higher load case is lower. However, normalized travel distance R_{flame} when the flame is quenched by the constraints is higher, as expected, since the diesel spray penetration at the initial condition is shorter.

Figure 14B shows model prediction of in-cylinder temperatures, including the unburned, burned and bulk gas temperatures. The unburned gas zone includes the gas that is not involved in the combustion while the burned gas temperature is the average temperature of the burned gas generated by the combustion of both diesel and NG. **Figure 14C** show the temperature predictions as a function of Crank Angle degrees for different packets. The i_{pac} in the legend denotes the index of packet on the x axis originating at the injector tip as defined in **Figure 1**. The smaller i_{pac} implies an earlier injection of the packet. The temperature histories demonstrate a phase lag and differences in peak values, therefore confirming the ability of the model to capture the temperature distribution within the spray. This in turn enables spatial resolution of the temperature distribution within spray, as well as prediction of emissions that would not otherwise be possible with the single burned zone models. In summary, model predictions shown in **Figure 14** provide valuable insights into dual-fuel combustion that would otherwise be very difficult to obtain experimentally.

DISCUSSION

In this work, a Quasi-D multi-zone dual-fuel combustion model is developed and validated with the experimental data obtained through testing of the modified Heavy Duty in-line six engine. The modeling approach is a combination of turbulent flame entrainment modeling and multi-zonal diesel spray-combustion modeling. Two combustion models run concurrently to provide a prediction of the heat-release and the pressure in the cylinder, as well as detailed insights into individual aspects of the dual-fuel combustion process. The modeling approach and the analysis of results are focused on the closed cycle, i.e., the crank angle range from IVC to EVO. The diesel spray-combustion model is activated after the Start of Injection. After the ignition delay period, the ignition of diesel triggers both diesel and NG combustion models.

The diesel combustion model is based on the multi-zonal framework which divides the spray into multiple packets. Each packet tracks the air and NG entrainment, fuel evaporation and reactions between both fuels and oxygen. The correlations in

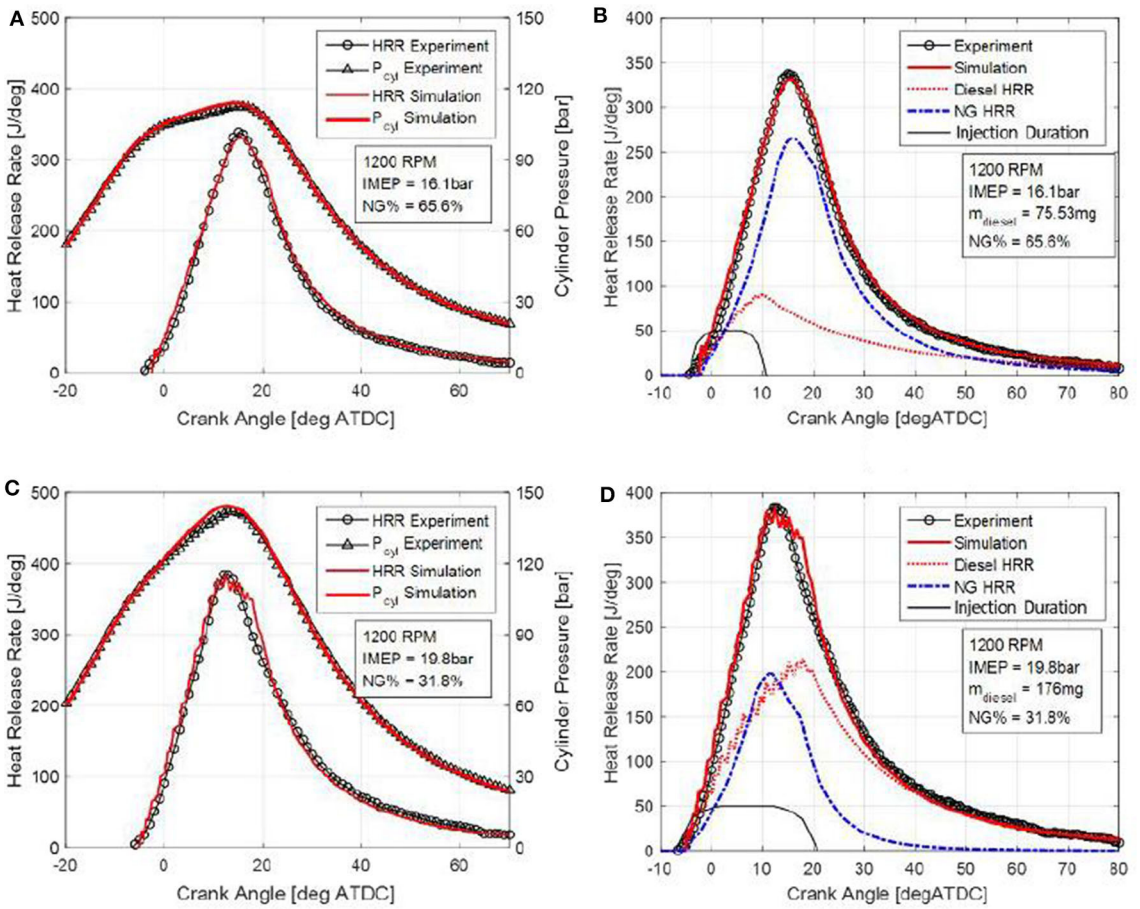

FIGURE 13 | (A–D) Validation results of heat release profile and cylinder pressure at dual-fuel operation conditions.

the model for a spray break-up time is modified to capture the features of modern diesel engines with high injection pressure systems. The NG combustion model relies the turbulent flame propagation modeling approach widely used in SI engines. However, a new method for modeling the flame front area of the burning NG-air charge was needed. The flame is assumed to initiate from the outer boundary of diesel spray and then propagate into the space outward from the spray until eventually starting to interacts with constraints imposed by the combustion chamber walls, the piston top, or the adjacent sprays. The shape of the flame front is represented with a cone and a hemispherical head surface. The proposed flame surface area algorithm solves the flame area in each main iteration of the combustion model and incorporates geometrical information of all constraints. Therefore, it has universal applicability for various piston bowl or cylinder head designs.

Due to limited access to injector diagnostics, a correlation is developed to generate diesel injection rate profile. A linear correlation was found between injected mass and injection duration with diesel only operation. The correlation is subsequently used for dual-fuel operation too.

The dual-fuel combustion model is validated with experimental data for both diesel only and dual-fuel operations. The model displays very good agreement with experimentally obtained heat release and cylinder pressure at various operating conditions. The model also generates valuable information that would otherwise be difficult to obtain experimentally, such as in-cylinder temperature of the unburned charge and burned gas, individual heat release rates from each of the fuels, flame area history, as well as histories of temperatures and composition of each of the packets. The latter enables valuable information for studies of temperature-dependent emissions.

This article includes a very detailed description of a Quasi-D dual-fuel combustion modeling algorithm, as well as equations comprising each of the combustion processes. Geometric modeling and tracking the flame front, correlations for determining injection rate and duration are discussed as well. Therefore, the modeling approach can easily be replicated by other researchers. By varying the number of packets and calculation time step, a balance between computing power requirement and model fidelity can be reached based on the simulation goal. The model can accelerate the calibration of the dual-fuel engine control, or the development process of the combustion system itself, e.g., investigations of the optimal substitution rates, fuel injection timings, knock limits etc.

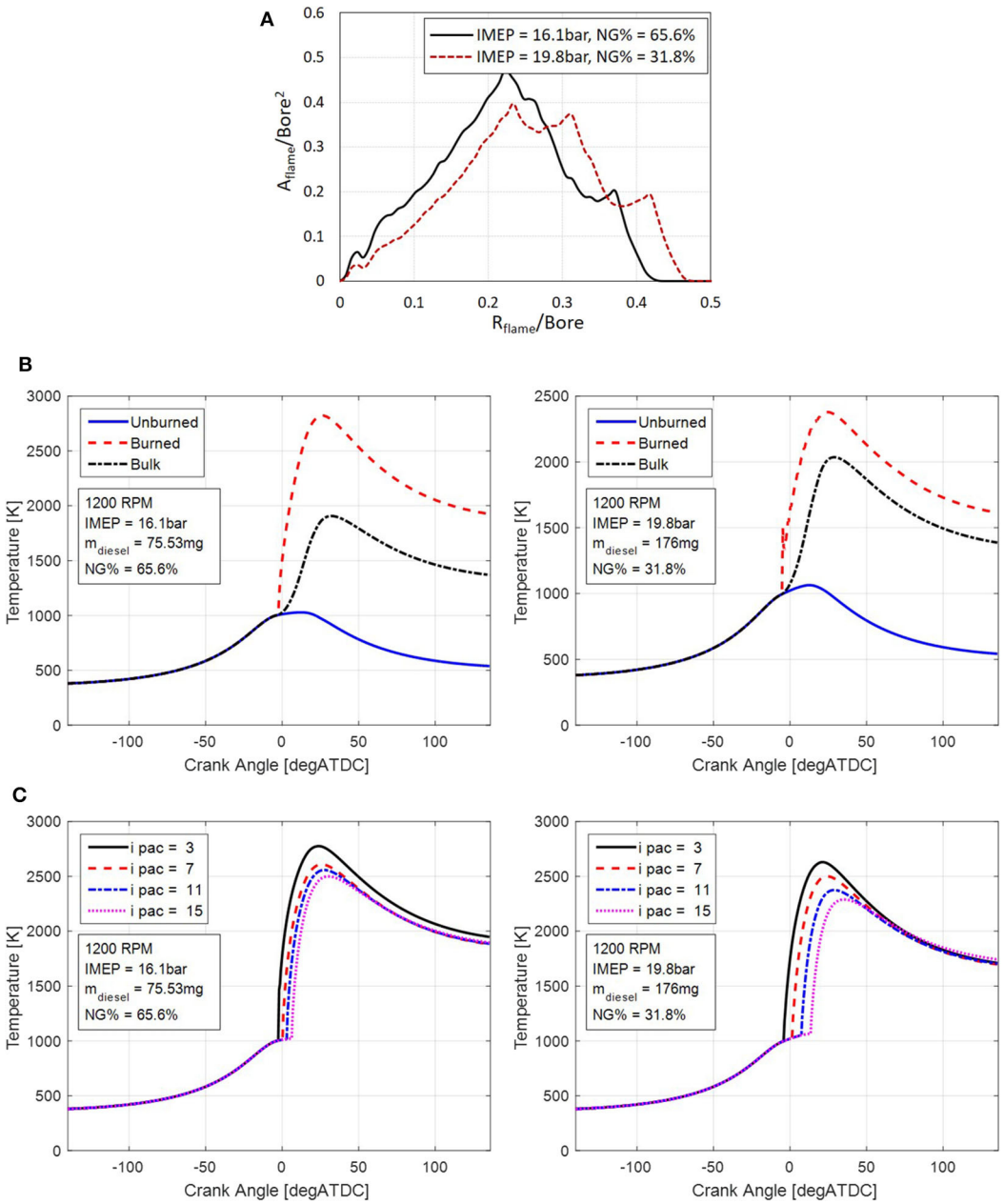

FIGURE 14 | (A) Model prediction results of NG flame front surface area. **(B)** Model prediction results of in-cylinder temperatures of unburned, burned and bulk gas temperatures. **(C)** Model prediction results of in-cylinder temperatures in individual diesel spray packets.

DATA AVAILABILITY STATEMENT

The datasets generated for this study are available on request to the corresponding author.

AUTHOR CONTRIBUTIONS

ZF contributed to the concept. SX contributed to the bulk of the work, including modeling, simulation, and data analysis. All authors contributed to manuscript revision and approved the submitted version.

ACKNOWLEDGMENTS

The authors wish to gratefully acknowledge Prof. Keiya Nishida from Hiroshima University for providing the original version of the multi-zonal code and valuable guidance regarding its refinement published in Xu et al. (2017b).

REFERENCES

Abd Alla, G. H., Soliman, H. A., Badr, O. A., and Abd Rabbo, M. F. (2000). "Using of quasi-two zone combustion model to predict the performance of a dual fuel engine," *SAE Technical Papers*.

Assanis, D. N., and Heywood, J. B. (1986). Development and use of a computer simulation of the turbocompounded diesel system for engine performance and component heat transfer studies. *SAE Trans.* 95, 451–476. doi: 10.4271/860329

Assanis, D. N., Zoran, S. F., Fiveland, S. B., and Michalis, S. (2003). A predictive ignition delay correlation under steady-state and transient operation of a direct injection diesel engine. *J. Eng. Gas Turbines Power* 125, 450–457. doi: 10.1115/1.1563238

Dec, J. E. (1997). *A Conceptual Model of DL Diesel Combustion Based on Laser-Sheet Imaging*. SAE Transactions, 1319–1348.

Gordon, S., and McBride, B. J. (1976). *Computer Program for Calculation of Complex Chemical Equilibrium Compositions, Rocket Performance, Incident and Reflected Shocks, and Chapman-Jouguet Detonations,* Vol. 273. Scientific and Technical Information Office National Aeronautics and Space Administration.

Halstead, M. P., Kirsch, L. J., and Quinn, C. P. (1977). The autoignition of hydrocarbon fuels at high temperatures and pressures—fitting of a mathematical model. *Combust. Flame* 30, 45–60. doi: 10.1016/0010-2180(77)90050-5

Hernandez, J. J., Magin, L., Clara, S., and Andres, M. (2005). Estimation of the laminar flame speed of producer gas from biomass gasification. *Energy Fuels* 19, 2172–2178. doi: 10.1021/ef058002y

Heywood, J. B. (1988). *Internal Combustion Engine Fundamentals, Vol. 930*. New York, NY: Mcgraw-hill.

Hiroyasu, H. (1980). Fuel spray penetration and spray angle in diesel engines. *Trans. JSME* 44, 3208–3220.

Hiroyasu, H. (1985). Diesel engine combustion and its modeling. *Comodia* 85, 53–75.

Hiroyasu, H., and Kadota, T. (1976). Models for combustion and formation of nitric oxide and soot in direct injection diesel engines. *SAE Trans*. 85, 513–526. doi: 10.4271/760129

Hiroyasu, H., Masataka, A., and Michihiko, T. (1989). *Empirical Equations for the Sauter Mean Diameter of a Diesel Spray*. SAE Transactions, 868–877.

Johnson, S. L., Clarke, A., Fletcher, T., and Hylands, D. (2012). "A phenomenological approach to dual fuel combustion modelling," in: *ASME 2012 Internal Combustion Engine Division Fall Technical Conference* (Vancouver, BC: American Society of Mechanical Engineers Digital Collection), 781–791.

Kadota, T., and Hiroyasu, H. (1976). Evaporation of a single droplet at elevated pressures and temperatures: 2nd report, theoretical study. *Bull. JSME* 19, 1515–1521. doi: 10.1299/jsme1958.19.1515

Kadota, T., Hiroyasu, H., and Hideo, O. Y. A. (1976). Spontaneous ignition delay of a fuel droplet in high pressure and high temperature gaseous environments. *Bull. JSME* 19, 437–445. doi: 10.1299/jsme1958.19.437

Karim, G. A. (1987). "The dual fuel engine," in *Automotive Engine Alternatives* (Boston, MA: Springer), 83–104.

Karim, G. A. (2003). Combustion in gas fueled compression: ignition engines of the dual fuel type. *ASME J. Eng. Gas Turbines Power* 125, 827–836. doi: 10.1115/1.1581894

Karim, G. A., and Khan, M. O. (1968). Examination of effective rates of combustion heat release in a dual-fuel engine. *J. Mech. Eng. Sci.* 10, 13–23.

Karim, G. A., Klat, S. R., and Moore, N. P. W. (1966). Knock in dual-fuel engines. *Proc. Inst. Mech. Eng.* 181, 453–466.

Karim, G. A., and Liu, Z. (1992). "A predictive model for knock in dual fuel engines," in *Future Transportation Technology Conference & Exposition*.

Kobori, S., Kamimoto, T., and Aradi, A. A. (2000). A study of ignition delay of diesel fuel sprays. *Int. J. Eng. Res.* 1, 29–39. doi: 10.1243/1468087001545245

Korakianitis, T., Namasivayam, A. M. and Crookes, R. J. (2011). Natural-gas fueled spark-ignition (SI) and compression-ignition (CI) engine performance and emissions. *Prog. Energy Combust. Sci.* 37, 89–112. doi: 10.1016/j.pecs.2010.04.002

Krishnan, S. R., Biruduganti, M., Mo, Y., Bell, S. R., Midkiff, K. C., Gong, W., et al. (2002). Performance and heat release analysis of a pilot-ignited natural gas engine. *Int. J. Eng. Res.* 3, 171–184. doi: 10.1243/14680870260189280

Krishnan, S. R., and Srinivasan, K. K. (2010). Multi-zone modelling of partially premixed low-temperature combustion in pilot-ignited natural-gas engines. *Proc. Inst. Mech. Eng. Part D J. Auto. Eng.* 224, 1597–1622. doi: 10.1243/09544070JAUTO1472

Krishnan, S. R., Srinivasan, K. K., and Midkiff, K. C. (2009). "Ignition in pilot-ignited natural gas low temperature combustion: multi-zone modeling and experimental results," in *ASME 2009 Internal Combustion Engine Division Spring Technical Conference* (Milwaukee, WI: American Society of Mechanical Engineers Digital Collection), 625–634.

Krishnan, S. R., Srinivasan, K. K., Singh, S., Bell, S. R., Midkiff, K. C., Gong, W., et al. (2004). Strategies for reduced Nox emissions in pilot-ignited natural gas engines. *J. Eng. Gas Turbines Power* 126, 665–671. doi: 10.1115/1.1760530

Liu, Z., and Karim, G. A. (1997). Simulation of combustion processes in gas-fuelled diesel engines. *Proc. Inst. Mech. Eng. Part A J. Power Energy* 211, 159–169. doi: 10.1243/0957650971537079

Liu, Z., and Karim, G. A. (1998). An examination of the ignition delay period in gas-fueled diesel engines. *J. Eng. Gas. Turbines Power* 120, 225–231. doi: 10.1115/1.2818080

Papagiannakis, R. G., Hountalas, D. T., and Kotsiopoulos, P. N. (2005). "Experimental and theoretical analysis of the combustion and pollutants formation mechanisms in dual fuel DI diesel engines," *SAE Technical Paper* (Detroit, MI).

Papagiannakis, R. G., Hountalas, D. T., and Rakopoulos, C. D. (2007). Theoretical study of the effects of pilot fuel quantity and its injection timing on the performance and emissions of a dual fuel diesel engine. *Energy Convers. Manage.* 48, 2951–2961. doi: 10.1016/j.enconman.2007.07.003

Poulos, S. G., and Heywood, J. B. (1983). The effect of chamber geometry on spark-ignition engine combustion. *SAE Trans.* 92, 1106–1129.

Sazhina, E. M., Sazhin, S. S., Heikal, M. R., and Marooney, C. J. (1999). The shell autoignition model: applications to gasoline and diesel fuels. *Fuel* 78, 389–401. doi: 10.1016/S0016-2361(98)00167-7

Singh, S., Long, L., Song-Charng, K., and Rolf, R. (2006). Development of a flame propagation model for dual-fuel partially premixed compression ignition engines. *Int. J. Engine Res.* 7, 65–75. doi: 10.1243/14680870 5X7464

Singh, S., Song-Charng, K., Reitz, R. D., Krishnan, S. R., and Midkiff, K. C. (2004). *Modeling and Experiments of Dual-Fuel Engine Combustion and Emissions*. SAE Transactions, 124–133.

Srinivasan, K. K., Krishnan, S. R., and Midkiff, K. C. (2006a). Improving low load combustion stability, and emissions in pilot-ignited natural gas engines. *Proc. Inst. Mech. Eng. Part D J. Auto. Eng.* 220, 229–239. doi: 10.1243/09544070JAUTO104

Srinivasan, K. K., Krishnan, S. R., Sabir, S., Midkiff, K. C., Bell, S. R., Gong, W., et al. (2006b). The advanced injection low pilot ignited natural gas engine: a combustion analysis. *J. Eng Gas Turbines Power* 128, 213–218. doi: 10.1115/1.1915428

Tabaczynski, R. J., Ferguson, C. R., and Radhakrishnan, K. (1977). *A Turbulent Entrainment Model for Spark-Ignition Engine Combustion*. SAE Transactions, 2414–2433.

Walther, H. P., Schlatter, S., Wachtmeister, G., and Boulouchos, K. (2012). Combustion models for lean-burn gas engines with pilot injection. *MTZ Worldwide* 73, 56–63. doi: 10.1365/s38313-012-0144-3

Watson, N., Pilley, A. D., and Marzouk, M. (1980). "A combustion correlation for diesel engine simulation," *SAE Technical Paper*.

Westbrook, C. K., and Dryer, F. L. (1981). Simplified reaction mechanisms for the oxidation of hydrocarbon fuels in flames. *Combust. Sci. Technol.* 27, 31–43. doi: 10.1080/00102208108946970

Wolfer, H. H. (1938). Ignition lag in diesel engines VDI. *Forschungsheft* 392:621-436.047.

Woschni, G. (1967). "A universally applicable equation for the instantaneous heat transfer coefficient in the internal combustion engine," *National Fuels and Lubricants, Powerplants, Transportation Meetings*.

Xu, S., David, A., Amrit, S., Hoffman, M. A., Prucka, R., and Filipi, Z. (2014). Development of a phenomenological dual-fuel natural gas diesel engine simulation and its use for analysis of transient operations. *SAE Int. J. Engines* 7, 1665–1673. doi: 10.4271/2014-01-2546

Xu, S., David, A., Hoffman, M. A., Prucka, R., and Filipi, Z. (2017a). A phenomenological combustion analysis of a dual-fuel natural-gas diesel engine. *Proc. Inst. Mech. Eng. Part D J. Auto. Eng.* 231, 66–83. doi: 10.1177/0954407016633337

Xu, S., Yamakawa, H., Nishida, K., and Filipi, Z. (2017b). Quasi-dimensional diesel engine combustion modeling with improved diesel spray tip penetration, ignition delay and heat release, submodels. *J. Eng. Gas Turbines Power* 139:112802. doi: 10.1115/1.4036575

Zhang, Y., Kong, S.-C., and Reitz, R. (2003). *Modeling and Simulation of a Dual Fuel (diesel/natural gas) Engine With Multidimensional CFD*. SAE Transactions, 336–347.

Conflict of Interest: The authors declare that the research was conducted in the absence of any commercial or financial relationships that could be construed as a potential conflict of interest.

NOMENCLATURE

t_b	break up time
ρ_a	in-cylinder gas density
ρ_0	reference density of air at SATP
ρ_l	density of liquid fuel
d_0	injector hole diameter
ΔP	pressure difference between injection pressure and in-cylinder pressure
S	spray tip penetration
t	time after injection
x_s	non-dimensional parameter representing the distance from centerline of the spray
E_x	weighting factor
t_{bx}	breakup time at periphery region
S_x	penetration depth at periphery region
m_{f0}	in-packet fuel mass
α_b	breakup time coefficient
m_a	air mass entrained
d_0	diameter of nozzle hole
x_{NG}	mass fraction of NG in the premixed NG-air mixture
$\dot{m}_{NG}$	NG entrainment rate into the packet
μ_l	diesel fuel viscosity
μ_a	air viscosity
D_{32}	Sauter mean diameter
We	Weber number
Re	Reynolds number
m_l	mass of liquid fuel droplet
D_l	droplet diameter
D_{l0}	initial diameter of the fuel droplet
m_{fg}	mass of fuel vapor in a packet
N	number of fuel droplets
ρ_{l0}	initial liquid droplet density
τ_{ID}	ignition delay
ϕ	equivalence fuel-air ratio
P	cylinder pressure
T	cylinder temperature
E_a/R_u	constant for ignition delay
ϕ_{total}	total equivalence ratio
m_{fuel}	total fuel mass
m_{O_2}	mass of oxygen
$(m_{fuel}/m_{O_2})_{st}$	stoich fuel-oxygen ratio
ϕ_{pD}	pseudo diesel equivalence ratio
AFR_{stoich}	stoichiometric air fuel ratio obtained from mass of air, diesel vapor and NG
$\dot{m}_{chemD}$	chemical reaction rates of diesel-air mixture
$\dot{m}_{chemNG}$	chemical reaction rates of NG-air mixture
Δm_D	mass of diesel burned in a packet in each calculation step
A_d	adjustable constant for diesel
A_{NG}	adjustable constants for NG
E_a	activation energy
R	universal gas constant
V_{pac}	packet volume
M_D	molecular weights of diesel
M_{NG}	molecular weights of NG
$\dot{Q}_{fuel}$	total heat release rate from the combustion of fuel
LHV_D	lower heating value of diesel
LHV_{NG}	lower heating values of NG
n_{pac}	total number of packets
m_e	mass entrained into the reaction zone
ρ_u	unburned gas density
A_f	surface area of flame front
S_L	laminar flame speed
u'	turbulent intensity
m_b	burned mass
τ	characteristic burning time
λ	Taylor microscale
S_{L0}	constant for a given fuel and equivalence ratio
α_0	constant for a given fuel and equivalence ratio
β_0	constant for a given fuel and equivalence ratio
T_0	reference temperature
p_0	reference pressure
T_u	unburned gas temperature
$\tilde{x}_b$	mole fraction of burned gas diluent
B_m, B_ϕ, ϕ_m	Constants for S_{L0}
L	integral length scale
ν	kinematic viscosity
V	cylinder volume
B	bore size
K	mean kinetic energy
k	kinetic turbulent energy
m	mass in the cylinder
U	mean flow velocity
$\dot{K}$	change rate of mean kinetic energy
$\dot{k}$	change rate of kinetic turbulent energy
$\dot{m}_i$	mass flow rate into the cylinder
$\dot{m}_e$	mass flow rate out of the cylinder
v_i	velocity of flow into the cylinder
P_t	production rate of turbulent kinetic energy
ε	dissipation rate of turbulent kinetic energy
c_β	adjustable constant
L_0	integral length scale at SOC
u'_0	turbulence intensity at SOC
ρ_{u0}	unburned gas density at SOC
θ	spray angle
α	angle between the spray centerline and cylinder head
x_0	height of the spray cone
L_{p0}	The spray tip penetration at SOC
L_p	distance between the injector hole and the furthest location of flame front
r	the radius of the hemisphere flame front
X_p	furthest distance between flame front and the injector hole in the direction perpendicular to the cylinder head
Y_p	furthest distance between flame front and the injector hole in the direction parallel to the cylinder head

r_x	radius of projected free evolving flame front
x	distance between reference plane and Plane C
h_{p2}	distance between piston top and cylinder head
h_{p1}	distance between the piston bowl plane and cylinder head
V_{cyl}	instant volume of the cylinder
R_{cyl}	radius of the cylinder
x_t	furthest location of x
l_x	effective flame length
A	total flame surface area
A_{ini}	igniting diesel spray surface area
d	distance between neighboring ignition sites
N_{ign}	number of ignition sites from a diesel spray
A_0	surface area of each flame front initiated from individual ignition site
$\dot{Q}_{total}$	total heat input
$\dot{Q}_{fuel}$	heat release from combustion
$\dot{Q}_{ht}$	heat transfer loss
$\dot{Q}_c$	convective heat transfer rate
A_{wall}	area of wall available for heat transfer
T_{wall}	wall temperature
h_c	Woschni convective transfer coefficient
w	characteristic velocity
P_r, T_r, V_r	reference cylinder pressure, temperature and volume at IVC
P_m	motored cylinder pressure
$\dot{Q}_w$	heat transfer rate to the control volume
c_p	specific heat capacity
γ	heat capacity ratio
$\dot{m}_{inj}$	diesel injector injection rate
A_s	shaping array
CA_{inj}	injection duration

frontiers in Mechanical Engineering

ORIGINAL RESEARCH
published: 05 August 2020
doi: 10.3389/fmech.2020.00048

Model-Based Control for Dual-Fuel Engines

Hiroaki Ichihashi[1], *Yudai Yamasaki*[1]*, *Yoshitane Takashima*[2] and *Takahiro Sako*[2]

[1] Department of Mechanical Engineering, The University of Tokyo, Tokyo, Japan, [2] Energy Technology Laboratories, OSAKA GAS CO., LTD, Osaka, Japan

The dual-fuel engine (DFE) has been focused on in order to improve its efficient use of natural gas. It has been reported that in DFE the combustion efficiency of the natural gas decreases at a low load. In an attempt to tackle this problem, it has been reported that a multi-stage diesel injection can improve the combustion efficiency of natural gas at a low load. The aim of this research is, therefore, to explain the mechanism for improving combustion efficiency with a multi-stage diesel injection and to develop a control model that predicts engines' combustion efficiency by multi-stage injection. Additionally, a controller was developed using the control model to improve the combustion efficiency by changing the diesel injection conditions. Experimental results show that the controller improves combustion efficiency. Furthermore, taking in to account the heat ratio of natural gas to diesel fuel in addition to combustion efficiency, it has been shown that it is possible to design a controller to leverage the advantage of DFE, which reduces the quantity of fossil fuels.

Keywords: dual-fuel engines, natural gas, control model, model-based control, combustion efficiency

OPEN ACCESS

Edited by:
Masahiro Shioji,
Kyoto University, Japan

Reviewed by:
Khanh Duc Cung,
Southwest Research Institute (SwRI), United States
Ezio Mancaruso,
National Research Council (CNR), Italy

***Correspondence:**
Yudai Yamasaki
yudai_y@fiv.t.u-tokyo.ac.jp

Specialty section:
This article was submitted to Engine and Automotive Engineering, a section of the journal Frontiers in Mechanical Engineering

Received: *13 March 2020*
Accepted: *02 June 2020*
Published: *05 August 2020*

Citation:
Ichihashi H, Yamasaki Y, Takashima Y and Sako T (2020) Model-Based Control for Dual-Fuel Engines. Front. Mech. Eng. 6:48. doi: 10.3389/fmech.2020.00048

INTRODUCTION

Natural gas has a lower environmental effect compared to diesel or gasoline fuel as its CO_2 emission per unit heat value is lower. The development of a dual-fuel engine (DFE), a gas engine, has been a popular topic for the efficient use of natural gas. DFE combusts natural gas through the self-ignition of a small quantity of diesel fuel. It is known that under high load, DFE has higher thermal efficiency compared to the spark ignition gas engine, and the emission of NOx and soot are lower compared to diesel engines. However, DFE is also known to have poor combustion efficiency of natural gas under a low load and to worsen the thermal efficiency and emission of total hydrocarbon (THC) (Papagiannakis and Hountalas, 2004). Hence, in order to utilize the advantage of natural gas in DFE, improving the combustion efficiency under a low load is important to obtain high thermal efficiency and low emission of THC. To improve the combustion in low load, combustion characteristics under various operating conditions have been clarified so far. By introducing a multi-stage diesel injection using the common rail system, high thermal efficiency and low THC emission can be achieved, as the combustion efficiency improves, and by adjusting the injection timing and injection pressure, low NOx emission and stable combustion can be realized (Carlucci et al., 2006, 2015; Min et al., 2016; Yang and Zeng, 2018; Yousefi et al., 2018; Ichihashi et al., 2019). Also, it has been reported that, by using an EGR (Exhaust Gas Recirculation) system and a turbocharger system, thermal efficiency, and emission characteristics improved under low loads (Abdelaal and Hegab, 2012; Kojima et al., 2016; Krishnan et al., 2016). To date, several studies have been undertaken under individual conditions to improve combustion efficiency in low load, but the consideration toward controlling DFE as an engine system is insufficient. Traditionally,

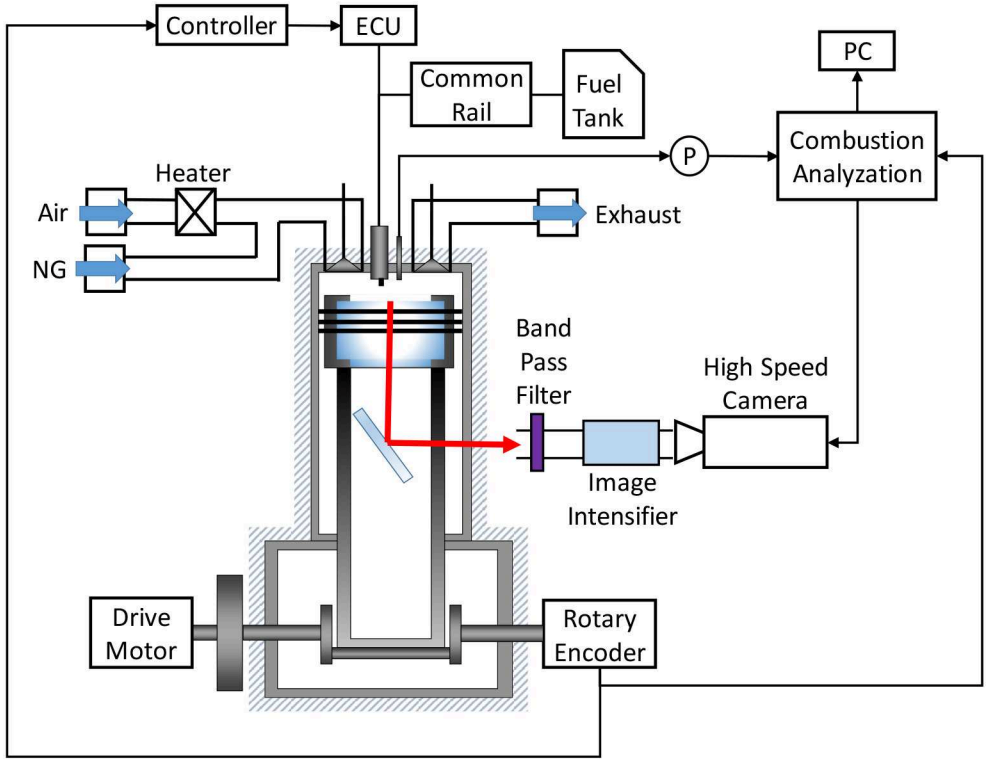

FIGURE 1 | Visualization engine setup.

TABLE 1 | The engine specifications for visualization engine.

Engine type	Single cylinder diesel engine
Bore / Stroke [mm]	70/72
Connecting rod [mm]	110
Compression ratio	16
Displacement [cc]	277
Injection system	Common rail direct injection
Combustion chamber	Toroidal type

map control has been used to control an engine as a system. However, in DFE, a large number of experiments are required to construct the control map, since DFE has more manipulated variables than spark ignition gas engines or diesel engines. To solve this problem, a control method called model-based control appears to be usable, but no existing control model assumed various operation conditions, such as multi-stage diesel injection. Therefore, in this research, a control model was developed to predict the combustion in DFE under a low load, assuming various operation conditions and a control system was implemented using that model. As explained above, the diesel injection strategy has the potential to improve combustion efficiency in low load, so the purpose of the controller implemented in this research is to obtain the diesel injection condition that maximizes the combustion efficiency.

THE TARGET COMBUSTION IN DFE

First, a diesel injection strategy was organized to clarify the target combustion that realizes high thermal efficiency and low emissions under low load in DFEs. Ichihashi et al. (2019) reported that a triple-stage diesel injection, including an early injection, improved the combustion efficiency. The mechanism for improving the combustion efficiency assumes that diesel fuel spreads in the combustion chamber from the early injection, and the number of ignition points of natural gas increases. However, it is not sufficient to confirm the change in the number of ignition points by simply analyzing the in-cylinder pressure.

Therefore, to clarify the mechanism for improving combustion efficiency and to decide the modeling concept for DFE with multiple injections, experiments with an optical access engine (see **Figure 1**) were carried out. The engine specifications of the optical access engine are shown in **Table 1.** OH radical luminescence photographs by changing the diesel injection condition using the optical access engine were taken and analyzed to clarify the ignition area. The knowledge obtained from the analysis of the photograph was mainly reflected to express the combustion of the natural gas.

The self-emission of OH radical was captured by setting a bandpass filter (310 nm) and an image intensifier before a high-speed camera. The exposure time of the high-speed camera was set to 60 μs. The diesel injection condition was set to single ($\theta_{Main} = -10$ deg. ATDC), double (Case1: $\theta_{Pre} = -50$ deg. ATDC, $\theta_{Main} = -10$ deg. ATDC, Case2: $\theta_{Pre} = -90$ deg. ATDC, θ_{Main}

$= -10$ deg. ATDC), and triple ($\theta_{Pilot} = -90$ deg. ATDC, $\theta_{Pre} = -50$ deg. ATDC, $\theta_{Main} = -10$ deg. ATDC) to observe the effect of a multi-stage injection. By implementing a multi-stage diesel injection, including an early injection, the number of combustion starting points increased (**Figure 2**). In a single injection, the combustion started only from the upper end of the combustion chamber. On the other hand, in double injection case 1 and triple injection, the combustion started at 2∼3 points. It shows that, with a multi-stage diesel injection including an early injection, the ignition points of natural gas increased. However, as seen in double injection (case 2), the ignition points of natural gas did not increase in some injection timings. This shows that the diesel injection strategy is important for increasing ignition points and achieving high combustion efficiency.

DFE CONTROL MODEL

Since the diesel injection strategy is important to achieve high combustion efficiency, constructing a controller to derive the injection condition that maximizes the combustion efficiency is important. To implement this controller in DFE, first, a control model for DFE was constructed. This control model is required to predict the combustion efficiency for various operation conditions, especially the injection conditions under low load, and for a multi-stage diesel injection including an early injection. Therefore, the inputs of this model are the operating conditions that can be obtained from the ECU (Engine Control Unit), and the output is the combustion efficiency. Also, to use the model for iterative calculation for optimization, the calculation load needs to be minimal. To minimize the calculation overhead, the model was designed to only predict discrete points in the engine cycle. Such a concept to calculate several discretized points was proposed for HCCI (Homogeneous Charge Compression Ignition) engine by Ravi et al. (2006). The author's group also developed models for advanced diesel combustion based on such a concept (Yasuda et al., 2016; Yamasaki et al., 2019a) and the controllers were designed using the model (Yamasaki et al., 2019b). The developed controller for the advanced diesel engine was validated in engine experiments

TABLE 2 | Discrete points of the DFE combustion control model.

IVO	Intake Valve Open
IVC	Intake Valve Close
Pilot INJ	Pilot Injection
Pre INJ	Pre-Injection
Main INJ	Main Injection
IGN	Ignition
EC	End of Combustion
EVO	Exhaust Valve Open
EVC	Exhaust Valve Close

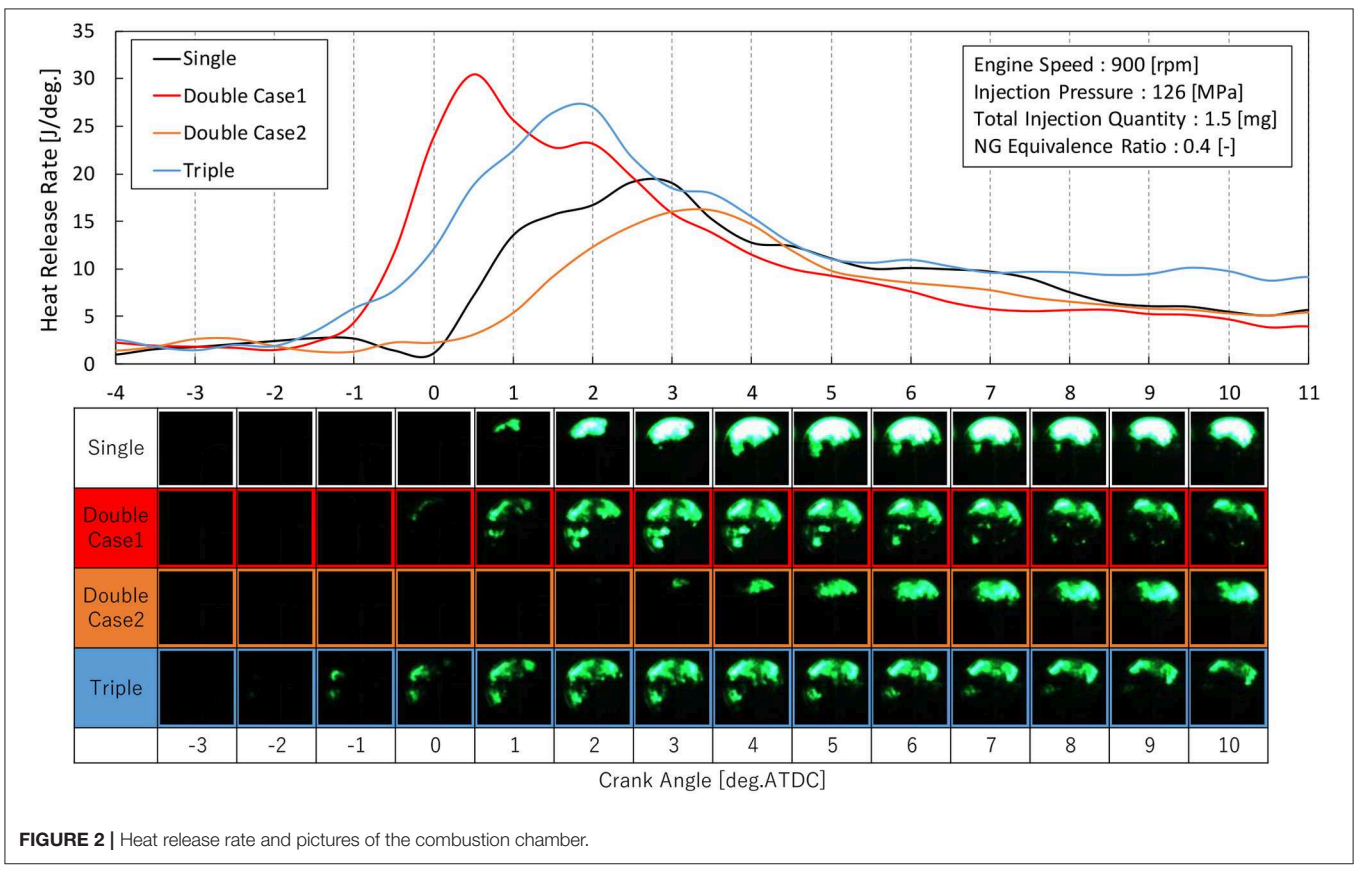

FIGURE 2 | Heat release rate and pictures of the combustion chamber.

(Takahashi et al., 2019). It has been clarified that such control-oriented models calculating discretized points are useful to construct a model-based control system for engines. However, in DFE, two kinds of combustion, the self-ignition of diesel fuel and flame propagation of gas fuel, occur simultaneously, and this has become a complicated phenomenon and it was thought to be difficult to predict the combustion only by discrete points. Therefore, the developed model in this paper employs both the discrete model and the continuous model. The continuous model predicts the combustion only in the combustion process (IGN∼EC). The discrete points (see **Table 2**) and each process, including the combustion process in the cycle, are shown in **Figure 3**. Also, the calculation flow of the DFE control model is shown in **Figure 4**.

The following explains the detail of the model. To consider the effect of residual gas, the calculation was done 10 times from the intake model to the residual gas model.

In the intake model, the pressure and temperature at IVC was predicted as,

$$P_{IVC} = A + B \cdot P_{boost} + C \cdot N_e \tag{1}$$

$$T_{IVC} = A + B \cdot T_{intake} + C \cdot T_{RG} + D \cdot r_{EGR} + E \cdot Q_{prevdiesel} + F \cdot F_{prevNG} + G \cdot N_e \tag{2}$$

Where A ∼ G are coefficients which need to be adapted, P_{boost} is the boost pressure, N_e is the engine speed in rpm, T_{intake} is the temperature of fresh air, T_{RG} is the temperature of residual gas, r_{EGR} is the EGR ratio, and $Q_{prevdiesel}$ and F_{prevNG} are the quantities of fuel input in the previous cycle. In this model, the intake sub-model was developed using multiple regression analysis. The pressure at IVC is thought to be affected by the boost pressure and the engine speed, since the time frame for the intake valves to remain open decreases as the engine speed increases. The temperature at the IVC was explained by the temperature of each gas, which constitutes the in-cylinder gas. Also, the amount of fuel input in the previous cycle was included since the temperature of the cylinder wall changes and the amount of heat transfer from the cylinder wall to the in-cylinder gas changes as well. In addition, the engine speed was included since the time for heat loss will change.

Then the total amount of substance of the in-cylinder gas is calculated using the ideal gas equation.

$$n_{IVC} = \frac{P_{IVC} V_{IVC}}{R T_{IVC}} \tag{3}$$

Using the total amount of substance at IVC, the amount of substance for each composition is calculated.

$$\begin{bmatrix} n_{air} \\ n_{EGR} \end{bmatrix} = \begin{bmatrix} 1 - r_{EGR} \\ r_{EGR} \end{bmatrix} \times (n_{IVC} - n_{RG} - n_{NG}) \tag{4}$$

$$\begin{bmatrix} n_{O_2,IVC} \\ n_{CO_2,IVC} \\ n_{N_2,IVC} \\ n_{H_2O,IVC} \\ n_{NG,IVC} \end{bmatrix} = \begin{bmatrix} 0.21 \\ 0 \\ 0.79 \\ 0 \\ 0 \end{bmatrix} \times n_{air} + \begin{bmatrix} n_{O_2,RG} \\ n_{CO_2,RG} \\ n_{N_2,RG} \\ n_{H_2O,RG} \\ n_{NG,RG} \end{bmatrix} \times \frac{n_{EGR}}{n_{RG}} + \begin{bmatrix} n_{O_2,RG} \\ n_{CO_2,RG} \\ n_{N_2,RG} \\ n_{H_2O,RG} \\ n_{NG,RG} \end{bmatrix} + \begin{bmatrix} 0 \\ 0 \\ 0 \\ 0 \\ 1 \end{bmatrix} \times n_{NG} \tag{5}$$

Where n_{RG} and n_{NG} are the quantity of substance of residual gas and input natural gas. In this research, the composition of the EGR gas was assumed to be the same as the residual gas.

In the compression model (IVC ∼ INJ), the pressure, temperature, and quantity of substance for each composition are

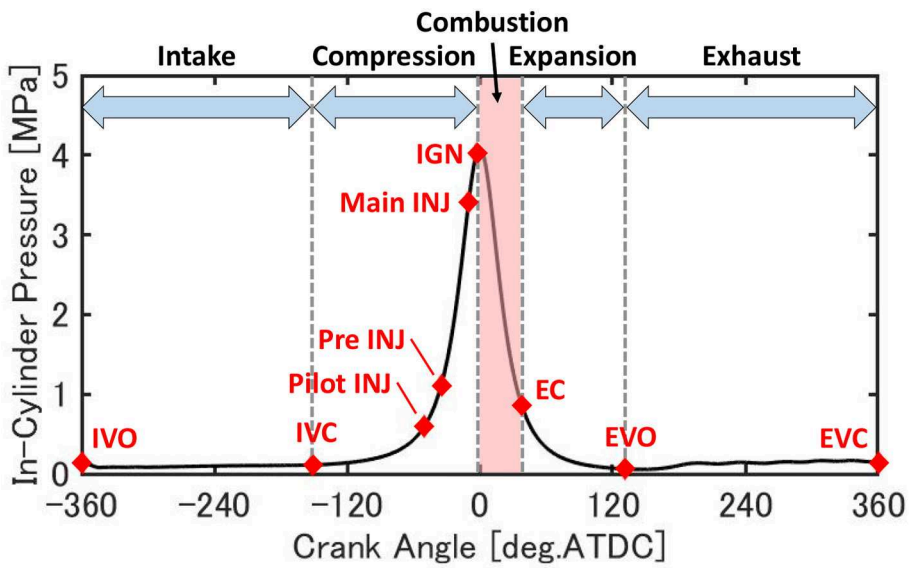

FIGURE 3 | The discrete points and processes in the cycle.

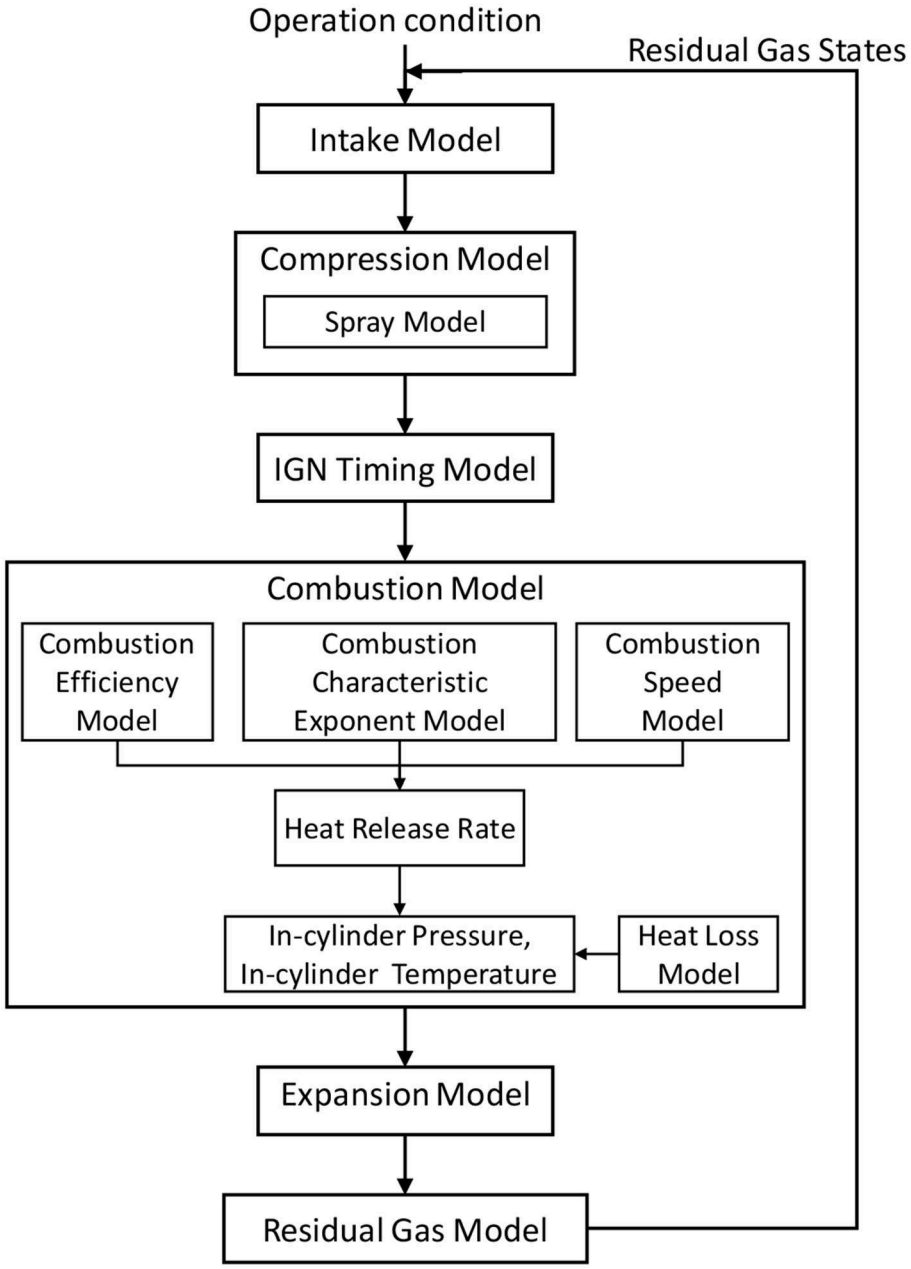

FIGURE 4 | Calculation flow of the DFE combustion control model.

predicted at each injection timing. The pressure and temperature are predicted from polytropic change. The polytropic index is calculated from the temperature of IVC and engine speed, which are considered to affect the heat loss during the compression process. The composition is assumed to be the same as the IVC. A, B, and C are coefficients that need to be adapted.

$$P_{INJ} = P_{IVC}\left(\frac{V_{IVC}}{V_{INJ}}\right)^{\gamma_{comp}} \tag{6}$$

$$T_{INJ} = T_{IVC}\left(\frac{V_{IVC}}{V_{INJ}}\right)^{\gamma_{comp}-1} \tag{7}$$

$$\gamma_{comp} = A + B \cdot \mathrm{T}_{IVC} + C \cdot N_e \tag{8}$$

In the spray model, the volume of the diesel spray was calculated using the Reitz spray shape model (Reitz and Bracco, 1979). L_{Spray} is the penetration and tan (φ) is the spray angle.

$$L_{Spray} = 2.95\left(\frac{P_{rail} - P_{INJ}}{\rho_{diesel}}\right)^{0.25}\sqrt{d_{Hole}t_{spray}} \quad (9)$$

$$tan\,(\varphi) = \left\{3.0 + 0.28\left(\frac{L_{Nozzle}}{d_{Hole}}\right)\right\}^{-1}\sqrt{\frac{\rho_{Gas}}{\rho_{diesel}}}\frac{4\sqrt{3}\pi}{6} \quad (10)$$

In the ignition timing model (INJ ∼ IGN), ignition timing was predicted using the Livengood-Wu ignition model (Livengood and Wu, 1995).

$$\tau = A^{-1}\left[Diesel\right]^{-B}[O_2]^{-C}\,exp\left(-\frac{E}{RT}\right) \quad (11)$$

$$\int_{INJ}^{IGN}\frac{1}{\tau}dt = K \quad (12)$$

Where $\left[Diesel\right]$ and $[O_2]$ are the concentrations of diesel fuel and oxygen and T is the temperature of the in-cylinder gas at the main injection. A, B, C, and E are coefficients that need to be adapted. The pressure and temperature at IGN are predicted from polytropic change, as shown in Equations (6, 7) and the composition is assumed to be the same as each injection timing.

In the combustion model (IGN ∼ EC), Wiebe function (Vibe, 1970) was used to predict the history of heat release rate, in-cylinder pressure, and temperature. Wiebe function predicts the rate of fuel consumption in internal combustion engines in a simple function and it is commonly used to predict the heat release rate of auto-ignition combustion, such as in the diesel engine and HCCI engine (Yasar et al., 2008; Maroteaux et al., 2015). Also, by combining several Wiebe functions, it is possible to express complicated combustion where various combustion forms occur simultaneously (Awad et al., 2013; Aklouche et al., 2018). The heat release rate was predicted as,

$$\frac{dQ_{comb}}{d\theta} = \frac{dX_{b,diesel}}{d\theta}\cdot Q_{diesel} + \frac{dX_{b,NG}}{d\theta}\cdot Q_{NG}\cdot\eta_{NG} \quad (13)$$

where X_b is the rate of the fuel consumed, written by the Wiebe function, and η_{NG} is the combustion efficiency of natural gas, and Q_{diesel} and Q_{NG} are supplied calories of diesel fuel and natural gas. In this research, two forms of combustion, self-ignition of diesel fuel and flame propagation of natural gas, are assumed, hence a double Wiebe function was used.

$$X_{b,i}(\theta) = 1 - exp\left\{-6.9\left(\frac{\theta - \theta_{IGN}}{\Delta\theta_i}\right)^{m_i+1}\right\}\ (i = diesel,\ NG) \quad (14)$$

There are several parameters in the Wiebe function which need to be adapted. m_i and $\Delta\theta_i$ are combustion characteristic exponent and combustion duration, respectively. In addition, η_{NG} needs to be predicted, hence a model was constructed to predict these parameters for various operation conditions. $m_i$and η_{NG} are predicted by statistic equations, as shown below

$$m_{diesel} = a + b\cdot t_e + c\cdot\theta_{PilotINJ} + d\cdot{\theta_{PilotINJ}}^2 + e\cdot\theta_{PreINJ} + f\cdot{\theta_{PreINJ}}^2 + g\cdot\theta_{MainINJ} + h\cdot{\theta_{MainINJ}}^2 \quad (15)$$

$$m_{NG} = a + b\cdot tan\,(\varphi_{Pilot}) + c\cdot L_{Spray,Pilot} + d\cdot\tan\,(\varphi_{Pre}) + e\cdot L_{Spray,Pre} + f\cdot tan\,(\varphi_{Main}) + g\cdot L_{Spray,Main} + h\cdot P_{IGN} + i\cdot T_{IGN} \quad (16)$$

$$\eta_{NG} = a + b\cdot\theta_{IGN} + c\cdot\phi_{NG} + d\cdot P_{IGN} + e\cdot T_{IGN} + f\cdot tan\,(\varphi_{Pilot}) + g\cdot L_{Spray,Pilot} + +h\cdot tan\,(\varphi_{Pre}) + i\cdot L_{Spray,Pre} + j\cdot tan\,(\varphi_{Main}) + k\cdot L_{Spray,Main}$$
$$a = -3.6,\ b = -3.5\times10^{-2},\ c = 2.3,\ d = 4.3\times10^{-8},\ e = 1.2\times10^{-3},\ f = -7.2,\ g = 49,\ h = 1.5,\ i = 220,\ j = -3.9,\ k = 76.9 \quad (17)$$

Where t_e is the ignition delay time and ϕ_{NG} is the equivalence ratio of natural gas. For the combustion characteristic exponent for diesel self-ignition, the ignition delay time and the ignition timing were assumed to affect the combustion characteristic exponent for diesel self-ignition; as the diesel fuel become more premixed, steep combustion occurs. Then, for the combustion efficiency, the ignition timing was included since it showed a strong correlation with the combustion efficiency. In addition, the equivalence ratio of natural gas, pressure, and temperature were included since they affect the combustion speed of natural gas, and shape parameters of the diesel spray were included to express the change of ignition points confirmed from the

TABLE 3 | Details of the neural network for prediction of parameters in the Wiebe function.

Input layer	Inputs: $\begin{bmatrix} N_e \\ tan\,(\varphi_{Spray}) \\ L_{Spray} \\ \theta_{IGN} \\ P_{IGN} \\ T_{IGN} \\ n_{O_2,IGN} \\ n_{NG,IGN} \end{bmatrix}$
Hidden layer	Number of nodes: 21 Activation function: Sigmoid function
Output layer	Outputs: $\begin{bmatrix} r_{diesel} \\ r_{NG} \end{bmatrix}$ Activation function: Sigmoid function
Training method	Backpropagation (Gradient descent)
Loss function	$L = \|t - y\|$

optical experiment in section The Target Combustion in DFE. Also, $\Delta\theta_i$ was predicted by a neural network (NN) model since the combustion process is a non-linear phenomenon and complex. The NN model developed in this research is a 3-layer fully connected NN and backpropagation (BP) by gradient descent is used as the training method, as shown in **Table 3**. Using the heat release rate predicted by Wiebe function, the in-cylinder pressure, temperature, and composition are calculated as,

$$P(\theta) = \frac{(\kappa(\theta) - 1)\left(\frac{dQ_{comb}}{d\theta}(\theta) - \frac{dQ_{loss}}{d\theta}(\theta)\right) + V(\theta) P(\theta - 1)}{V(\theta) + \kappa(\theta)\frac{dV}{d\theta}(\theta)} \tag{18}$$

$$T(\theta) = \frac{P(\theta) V(\theta)}{n(\theta) R} \tag{19}$$

$$\begin{bmatrix} n_{O_2}(\theta) \\ n_{CO_2}(\theta) \\ n_{N_2}(\theta) \\ n_{H_2O}(\theta) \\ n_{NG}(\theta) \end{bmatrix} = \begin{bmatrix} n_{O_2,IGN} \\ n_{CO_2,IGN} \\ n_{N_2,IGN} \\ n_{H_2O,IGN} \\ n_{NG,IGN} \end{bmatrix} + \begin{bmatrix} -15.5 \\ 10.8 \\ 0 \\ 9.35 \\ 0 \end{bmatrix} \times \frac{dX_{b,diesel}}{d\theta} \cdot n_{diesel} + \begin{bmatrix} -2.25 \\ 1.17 \\ 0 \\ 2.17 \\ -1 \end{bmatrix} \times \frac{dX_{b,NG}}{d\theta} \cdot n_{NG} \cdot \eta_{NG} \tag{20}$$

Where κ is heat capacity ratio and $\frac{dQ_{loss}}{d\theta}$ is the heat loss calculated by the model of Woschni (Merker et al., 2005). Prediction of the in-cylinder pressure, temperature, and composition by Equations (18–20) are calculated based on IGN pressure, temperature, and composition that continues until the end of the combustion predicted from the combustion duration.

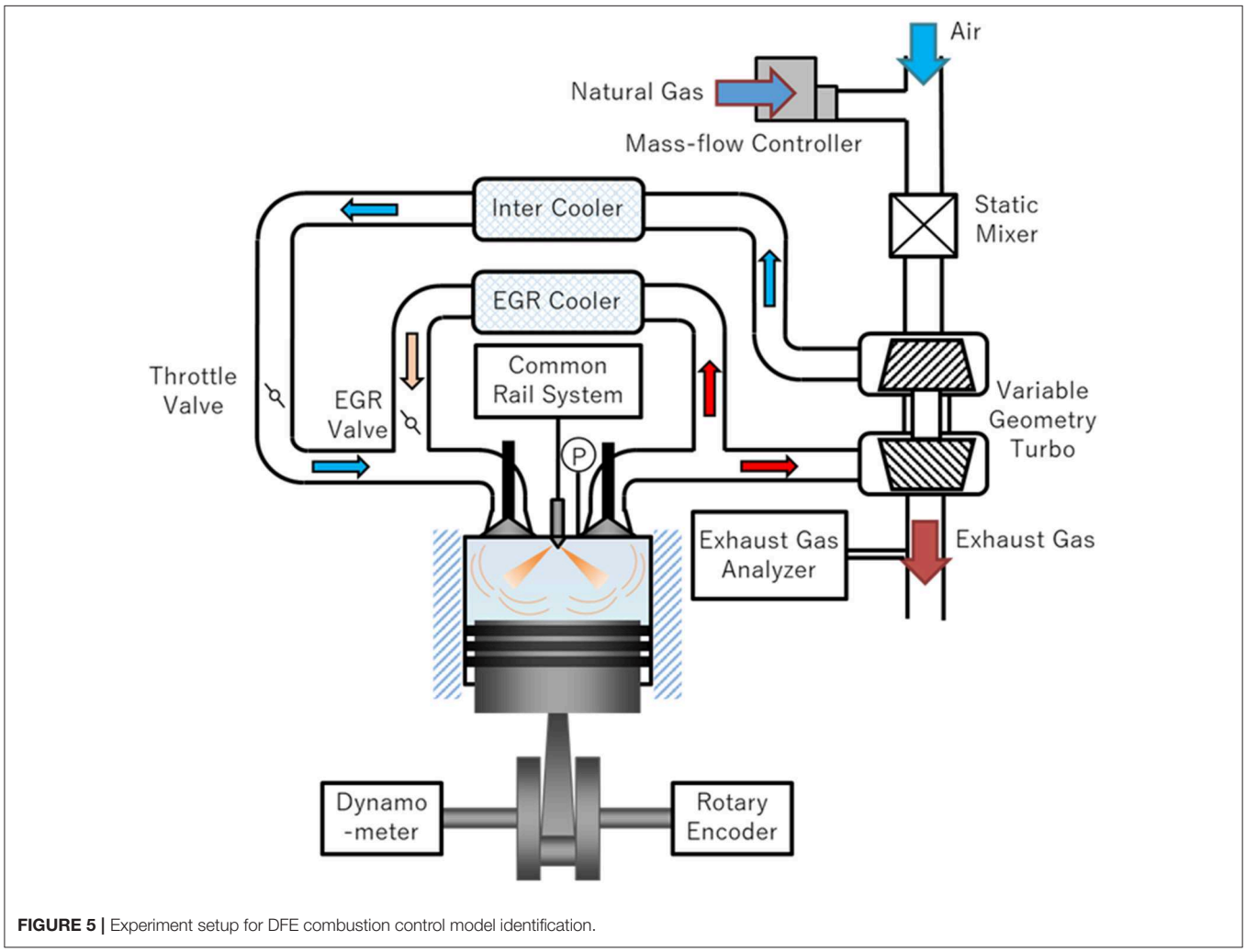

FIGURE 5 | Experiment setup for DFE combustion control model identification.

In the expansion model (EC ∼ EVO), the pressure and temperature are predicted by polytropic change, just as in the compression model. The polytropic index in the expansion process is calculated as,

$$\gamma_{exp} = A + B \cdot T_{EC} + C \cdot N_e \tag{21}$$

Finally, in the residual gas model (EVO ∼ EVC), the temperature and composition at EVC are predicted. The pressure at EVC is assumed to be the same as the boost pressure and the temperature is predicted by polytopic change using the polytropic index in the expansion model.

$$T_{EVC} = T_{EVO}\left(\frac{P_{boost}}{P_{EVC}}\right)^{\frac{1-\gamma_{exp}}{\gamma_{exp}}} \tag{22}$$

The total quantity of substance at EVC is calculated using the ideal gas equation and the quantity of substance for each composition is calculated by assuming the same ratio at EVO. The temperature and composition are assumed to be the same as the temperature and composition of the residual gas.

TABLE 4 | The engine specifications for the DFE combustion control model.

Engine type	Inline 4 cylinder diesel engine
Bore × Stroke [mm]	92 × 103.6
Connecting rod [mm]	155
Compression ratio [-]	15.6
Displacement [cm^3]	2754
Injection system	Common rail direct injection
Turbo charger	Variable geometry
EGR system	High pressure EGR

TABLE 5 | Experiment condition for the DFE combustion control model identification.

Engine speed [rpm]		1000 / 1500 / 2000
Injection pressure [MPa]		85 / 95 / 105
Boost pressure [kPa]		95 / 100 / 105
EGR rate [-]		0 / 0.2 / 0.3 / 0.4
Natural gas Equivalence ratio [-]		0.3 / 0.4 / 0.5
Total injection quantity [mm^3/cycle]		2.6 ∼ 5.1
Injection timing [deg.ATDC]	Single	Main:−5 /−10 /−15
	Double	Pre:−15 /−20 /−25 /−30 /−40 Main:−5 /−10 /−15
	Triple	Pilot:−45 /−50 /−55 Pre:−25,−30 /−35 Main:−5 /−10 /−15

EXPERIMENTS

The DFE control model includes some coefficients that need to be adapted and the NN model also needs to be trained. To identify the DFE control model, experiments were carried out using a common inline 4-cylinder diesel engine (**Figure 5**). The engine specifications are shown in **Table 4.** This engine is equipped with the common rail injection system, high-pressure EGR, and variable geometry turbocharger. It is possible to operate this engine as a DFE, by providing an inlet for natural gas at the upstream of the intake pipe and controlling the natural gas flow rate with a mass flow controller. The in-cylinder pressure was measured by a pressure sensor and the average value of 200 cycles was used. Also, the exhaust gas composition was measured and the measurement time length was 10 s for each condition. Further, to change the operation condition, an ECU by-pass tool was used. The experimental conditions are shown in **Table 5**. These conditions realize multi-stage diesel injection, including early injection, in low load. The number of experiments would be enormous if the experiment had been conducted on all combinations, hence the experiment was conducted under 135 conditions using the design of experiments. Out of the 135 conditions, 120 conditions were used for model adaptation and the remaining 15 conditions were used for verification. By adapting the DFE control model using the experimental data, the DFE control model was able to predict combustion efficiency with good accuracy, **Figure 6**. Among the range where the experiment was done, **Table 5**, using this model it is possible to predict the combustion efficiency due to the changes in various operating conditions such as the diesel injection conditions, intake conditions, or engine speed. However, it might be difficult to predict accurately out of this range. This is because the model

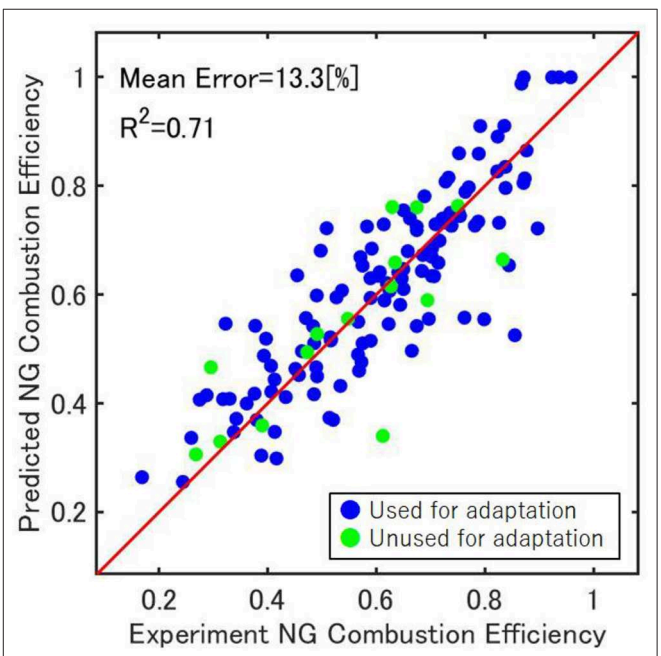

FIGURE 6 | Prediction accuracy of the combustion efficiency.

includes several statistical models, such as multiple regression analysis and neural network model.

DFE CONTROL SYSTEM

The purpose of the controller to be constructed in this research is to predict the proper diesel injection condition to maximize combustion efficiency. Since the DFE control model is a non-linear model, a non-linear optimal control using the gradient method was introduced. The diagram of the constructed controller in this research is shown in **Figure 7.** The inputs of this controller are u_{ini} (initial injection timing, quantity, and pressure) and x (engine speed, EGR rate, boost pressure, and equivalence ratio of natural gas). Also, the purpose of this controller is to maximize combustion efficiency, therefore the objective function was set, as shown in Equation (23). First, to obtain the gradient of the objective function against the injection conditions, a deviation u was given to the initial injection conditions u_{ini}, and the combustion efficiency was calculated for each case by the DFE control model. The gradient against the injection conditions is calculated using these calculated results, and the injection conditions are updated according to this gradient and renewal rate λ. The injection conditions were updated until the gradient was smaller than a constant α, and output the injection condition at the same time as the optimized injection condition. However, the injection conditions were updated in the range of the experiment done (see **Table 5**). Also, λ and α were set as a constant in this research.

$$L = {\eta_{NG}}^2 \tag{23}$$

To evaluate this controller, the combustion efficiency was compared by experiments in 36 conditions against random combinations of operating conditions, after which the conditions of injection were changed to that which the controller outputted. When changing the injection condition, the engine speed and intake conditions were set to be the same. By changing the injection conditions to which the controller outputted, the combustion efficiency improved in all 36 conditions (see, **Figure 8A)**.

Also, the change of the emission of CO and THC are shown in **Figures 8B,C.** Each plot represents the average value during the measurement at each condition and the error bar represents the maximum and minimum value. From **Figure 8B**, the emission of THC has decreased in most experiment numbers by the DFE controller. Also, from **Figure 8C**, the emission of CO decreased, especially when there was a lot. This controller changes the diesel injection conditions to maximize the combustion efficiency and this directly improves the emission of THC and CO. However, in some experiment numbers, the emission of THC slightly increased. In these numbers, the emission of CO decreased and the combustion efficiency improved overall. The reason why the emission of THC did not improve in these numbers is believed to be because the diesel injection conditions at the random combinations were already close to the conditions which maximize the combustion efficiency and the combustion efficiency was restricted by the intake conditions. As mentioned earlier, the controller changes only the diesel injection conditions, and the intake conditions, such as the EGR rate or the boost pressure, were set the same. As a further study, to design a controller that also considers the intake conditions is needed.

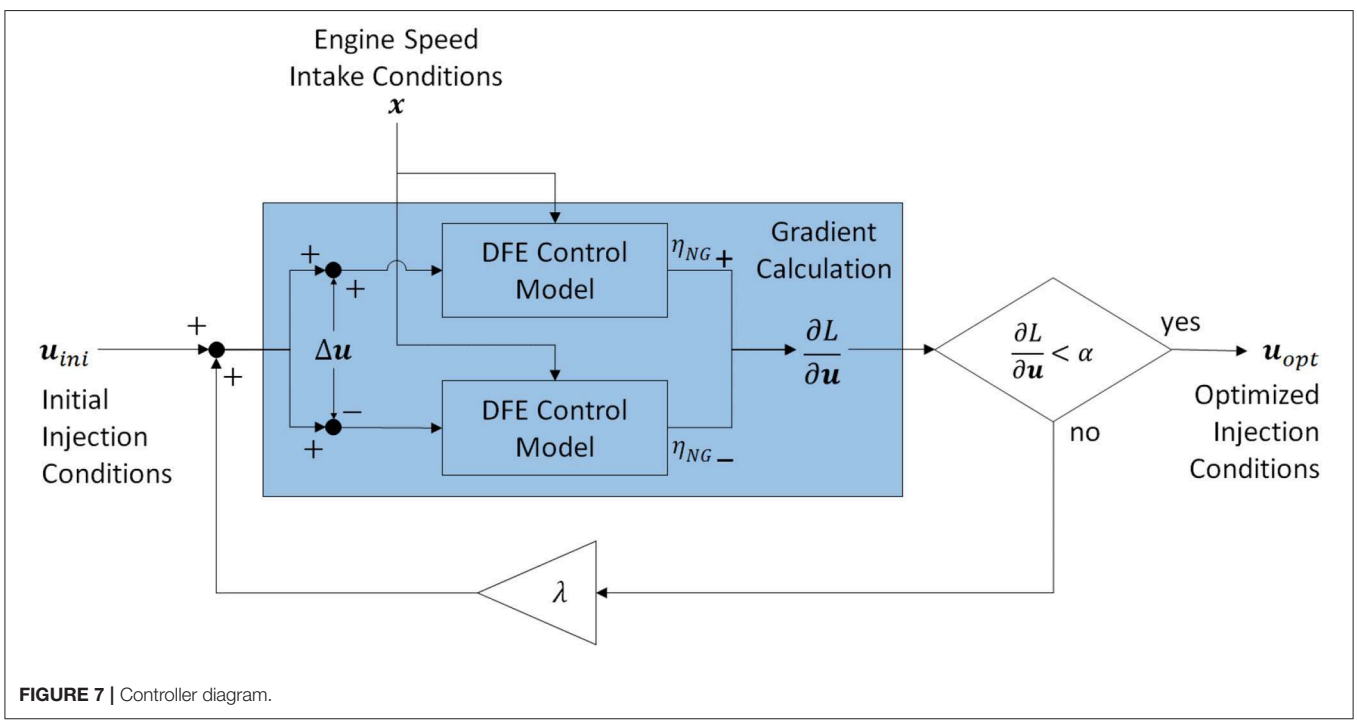

FIGURE 7 | Controller diagram.

Furthermore, the emission of NOx was also measured and the NOx emission increased to a high level in some experiment numbers, **Figure 8D**. Just as with THC and CO, each plot represents the average value during the measurement at each condition and the error bar represents the maximum and minimum value. This research focused on maximizing the combustion efficiency and does not consider NOx emission for fuel injection conditions, but consideration of NOx emission is required even in DFE under a low load. Therefore, as a further study, in order to control for the NOx emission as high combustion efficiency, a prediction model of NOx emission from DFE is needed and optimization is required

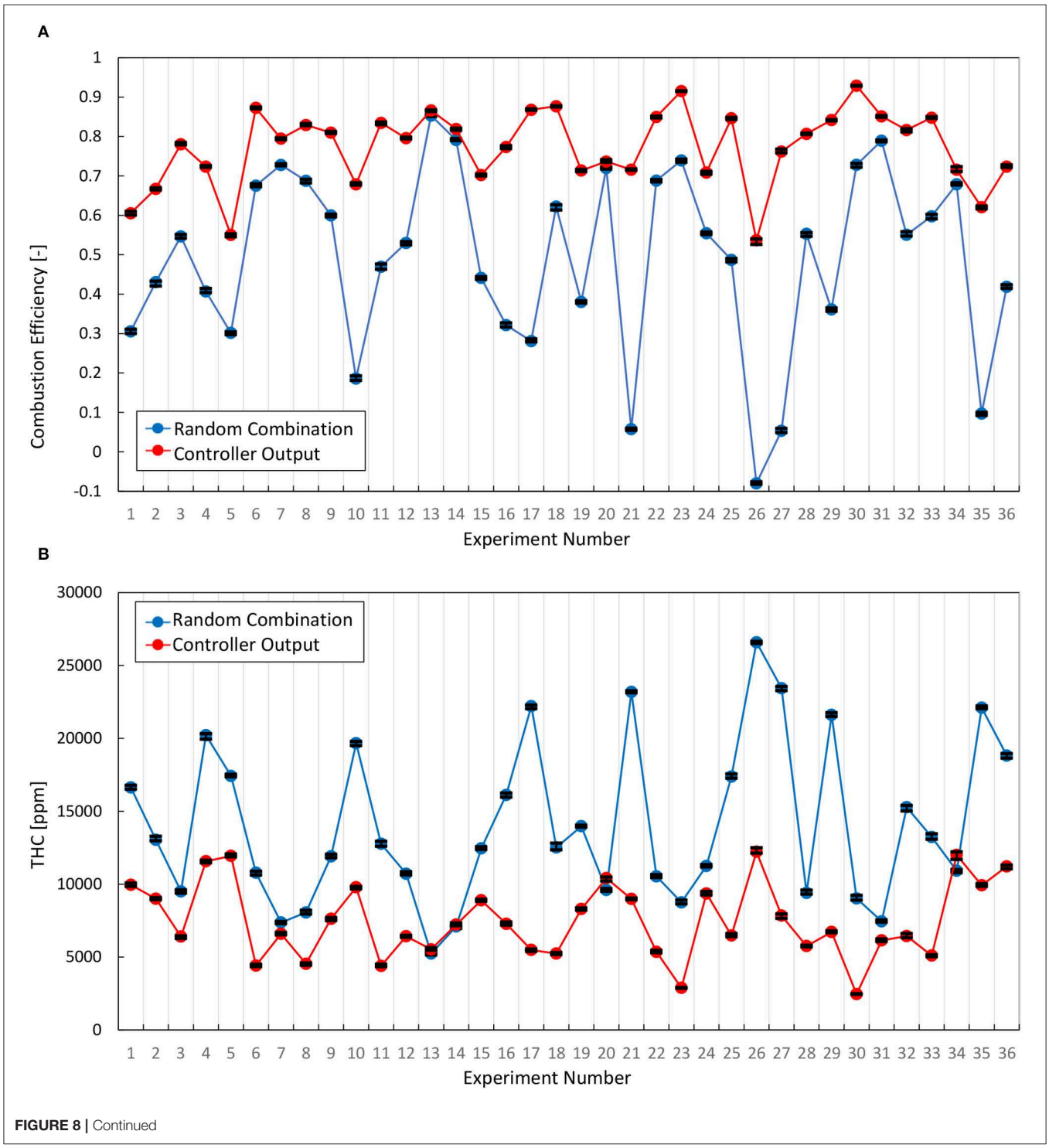

FIGURE 8 | Continued

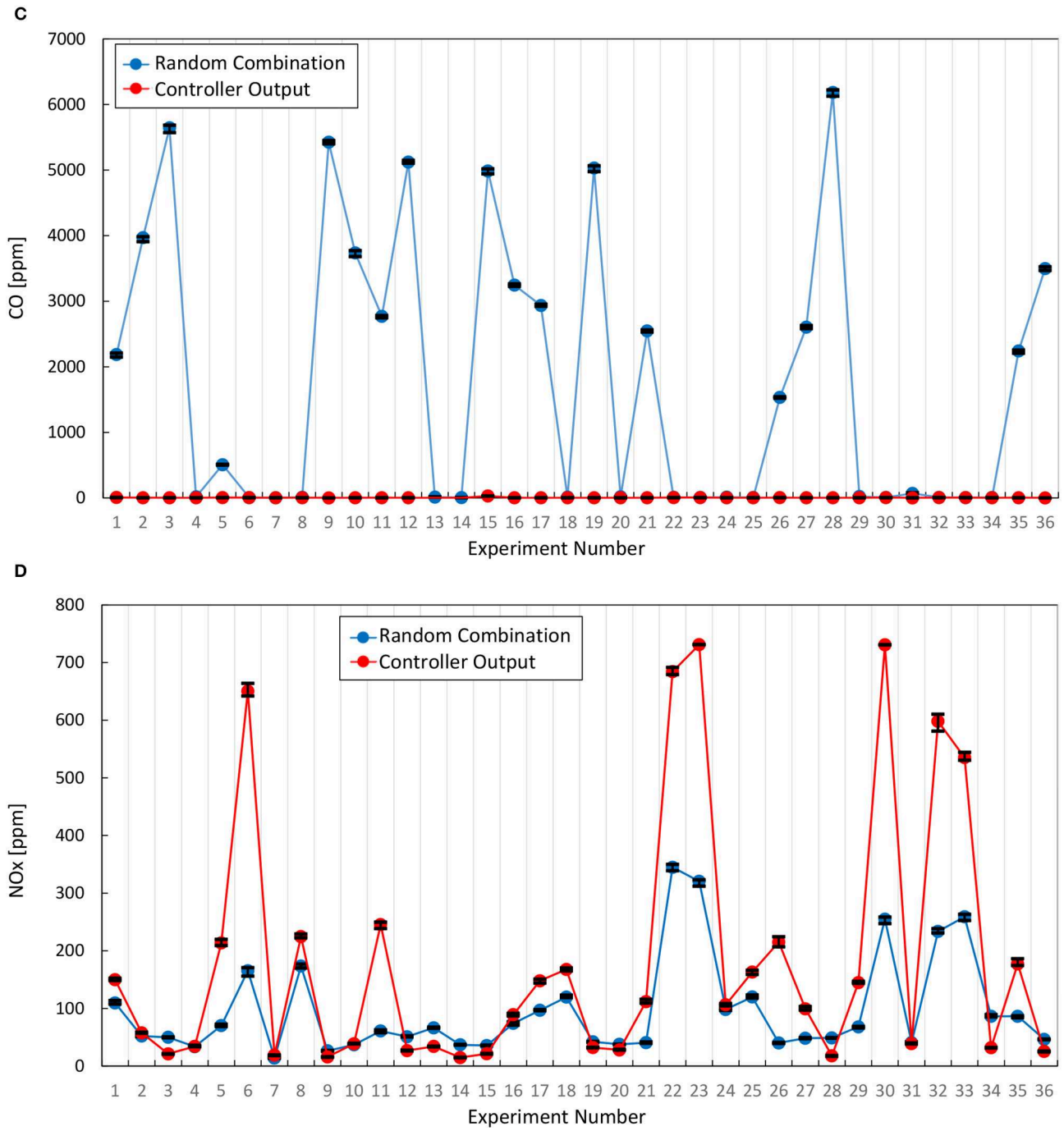

FIGURE 8 | Comparison of combustion efficiency and emissions. **(A)** Combustion efficiency, **(B)** THC, **(C)** CO, **(D)** NOx.

by coupling with the NOx emission model and the present combustion model.

Also, to confirm that the controller predicted the change of the combustion efficiency against the injection conditions, the experiment was conducted around the injection conditions outputted by the controller (see **Figure 9**). Also, the combustion efficiency predicted by the model is the parameter used to predict the heat release rate (Equation, 17), while combustion efficiency measured in the experiment is calculated from the unburned fuel concentration in the exhaust gas. Therefore, these two compared in **Figure 9** do not match in absolute value, hence the issue now is whether the change trends are consistent. Regarding the injection pressure, quantity, and the main injection timing, the model predicted the trend of combustion efficiency in the real

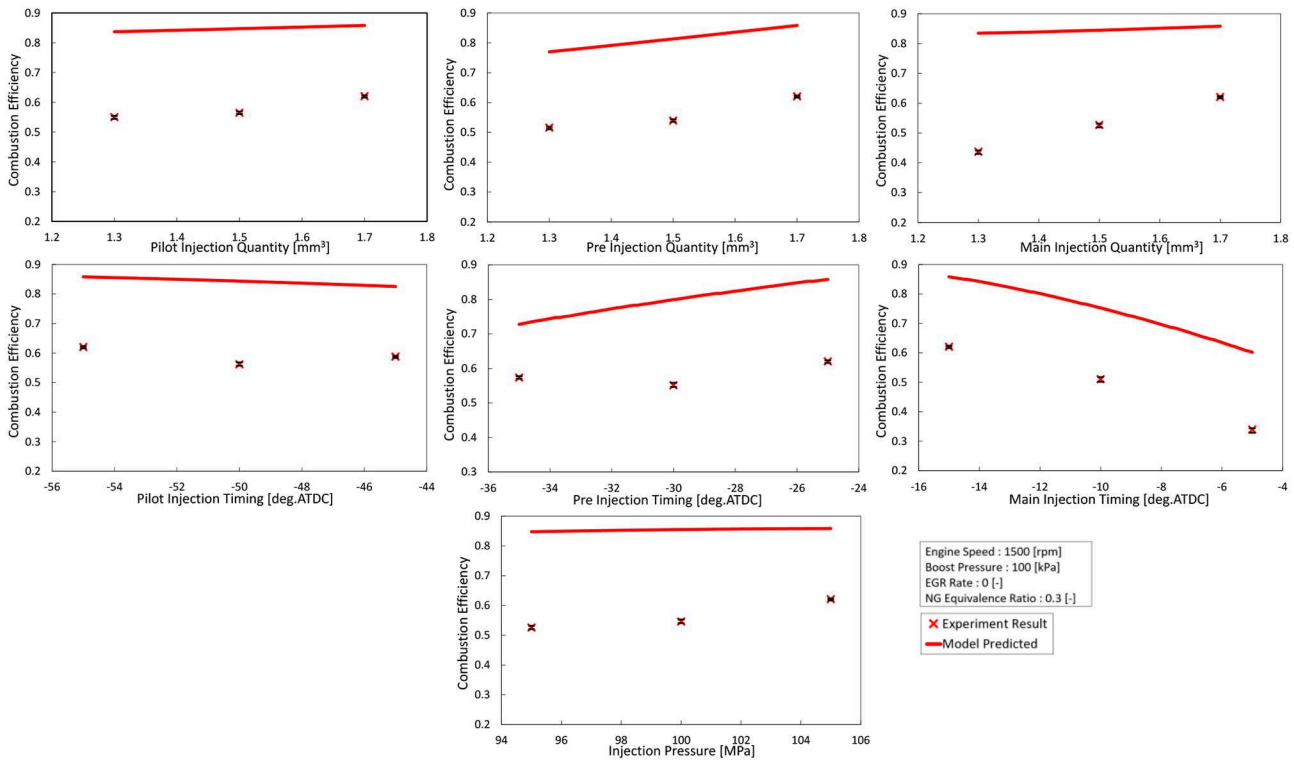

FIGURE 9 | When the injection conditions were changed around the output of the controller.

engine. On the other hand, regarding the pilot and pre-injection timing, the model was able to predict the maximum point among the range of the experiment done. However, the model could not predict the slight downward convex which the real engine showed. The constructed model in this research includes non-linear models such as the ignition timing model or the diesel spray model, but since the formula for ultimate prediction of the combustion efficiency (Equation 17) is a linear format, the model could not predict the non-linearity.

The combustion efficiency increases monotonically with the injection quantity (**Figure 9**). Therefore, when the controller considers only the combustion efficiency (Equation 23), the injection quantity of diesel fuel increases. If the injection quantity increases, the combustion efficiency improves, but increasing the heat ratio of diesel fuel to natural gas is not desirable from the viewpoint of the effective use of natural gas, as it has a smaller environmental impact. Therefore, the objective function of Equation (23) was reconsidered to consider the combustion efficiency and the heat ratio of natural gas. The objective function was changed to,

$$L = {\eta_{NG}}^2 \times \left(\frac{Q_{NG}}{Q_{diesel} + Q_{NG}} \right)^2 \tag{24}$$

where Q_{NG} is the input heat of natural gas and Q_{diesel} is the input heat of diesel fuel. When considering only the combustion efficiency (Equation 23), the combustion efficiency did improve against the random conditions, but the heat ratio of natural gas did not show a difference. However, by considering the heat ratio of natural gas (Equation 24), the points where the heat ratio of natural gas was low shifted toward the higher heat ratio of

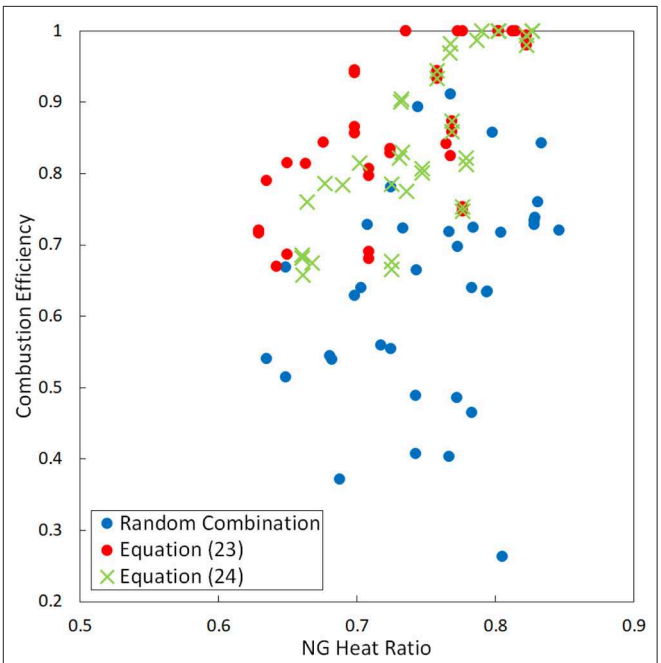

FIGURE 10 | Relation between combustion efficiency and the heat ratio of natural gas.

natural gas without the combustion efficiency becoming worse (**Figure 10**).

CONCLUSION

In this research, a model-based control system was constructed for DFE using natural gas and diesel fuel, to maximize the combustion efficiency at low load by adjusting the diesel injection conditions. First, by the visualization experiment, it has been explained that the combustion efficiency improves when using a multi-stage diesel injection including early injection, since the ignition points increase. Also, a control model that predicts the combustion efficiency of the natural gas was constructed, assuming a multi-stage diesel injection at low load. Then, by using this control model, it was able to construct a controller that outputs the diesel injection condition to maximize the combustion efficiency of natural gas.

This research mainly focused on improving the low combustion efficiency under low loads in order to save fuel and reduce CO_2. The issue of the low combustion efficiency must be solved first, hence this paper focused on the combustion efficiency. By improving combustion efficiency, the emission of HC and CO also improved since these substances are mostly caused by unburned natural gas. However, further study is required to correctly evaluate the benefit on the fuel and CO_2 saving with the consideration of NOx emission, as NOx emission will give several constraints to injection conditions. In order to control NOx emission with high combustion efficiency, an NOx emission model is required, and the controller should be designed using the combined model of the combustion model and the NOx emission model.

DATA AVAILABILITY STATEMENT

The datasets generated for this study are available on request to the corresponding author.

AUTHOR CONTRIBUTIONS

YY managed whole of this study. HI carried out experiments, modeling, and analyzed data. YT and TS developed experimental apparatus and carried out experiments. All authors contributed to the article and approved the submitted version.

REFERENCES

Abdelaal, M. M., and Hegab, A. H. (2012). Combustion and emission characteristics of a natural gas-fueled diesel engine with EGR. *Energy Convers. Manage.* 64, 301–312. doi: 10.1016/j.enconman.2012.05.021

Aklouche, F. Z., Loubar, K., Bentebbiche, A., Awad, S., and Tazerout, M. (2018). Predictive model of the diesel engine operating in dual-fuel mode fueled with different gaseous fuels. *Fuel* 220, 599–606. doi: 10.1016/j.fuel.2018.02.053

Awad, S., Varuvel, E. G., Loubar, K., and Tazerout, M. (2013). Single zone combustion modeling of biodiesel from wastes in diesel engine. *Fuel* 106, 558–568. doi: 10.1016/j.fuel.2012.11.051

Carlucci, A. P., Colangelo, G., Ficarella, A., Laforgia, D., and Strafella, L. (2015). Improvements in dual-fuel biodiesel-producer gas combustion at low loads through pilot injection splitting. *J. Energy Eng.* 141, 1–8. doi: 10.1061/(ASCE)EY.1943-7897.0000231

Carlucci, A. P., Ficarella, A., and Laforgia, D. (2006). Control of the combustion behavior in a diesel engine using early injection and gas addition. *Appl. Therm. Eng.* 26, 2279–2286. doi: 10.1016/j.applthermaleng.2006.03.016

Ichihashi, H., Yamasaki, Y., and Kaneko, S. (2019). Combustion and emission characteristics of multiple fuel injections on a dual fuel engine (in Japanese). *Trans. JSME* 85:874. doi: 10.1299/transjsme.18-00363

Kojima, H., Yoshida, A., Tsujimura, T., Fujino, T., Kawakita, S., Kondo, W., et al. (2016). A strategy of intake gas control for diesel dual fuel engine with natural gas and diesel fuel (in Japanese). *Trans. Soc. Autom. Eng. Jpn.* 47, 889–894. doi: 10.11351/jsaeronbun.47.889

Krishnan, S. R., Srinivasan, K. K., and Raihan, M. S. (2016). The effect of injection parameters and boost pressure on diesel-propane dual fuel low temperature combustion in a single-cylinder research engine. *Fuel* 184, 490–502. doi: 10.1016/j.fuel.2016.07.042

Livengood, J. C., and Wu, P. C. (1995). Correlation of autoignition phenomena in internal combustion engines and rapid compression machines. *Int. Sympos. Combust.*5, 347–356.

Maroteaux, F., Saad, C., and Aubertin, F. (2015). Development and validation of double and single Wiebe function for multi-injection mode Diesel engine combustion modeling for hard-ware-in-the-loop applications. *Energy Convers. Manage.* 105, 630–641. doi: 10.1016/j.enconman.2015.08.024

Merker, G. P., Schwarz, C., Stiesch, G., and Otto, F. (2005). *Simulating Combustion: Simulation of Combustion and Pollutant Formation for Engine-Development*. Springer Science & Business Media.

Min, X., Wei, C., Zhi, L., Hongfei, Z., Tao, A., and Zhaokang, M. (2016). Pre-injection strategy for pilot diesel compression ignition natural gas engine. *Appl. Energy* 179, 1185–1193. doi: 10.1016/j.apenergy.2016.07.024

Papagiannakis, R. G., and Hountalas, D. T. (2004). Combustion and exhaust emission characteristics of a dual fuel compression ignition engine operated with pilot Diesel fuel and natural gas. *Energy Convers. Manage.* 45, 2971–2987. doi: 10.1016/j.enconman.2004.01.013

Ravi, N., Jungkunz, A. F., Roelle, M. J., and Gerdes, J. C. (2006). A physically based two-state model for controlling exhaust recompression hcci in gasoline engines. *ASME IMECE* 2006-15331, 483–492. doi: 10.1115/IMECE2006-15331

Reitz, R. D., and Bracco, F. B. (1979). "On the dependence of spray angle and other spray parameters on nozzle design and operating conditions," in *SAE Technical Paper* (Detroit, MI). doi: 10.4271/790494

Takahashi, M., Yamasaki, Y., Kaneko, S., Fujii, S., Mizumoto, I., Hayashi, T., et al. (2019). "Model-based control system for a diesel engine," in *IFAC 9th AAC* (Orléans), 23–27.

Vibe, I. I. (1970). *Brennverlauf und Kreisprocess von Verbennungsmotoren*. Berlin: VEB Verlag Technik.

Yamasaki, Y., Ikemura, R., Shimizu, F., and Kaneko, S. (2019a). Simple combustion model for a diesel engine with multiple fuel injections. *Int. J. Eng. Res.* 20, 167–180. doi: 10.1177/1468087417742764

Yamasaki, Y., Ikemura, R., Takahashi, M., Kaneko, S., and Uemichi, A. (2019b). Multiple-input multiple-output control of diesel combustion using a control-oriented model. *Int. J. Eng. Res.* 20, 1005–1016. doi: 10.1177/1468087418820739

Yang, B., and Zeng, K. (2018). Effects of natural gas injection timing and split pilot fuel injection strategy on the combustion performance and emissions in a dual-fuel engine fueled with diesel and natural gas. *Energy Convers. Manage.* 168, 162–169. doi: 10.1016/j.enconman.2018.04.091

Yasar, H., Soyhan, H. S., Walmsley, H., Head, B., and Sorusbay, C. (2008). Double-Wiebe function: an approach for single-zone HCCI engine modeling. *Appl. Therm. Eng.* 28, 1284–1290. doi: 10.1016/j.applthermaleng.2007.10.014

Yasuda, K., Yamasaki, Y., Kaneko, S., Nakamura, Y., Iida, N., and Hasegawa, R. (2016). Diesel combustion model for on-board application. *Int. J. Eng. Res.* 17, 748–765. doi: 10.1177/1468087415611331

Yousefi, A., Guo, H., and Birouk, M. (2018). An experimental and numerical study on diesel injection split of a natural gas/diesel dual-fuel engine at a low engine load. *Fuel* 212, 332–346. doi: 10.1016/j.fuel.2017.10.053

Conflict of Interest: YT and TS were employed by the company OSAKA GAS CO., LTD.

The remaining authors declare that the research was conducted in the absence of any commercial or financial relationships that could be construed as a potential conflict of interest.

frontiers in Mechanical Engineering

ORIGINAL RESEARCH
published: 19 August 2020
doi: 10.3389/fmech.2020.00067

Trade-off Improvements by Combining EGR and Supercharging Ignited by Next Generation Bio-alcohol Blended FAME Fuels in Diesel Dual Fuel Operation Using Natural Gas

Yasufumi Yoshimoto[1]*, *Eiji Kinoshita*[2] and *Takeshi Otaka*[2]

[1] Department of Engineering, Niigata Institute of Technology, Kashiwazaki, Japan, [2] Department of Mechanical Engineering, Kagoshima University, Kagoshima, Japan

OPEN ACCESS

Edited by:
Hongsheng Guo,
National Research Council Canada (NRC-CNRC), Canada

Reviewed by:
Hannu Jaaskelainen,
Ecopoint Inc., (DieselNet), Canada
Shouvik Dev,
National Research Council Canada (NRC-CNRC), Canada

***Correspondence:**
Yasufumi Yoshimoto
yosimoto@mce.niit.ac.jp

Specialty section:
This article was submitted to Engine and Automotive Engineering, a section of the journal Frontiers in Mechanical Engineering

Received: 28 January 2020
Accepted: 07 July 2020
Published: 19 August 2020

Citation:
Yoshimoto Y, Kinoshita E and Otaka T (2020) Trade-off Improvements by Combining EGR and Supercharging Ignited by Next Generation Bio-alcohol Blended FAME Fuels in Diesel Dual Fuel Operation Using Natural Gas. Front. Mech. Eng. 6:67. doi: 10.3389/fmech.2020.00067

Studies in diesel dual fuel operation (DDF), introducing compressed natural gas (CNG) from the intake pipe and ignited by a liquid fuel injection in the combustion chamber have been conducted with conventional diesel engines. The present study investigated the effects of trade-off improvements between NOx and smoke emissions with next generation bio-alcohol blended FAME fuel ignition in DDF with a combination of EGR and supercharging. The CNG supply rates were set at 0% (diesel operation) and at 41–44% (DDF) on a heat energy basis, the boost pressures were set to two conditions with supercharger operation: 100 kPa (naturally aspirated operation, N/A) or 120 kPa (supercharged operation, S/C), and the EGR rates were varied from 0 to 25%. Blended fuels with a base fuel vs. alcohol ratio of 7: 3 were prepared using what in the following is termed PLME containing equal proportions of methyl palmitate (PME) and methyl laurate (LME) as the base fuel. The next generation bio-alcohols used here were iso-pentanol (C5) and iso-butanol (C4), and the engine performance, combustion characteristics, and exhaust emissions were investigated with iso-pentanol blended PLME (termed PLiP30), iso-butanol blended PLME (PLiB30), and neat PLME, as the ignition fuel. The results showed that with all ignition fuels, the DDF combining cooled EGR and supercharging improved the trade-off relation between NOx and smoke emissions significantly while maintaining relatively high brake thermal efficiencies.

Keywords: diesel dual fuel operation, alternative fuel, fatty acid methyl ester, next generation bio-alcohol, EGR, supercharging, trade-off improvement

INTRODUCTION

From the viewpoints of CO_2 emission reductions and energy security, natural gas could be a promising alternative fuel for internal combustion engines. A number of studies of diesel dual fuel operation (DDF) which introduce compressed natural gas (CNG) from the intake pipe and ignite it by a liquid fuel injected into the combustion chamber and have used conventional diesel engines. Dual fuel engines of this type require only limited modifications of presently used engines

for cleaner operation with remarkable reductions in PM emissions and a relatively high thermal efficiency at high load conditions. Drawbacks include large amounts of unburned HC and CO emissions, specifically at low loads, which is a major factor to decrease thermal efficiency at partial loads. To improve partial load performance many studies with various approaches have been conducted (Mizushima et al., 2003; Ogawa et al., 2003; Aroonsrisopon et al., 2009; Wannatong et al., 2009; Abdelaal and Hegab, 2012; Taniguchi et al., 2012; Li et al., 2015; Yang et al., 2015; Guerry et al., 2016; Blasio et al., 2017).

From the viewpoint of environmental concerns, biodiesel as a diesel alternative fuel has been attracting attention, and some studies have been reported to apply biodiesel as an ignition fuel for the DDF mode. Paul et al. (2014) have conducted a study to apply *pongamia pinnata* methyl ester (PPME) as an ignition fuel to a diesel dual fuel engine in which CNG, as the primary fuel, is injected into the intake pipe. The experiments there were conducted in four modes: diesel mode using conventional diesel fuel and PPME, and Diesel-CNG and PPME-CNG dual fuel modes. The results showed that the DDF of the PPME-CNG has the best engine performance and emission characteristics of all the fuel combinations tested. In the PPME-CNG mode, the brake thermal efficiency increased, as well as the smoke opacity, CO emissions, and unburned hydrocarbon emissions significantly reduced, in total showing this as more effective in improving engine performance and emission characteristics than Diesel-CNG dual fuel mode. Çelebi et al. (2017) introduced CNG from an intake manifold and applied biodiesel-diesel blended fuels. The experiments were conducted with five kinds of ignition fuels: neat diesel, 20 and 40% by volume of canola oil biodiesel and sunflower oil biodiesel blended with diesel. In the Çelebi et al. investigation, the CNG flow rates were changed in three stages (5, 10, and 15 L/min), and the sound pressure level (SPL), vibration acceleration characteristics, and emission characteristics (CO, NOx, and CO_2) were investigated at five different engine speeds (1,200–2,400 rpm). The results showed that compared with conventional diesel fuel, the biodiesel blends improved SPL, vibration acceleration, and CO emissions over those of ordinary diesel operation. The DDF with natural gas supplied to the intake manifold reduced vibration acceleration and SPL values, while CO emissions increased significantly. Also, the study reports that the biodiesel blended fuels increased NOx and CO_2, while the NOx and CO_2 emissions were improved by the CNG supply. The dual fuel engine offers reliable ignition by the diesel spray injected in the CNG-air pre-mixture, and it is possible to use low calorie gas fuels like pyrolysis gas from wood- and waste-biomass (Roy et al., 2009; Bora et al., 2014; Aklouche et al., 2017; Verma et al., 2017). The above features of DDF engines would suit cogeneration systems well, but substantial reductions in NOx emissions will be needed for this to be adopted.

It is well-known that a combined technique of EGR with supercharging is an effective measure to obtain simultaneous reductions in NOx and PM emissions. For that, the basic concept is that cooled EGR reduces NOx emissions due to lowered local oxygen concentrations and flame temperatures, while supercharging would be able to compensate for the output loss caused by increases in the EGR rates. There are some reports on the characteristics of DDF with gas fuels combined with EGR and supercharging. For instance, the combustion characteristics in DDF using high degrees of freedom in the injection variables with a common rail fuel injection system have investigated (Tomita et al., 2009; Azimov et al., 2011; Ogawa et al., 2015, 2016; Aksu et al., 2016). Iorio et al. (2017) examined the brake specific fuel consumption, combustion characteristics, and NOx emission characteristics using a compression ignition engine with three cylinders equipped with an electronically controlled methane injection system at the intake pipe. They also conducted optical measurements with an endoscope. Although neither EGR nor supercharging techniques were employed in that study, the analysis of the flame images by a two color method showed that compared with ordinary diesel combustion the DDF has lower flame temperatures and less soot combustion. The study concluded that this phenomenon is a reason why the DDF leads to low NOx and low PM emissions.

A few studies have reported investigations with a jerk type fuel injection system: Selim (2003) examined the influence of EGR rates (0–15%) and boost pressures (1–1.4 atm) on combustion noise reductions with a swirl chamber IDI engine with CNG-diesel dual fuel operation (that study used pure methane as a CNG substitute). The results showed remarkable reductions in the rate of maximum pressure rise when combining EGR and supercharging, but the influence on the engine performance and emission characteristics are unclear. A literature survey by the present authors showed only one other similar study, reported by Park and Terao (2003). That study examined the effects of combining supercharging and hot or cooled EGR with a cogeneration system by biogas. As shown here, the improvements with the DDF engine with conventional injection systems are limited.

The present authors have studied diesel dual fuel operation (DDF) with a small single cylinder DI diesel engine equipped with a jerk type injection system using CNG as the gaseous fuel. These reports used biodiesels or fatty acid methyl esters (FAMEs) as the ignition fuel (Kinoshita et al., 2009; Yoshimoto, 2010; Yoshimoto et al., 2010, 2018a), and reported the influence of the cetane number of the ignition fuel (Yoshimoto and Kinoshita, 2011; Yoshimoto et al., 2012), the effects of the intake air dilution by CO_2 or N_2 (Yoshimoto and Kinoshita, 2013), and the effects of boost pressures (Yoshimoto et al., 2016, 2017). One study (Yoshimoto et al., 2017) used 60% mass coconut oil methyl ester (CME) and 40% n-butanol blends (termed CMEB) as the ignition fuel in a DDF engine, and the influence of the boost pressure was examined. The results showed that with supercharging at 120 or 130 kPa boost pressures, the ignition delays of the CMEB shortened substantially, resulting in a brake thermal efficiency similar to diesel operation with conventional diesel fuel. In a previous study (Yoshimoto et al., 2018b), four kinds of next generation bio-alcohol isomer and diesel fuel blends were used in diesel operation and the effects of combining supercharging and EGR were examined. The bio-alcohol isomers were n-butanol, iso-butanol, n-pentanol, and iso-pentanol. Both with and without supercharging, all the bio-alcohol isomer blended fuels offer substantial improvements in the NOx and smoke emissions trade-off while maintaining good brake thermal efficiency. In

a following study (Yoshimoto et al., 2019), two iso-pentanol blended fuels at a constant 3: 7 mass ratio were used with LME (methyl laurate) and with diesel fuel as the base fuel, and here the DDF was conducted with four ignition fuels: neat LME, neat diesel, iso-pentanol blended LME, and iso-pentanol blended diesel. The results showed that all of the bio-alcohol blended fuels improved the NOx and smoke emission trade-off substantially, while the brake thermal efficiency decreased significantly with increasing EGR rates even when supercharging was employed. The reason was considered to be that the degree of constant volume of combustion decreased due to a large increase in the ignition delay of the alcohol blended fuels, resulting in the brake thermal efficiency deterioration.

In the present study, iso-pentanol and iso-butanol were used as the next generation bio-alcohols because the Research and Development of the yield improvement with advanced high fermentation methods have been progressing (Peralta-Yahya and Keasling, 2010; Zheng et al., 2015). Using an equal proportion of PME (methyl palmitate) that has a higher cetane number than LME, and LME, as the base fuel, two bio-alcohol blended fuels at a constant mass ratio of 7: 3 were prepared and supplied as the ignition fuel for the DDF. It was found that the DDF with the two bio-alcohol blends, with ignition combining cooled EGR and supercharging improved the NOx and smoke emission trade-off relation substantially while maintaining relatively high values in the brake thermal efficiency. Recently, a number of studies with next generation bio-alcohol blended fuels have been carried out targeting diesel operation (Han et al., 2016; Ileri, 2016; Kumar and Saravanan, 2016; Imdadul et al., 2017; Saravanan et al., 2017; Anil Bhaurao et al., 2018; Killol et al., 2019; Pan et al., 2019). But, many of these studies have been conducted with n-butanol, iso-butanol, or n-pentanol, and there are few reports with iso-pentanol (Yoshimoto et al., 2018b).

EXPERIMENTAL APPARATUS AND METHODS

Test Fuel

The study used CNG (compressed natural gas) as the premixed with intake gas. **Table 1** shows the particulars of the used gas. To ignite the pre-mixture, the experiments used two kinds of next generation bio-alcohol blended fuels and neat PLME. Here, the PLME stands for a blend with equal proportions of PME (methyl palmitate, purity > 95%) and LME (methyl laurate, purity > 96%). Using a PLME as the base fuel, two alcohol blends with a constant mass ratio of 7: 3 were prepared by iso-pentanol (termed PLiP30) and iso-butanol (PLiB30). In a previous paper, as a result of using 30% iso-pentanol blended LME fuel (LiP30) as the ignition fuel for the DDF, the ignition delay became very long and the brake thermal efficiency decreased significantly at a high EGR rate condition (Yoshimoto et al., 2019). One way to prevent such a deterioration of engine performance is to use PME with the high cetane number as the base fuel. However, as PME has a high melting point of about 35°C, it cannot be applied to the engine without heating the fuel. Therefore, the present study employed an equal proportion of PME and LME as a base fuel that can be handled at room temperatures while improving ignitability. The authors have conducted studies with butanol (including isomers) or pentanol blended fuels under diesel operation. For the alcohol blending, the base fuels such as diesel fuel, biodiesels, or FAME were used. Among these, for butanol, we investigated the influence of the isomer kind and blending ratio in detail (Fushimi et al., 2013; Yoshimoto et al., 2013, 2018b). Considering these results, we conducted the above experiments (Yoshimoto et al., 2019) with 30% iso-pentanol blended LME (LiP30) or 30% iso-pentanol blended diesel fuel (GiP30) in the DDF mode. As a result of the DDF with the LiP30 fuel, a deterioration in ignitability occurred as described above. In this study, the experiments were designed with PLME, which has a better ignitability than the LME as the base fuel, while iso-butanol as the blending component having a low cetane number is applied to the DDF. Considering this-, we decided that 30% iso-butanol is a suitable ratio for blending to PLME.

Table 2 shows the tested ignition fuels including iso-pentanol and iso-butanol, the blended components. The PME and LME have sixteen and twelve saturated carbon atoms and their cetane numbers are higher than ordinary diesel fuel, the ignitability of the PLME is good. The cetane number of iso-pentanol is unknown, but from the ignition delay characteristics examined by the authors, the cetane number of the iso-pentanol was estimated to be between 17 and 20 (Yoshimoto et al., 2018b). Here, the cetane number of the n-butanol is 17, and that of n-pentanol 20 (Kumar and Saravanan, 2015). As the PLiP30 and PLiB30 contain alcohols with a low boiling point, the 10% distillation temperatures are low and the evaporation characteristics are better than those of PLME.

TABLE 1 | Properties of the used gases.

Test gas fuel			CNG
Composition	CH_4	vol.%	90.0
	C_2H_6	vol.%	5.5
	C_3H_8	vol.%	3.8
	C_4H_{10}	vol.%	0.6
Mean molecular weight		g/mol	18.16
Density		kg/m_N^3	0.811
Net calorific value		MJ/m_N^3	40.01
Net calorific value		MJ/kg	49.35
Stoichiometric air-fuel ratio			17.05

Engine Setup

Figure 1 shows the experimental apparatus: a test engine, a CNG supply unit, a supercharging system, and an EGR cooling device. The tested engine is a horizontal, four stroke, water-cooled small single cylinder direct injection diesel engine with a toroidal type combustion chamber and the specifications of the engine and the fuel injection system are shown in **Table 3**. The jerk type fuel injection system was set to standard diesel fuel specifications except for changing the plunger diameter to 7 mm from the original size of 6.5 mm. This is to increase the injected fuel quantity to maintain the specified engine output for

TABLE 2 | Properties of the tested fuels.

Test fuel	Diesel	PME	LME	PLME	iso-pentanol	iso-butanol	PLiP30	PLiB30
Density [15 °C] (kg/m^3)	836	867[b]	873	870[c]	813	807	851[c]	848[c]
Viscosity [30 °C] (mm^2/s)	3.89	—	2.90	3.92	—	2.63[d]	3.32	3.23
Cetane number	—	74.3[b]	61.2[b]	—	—	<15[e]	—	—
Cetane index	57.1	—	—	—	—	—	—	—
Lower heating value (MJ/kg)	42.95	37.12	35.35	36.11[a]	34.62	32.61	35.66[a]	35.06[a]
B.P. at 10% distillation (°C)	—	—	260.5	271.5			132.0	107.5
B.P. at 50% distillation (°C)	—	—	260.5	285.5			276.0	275.5
B.P. at 90% distillation (°C)	336	—	261.0	316.0	131[f]	108[f]	313.5	314.0
Carbon[a] (mass %)	86.1	75.5	72.8	74.2	68.1	64.8	72.4	71.4
Hydrogen[a] (mass %)	13.8	12.7	12.2	12.5	13.7	13.6	12.9	12.8
Oxygen[a] (mass %)	—	11.8	14.9	13.4	18.2	21.6	14.8	15.9
Stoichiometric air-fuel ratio[a]	14.6	12.5	11.9	12.2	11.7	11.2	12.1	11.9

[a]*estimated value,* [b]*from Graboski et al. (2003),* [c]*estimated from the measuring value at 30 °C,* [d]*at 40 °C, from Saravanan et al. (2017),* [e]*from Saravanan et al. (2017)* [f]*boiling point.*

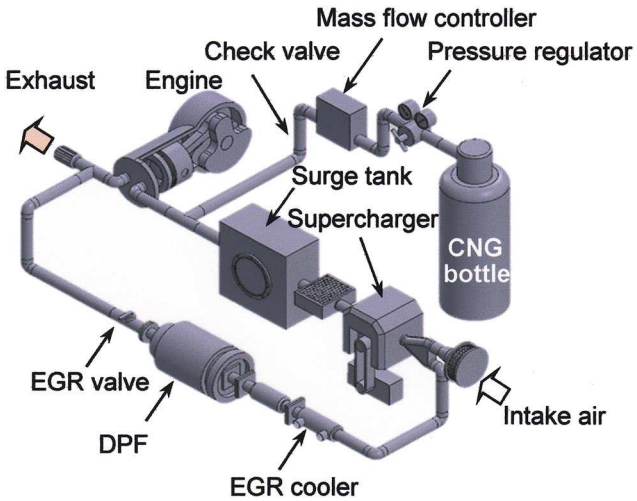

FIGURE 1 | Experimental setup.

TABLE 3 | Engine specifications.

Engine model	4 Stroke, horizontal, water cooled
Bore	82 mm
Stroke	78 mm
Stroke volume	411 cc (Single cylinder)
Compression ratio	18
Combustion chamber	DI (Toroidal type)
Rated output	5.1 kW/2,400 rpm (BMEP=0.62 MPa)
Injection pump	Bosch PFR (Plunger 7 mm)
Injection nozzle	DLLA 150 (4–ϕ0.2)
Opening pressure	21.7 MPa
Injection timing	Fixed (19 °CA.BTDC)

the tested bio-fuels that have low heat values. The tested engine has a mechanical governor to maintain a constant engine speed and an eddy current type dynamometer was used to absorb the engine output.

As shown in **Figure 1**, the CNG supply unit has a CNG bottle, a pressure regulator, a mass flow controller, and a check valve. The CNG is fed directly into the intake-pipe, normal to the intake charge flow. The study employed a Roots type blower supercharger driven by a motor, making it possible to control the boost pressure independently from the engine operating variables. The boost pressures were 100 kPa (naturally aspirated operation, N/A here) and 120 kPa (supercharged operation, S/C). The back pressure in the exhaust pipe was set at a constant 110 kPa during the supercharged operation. The diesel dual fuel operation was carried out with the following procedure: the warm-up operation with the tested fuel was performed under ordinary diesel mode, next the CNG flow rate was increased while reducing the injected fuel quantity. This operation was carried out step by step, and finally the CNG supply rate was set at a constant 8 L/min (0°C, 1 atm) in all the experiments. During the measurements, the engine torque and speed were kept constant by finely adjusting the fuel injection quantity and the field current of the eddy current type dynamometer.

The EGR rate was adjusted by an EGR valve upstream of a diesel particulate filter (DPF). The experiments employed low-pressure loop type cooled EGR and the recirculated gas was introduced to the intake air upstream of the supercharger. The EGR rate was determined from Equation (1) and the CO_2 concentration in the exhaust and intake gases was measured using an NDIR analyzer. Since it is necessary to estimate the EGR rate quickly during the experiments, the opening of the EGR valve was adjusted so the oxygen concentration reached the target value while monitoring the oxygen concentration of the intake air corresponded to the EGR rate. The oxygen

concentration was monitored by a magnetic force type oxygen analyzer.

$$EGR\ \% = \frac{(CO_2)_{intake} - (CO_2)_{ambient}}{(CO_2)_{exhaust} - (CO_2)_{ambient}} \times 100 \quad (1)$$

The intake air quantity was measured with a laminar flowmeter upstream of the supercharger. The gas temperatures in the intake pipe were controlled at 30 ± 2°C. During the experiments, the engine speed was a constant 1,900 rpm, the maximum brake torque conditions, 87 ± 2°C cooling water, and 70 ± 3°C lubricating oil. The engine load was set at a constant high load condition (BMEP = 0.67 MPa) where the trade-off relation between NOx and smoke emissions assumes critical values. The brake thermal efficiency, *BTE* was determined from Equation (2). Where, N_e is the braking power, $\dot{m}_f$ is the mass flow rate of ignition fuel, $\dot{m}_g$ is the mass flow rate of gaseous fuel, while LHV_f and LHV_g are the lower heating values of the ignition fuel and gaseous fuel, respectively. The flow rate of the ignition fuel was determined by time interval measurement per specified volume, and its mass flow rate was calculated from the density.

$$BTE = \frac{N_e}{\dot{m}_f\ LHV_f + \dot{m}_g\ LHV_g} \quad (2)$$

Measuring Apparatus and Procedures

The combustion pressure was measured with a piezoelectric type pressure pick-up and the crank angle was recorded by a rotary encoder; the needle lift of the nozzle was monitored by a Hall-effect element. The signals recorded digitally in about 160 continuous cycles, and the rate of heat release and the degree of constant volume of combustion, η_{glh} determined from the average pressure of 50 cycles. The energy equilibrium of the gas in the cylinder as in Equation (3) and the degree of constant volume of combustion, η_{glh}, determined from Equation (4):

$$dQ = dQ_E - dQ_C = \frac{1}{\kappa - 1}\left(\kappa\ pdV + VdP\right) \quad (3)$$

$$\eta_{glh} = \frac{1}{Q}\int \frac{1 - \frac{1}{\varepsilon_\theta^{\kappa-1}}}{1 - \frac{1}{\varepsilon^{\kappa-1}}}\frac{dQ}{d\theta}d\theta \quad (4)$$

From any 50 continuous cycles, the ignition delay was determined from the crank angle interval between the start of the needle lift and the pressure rise due to the combustion. The detection of the rise timings of the needle lift and pressure signal necessary for the ignition delay analysis was carried out by using a method that automatically discriminates by programming based on the set threshold value for any 50 combustion cycles. The NOx emissions were measured using a CLD analyzer, the HC as ppm methane using a FID analyzer, the CO used an NDIR analyzer, and the smoke density an opacimeter.

With the dual fuel operation, the proportion of CNG supplied, Q_g/Q_t, was defined as the rate of the heat energy of the supplied CNG, Q_g, to the total heat energy available in the cylinder, Q_t. In a previous study (Yoshimoto et al., 2016), the experiments were carried out up to a 140 kPa boost pressure with 0–81% CNG supply rates using JIS No. 2 diesel fuel. Here, the HC and CO emissions increased substantially with increasing boost pressure and CNG supply: the optimum operating conditions were determined to be below 120 kPa boost pressures and below 42% CNG supply rates. In the present study, the DDF with supercharging was conducted at a constant 120 kPa boost pressure and the CNG flow rate was set at a constant 8 L/min (0°C, 1 atm) with and without supercharging. The equivalence ratio of the pre-mixture, ϕ_g, was 0.18–0.24 at the supercharged operation (S/C) and ϕ_g = 0.26–0.30 at a naturally aspirated condition (N/A). The proportion of CNG, Q_g/Q_t was 41–44%. The operating conditions are listed in **Table 4**.

EXPERIMENTAL RESULTS AND DISCUSSION

Influence of the Kind of Ignition Fuel, With and Without Supercharging and EGR Rate on Engine Performance and Emissions at the Operation Modes

Figure 2 shows the changes in brake thermal efficiency, η_e, smoke density, equivalence ratio of the total in-cylinder charge, ϕ_t, and exhaust temperature as a function of the EGR rate at two intake charge pressures, 100 and 120 kPa with the Roots type blower supercharger operating. **Figure 3** shows the changes in emission characteristics. The left columns (**Figures 2**, **3**) show the diesel operation (**Figures 2A**, **3A**, Q_g/Q_t = 0%) and the right columns are the diesel dual fuel operation, DDF (**Figures 2B**, **3B**, Q_g/Q_t = 41–44%), respectively. As the injection fuel (or ignition fuel), the experiments here used JIS No. 2 diesel fuel (gas oil) as a reference, neat PLME (equal proportions of methyl palmitate and methyl laurate), PLiP30 (70% PLME and 30% iso-pentanol blend), and PLiB30 (70% PLME and 30% iso-butanol blend); the supercharger power input was not considered in the thermal efficiency calculations. The upper limit of EGR rate was set to about 11% at a naturally aspirated condition as well as 25% at supercharged operation, respectively, because of the substantial increase in the smoke emissions under diesel operation with diesel fuel.

As shown in the top panel of **Figure 2A**, the brake thermal efficiency η_e with diesel fuel without supercharging (N/A) with diesel operation decreased remarkably with increasing EGR rates. Here, the smoke emissions with the diesel fuel increased substantially (second panel of **Figure 2A**), and operation with high EGR rates could not be maintained. As shown in **Figure 2B**, the DDF without supercharging maintained extremely low smoke densities, and the η_e were maintained at relatively high values. As shown here (**Figure 2B**), this type of DDF engine introducing CNG from the intake pipe strongly suppresses smoke emissions in N/A operation employing EGR. The reason is that as the engine is operated at a constant output, the injected fuel quantity with the DDF decreases and this may cause the soot formation in the fuel rich zone to be suppressed, and become a major reason for the smoke reductions (Kinoshita et al., 2009).

TABLE 4 | Combination of experimental conditions.

Boost pressure [kPa]	Fuel/EGR	CNG supply					
		0% (Diesel operation)			41–44% (DDF)		
100 kPa N/A	Fuel	Diesel, PLME			PLME, PLiP30, PLiB30		
	EGR	Targeted oxygen concentration in intake gas (%)					
		21	20	19	21	20	19
		Approximately EGR rate (%)					
		0	6	11	0	6	11
120 kPa S/C	Fuel	Diesel, PLME, PLiP30, PLiB30			PLME, PLiP30, PLiB30		
	EGR	Targeted oxygen concentration in intake gas (%)					
		21	19	17	21	19	17
		Approximately EGR rate (%)					
		0	13	25	0	13	25

Next, a discussion will be made of the influence of the presence or absence of supercharging on the brake thermal efficiency η_e focusing especially on the ordinary and DDF modes. As shown in the top panel of **Figure 2A**, the η_e with all the injection fuels under diesel operation with supercharging increased considerably over the tested EGR region, compared to the N/A operation. Here, the trend in the η_e increase is specifically significant with the neat PLME. The relation among the brake thermal efficiency η_e, the theoretical thermal efficiency η_{th}, the degree of constant volume of combustion η_{glh}, the combustion efficiency η_u, the cooling loss ϕ_w, and the mechanical efficiency η_m is:

$$\eta_e = \eta_{th} \cdot \eta_{glh} \cdot \eta_u \, (1 - \varphi_w) \cdot \eta_m \tag{5}$$

The experimental variables set in this study such as with and without supercharging, EGR rates, and the two operation modes affect the ratio of specific heats of the working fluid. Therefore, the theoretical thermal efficiency, η_{th} of the fuel-air cycle shown in Equation (5) may have been complicatedly influenced by these experimental variables. However, simulation analysis is necessary to clarify the effect of the ratio of specific heats, which is outside the scope of this study. In this report discussion is limited to influencing factors that can be examined with the experimental results.

When supercharging is employed, the equivalence ratio of the total in-cylinder charge ϕ_t, decreases (third panel of **Figure 2A**). This is because the air density in the combustion chamber increases giving rise to the tendency toward reductions in local oxygen concentration shortages, resulting in the reductions in smoke emissions (solid curves, second panel of **Figure 2A**) and CO emissions (bottom panel of **Figure 3A**). This is the reason why the combustion efficiency η_u in Equation (5) improves, and may be a reason for the increases in the brake thermal efficiencies with supercharging. As shown in the top panel of **Figure 2B**, the η_e with the supercharged DDF was similar to that of the diesel operation using diesel fuel without EGR and there were also no improvements in the DDF without EGR. The reason may be that, as shown in the middle panel of **Figure 3B**, the HC emissions with DDF increased substantially even when the engine was operated without supercharging, resulting in the decrease in the combustion efficiency η_u.

Discussing the influence of the EGR rate on the brake thermal efficiency η_e, both modes of operation with supercharging showed that the η_e clearly decreased above the 20% EGR region. At the diesel operation, the smoke emissions (**Figure 2A**) and CO emissions (**Figure 3A**) increased substantially here. This is because the equivalence ratio of the total in-cylinder charge increases due to intake air quantity decreases by the EGR (third panel of **Figure 2A**). Therefore, it may be considered that the decreases in combustion efficiency η_u resulted in the decreases in η_e in the diesel operation with supercharging at high EGR rates. As shown in the bottom panels of **Figure 2**, all the tested fuels showed substantial reductions in exhaust gas temperature with the supercharging, regardless of operation mode. The reason for this is considered to be that the heat capacity of the in-cylinder charge increases due to the increasing air density brought about by the supercharging, resulting in a decrease in the mean gas temperature during combustion.

Considering the influence of injection or ignition fuel kind on the brake thermal efficiency η_e, the neat PLME without supercharging under diesel operation showed high values of η_e, compared with diesel fuel. This can be explained by the differences in smoke (second panel of **Figure 2A**) and CO emissions (bottom panel of **Figure 3A**). The PLME is an oxygenated fuel (oxygen content 13.4%) and the oxygen contained in the fuel would promote the oxidation reaction in the fuel-air mixture, resulting in decreases in smoke and CO emissions, increasing the combustion efficiency η_u. With supercharging under diesel operation, the η_e with the neat PLME also tends to be higher than the other fuels. In the DDF mode, regardless of supercharging, there is little effect of the fuel kind on the η_e, and a relatively high brake thermal efficiency was maintained in the tested EGR regions. As shown in the second panel of **Figure 2A**, the smoke emissions with the bio-alcohol blended PLME fuels compared to those of the neat PLME under supercharged operation decreased at high EGR rate conditions. It is clear that PLiP30 and PLiB30 with 14.8 and 15.9% oxygen

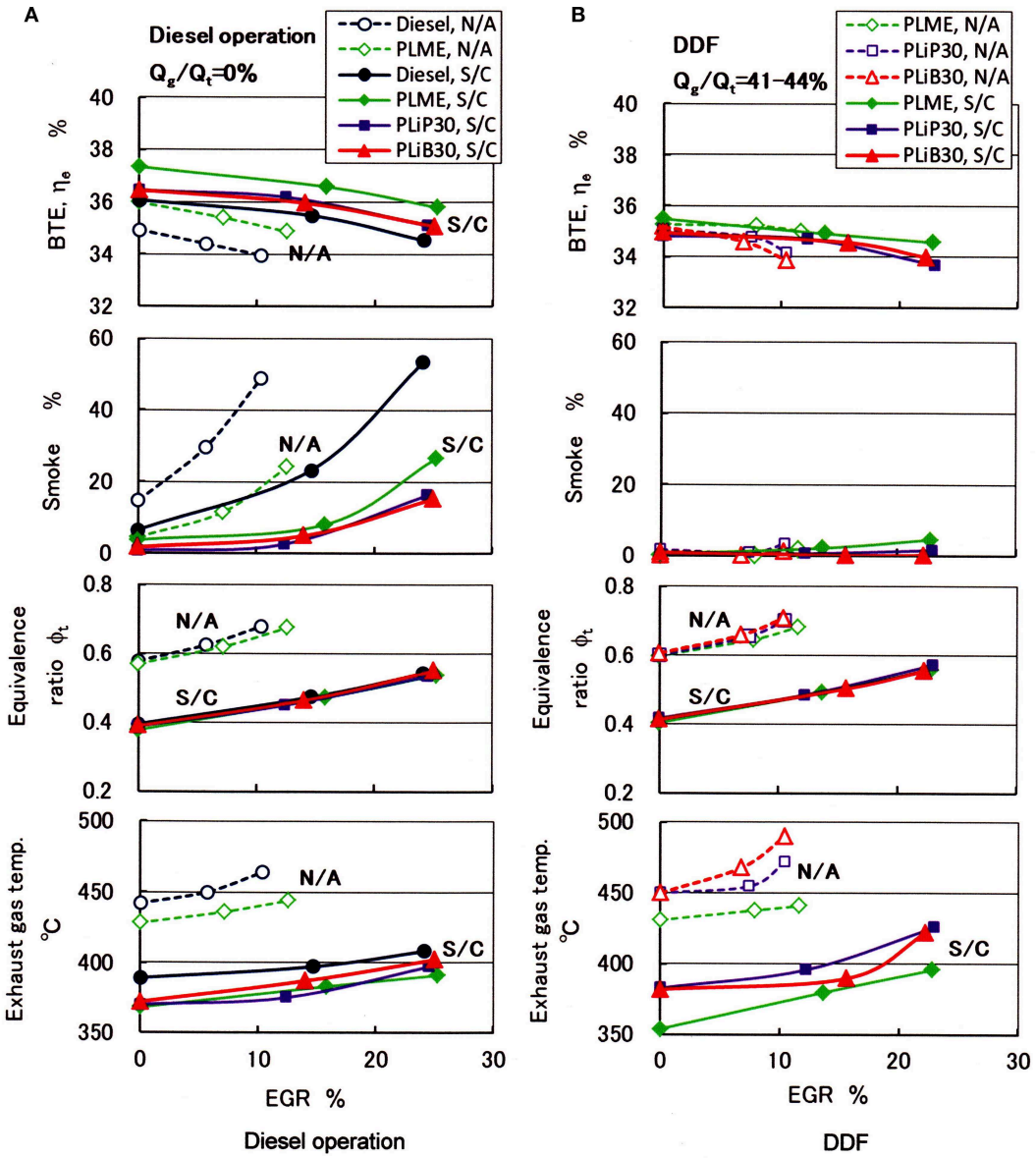

FIGURE 2 | Plots of results with EGR and supercharging vs. brake thermal efficiency, smoke density, equivalence ratio of the total in-cylinder charge, and exhaust gas temperature with diesel fuel, PLME, PLiP30, and PLiB30 with diesel and DDF (BMEP=0.67 MPa). **(A)** Diesel operation and **(B)** DDF.

content generates lower smoke emissions than the PLME which has 13.4% oxygen.

Figure 3 shows the changes in NOx, HC, and CO emissions as a function of the EGR rate. Regardless of operation mode, the NOx emissions decreased monotonously with increasing EGR and it is clear that EGR is an effective measure to achieve NOx reductions. The NOx reductions showed no clear trends by the kind of ignition fuel, with or without supercharging, and in all operation modes, except for the condition with diesel fuel under diesel operation with supercharging without EGR.

As shown in the middle panel of **Figure 3B**, the HC emissions with the DDF increased substantially at the N/A condition and this tendency became very strong at the S/C operation. It has been pointed out that the main source of HC (methane) emissions for diesel engines converted to dual fuel operation with CNG is the blow-through of CNG during the valve overlap period. The following two factors are considered as other reasons. With diesel dual fuel operation at the N/A condition and due to the CNG supply, unburned mixture easily enters the quench regions, giving rise to HC emission increases (Kinoshita et al., 2009). A further reason may be that there are parts of the CNG-air mixture that are not entrained into the spray flux of the ignition fuel. As the CNG-air pre-mixture is outside the flammable range, flames do not propagate here and this mixture may remain

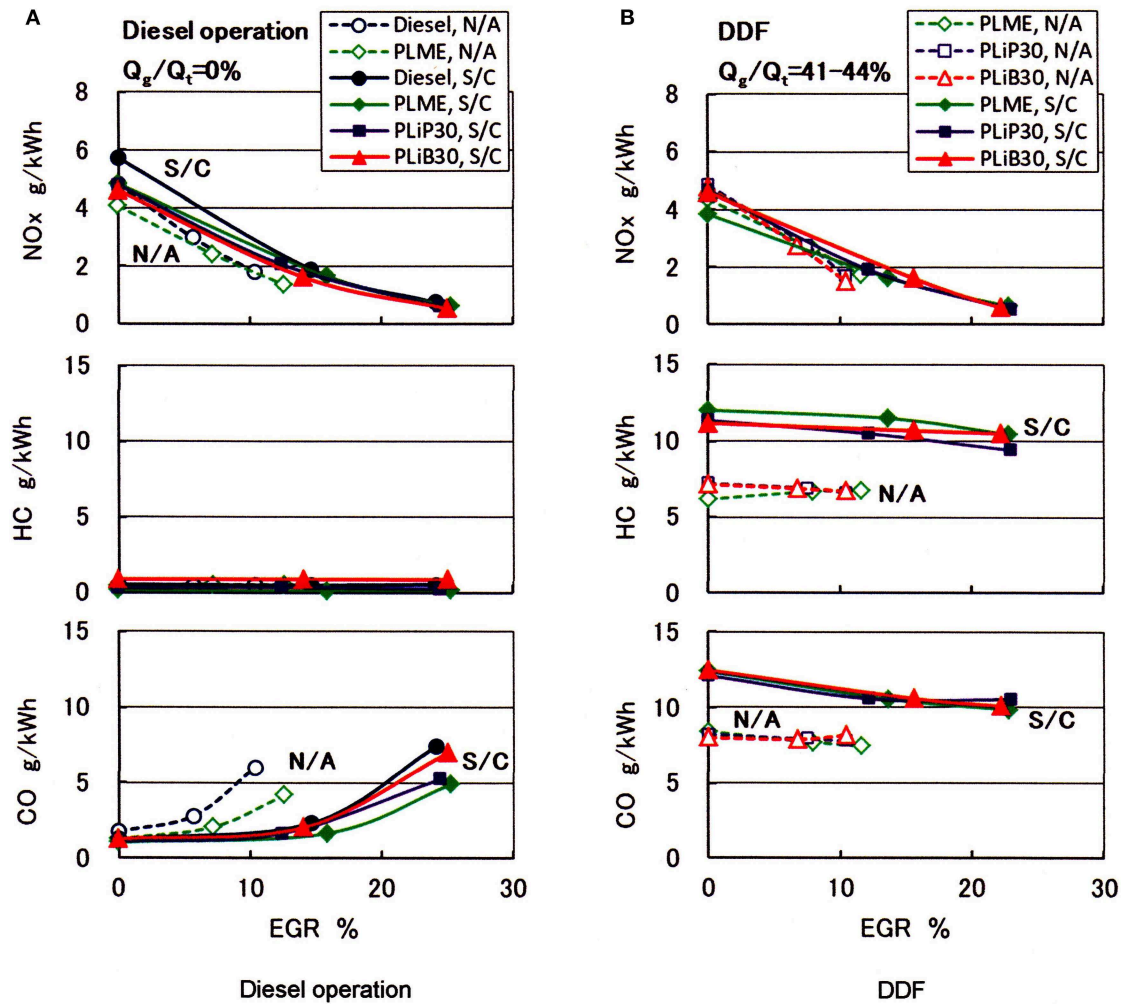

FIGURE 3 | Plots with EGR and supercharging vs. emission characteristics with diesel fuel, PLME, PLiP30, and PLiB30 with diesel and DDF (BMEP = 0.67 MPa). **(A)** Diesel operation and **(B)** DDF.

without taking part in the combustion, such a situation would also result in higher HC emissions (Yoshimoto et al., 2012). With supercharging, the CNG-air pre-mixture became very lean and flame propagating combustion deteriorated more, and it may be that such incomplete combustion, an expansion of the unburned regions, leads to substantial increases in HC emissions. The HC emissions with the DDF with supercharging showed a weakly decreasing trend with increasing EGR. The reason is not clear, but Srinivasan et al. (2007) have suggested the possibility of an active recycling effect, unburned hydrocarbons in the recirculated gas influences the re-burning of the hydrocarbons during the next combustion cycle.

Regardless of ignition fuel, the CO emissions increased substantially with increasing EGR at the N/A operation under the ordinary diesel mode (bottom panel in **Figure 3A**). The reason may be that the oxygen concentration of the in-cylinder charge decreases due to EGR. The addition of supercharging did however improve the CO emissions remarkably. Compared with the diesel operation, the CO emissions with the DDF showed high values across the tested EGR regions. The reasons would be similar to those causing HC emissions: the CNG-air pre-mixture became very lean and the incomplete combustion regions expanded. A further reason may be that the pre-mixture became much leaner due to longer ignition delays, as will be described in the next section.

Influence of the Kind of Ignition Fuel, With and Without Supercharging, and of the EGR Rate on Combustion Characteristics Under Different Operation Modes

Figure 4 shows the changes in indicator diagrams and heat release rates with and without EGR at the supercharged condition under two operation modes: the top panels are for diesel operation (**Figures 4A,B**, $Q_g/Q_t = 0\%$) and the bottom panels are for DDF mode (**Figures 4C,D**, $Q_g/Q_t = 41–44\%$). Plots in

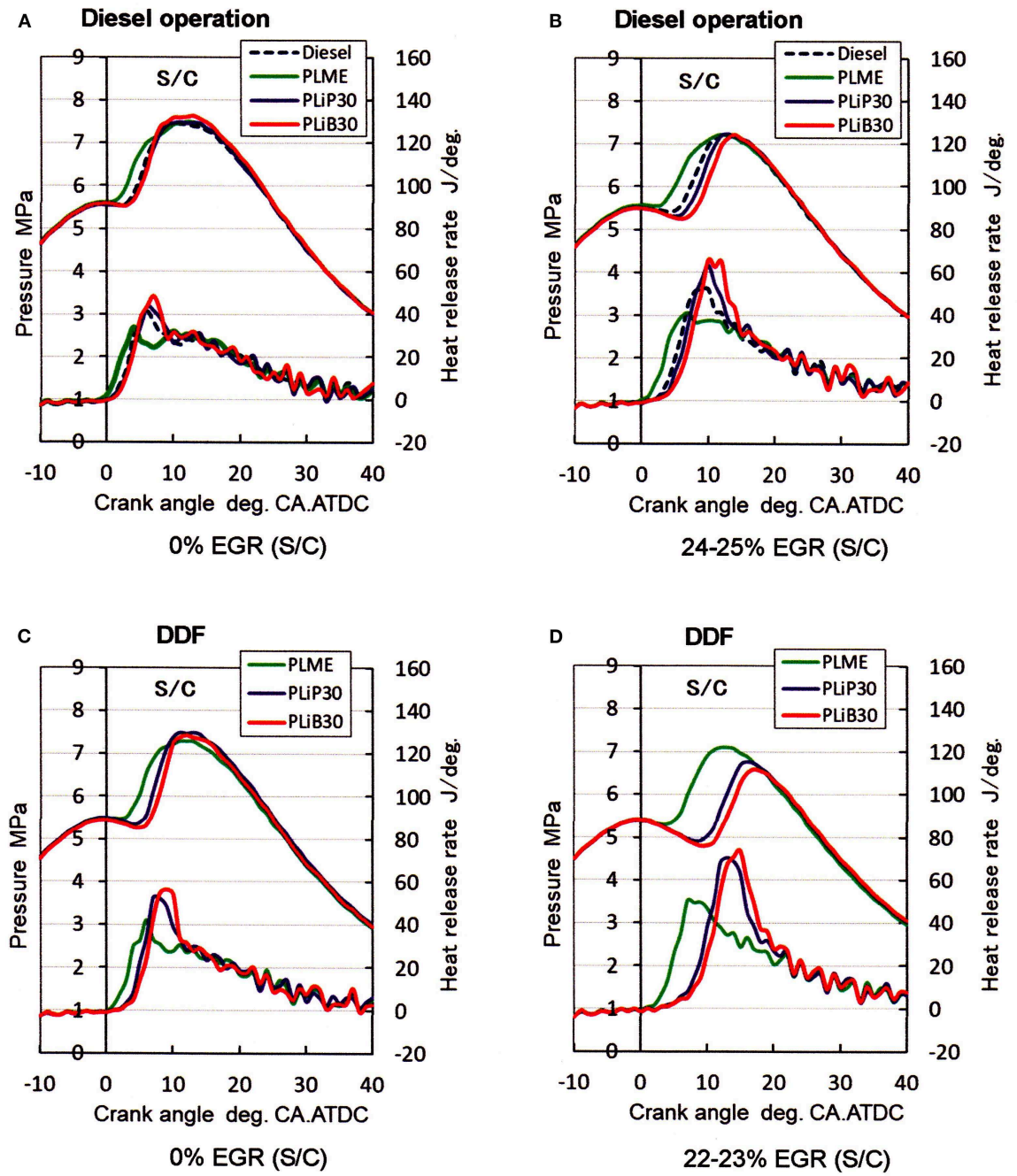

FIGURE 4 | Plots of results with EGR and supercharging vs. indicator diagrams and heat release rates with diesel fuel, PLME, PLiP30, and PLiB30 with diesel and DDF (BMEP = 0.67 MPa). **(A,B)** Diesel operation and **(C,D)** DDF.

the four panels in **Figures 4A,B** vs. **Figures 4C,D** show that regardless of the addition of EGR, the ignition timings with the DDF operation were delayed more than in the ordinary diesel operation. This delay is especially remarkable when bio-alcohol blended PLME fuels were used as the ignition fuel.

Figure 5 plots combustion characteristics for all of the data of the present experiments. Here, it is noted that the bulk modulus of the fuel affects the timing of the start of fuel injection, and consequently the ignition characteristics. Especially with biodiesel, it has been reported that the bulk modulus varies depending on the kind of FAME (Tat and Van Gerpen, 2003). In ordinary diesel operation, the dynamic timings of the start of injections for the tested fuels were in the range of −5.0 to −4.6 °CA.ATDC. Compared with diesel fuel, the PLME

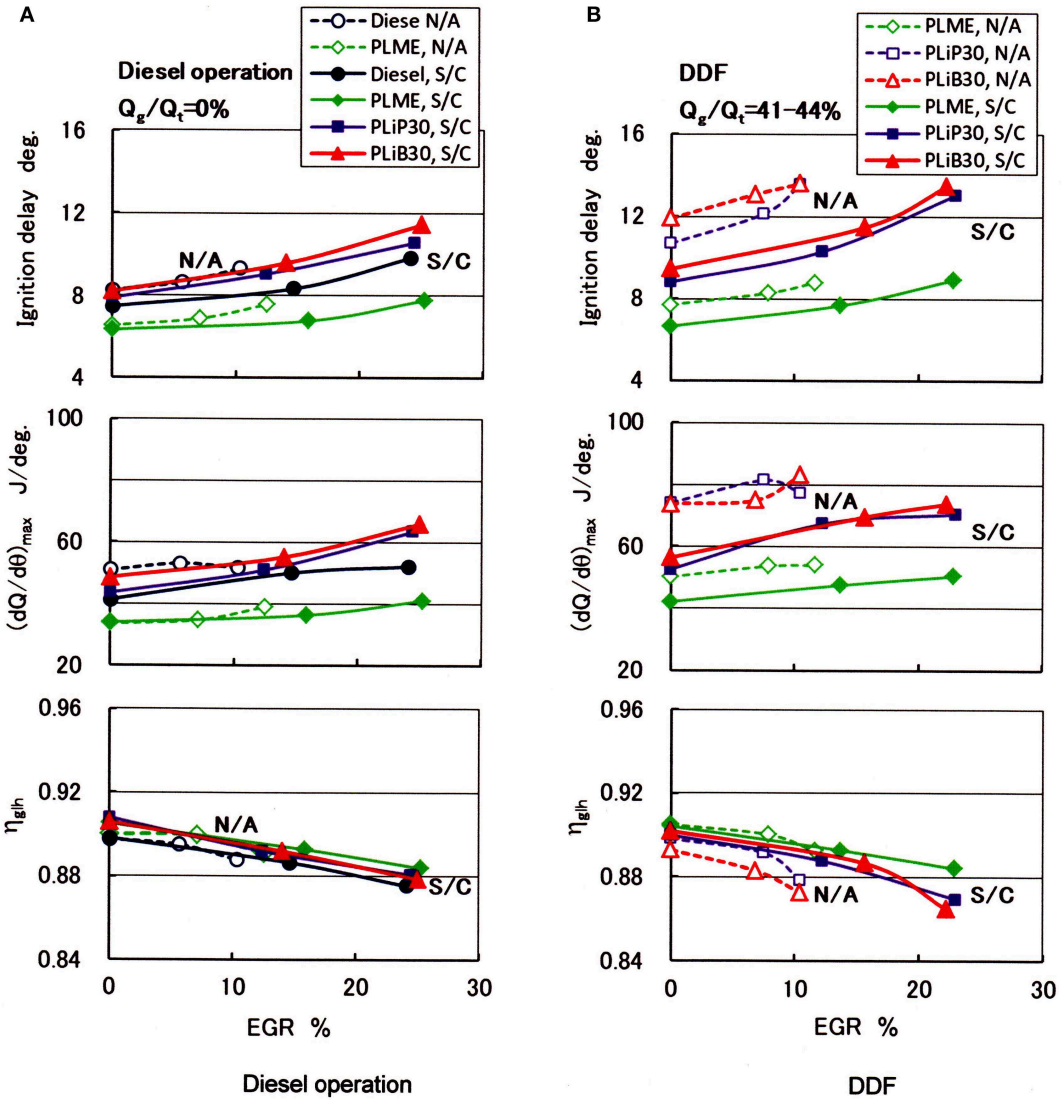

FIGURE 5 | Plots of EGR and supercharging vs. combustion characteristics with diesel fuel, PLME, PLiP30, and PLiB30 with diesel and DDF (BMEP = 0.67 MPa). **(A)** Diesel operation and **(B)** DDF.

showed a tendency for the start of injection to advance in the range of 0.1 to 0.3 °CA. However, no clear difference between alcohol blended PLME fuels and diesel fuel have been observed. It is also an important issue to clarify the fluctuation in the combustion characteristics shown here. The signals (data, values) of the in-cylinder pressure, nozzle needle lift, and crank angle were recorded for 160 continuous cycles. From many experiments with diesel fuel, biodiesels, and FAME fuels, it has been confirmed that when the CNG supply rate is below 77% the combustion fluctuation rate, COV_{imep} (defined as the ratio of standard deviation in imep to the mean value of the imep) is low, and stable combustion is obtained. In the present experiments, the COV_{imep} was below 3.5% under all conditions, so the cycle to cycle variation may be considered to be small. The fluctuation rate of the ignition delay, COV_{delay} was as high as about 10% only under the conditions of the DDF mode using PLiB30, N/A, and the EGR rate of 10.4%. However, the COV_{delay} was lower than 6% under all other conditions.

Comparing the top panels of **Figures 5A,B**, the ignition delays with the DDF are longer than those with diesel operation. A reason may be, as reported by Papagiannakis et al. (2008) that the cylinder charge temperature close to the point of the liquid fuel injection is lower with DDF due to the higher overall specific heat capacity of the CNG-air mixture. The ignition delays with supercharging were short and this trend was enhanced with the DDF mode, suggesting that applying supercharging in the DDF is an effective measure to shorten the ignition delay. The major reason why supercharging shortens the ignition delay is considered to be an effect of the in-cylinder pressure increases.

At the N/A condition, the ignition delay with the DDFD is reported as longer than with the diesel operation, and the

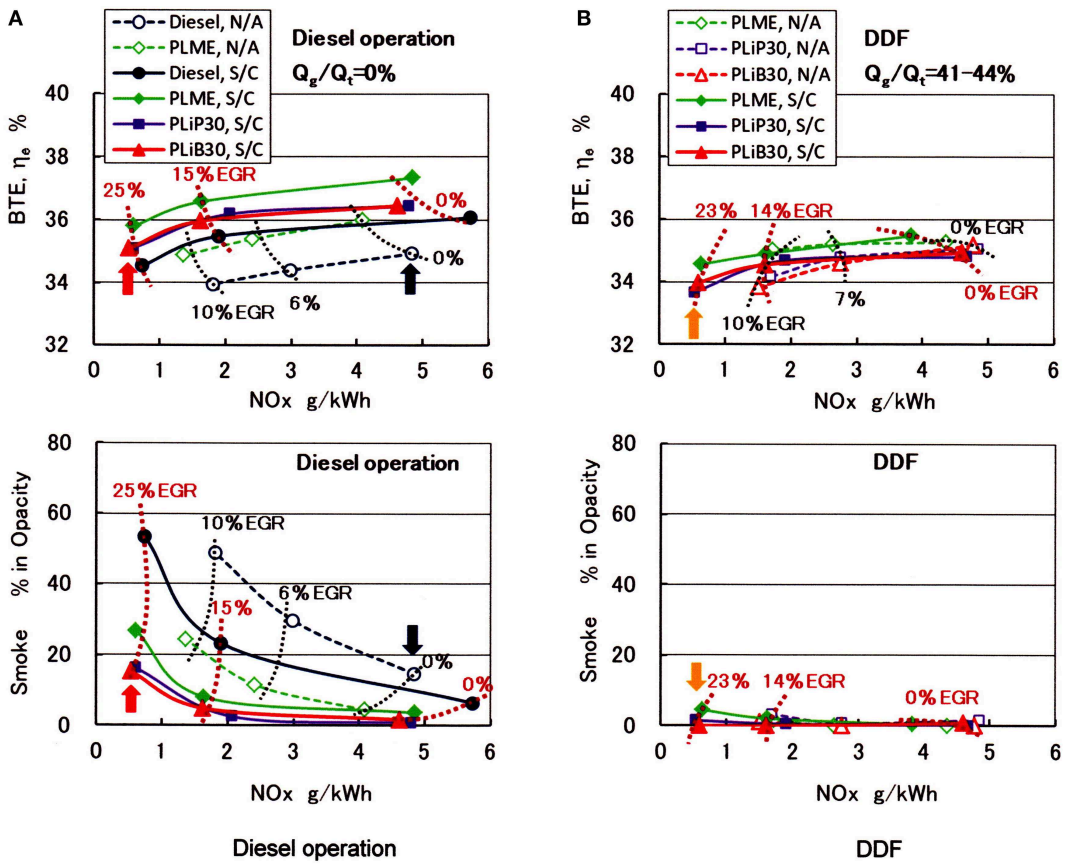

FIGURE 6 | Plots of trade-off relation results for NOx vs. brake thermal efficiency and NOx vs. smoke emissions with diesel fuel, PLME, PLiP30, and PLiB30 with diesel and DDF (BMEP = 0.67 MPa). **(A)** Diesel operation and **(B)** DDF.

premixed combustion after the ignition is enhanced (Yoshimoto et al., 2010). In the premixed combustion phase, the injected fuel spray in the cylinder forms a combustible mixture during the ignition delay, and combustion of this mixture occurs simultaneously with the ignition fuel in the regions where the CNG-air pre-mixture is entrained by the spray. This increases the maximum rate of heat release $(dQ/d\theta)_{max}$, resulting in the increases in the heat release in the premixed combustion phase shown in the middle panel of **Figure 5B**. It may be concluded that following the premixed combustion, both the entrained CNG from the ignition fuel spray and the previously injected fuel spray burn simultaneously. At all of the operation modes and with the addition of supercharging, the ignition delays with neat PLME were shorter than with other fuels for all the tested EGR rates. This may be ascribed to the cetane number of the PLME being higher than that of the diesel fuel, as shown in **Table 2**. As shown in **Figures 5A,B**, the ignition delays with the bio-alcohol blended PLME fuels (PLiP30 and PLiB30) increased substantially as well as the $(dQ/d\theta)_{max}$ increased over the tested EGR range, compared with PLME. With the diesel operation, the degree of constant volume combustion, η_{glh} with the bio-alcohol blended PLME fuels are similar to those of the other injection fuels. This would suggest that after the ignition, the bio-alcohol blended PLME fuels the combustion proceeds at higher speeds. The reason may be considered to be that the mixture formation in the diffusion combustion phase is improved due to improvements in the evaporation characteristics and spray characteristics because of the low boiling point and lower kinematic viscosity of the PLiP30 and PLiB30 than that of diesel fuel. In the DDF, however, the ignition delays with the bio-alcohol blended PLME fuels became much longer, and the η_{glh} at the increased EGR conditions decreased substantially (bottom panel in **Figure 5B**). It is considered that such a delay in the combustion with the PLiP30 and PLiB30 resulted in the higher exhaust gas temperatures shown in the bottom panel of **Figure 2B**. The reason for the ignition delay increases in the bio-alcohol blended PLME fuels is due to the low cetane numbers of the bio-alcohols contained in the blends.

Trade-off Improvements With the Tested Ignition Fuels Under the Different Operation Modes Combining Supercharging and EGR

Figure 6 shows the trade-off relation between NOx and brake thermal efficiency, η_e as well as between NOx and smoke

emissions with the tested fuels as a function of the EGR rate, and with and without supercharging under different operation modes. As shown in **Figure 6A**, the NOx emissions with diesel fuel under diesel operation decreased significantly when the cooled EGR was employed at the N/A condition (boost pressure: 100 kPa). But, the EGR rates could not be increased because of the substantial increases in the smoke emissions with diesel fuel. When supercharging was employed (boost pressure: 120 kPa), the decrease in the η_e is suppressed as well as the trade-off relation between the NOx and smoke emissions improved, but the smoke emissions with PLiB30 that has the highest oxygen content reached 15% at a 25% EGR rate (red arrow in the bottom panel in **Figure 6A**). In the DDF mode with the supercharging as shown in **Figure 6B**, all the ignition fuels achieved almost smokeless combustion over the tested EGR regions and the η_e maintained relatively high values in these regions. The base line performance in the present study, under diesel operation with diesel fuel at the N/A condition without EGR, was that the brake thermal efficiency was 34.9%, smoke emissions 14.7%, and NOx emissions 4.8 g/kWh (dark blue arrows in **Figure 6A**). The DDF operation with bio-alcohol blended PLME fuels with supercharging with 22–23% EGR conditions showed that although the brake thermal efficiency decreased around 3%, very low NOx emissions of 0.5–0.6 g/kWh and almost smokeless combustion was realized (orange arrows in **Figure 6B**).

Figure 7 shows the relationship between brake thermal efficiency, η_e and degree of constant volume of combustion, η_{glh} in the DDF as a function of the ignition delay with the parameters fuel kind and with and without supercharging. **Figure 7A** shows the case with LME based blends [results in a previous study (Yoshimoto et al., 2019)], and **Figure 7B** shows the PLME based blends (present study). The CNG flow rate was at an 8 L/min (0Â°C, 1 atm), and the blending ratio of bio-alcohol to base fuel was at 3: 7 (mass) in both experiments. Also, both experiments were conducted within a similar EGR range. Specifically, iso-pentanol blended LME experiments were carried out within 0 to 11.0% EGR under N/A conditions, 0 to 22.4% EGR in S/C conditions, while the EGR rates were 0 to 12.6% at N/A and 0 to 25.3% at S/C for the PLME based blends. As shown in **Figures 7A,B**, it is clear that the constant volume of combustion η_{glh} decreases as the ignition delay increases, resulting in a decrease in brake thermal efficiency. As the EGR rate increased, ignition delays with the iso-pentanol blended LME fuels (LiP30, **Figure 7A**) became substantially longer than those of iso-pentanol blended PLMEs (PLiP30, **Figure 7B**) or iso-butanol blended PLMEs (PLiB30, **Figure 7B**). The LiP30 which consists of a low cetane number LME than PLME, its ignition delay increased remarkably at a high EGR rate condition with supercharging. It is considered that this caused a significant decrease in the η_{glh}, resulting in substantial decrease in the brake thermal efficiency. From **Figure 7**, it is also clear that when the ignition delay exceeds 15 °CA, the degree of constant volume of combustion decreases and brake thermal efficiency decreases substantially. Therefore, it can be concluded that using PLME which is a base fuel with a high cetane number the present experiments prevented the deterioration in ignitability due to alcohol blending, resulted in the suppression of very much longer ignition delays, and the relatively higher brake thermal efficiency was obtained.

CONCLUSIONS

A diesel dual fuel engine with compressed natural gas (CNG) introduced from the intake pipe was operated by combining cooled EGR and supercharging with ignition fuels with next generation bio-alcohol blended FAME fuels. The engine used is a small single cylinder direct injection diesel engine equipped with a jerk type injection system. The ignition fuels used here were neat PLME (equal proportions of methyl palmitate and methyl laurate), blended fuel with 70% mass PLME and 30% iso-pentanol (termed PLiP30), and 70% PLME and 30% iso-butanol blend (PLiB30). The CNG supply rates defined on an energy basis were set at two conditions of 0% (diesel operation) and 41–44% (DDF). Two intake charge pressures: 100 kPa (naturally aspirated operation, N/A) and 120 kPa (supercharged operation, S/C) were employed and the EGR rates were varied from 0 to 25%. The influence of the ignition fuel on engine performance, combustion characteristics, and emissions were examined and compared for the two operation modes, DDF and diesel operation, combining supercharging and EGR. The results of the present study may be summarized as follows:

1. Diesel operation at the naturally aspirated condition with EGR increased the smoke emissions, and the EGR rates could not be increased above 13%, even with PLME which has a 13.4% oxygen content. When the supercharging was employed under the ordinary diesel mode, all the injection fuels showed increases in brake thermal efficiency, but increasing EGR rates caused increased smoke emissions.
2. Regardless of ignition fuel kind and with and without supercharging, the DDF improved the trade-off relation between NOx and smoke emissions while at high brake thermal efficiencies could be maintained over the whole of the tested EGR regions.
3. Considering trade-off improvements, the optimum conditions obtained with the tested bio-alcohol blends were as follows: under diesel operation with S/C at 23–25% EGR showed a brake thermal efficiency of 35.1%, smoke densities of 15–16%, and NOx emissions of 0.53–0.60 g/kWh. Similarly, under the DDF with S/C at 22–23% EGR showed a brake thermal efficiency of 33.7–34.0%, smoke densities of 1.2–1.5%, and NOx emissions of 0.53–0.59 g/kWh.
4. Comparing the results obtained with the next generation bio-alcohol blends under DDF with S/C at 22–23% EGR conditions to baseline performance (ordinary diesel mode, diesel fuel, N/A, without EGR), the brake thermal efficiency decreased 2.6–3.4%, while reduction rates in NOx and smoke emissions were 88–89% and 90–92%, respectively.
5. It was found that the cetane number of the base fuel used for alcohol blending has a strong influence on the engine performance in the DDF mode. Using PLME which is a base fuel with a high cetane number prevented the deterioration in ignitability due to alcohol blending, resulting in the relatively higher brake thermal efficiency that was realized.

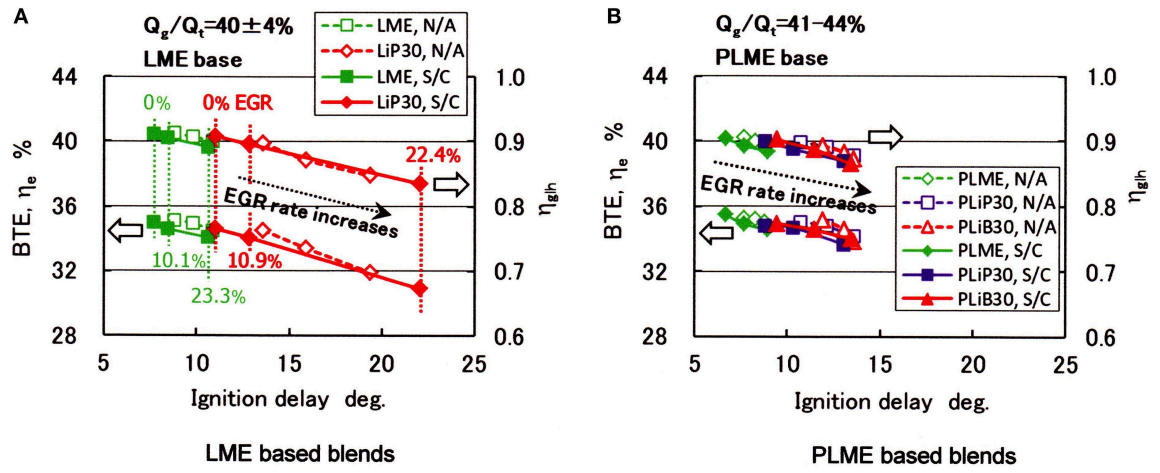

FIGURE 7 | Plots of ignition delay vs. brake thermal efficiency and degree of constant volume of combustion with LME based blends and PLME based blends with DDF (BMEP=0.67 MPa). **(A)** LME based blends and **(B)** PLME based blends.

In this study, diesel dual fuel operation was investigated supplying CNG to the intake pipe with next generation bio-alcohol blended FAME fuels as the ignition fuel. As a result of the combination of EGR and supercharging, it was found that NOx and smoke emissions could be significantly reduced while suppressing the deterioration of the brake thermal efficiency. However, a large amount of HC was discharged in the dual fuel operation in this experiment, and most of this is methane with a high GHG effect. This is a major drawback, and its solution remains as a problem to be solved. To suppress unburned CNG emissions, measures such as CNG direct injection in the cylinder or preventing blow-through of CNG during the valve overlap period will be necessary.

DATA AVAILABILITY STATEMENT

All datasets generated for this study are included in the article/supplementary material.

AUTHOR'S NOTE

To improve the trade-off relation between NOx and smoke emissions, diesel dual fuel operation (DDF) which introduces natural gas from the intake pipe and injects biofuel into the combustion chamber was conducted combining supercharging and cooled EGR. Natural gas is an attractive alternative fuel for engines and the DDF of this type has the advantages that only limited modifications are needed. The research contributes to energy security and improving the NOx and smoke emission trade-off. The study used blended fuels with next generation bio-alcohols and fatty acid methyl esters (FAME) as the ignition fuel. As the next generation bio-alcohols can be produced from non-food based sources like cellulosic biomass, this system realizes a petroleum free fuel. Recently, a number of studies with next generation bio-alcohol blended fuels have been carried out targeting ordinary diesel operation. However, many of these studies have been conducted with n-butanol, iso-butanol, or n-pentanol, and there are few reports with iso-pentanol. Also, there are no reports with the DDF. The present study concluded that there are conditions that may improve the NOx and smoke emissions trade-off about 90% while suppressing the deterioration of the brake thermal efficiency by about 3%.

AUTHOR CONTRIBUTIONS

YY have made a substantial and direct contribution to the work. EK and TO have made an intellectual contribution. All authors contributed to manuscript revision and approved the submitted version.

FUNDING

This study was supported by a grant-in-aid-for scientific research (17K07031) from the JSPS.

ACKNOWLEDGMENTS

The authors wish to thank the students at the Heat Energy Laboratory, Niigata Institute of Technology, for their cooperation.

REFERENCES

Abdelaal, M. M., and Hegab, A. H. (2012). Combustion and emission characteristics of a natural gas-fueled diesel engine with EGR. *Energy Conv. Manage.* 64, 301–312. doi: 10.1016/j.enconman.2012.05.021

Aklouche, F. Z., Loubar, K., Bentebbiche, A., Awad, S., and Tazerout, M. (2017). Experimental investigation of the equivalence ratio influence on combustion, performance and exhaust emissions of a dual fuel diesel engine operating on synthetic biogas fuel. *Energy Conv. Manage.* 152, 291–299. doi: 10.1016/j.enconman.2017.09.050

Aksu, C., Kawahara, N., Tsuboi, K., Kondo, M., and Tomita, E. (2016). Extension of PREMIER combustion operation range using split micro pilot fuel injection in a dual fuel natural gas compression ignition engine: a performance-based and visual investigation. *Fuel* 185, 243–253. doi: 10.1016/j.fuel.2016.07.120

Anil Bhaurao W., Banerjee, S., and Banerjee, R. (2018). Experimental and chemical kinetic study of the impact of n-butanol blending on the gross engine performance of a CRDI engine. *Energy Conv. Manage.* 178, 400–414. doi: 10.1016/j.enconman.2018.10.031

Aroonsrisopon, T., Salad, M., Wirojsakunchai, E., Wannatong, K., Siangsanorh, S., and Akarapanjavit, N. (2009). *Injection Strategies for Operational Improvement of Diesel Dual Fuel Engines Under Low Load Conditions*. SAE Technical Paper. (No. 2009-01-1855). doi: 10.4271/2009-01-1855

Azimov, U., Tomita, E., and Kawahara, N. (2011). *Ignition, Combustion and Exhaust Emission Characteristics of Micro-Pilot Ignited Dual-Fuel Engine Operated Under PREMIER Combustion Mode*. SAE Technical Paper. (No. 2011-01-1764). doi: 10.4271/2011-01-1764

Blasio, G. D., Belgiorno, G., and Beatrice, C. (2017). Effects on performances, emissions and particle size distributions of a dual fuel (methane-diesel) light-duty engine varying the compression ratio. *Appl. Energy* 204, 726–740. doi: 10.1016/j.apenergy.2017.07.103

Bora, B. J., Saha, U. K., Chatterjee, S., and Veer, V. (2014). Effect of compression ratio on performance, combustion and emission characteristics of a dual fuel diesel engine run on raw biogas. *Energy Conv. Manage.* 87, 1000–1009. doi: 10.1016/j.enconman.2014.07.080

Çelebi, K., Uludamar, E., Tosun, E., Yildizhan, S., Aydin, K., and Ozcanli, M. (2017). Experimental and artificial neural network approach of noise and vibration characteristic of an unmodified diesel engine fuelled with conventional diesel, and biodiesel blends with natural gas addition. *Fuel* 197, 159–173. doi: 10.1016/j.fuel.2017.01.113

Fushimi, K., Kinoshita, E., and Yoshimoto, Y. (2013). *Effect of Butanol Isomer on Diesel Combustion Characteristics on Butanol/Gas Oil Blend*. SAE Technical Paper. (No. 2013-32-9097). doi: 10.4271/2013-32-9097

Graboski, M. S., McCormick, R. L., Alleman, T. L., and Herring, A. M. (2003). *The Effect of Biodiesel Composition on Engine Emissions From a DDC Series 60 Diesel Engine*. NREL/SR-510-31461. National Renewable Energy Laboratory, 1–81. doi: 10.2172/15003583

Guerry, E. S., Raihan, M. S., Srinivasan, K. K., Krishnan, S. R., and Sohail, A. (2016). Injection timing effects on partially premixed diesel–methane dual fuel low temperature combustion. *Appl. Energy* 162, 99–113. doi: 10.1016/j.apenergy.2015.10.085

Han, X., Yang, Z., Wang, M., Tjong, J., and Zheng, M. (2016). Clean combustion of n-butanol as a next generation biofuel for diesel engines. *Appl. Energy* 198, 347–359. doi: 10.1016/j.apenergy.2016.12.059

Ileri, E. (2016). Experimental study of 2-ethylhexyl nitrate effects on engine performance and exhaust emissions of a diesel engine fueled with n-butanol or 1-pentanol diesel–sunflower oil blends 2016. *Energy Conv. Manage.* 118, 320–330. doi: 10.1016/j.enconman.2016.04.015

Imdadul, H. K., Rashed, M. M., Shahin, M. M., Masjuki, H. H., Kalam, M. A., Kamruzzaman, M., et al. (2017). Quality improvement of biodiesel blends using different promising fuel additives to reduce fuel consumption and NO emission from CI engine. *Energy Conv. Manage.* 138, 327–337. doi: 10.1016/j.enconman.2017.01.077

Iorio, S. D., Magno, A., Mancaruso, E., and Vaglieco, B. M. (2017). Analysis of the effects of diesel/methane dual fuel combustion on nitrogen oxides and particle formation through optical investigation in a real engine. *Fuel Proces. Technol.* 159, 200–210. doi: 10.1016/j.fuproc.2017.01.009

Killol, A., Reddy, N., Paruvada, S., and Murugan, S. (2019). Experimental studies of a diesel engine run on biodiesel n-butanol blends. *Renew. Energy.* 135, 687–700. doi: 10.1016/j.renene.2018.12.011

Kinoshita, E., Ueda, Y., and Yoshimoto, Y. (2009). Combustion characteristics of a dual fuel diesel engine with coconut oil methyl ester as an ignition fuel. *Trans. JSME, Series B* 75,1706–1711. doi: 10.1299/kikaib.75.756_1706

Kumar, B. R., and Saravanan, S. (2015). Effect of exhaust gas recirculation (EGR) on performance and emissions of a constant speed DI diesel engine fueled with pentanol/diesel blends. *Fuel* 160, 217–226. doi: 10.1016/j.fuel.2015.07.089

Kumar, B. R., and Saravanan, S. (2016). Effects of iso-butanol/diesel and n-pentanol/diesel blends on performance and emissions of a DI diesel engine under premixed LTC (low temperature combustion) mode. *Fuel* 170, 49–59. doi: 10.1016/j.fuel.2015.12.029

Li, W., Liu, Z., Wang, Z., and Dou, H. (2015). Experimental and theoretical analysis of effects of atomic, diatomic and polyatomic inert gases in air and EGR on mixture properties, combustion, thermal efficiency and NOx emissions of a pilot-ignited NG engine. *Energy Conv. Manage.* 105, 1082–1095. doi: 10.1016/j.enconman.2015.08.052

Mizushima, N., Ito, S., Kusaka, J., and Daisho, Y. (2003). *Improvement of Combustion in a Dual Fuel Natural Gas Engine With Half the Number of Cylinders*. SAE Technical Paper. (No. 2003-01-1938). doi: 10.4271/2003-01-1938

Ogawa, H., Miyamoto, N., Li, C., Nakazawa, S., and Akao, K. (2003). Smokeless and low NOx combustion in a dual-fuel diesel engine with induced natural gas as the main fuel. *Int. J. Eng. Res.* 4, 1–9. doi: 10.1177/1468087403004 00101

Ogawa, H., Shibata, G., Goto, J., and Jiang, L. (2016). *Performance Improvements in a Natural Gas Dual Fuel Compression Ignition Engine With 250 MPa Pilot Injection of Diesel Fuel as an Ignition Source*. SAE Technical Paper. (No. 2016-01-2306). doi: 10.4271/2016-01-2306

Ogawa, H., Zhao, P., Kato, T., and Shibata, G. (2015). *Improvement of Combustion and Emissions in a Dual Fuel Compression Ignition Engine With Natural Gas as the Main Fuel*. SAE Technical Paper. (No. 2015-01-0863). doi: 10.4271/2015-01-0863

Pan, M., Huang, R., Liao, J., Jia, C., Zhou, X., Huang, H., et al. (2019). Experimental study of the spray, combustion, and emission performance of a diesel engine with high n-pentanol blending ratios. *Energy Conv. Manage.* 194, 1–10. doi: 10.1016/j.enconman.2019.04.054

Papagiannakis, R. G., Hountalas, D. T., Rakopoulos, C. D., and Rakopoulos, D. C. (2008). *Combustion and Performance Characteristics of a DI Diesel Engine Operating From Low to High Natural Gas Supplement Ratios at Various Operating Conditions*. SAE Technical Paper. (No. 2008-01-1392). doi: 10.4271/2008-01-1392

Park, J. S., and Terao, H. (2003). Performance characteristics of a biogas cogeneration system using supercharging together with EGR. *J. JSAM* 65, 93–100. doi: 10.11357/jsam1937.65.6_93

Paul, A., Panua, R. S., Debroy, D., and Bose, P. K. (2014). Effect of compressed natural gas dual fuel operation with diesel and Pongamia pinnata methyl ester (PPME) as pilot fuels on performance and emission characteristics of a CI (compression ignition) engine. *Energy* 68, 495–509. doi: 10.1016/j.energy.2014.03.026

Peralta-Yahya, P. P., and Keasling, J. D. (2010). Advanced biofuel production in microbes. *Biotechnol. J.* 5, 147–162. doi: 10.1002/biot.200900220

Roy, M. M., Tomita, E., Kawahara, N., Harada, Y., and Sakane, A. (2009). *Effect of Fuel Injection Parameters on Engine Performance and Emissions of a Supercharged Producer Gas-Diesel Dual Fuel Engine*. SAE Technical Paper. (No. 2009-01-184). doi: 10.4271/2009-01-1848

Saravanan, S., Kumar, B. R., Varadharajan, A., Balaji Sethuramasamyraja, D. R., and Narayana rao, G. L. (2017). Optimization of DI diesel engine parameters fueled with iso-butanol/diesel blends – response surface methodology approach. *Fuel* 203, 658–670. doi: 10.1016/j.fuel.2017.04.083

Selim, M. Y. E. (2003). *A Study of Some Combustion Characteristics of Dual Fuel Engine Using EGR*. SAE Technical Paper. (No. 2003-01-0766). doi: 10.4271/2003-01-0766

Srinivasan, K. K., Krishnan, S. R., Qi, Y., Midkiff, K. C., and Yang, H. (2007). Analysis of diesel pilot-ignited natural gas low-temperature combustion with hot exhaust gas recirculation. *Combust. Sci. Technol.* 179, 1737–1776. doi: 10.1080/00102200701259882

Taniguchi, S., Masubuchi, M., Kitano, K., and Mogi, K. (2012). *Feasibility Study of Exhaust Emissions in a Natural Gas Diesel Dual Fuel (DDF) Engine*. SAE Technical Paper. (No. 2012-01-1649). doi: 10.4271/2012-01-1649

Tat, M. E., and Van Gerpen, J. H. (2003). Measurement of biodiesel speed of sound and its impact on injection timing. *NREL/SR* 510–31462. doi: 10.2172/150 03584

Tomita, E., Harada, Y., Kawahara, N., and Sakane, A. (2009). *Effect of EGR on Combustion and Exhaust Emissions in Supercharged Dual-Fuel Natural Gas Engine Ignited With Diesel Fuel*. SAE Technical Paper. (No. 2009-01-1832). doi: 10.4271/2009-01-1832

Verma, S., Das, L. M., Bhatti, S. S., and Kaushik, S. C. (2017). A comparative exergetic performance and emission analysis of pilot diesel dual-fuel engine with biogas, CNG and hydrogen as main fuels. *Energy Conv. Manage.* 151, 764–777. doi: 10.1016/j.enconman.2017.09.035

Wannatong, K., Akarapanyavit, N., Siengsanorh, S., Aroonsrisopon, T., and Chanchaona, S. (2009). *New Diesel Dual Fuel Concepts: Part Load Improvement*. SAE Technical Paper. (No. 2009-01-1797). doi: 10.4271/2009-01-1797

Yang, B., Xi, C., Wei, X., Zeng, K., and Lai, M. C. (2015). Parametric investigation of natural gas port injection and diesel pilot injection on the combustion and emissions of a turbocharged common rail dual-fuel engine at low load. *Appl. Energy* 143, 130–137. doi: 10.1016/j.apenergy.2015.01.037

Yoshimoto, Y. (2010). *Combustion Characteristics of a Dual Fuel Diesel Engine With Natural Gas (Study With Fatty Acid Methyl Esters Used as Ignition Fuels)*. SAE Technical Paper. (No. 2010-32-0050). doi: 10.4271/2010-32-0050

Yoshimoto, Y., Enkhjargal, T., Kinoshita, E., and Otaka, T. (2018b). Combustion improvements by C_4/C_5 bio-alcohol isomer blended fuels combined with supercharging and EGR in a diesel engine. *Int. J. Mech. Indus. Aerospace Sci.* 11, 1–9. doi: 10.5281/zenodo.1474930

Yoshimoto, Y., Kaneko, K., and Kinoshita, E. (2010). Combustion characteristics of a dual fuel diesel engine with CNG as the main fuel (Study for methyl oleate used as an ignition fuel). *Trans. JSME Series B* 76, 916–923. doi: 10.1299/kikaib.76.765_916

Yoshimoto, Y., and Kinoshita, E. (2011). Combustion characteristics of a dual fuel diesel engine with natural gas (influence of cetane number of ignition fuel). *ASME Power* 2011:55362. doi: 10.1115/POWER2011-55362

Yoshimoto, Y., and Kinoshita, E. (2013). *Influence of Intake Air Dilution With N_2 or CO_2 Gases on the Combustion Characteristics of a Dual Fuel Diesel Engine With Natural Gas*. SAE Technical Paper. (No. 2013-01-2691). doi: 10.4271/2013-01-2691

Yoshimoto, Y., Kinoshita, E., Luge, S., and Ohmura, T. (2012). Combustion characteristics of a dual fuel diesel engine with natural gas (lower limit of cetane number for ignition of the fuel). *SAE Int. J. Fuels Lubr.* 5, 1165–1173. doi: 10.4271/2012-01-1690

Yoshimoto, Y., Kinoshita, E., and Otaka, T. (2017). "Influence of boost pressure on the combustion characteristics of a dual fuel diesel engine ignited by biofuels with natural gas," in: *The Ninth International Conference on Modeling and Diagnostics for Advanced Engine Systems (COMODIA 2017)* (Okayama: Japan Society of Mechanical Engineers). doi: 10.1299/jmsesdm.2017.9.C204

Yoshimoto, Y., Kinoshita, E., and Otaka, T. (2018a). Effects of combining EGR and supercharging on the combustion characteristics of a diesel dual fuel engine with induced natural gas, *Trans. JSME* 84, 1–15. doi: 10.1299/transjsme.18-00219

Yoshimoto, Y., Kinoshita, E., and Otaka, T. (2019). *Influence of the Kind of Fuel Kind in the Ignition of Diesel Dual Fuel Operation With Introduced Natural Gas Combining EGR and Supercharging*. SAE Technical Paper. (No. 2019-32-0581)

Yoshimoto, Y., Kinoshita, E., Shanbu, L., and Ohmura, T. (2013). Influence of 1-butanol addition on diesel combustion with palm oil methyl ester/gas oil blends. *Energy* 61, 44–51. doi: 10.1016/j.energy.2012.11.039

Yoshimoto, Y., Yamada, M., Kinoshita, E., and Fushimi, K. (2016). Influence of supercharging on the combustion characteristics of a dual fuel diesel engine with induced natural gas. *Trans. JSME* 82, 1–11. doi: 10.1299/transjsme.15-00542

Zheng, J., Tashiro, Y., Wang, Q., and Sonomoto, K. (2015). Recent advances to improve fermentative butanol production: genetic engineering and fermentation technology. *J. Biosci. Bioeng.* 119, 1-9. doi: 10.1016/j.jbiosc.2014.05.023

Conflict of Interest: The authors declare that the research was conducted in the absence of any commercial or financial relationships that could be construed as a potential conflict of interest.

NOMENCLATURE

DDF: diesel dual fuel operation
DDFD: diesel dual fuel operation with diesel fuel ignition
CNG: compressed natural gas
EGR: exhaust gas recirculation
N/A: naturally aspirated operation
S/C: supercharged operation
FAME: fatty acid methyl ester
PME: methyl palmitate
LME: methyl laurate
PLME: equal proportion of PME and LME
PLiP30: 70% PLME and 30% iso-pentanol blend (mass ratio)
PLiB30: 70% PLME and 30% iso-butanol blend (mass ratio)
LiP30: 70% LME and 30% iso-pentanol blend (mass ratio)
DPF: diesel particulate filter
CLD: chemiluminescence detector
FID: flame ionization detector
NDIR: non-dispersed infrared detector
Q_g/Q_t: CNG supply rate
Q_g: heat energy of supplied CNG
Q_t: total heat energy available in cylinder
θ: crank angle
Q: heat release in cylinder
Q_E: heating value of fuel
Q_C: cooling heat to cylinder wall
P: in-cyinder gas pressure
V: in-cyinder gas volume
κ: ratio of specific heat
ε: compression ratio
ε_θ: compression ratio at crank angle
ϕ_g: equivalence ratio of CNG-air pre-mixture
ϕ_t: equivalence ratio of total in-cylinder charge
BMEP: brake mean effective pressure
BTE, η_e: brake thermal efficiency
N_e: brake power
$\dot{m}$: mass flow rate
LHV: lower heating value
η_u: combustion efficiency
η_{glh}: degree of constant volume of combustion
$(dQ/d\theta)_{max}$: maximum heat release rate

frontiers in Mechanical Engineering

ORIGINAL RESEARCH
published: 21 October 2020
doi: 10.3389/fmech.2020.543808

Experimental and Simulation Analysis of Natural Gas-Diesel Combustion in Dual-Fuel Engines

Pavlos Dimitriou[1], *Taku Tsujimura*[1]*, *Hirokazu Kojima*[1], *Kenji Aoyagi*[2], *Naoki Kurimoto*[2] *and Yoshiaki Nishijima*[3]

[1]National Institute of Advanced Industrial Science and Technology (AIST), Renewable Energy Research Center, Koriyama, Japan, [2]DENSO CORPORATION, Kariya, Japan, [3]Aichi Institute of Technology, Toyota, Japan

The recent strict emission regulations and the necessity to reduce the global CO_2 levels have promoted research studies in alternative fuel combustion technologies. Dual-fuel technology is a fascinating approach as it can combine the benefits of two fuels to achieve high thermal efficiency and lower harmful emissions. Natural gas burns cleaner than other fossil fuels, and its recent low price makes it an attractive fuel as a near-term solution. The utilization of natural gas with diesel in a compression ignition engine can result in efficiency improvement and lower CO_2 emissions. However, at low engine loads, natural gas-diesel operation suffers from low combustion efficiency and high unburned hydrocarbon and carbon monoxide emissions. The present paper collates the work of experimental and simulation studies on natural gas-diesel dual-fuel operation over three different engine set-ups. Two single-cylinder, with and without optical access, and a multi-cylinder engine were used to analyze the effects of different diesel injection and air-path strategies on the combustion performance, with a focus on the low-load operation zone. The results show that the injection timing, as well as intake charge dilution, can severely promote clean combustion at the low-load zone. An advanced diesel injection can enhance the diesel-natural gas homogeneity within the cylinder and improve the combustion efficiency of the engine. On the other hand, high levels of exhaust gas recirculation are mandatory to suppress the NOx formation and further enhance the engine's brake thermal efficiency.

Keywords: natural gas, diesel, dual-fuel, engine combustion, simulation

OPEN ACCESS

Edited by:
Masahiro Shioji,
Kyoto University, Japan

Reviewed by:
Amin Paykani,
University of Hertfordshire, United Kingdom
Khanh Duc Cung,
Southwest Research Institute (SwRI), United States

***Correspondence:**
Taku Tsujimura
Tsujimura-taku@aist.go.jp

Specialty section:
This article was submitted to Engine and Automotive Engineering, a section of the journal Frontiers in Mechanical Engineering

Received: *18 March 2020*
Accepted: *22 September 2020*
Published: *21 October 2020*

Citation:
Dimitriou P, Tsujimura T, Kojima H, Aoyagi K, Kurimoto N and Nishijima Y (2020) Experimental and Simulation Analysis of Natural Gas-Diesel Combustion in Dual-Fuel Engines. Front. Mech. Eng. 6:543808. doi: 10.3389/fmech.2020.543808

INTRODUCTION

The compression ignition (CI) engine, also known as the diesel engine, has been a vital workhorse of the global energy industry for more than a hundred years. However, with the world currently facing an escalating environmental crisis and with government policies designed to promote clean energy solutions, the role of the CI engine in the coming sustainable energy economy is ambiguous.

The aspirational target of Paris agreement to limit greenhouse gas emissions by at least 40% by 2030 (UNFCC, 2015) will necessitate CI engines operating with low-polluting fuels. The dual-fuel operation of a CI engine with renewable eco-friendly fuels such as hydrogen (Dimitriou and Tsujimura, 2017) and ammonia (Dimitriou and Javaid, 2020) can contribute to significant, often higher than the target, CO_2 emission reductions. However, today around 95% of the world's hydrogen production is generated from non-renewable sources such as natural gas and coal, and only 5% is generated by water electrolysis (IRENA, 2019).

As a shorter-term solution, the use of compressed natural gas (CNG) as the primary fuel of a CI engine has received significant interest since it can produce lower specific CO_2 emissions than other petroleum-derived fuels. The recent low natural gas prices combined with the simple modifications required for the existing CI engines to operate on gas make it an attractive solution. However, the high autoignition limit of the gas prevents its combustion by compression (Sahoo et al., 2009), unless it is co-combusted with a lower autoignition fuel such as diesel.

In this combustion mode, the natural gas is supplied to the intake manifold or close to the intake ports leading to a homogeneous in-cylinder charge. The uniform natural gas–air mixture provides premixed combustion characteristics, which is triggered by the diffusion combustion of diesel fuel (Wei and Geng, 2016). Natural gas-diesel dual-fuel engines exhibit higher thermal efficiency than spark-ignition CNG engines over the entire engine load range (Kojima et al., 2016). Compared to the conventional diesel fuel operation, natural gas dual-fuel engines can yield significant CO_2 benefits as methane, which is CNG's primary component, has one of the lowest carbon contents among hydrocarbons. The CO_2 reductions can be enlarged at higher loads due to the engine's ability to run at higher natural gas energy share ratios (Lounici et al., 2014).

The effect of the natural gas on the NOx formation of the dual-fuel engine is highly dependent on the operating conditions and the diesel amount. At lower engine loads, the NOx formation of a dual-duel engine can be lower than that of a conventional engine. The reduction could be due to a lower in-cylinder temperature as a result of the higher specific heat capacity of natural gas than that of the air, and a longer ignition delay, which often leads to lower combustion efficiencies (Wei and Geng, 2016). At higher engine loads, the NOx deterioration is often a result of an intense heat release in the premixed combustion zone, followed by a higher pressure rise rate (Selim, 2001) and in-cylinder temperatures.

Natural gas can also provide significant reductions in soot formation due to it free of aromatics and sulfur composition (Maricq et al., 2002), and the fact that it promotes premixed combustion with lower diffusion flames (Liu et al., 2013). On the other hand, significant carbon monoxide (CO) and hydrocarbons (HC) emission penalties, due to a high amount of unburned methane, have been reported in the literature (Shenghua et al., 2003; Cheenkachorn et al., 2013; Liu et al., 2013).

Furthermore, the main challenge of the dual-fuel engine is the poor performance at low-load conditions. Previous studies (Karim, 2003; Paul et al., 2013) have shown that at low equivalence ratios, high carbon monoxide, and unburned hydrocarbon emissions are formed under high CNG-to-diesel energy share ratios. This increase in emissions results from a deteriorated combustion efficiency due to the incapacity of diesel fuel to ignite the lean natural gas-air mixture (Tsujimura et al., 2012), inducing bad and slow combustion (Lounici et al., 2014). Papagiannakis et al. (2010) reported a decrease of up to 50% on the brake thermal efficiency (BTE) of a dual-fuel engine compared to the conventional diesel operation. Abdelaal and Hegab (2012) could only achieve higher BTE for the dual-fuel engine at high load conditions with the maximum increase being in the level of 3% at 95% of the engine's full load. The presence of a higher diesel-to-CNG ratio could resolve this issue, but it eliminates the benefits of using CNG, such as increases the CO_2 emissions (Kojima et al., 2016).

Several studies have been performed in the past years to assess the optimum solutions to overcome the low combustion efficiency in the low-load zone. Liu et al. (2013) evaluated the effects of the pilot diesel quantity on the formation of unburned hydrocarbons. The authors observed a strong connection between the diesel amount and the level of HC with a higher diesel quantity resulting in lower HC levels. Nonetheless, their results showed that around 90% of the HC emission was composed of unburned methane. Yang et al. (2015) observed an improved combustion performance, such as shorter ignition delay and combustion duration, and higher BTE when the diesel pilot injection pressure raised from 46 to 72 MPa. However, despite the BTE increase, the COand total hydrocarbon (THC) emissions were increased in the high-pressure case. According to the authors, this was due to spray impingement on the piston and cylinder wall caused by the elevated injection pressure. Srinivasan et al. (2006) improved the combustion efficiency of the dual-fuel engine by advancing the start of diesel injection at about 60°CA before top dead center and increasing the intake gas temperature. Kusaka et al. (1998) highlighted that at low-load operation, the NO formation due to the natural gas combustion is low. The authors applied exhaust gas recirculation (EGR) and intake pre-heating to reduce diesel NOx and THC simultaneously while the thermal efficiency was improved.

The presents paper reports an overall approach to analyze the operation of the natural gas-diesel dual-fuel engine under different operating conditions and engine layouts. The study was conducted under different injection (i.e., pattern, timing) and airpath (i.e., EGR, boosting) strategies applied to assess the performance of the dual-fuel engine. The focus of this study is on the low-load region which is an area that suffers from low combustion efficiency. The experimental analysis presented in this paper is performed using three different engine set-ups, while the investigation is supported by computational fluid dynamics (CFD) simulations.

EXPERIMENTAL APPARATUS

In this paper, advanced experimental studies were performed under three engine set-ups presented in **Table 1**. Different engine layouts were used to gain a deeper understanding of the dual-fuel engine operation in single- and multi-cylinder layouts and obtaining visual access to the combustion process.

Engines set-up #1 (**Figure 1A**) and set-up #2 (**Figure 1B**) exhibit the same cylinder geometry characteristics with the later one featuring an optically accessible piston. As the optical engine could be operated only under cold-start conditions, a higher cetane pilot fuel, No. 0 Solvent M, was used to replace the lower cetane diesel. The third set-up (**Figure 1C**) is a multi-cylinder engine that was used to assess the effects of different air-path strategies on the combustion and emissions behavior of the dual-fuel engine. The details about the equipment used in the three engine set-ups are analytically illustrated in **Figure 1**. All the

TABLE 1 | Specifications of the three engine set-ups.

Test facility	Set-up #1	Set-up #2	Set-up #3
Engine type	4-Stroke single-cylinder diesel engine	4-Stroke single-cylinder diesel engine	4-Stroke 4-cylinder diesel engine
Bore × stroke (mm)	92 × 96	92 × 96	96 × 103
Displacement (cm^3)	638	638	2,981
Compression ratio	15:1	15:1	15:1
Combustion chamber	Dish (cavity φ: 56 mm)	Optical	Toroidal
Main fuel	CNG (port injection)	CNG (port injection)	CNG (port injection)
Pilot fuel	Diesel, CN: 56 (direct injection)	No. 0 Solvent M, CN: 89 (direct injection)	Diesel, CN: 56 (direct injection)
Injection system	Common rail @50 MPa	Common rail @50 MPa	Common rail @50 MPa
Nozzle type (inj. angle)	φ: 0.085 mm × 12 holes (θ: 130°)	φ: 0.085 mm × 12 holes (θ: 130°)	φ: 0.09 mm × 10 holes (θ: 155°)
Coolant temperature	80 ± 2	95 ± 2	80 ± 2

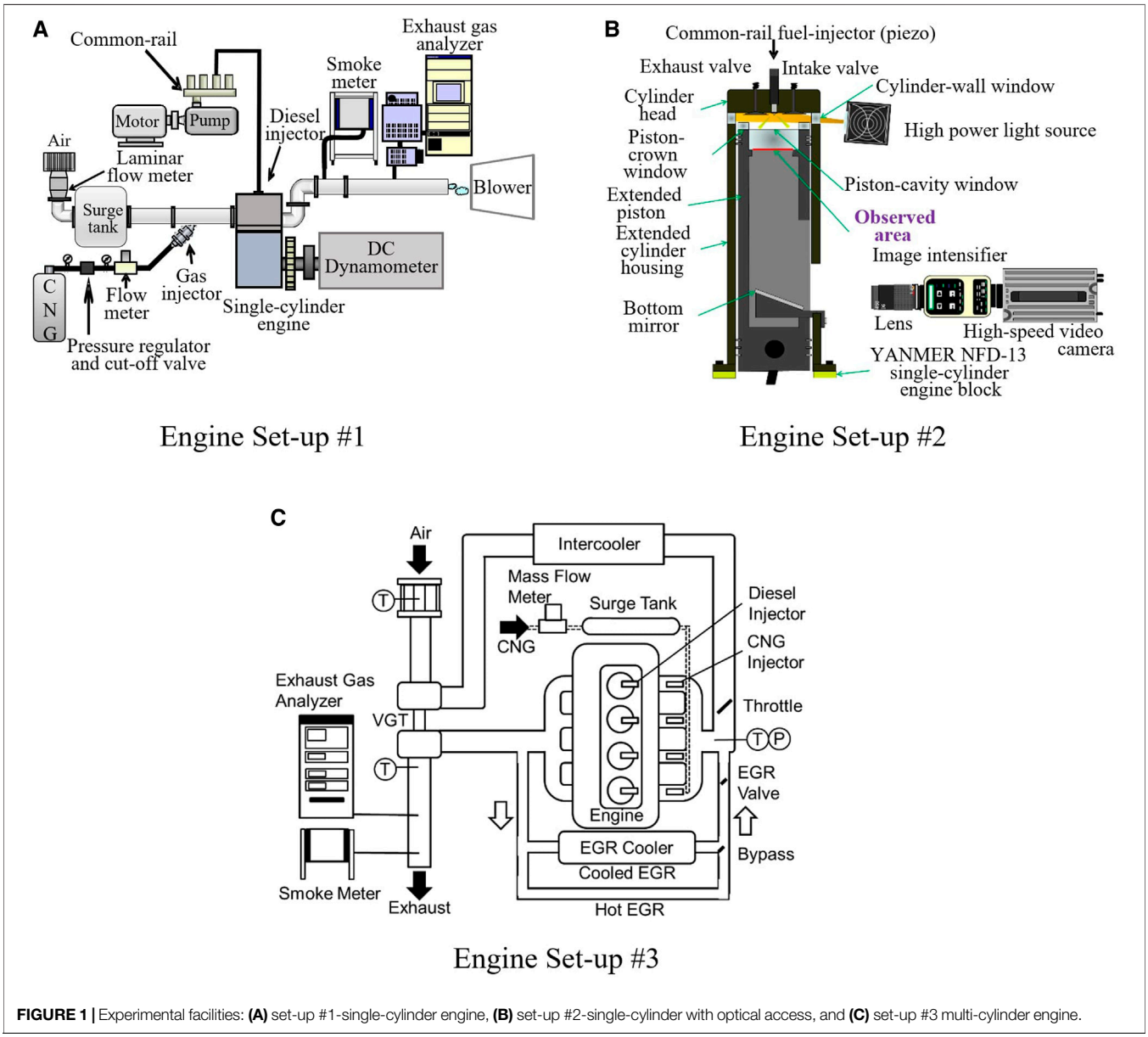

FIGURE 1 | Experimental facilities: **(A)** set-up #1-single-cylinder engine, **(B)** set-up #2-single-cylinder with optical access, and **(C)** set-up #3 multi-cylinder engine.

engine operating conditions tested in the three engine set-ups, as well as the main properties of the natural gas and liquid fuels, can be found in and 3, respectively.

For the engine set-up #1 and set-up #2 with a swept volume of 638 cm^3, a natural gas injector (Japan 13A grade) was placed at the intake port of the engine. The compressed gas was injected

TABLE 2 | Engines' operating conditions.

Test facility	Set-up #1	Set-up #2	Set-up #3
Engine speed (rpm)	1,200	1,200	1,200
BMEP/(IMEP) (MPa)	(0.05–1.1)	0.62/0.60	0.3
CNG air excess ratio	2.67	3	3.85
Diesel injection pattern	Single	Early single / split (double)	Single
Diesel injection timing (°CA ATDC)	−3, −13, −33, −53, −63	−60 / −40+TDC	−22.5 to −2.5 (steps of 2.5)
Diesel amount (mm^3/st)	2, 4, 10	10 / 5 + 5	5.7
Boost pressure (kPa)	100	100	100/120
EGR rate (%)	–	–	0, 10, 20, 30, 50

TABLE 3 | Fuel properties.

Fuel type	CNG (13A)	Diesel JIS (No. 2)	No. 0 Solvent M
Density (g/cm^3)	0.878	≈0.832	0.761
LHV[a] (MJ/kg)	52.47	43.12	43.8
CN[b]	–	56	89.4
Sulfur mass (ppm)	–	<50	<1
CNG composition	CH_4: 89.6%, C_2H_6: 5.62%, C_3H_8: 3.43%, C_4H_{10}: 1.35%		

[a]*Lower heating value.*
[b]*Cetane number.*

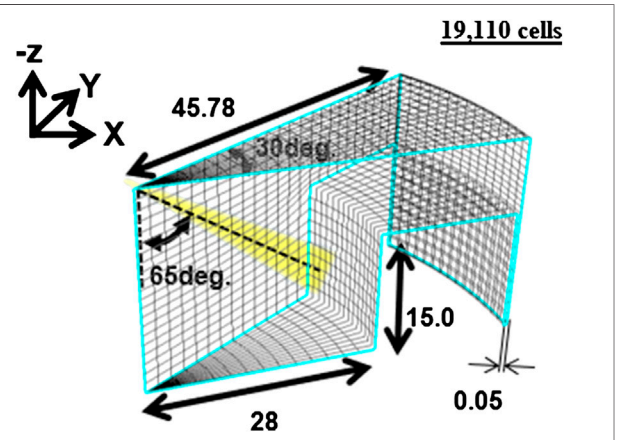

FIGURE 2 | Computational grid (30° sector mesh).

into the cylinder at 0.8 MPa during the intake valve opening time. A 12-hole piezo-type diesel injector with a 0.085 mm-diameter nozzle was mounted on the cylinder head. The diesel injection pressure was set at 50 MPa for all experiments by an in-house common-rail system. The exhaust gas emission analysis was performed using the HORIBA, MEXA-7000DEGR analyzer, and the AVL 415S smoke meter. The visual access on the engine set-up #2 was acquired by coupling a high-speed camera (FASTCAM APX RS) to an image intensifier (UVi–NAC Image Technology), as presented in **Figure 1B**. For the multi-cylinder engine, the CNG was supplied from a surge tank connected to the intake manifold. The gas injection period was adjusted to achieve a balanced gas flow among the cylinders, **Figure 1C**.

Although measurements of the exhaust smoke were taken for all three engine set-ups, it will not be reported in this paper. Since the scope of the present study is to focus on the low-load operation zone with a small diesel injection amount, the smoke levels for all cases presented were at a sufficiently low level of less than 0.10 FSN [Filter Smoke Number defined according to ISO 10054 (ISO 10054, 1998)].

COMPUTATIONAL FLUID DYNAMICS SIMULATION

Computational simulation analysis was used to obtain a better understanding of the in-cylinder combustion phenomena. For this analysis, the FORTÉ simulation package (Liang et al., 2010) linked to a chemical reaction model was used for the cylinder with a computational grid shown in **Figure 2**.

FORTÉ was developed from techniques used in KIVA-3V code (Amsden, 1997), and it has similar sub-models for atomization, vaporization, and interactions associated with turbulence. In this study, the Kelvin-Helmholtz Rayleigh-Taylor (KH-RT) model (Reitz and Beale, 1999) was applied to obtain an accurate prediction of the spray penetration. The KH-RT model is sensitive to the gas-drop relative velocity and mesh size. Moreover, the gas-jet model (Abani and Reitz, 2007) was also applied, aiming at mesh- and time step-independent simulation results (Wang et al., 2010). The authors employed the turbulence interaction model proposed by Kong and Reitz (2002) to simulate the turbulence effects on combustion kinetics. The model considers that the combustion chemistry should be partly controlled by the breakup of turbulent eddies due to the imperfect mixing of fuel and oxidizer or combustion products. The local chemical time scale and turbulent scalar mixing time scale t_{mix} are defined to take their interaction into consideration. Since, computational cell is not small enough to reproduce actual scales for turbulence and chemistry, the effect of turbulence of mixing on production rate of species needs to be considered. Therefore, the model requires a constant called the mixing time coefficient, C_{tki}, to adjust the influence of turbulence (ANSYS, Inc., 2019).

For the dual-fuel study, a parametric analysis on the effect of the C_{tki} to the ability of the model to represent the experimental combustion data was performed. **Figure 3** shows the results of the simulation model operated with C_{tki} ranging from 0 to 1 for an early fuel injection of −60°CA after top dead center (ATDC). As it can be seen in the figure, the C_{tki} level has a significant effect on the hot ignition close to the top dead center (TDC) but does not significantly affect the low-temperature reaction zone at around −20°CA ATDC. For this study, it was found that a C_{tki} value of 1 provides the best match between the simulated and experimental results.

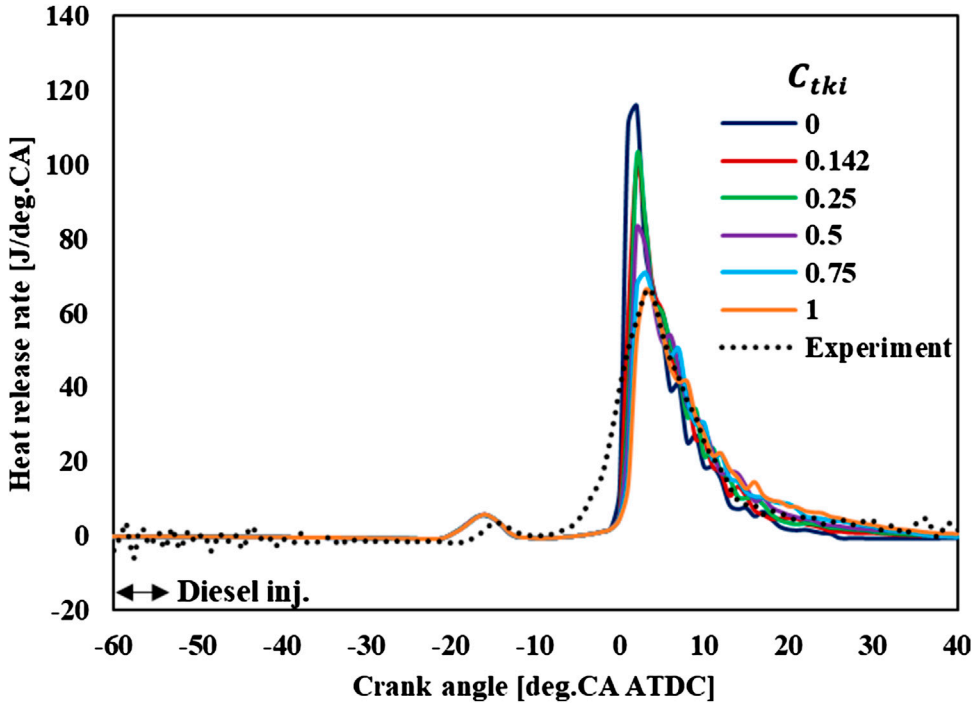

FIGURE 3 | Parametric study on the effect of C_{tki} parameter on the heat release prediction capacity of the model.

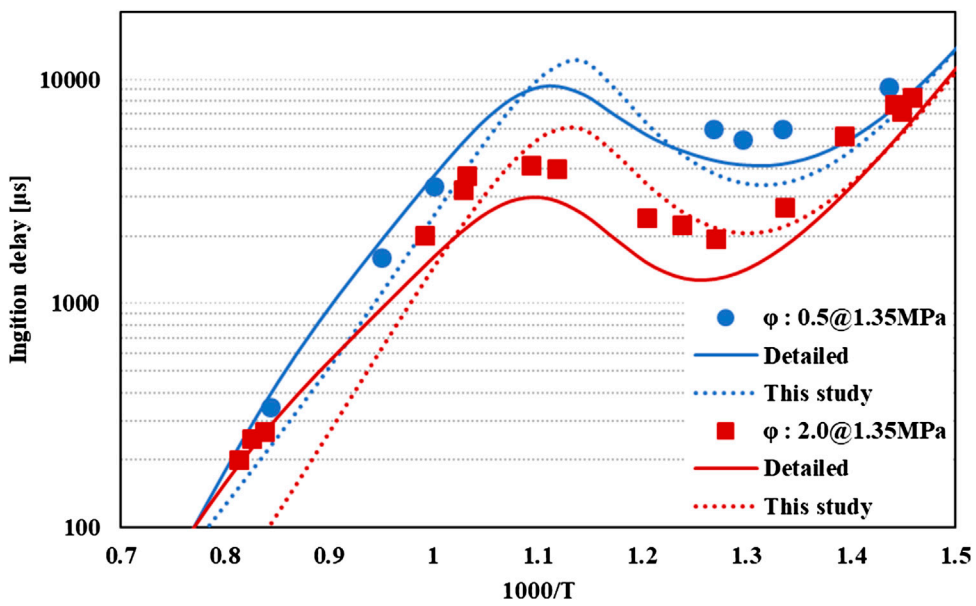

FIGURE 4 | Comparison of the ignition delay of n-heptane/air mixture in a shock-tube environment calculated by the reduced model of this study again the detailed model (Mehl and Curran, 2009) and experimental results (Ciezki and Adomeit, 1993).

The diesel physical properties were represented using an n-tetradecane model, while natural gas was represented by methane, which consists of almost 90% of its volume. The authors developed a new n-heptane/methane reduced model based on previous works (Patel et al., 2004; Mehl and Curran, 2009; Tsurushima, 2009) by adding reactions associated with species such as methane, methyl radical, acetylene and NOx formation. Details about the newly developed model with 47

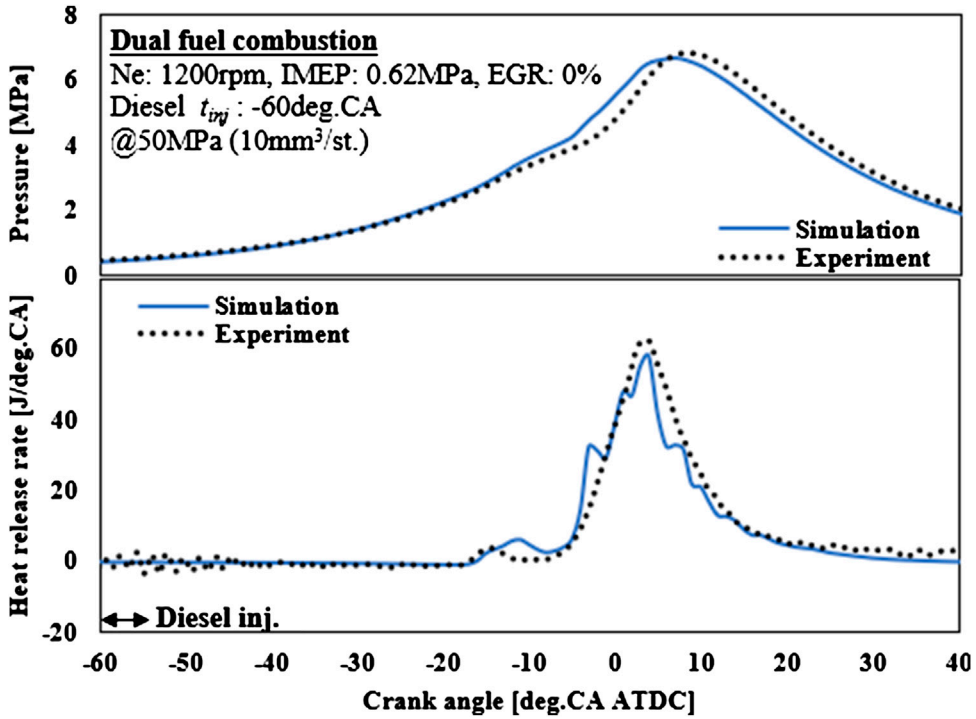

FIGURE 5 | Simulated in-cylinder pressure and heat release rate against experimental results for early diesel injection.

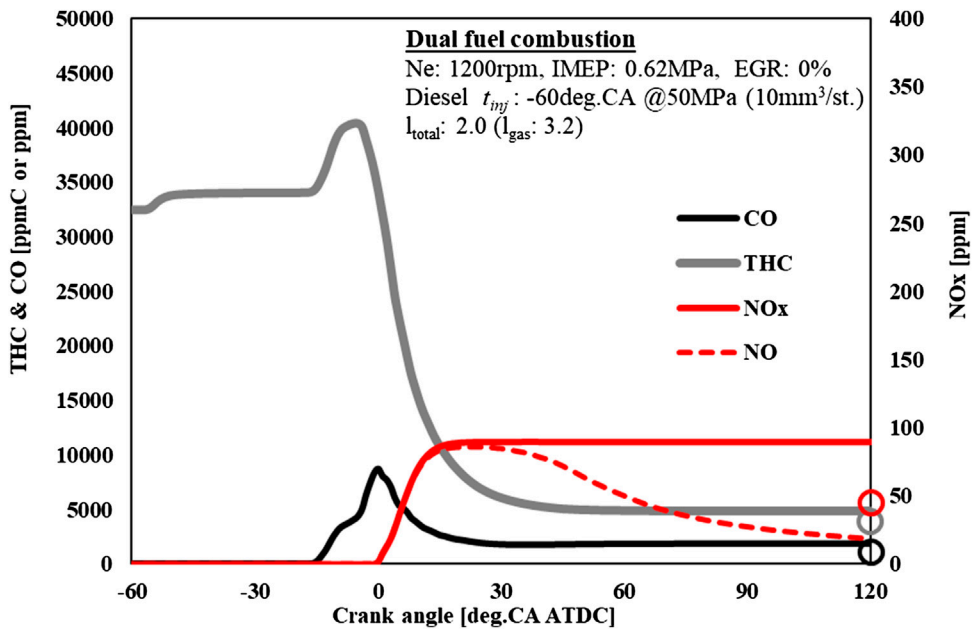

FIGURE 6 | Simulated emissions prediction (CO, THC, NOx, and NO) against experimental results (circles) for early diesel injection.

species and 87 reactions can found in (Tsujimura et al., 2012). The performance of the reduced model was compared to the detailed model by Mehl and Curran (2009) of 1,391 species and 5,935 reactions and experimental data obtained from Ciezki and Adomeit (1993). As presented in **Figure 4**, both models show similar characteristics with the reduced model slightly underpredicting

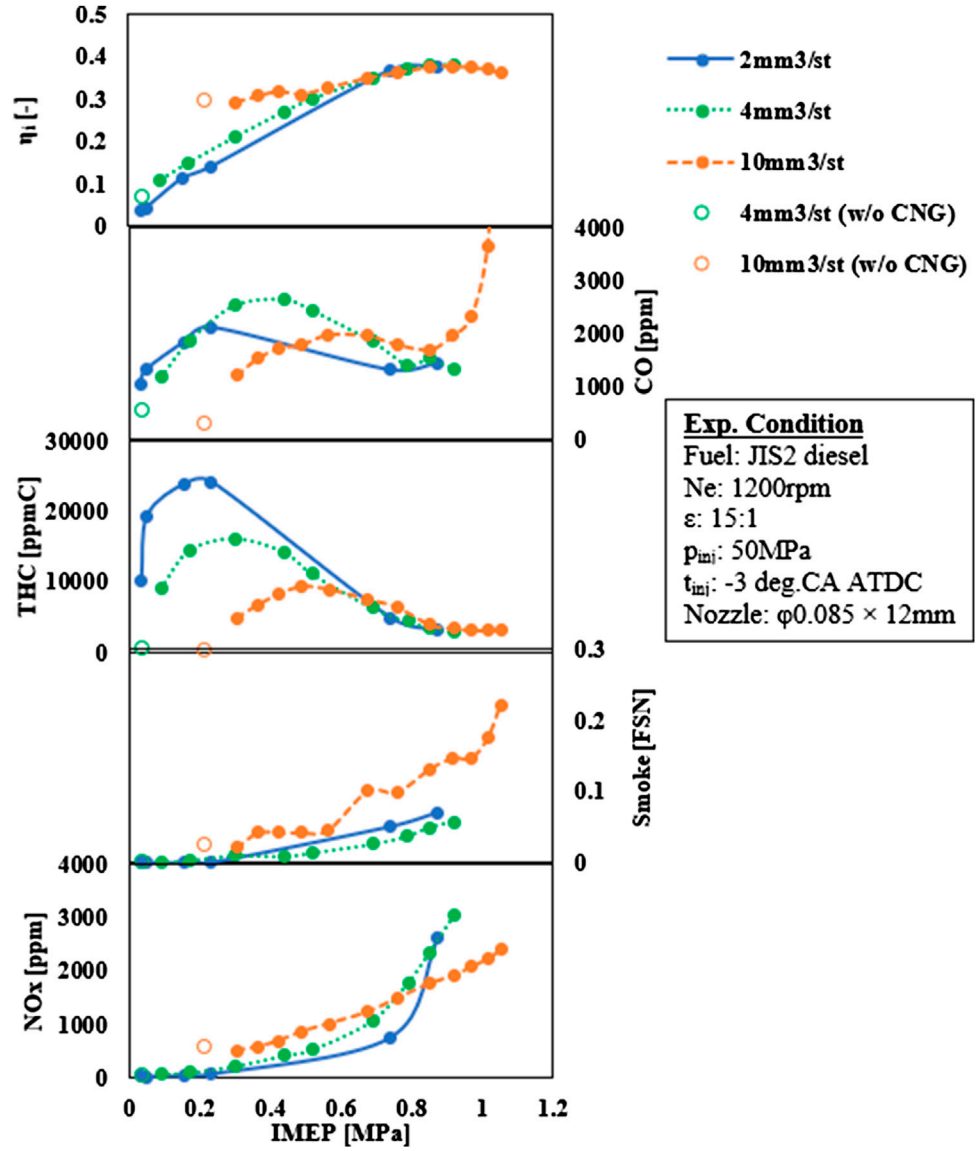

FIGURE 7 | Dual fuel engine performance characteristics under various IMEP and fuel ratios.

the ignition delay in high-temperature conditions. However, in the low-temperature region, both detailed and reduced models exhibit good agreement with the experimental data.

The reduced kinetic model was applied to the engine simulation case, and the results were compared to the data obtained from the experimental analysis in the engine set-up #1. The model validation analysis presented in **Figure 5** is for an early diesel injection at −60°CA ATDC. The comparison chart shows a good agreement between the experimental and simulation results for both in-cylinder pressure and heat release rate. The model captures the onset of the low-temperature heat release, the slope, and the maximum level accurately. The simulated emission profiles, in **Figure 6**, also show a good agreement with the experimental data for most of the species except the NOx.

RESULTS AND DISCUSSION

All the experimental results presented in this manuscript were acquired in three engine set-ups providing a wide range of data acquisition with different engine geometry configurations and allowing direct visualization of the in-cylinder combustion events. Moreover, CFD simulation analysis was performed to obtain a deeper understanding of the combustion and emission formation phenomena.

Baseline Operation

The baseline performance of the natural gas-diesel dual-fuel engine was tested using the single-cylinder engine set-up #1. Experimental tests were performed for pilot diesel injections of 2,

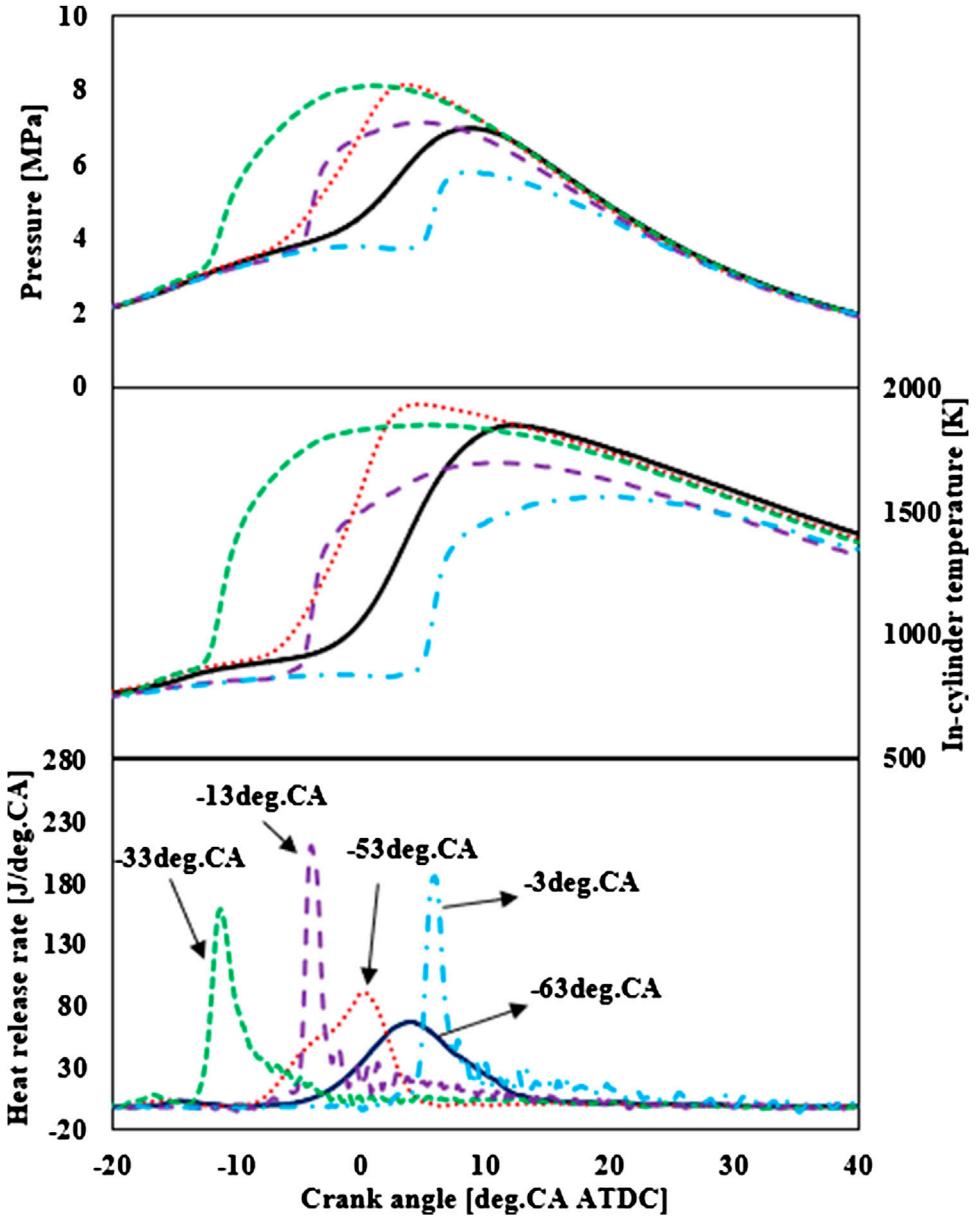

FIGURE 8 | In-cylinder pressure, temperature, and rate of heat release rate for different diesel injection timings.

4, and 10 mm^3/st at −3°CA ATDC, while the mass flow of the natural gas was varied to meet the targeted engine load.

Figure 7 shows the indicated thermal efficiency and emissions output behavior of the dual-fuel engine under different pilot injection amounts and indicated mean effective pressures. A strong correlation between the indicated efficiency and indicated mean effective pressure (IMEP) level is observed for all cases, with higher IMEP leading to maximum efficiency. The diesel amount has no significant effect in the high IMEP cases. However, when observing the low IMEP cases, it is evident that an increase in the pilot injection amount enhances the indicated thermal efficiency. From those mentioned above, it can be concluded that, at low engine loads, the lean natural gas pre-mixture conditions within the cylinder cannot guarantee a proper flame propagation when a small amount of diesel fuel is injected. At these conditions, the increase of the diesel/natural gas energy share ratio has a significant effect on the engine's combustion efficiency, which can be confirmed by the substantial drop in the number of THCs.

Diesel Injection Strategies

Injection Timing

The engine test results presented in the previous section were employing a fixed start of injection for diesel. In this section, the start of injection, for the engine set-up #1, was varied from −3°CA

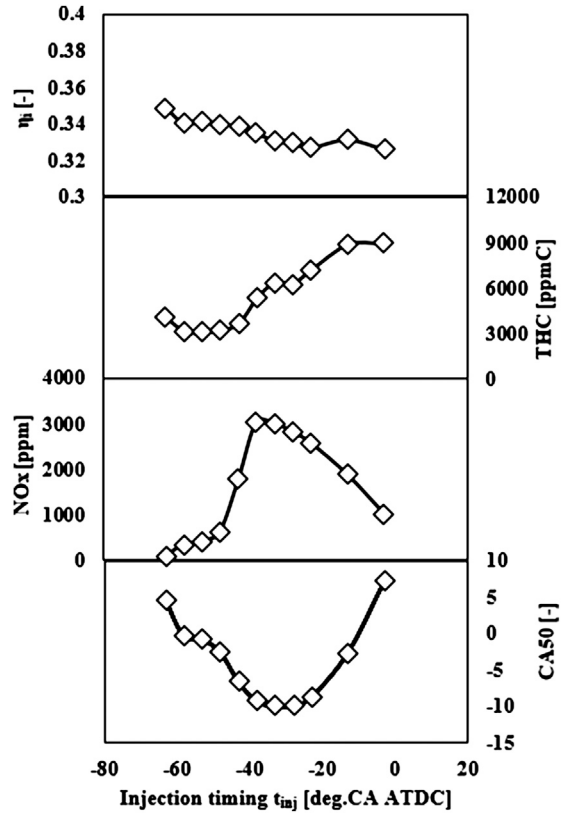

FIGURE 9 | Effect of diesel injection timing on indicated thermal efficiency, THC, NOx, and CA50 of the dual-fuel engine (experimental conditions as shown in **Figure 8**).

ATDC up to −63°CA ATDC. **Figure 8** shows the averaged in-cylinder pressure and heat release rate of dual-fuel combustion cases with the diesel injection timing set at −3, −13, −33, 53, and −63°CA ATDC.

It is clear from **Figure 8** that as the diesel injection timing advanced from −3°CA ATDC, the start of combustion also advanced. The onset of heat release for the −13°CA case takes place a few degrees CA before the TDC featuring a steep increase and reaching the maximum heat release level among all the cases. The −33°CA case showed an earlier start of combustion before the piston reaches the TDC and hence a milder heat release rate. When the start of injection was advanced to −53 and −63°CA, the start of combustion was delayed, with both cases showing a milder rate of heat release. Remarkably, this change of behavior can be seen in the NOx emissions chart presented in **Figure 9**. The NOx emission levels increase as the diesel injection timing advances from −3 to −33°CA. However, when the injection timing is further advanced, the NOx emissions drop with the earlier the injection giving lower NOx levels. The NOx behavior can be justified by observing the CA50 chart, which presents the piston location where 50% of the combustion occurred. The chart shows that the −13°CA case exhibits the earliest CA50 value before the piston reaches the top dead center due to the steep heat release behavior. For the rest of the cases, CA50 values closer to the TDC contribute to the reduction of the in-cylinder combustion temperature and hence NOx formation.

Furthermore, the injection timing shows a significant effect on the indicated thermal efficiency of the engine with earlier injections leading to increased efficiency. It is estimated that a late diesel injection reduces the ignition delay time, leading to a short diesel fuel dispersion period and hence limits the ability of igniting the lean natural gas mixture. On the other hand, an early diesel injection can provide enough time to homogenize the air-fuel mixture and improve the engine's combustion efficiency, confirmed by the reduced number of THCs at the exhaust of the engine.

Split Injection

The previous section revealed that the diesel injection timing is an important parameter to control the operating efficiency and emissions formation of a natural gas-diesel dual-fuel engine. Dual-fuel engine operation at low-load exhibited high amounts of THCs at the exhaust of the engine, indicating a low combustion efficiency due to unburned fuel. To further optimize the ability of diesel fuel to ignite natural gas under lean conditions, a split diesel injection strategy was assessed and presented in this section.

For this analysis, the optically accessible engine set-up #2 was preferred to visualize the in-cylinder combustion phenomena. For this type of engine, experiments can only be performed under cold-start conditions, which deteriorates the capacity of diesel fuel to ignite the lean natural gas-air mixture. For this reason, the No. 0 Solvent M with a cetane number higher than that of diesel fuel was used in this experimental analysis.

Figure 10 compares the heat release rate and combustion events of two cases with (A) an early single injection of 10 mm^3 at −60°CA ATDC and (B) a split injection strategy of 5 mm^3 per injection at −40 CA ATDC and the TDC of the engine.

As it can be observed from the in-cylinder images, for the early injection case, the combustion starts near the cylinder wall and the squish area and spreads towards the center of the cylinder. The numerical analysis images shown in **Figure 11** can confirm that in case (A), combustion started from the squish area, where a high-temperature level exists at the TDC and spreads towards the central axis of the combustion chamber. The premixed combustion case exhibits low-intensity flames that cover a wide area of the cylinder chamber with the generated NOx emission measured at the exhaust pipe being as low as 45 ppm.

On the other hand, for the split injection case, no combustion can be observed before the start of the second diesel injection. Once the second injection occurs, luminous diffusion flames can be seen near the cylinder wall causing the steep increase shown in the heat release diagram. The computational analysis in **Figure 11** illustrates that for the split injection case, case (B), the start of combustion was within the main area of the combustion chamber. The case exhibits much higher generated temperatures due to the second late injection leading to local fuel-rich regions within the combustion chamber. As a results, the NOx formation for the split injection case is over 15 times higher that the early injection case, with the experimental data reaching a reading of 758 ppm at the exhaust side of the engine.

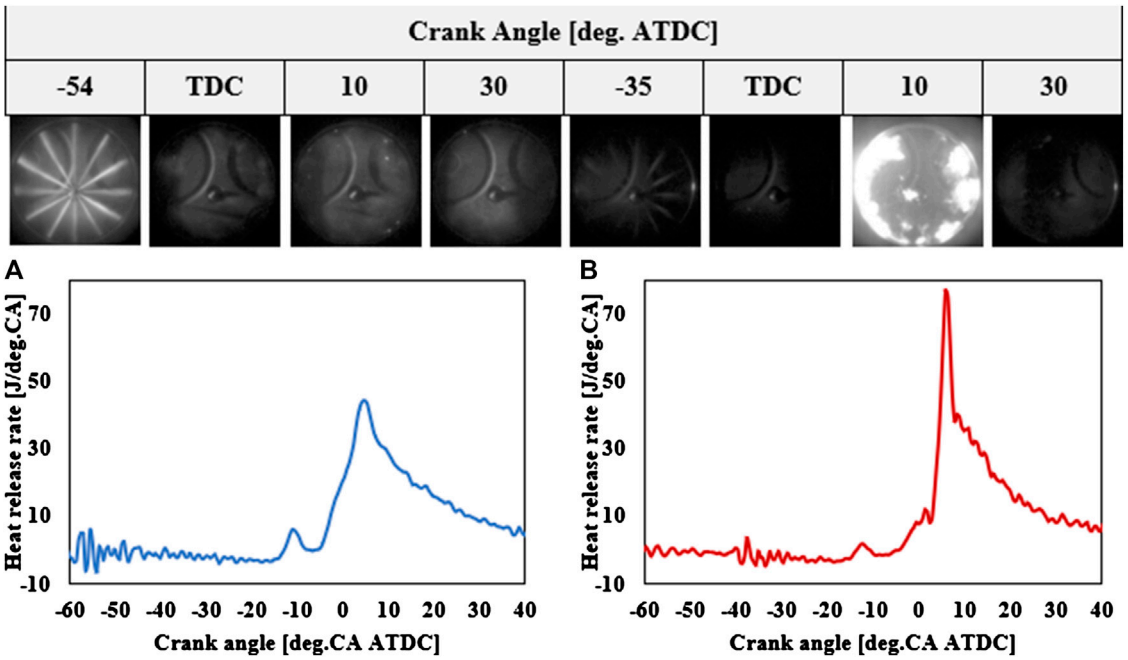

FIGURE 10 | Rate of heat realease and in-cylinder images for **(A)** early fuel inejction case (IMEP = 0.62 MPa, t_{inj} = −60°ATDC, Q_d = 10 mm^3/cycle), **(B)** split injection case (IMEP = 0.60 MPa, t_{inj} = −40°ATDC and TDC, Q_d = 5 and 5 mm^3/cycle).

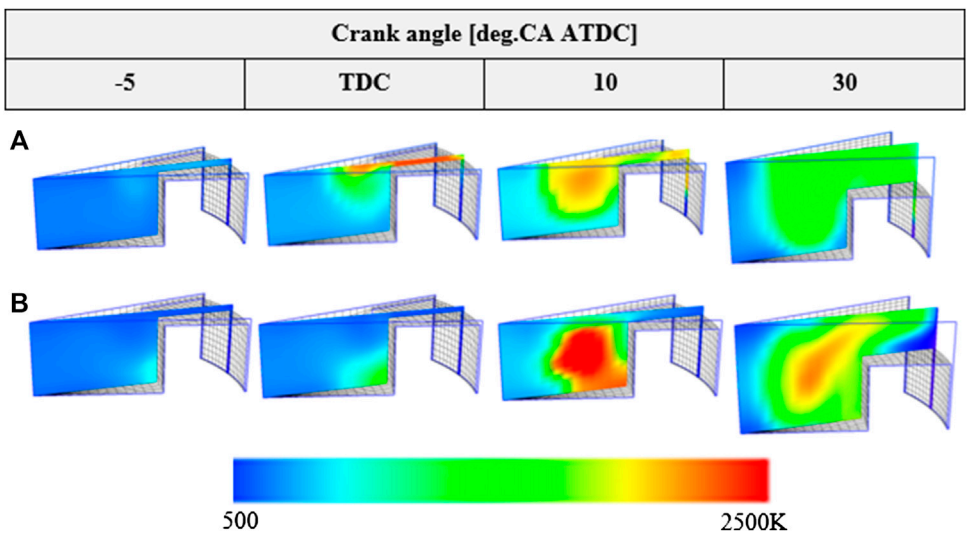

FIGURE 11 | In-cylinder temperature surface plots for **(A)** early fuel inejction case (IMEP = 0.62 MPa, t_{inj} = −60°ATDC, Q_d = 10 mm^3/cycle), **(B)** split injection case (IMEP = 0.60 MPa, t_{inj} = −40°ATDC and TDC, Q_d = 5 and 5 mm^3/cycle).

Figure 12 presents the heat release of the two cases against the main species profiles. A decrease in the C_7H_{16} coincides with the onset of the low-temperature heat release for both cases. It can be calculated that over 2/3 of the C_7H_{16} for case (A), and the vast majority of the C_7H_{16} from the first injection for case (B) react before the start of the high-temperature heat release zone. On the other hand, the CH_4 profiles for both cases remain unchanged until the start of the high-temperature heat release zone. Case (A) exhibits an improved CH_4 combustion efficiency, which is a result of the homogeneous diesel/CNG mixture covering a more extensive combustion area. A comparison over the unburned hydrocarbons and CH_4 profiles shows that 89% of the UHC is a source of CH_4 for case (A), while this ratio increases to 96% for case (B). Finally, the onset of the CO formation for both cases

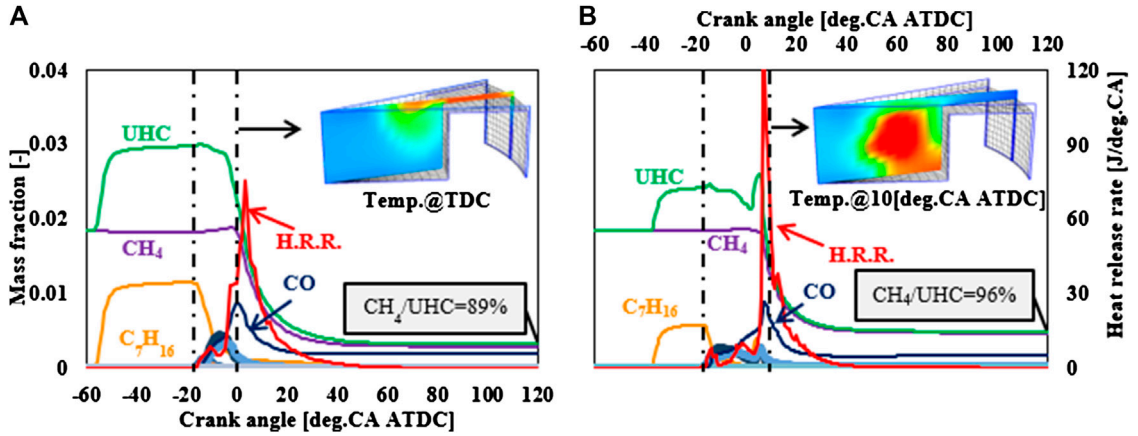

FIGURE 12 | Main species and heat release rate profiles for (A) early fuel injection case (IMEP=0.62MPa, tinj=−60deg.ATDC, Qd=10mm3/cycle), (B) split injection case (IMEP=0.60MPa, tinj=−40deg.ATDC & TDC, Qd=5 & 5mm3/cycle).

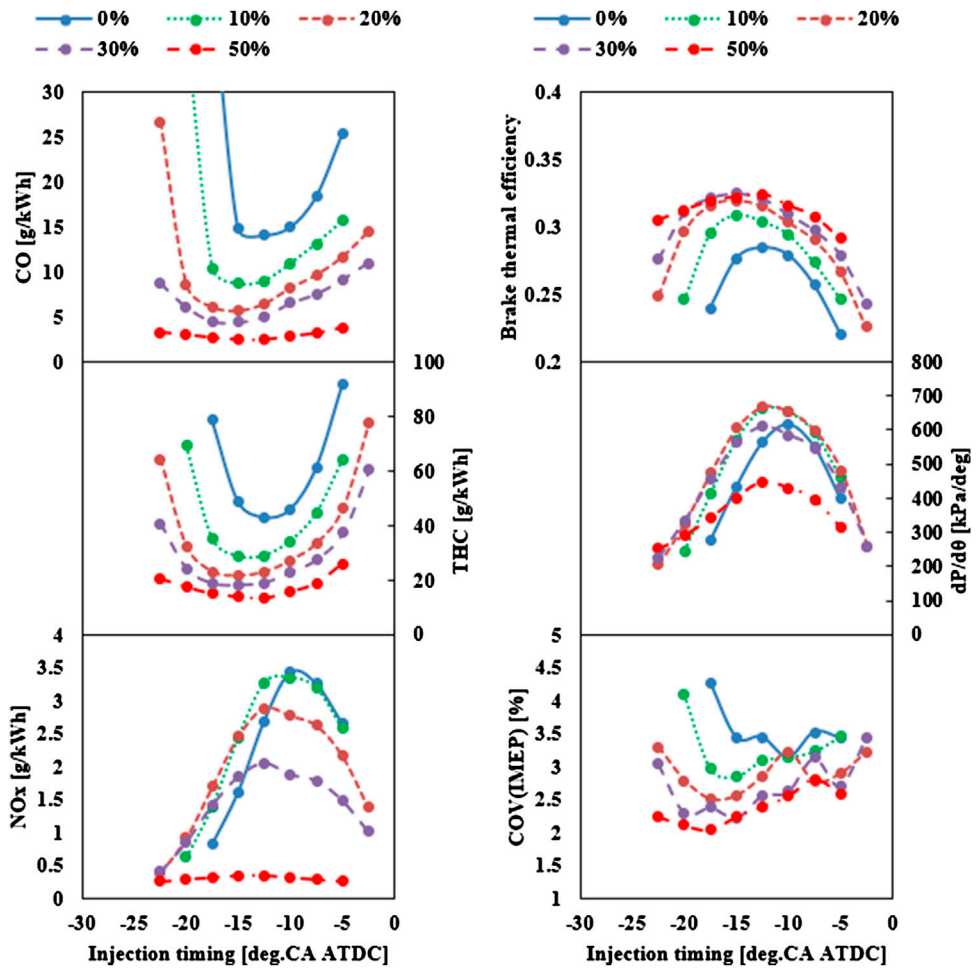

FIGURE 13 | Emissions and combustion performance characteristics for different diesel injection timings and EGR rates.

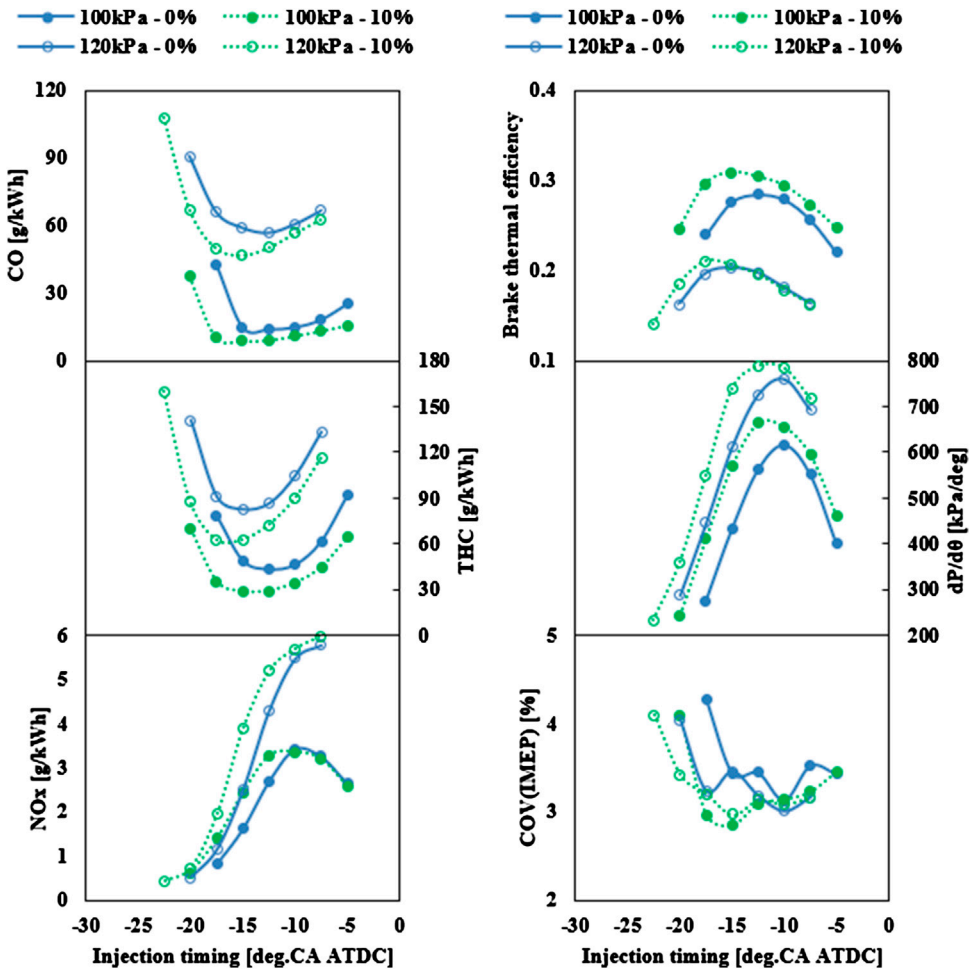

FIGURE 14 | Emissions and combustion performance characteristics for different diesel injection timings, intake pressure, and EGR rates.

indicates that the low temperature heat release (LTHR) of C_7H_{16} forms the CO emissions. The CO formation for case (B) is more significant due to the second diesel injection creating local fuel-rich areas within the cylinder.

Air-Path Strategies

The effects of different air-path strategies on the efficiency and emissions formation of the natural gas-diesel dual-fuel engine have been investigated and reported in this section. Two different strategies, i.e., EGR and intake boosting, have been tested for an engine speed of 1,200 rpm. For this set of experiments, the multi-cylinder engine set-up #3 was chosen to allow operation with a turbocharger and a high-pressure Hot-EGR system. The experimental procedure focused on the low-load engine zone, of 0.3 MPa brake mean effective pressure (BMEP) with a CNG-diesel ratio of 76:24, where high unburned gas emissions are observed.

Exhaust Gas Recirculation

The experimental analysis was performed for engine operation with EGR rates of up to 50%, and the diesel injection timing ranged from −30°CA ATD to TDC. The 50% EGR rate was set as the maximum limit as any operation with higher EGR rates led to unstable combustion operation with lower thermal efficiency. **Figure 13** compares the emission formation and engine performance for different EGR rates and diesel injection timings. As the EGR rate increases to 40%, the CO and THC are significantly reduced, leading to high combustion and BTE. The introduction of Hot-EGR, which bypasses the EGR cooler, leads to a significant increase of the intake charge temperature in the range of 10–90°C and promotes oxidation. Moreover, the injection timing plays a vital role in the combustion performance, CO and THC output of the engine with cases with an injection angle at −17.5 to −12.5°CA ATCD showing the lowest emissions.

A further increase of EGR rate (50%) did not provide any significant improvements to the CO and THC emissions. On the other hand, a small increase was observed for cases with an early diesel injection, which indicates that low oxygen rates within the cylinder could deteriorate the oxidation process. However, a 50% EGR rate contributes to a significant NOx reduction, while this level of EGR reduced the effect of injection timing on the NOx formation. Moreover, a high EGR rate was found to contribute

significantly to the reduction of the dP/dθ and coefficient of variance (COV) of the engine.

Intake Boosting

The effect of intake boosting at the low-load range of the engine for operation with and without EGR was experimentally tested. High rates of EGR were challenging to be achieved for the boosted case of 120 kPa intake pressure, and therefore the EGR rate was limited to 10%. The tendency of the boosted cases for the emissions output data is alike the non-boosted cases presented earlier. However, for the boosted cases, all the emissions significantly increase, particularly at the early diesel injection region. The COV of IMEP chart indicates that the COV for the boosted and non-boosted cases does not significantly increase, therefore the emissions increase is not due to combustion cycles fluctuations. It is estimated that the increase in CO and THC and the BTE reduction is a result of the excessive lean CNG-air mixture. Therefore, it can be concluded that boosting at a low-load operation level is not an appropriate strategy to optimize the combustion efficiency of the CNG-diesel dual duel engine. On the other hand, the throttling of the engine to reduce the intake pressure could potentially improve the emissions output, but this could harm the COV of IMEP rates.

CONCLUSIONS

The paper presents experimental and simulation studies on natural gas-diesel dual-fuel combustion. The research work was carried out on three different engine set-ups of single cylinder with and without optical access and multi-cylinder characteristics. CFD simulations with a developed well-correlated skeletal model were performed to gain a deeper understanding of the combustion phenomena. The analysis focused on the effect of diesel injection timing, quantity, and pattern as well as different airpath strategies, such as EGR and boosting, on the combustion and emissions performance of the dual-fuel engine, with a focus on the low-load region.

The results showed that an advanced diesel injection could significantly reduce the NOx formation and enhance the engine's thermal efficiency. The CFD study revealed that the unburned hydrocarbon emissions at low loads mostly result from unburned methane. A split diesel injection strategy did not provide any benefits on the emissions formation, and it further deteriorated the THCs by increasing the unburned CH_4. Hot EGR contributed significantly to the simultaneous reduction of NOx and unburned species while it increased the thermal efficiency of the engine at low-load operation. On the other hand, intake boosting did not provide any performance or emission benefits as it increased the unburned emission components and deteriorated the thermal efficiency of the engine.

DATA AVAILABILITY STATEMENT

The raw data supporting the conclusions of this article will be made available by the authors, without undue reservation.

AUTHOR CONTRIBUTIONS

PD analyzed the data and wrote the manuscript with the support of TT and HK. TT managed the project and developed the reaction mechanism used in the simulation study. HK was responsible for the multi-cylinder engine testing. KA. performed the experimental analysis on the single-cylinder engines. NK planned the project and designed the diesel injectors used in the study. YN managed the project and contributed to experimental studies.

FUNDING

The authors declare that part of the research was supported by DENSO CORPORATION.

REFERENCES

Abani, N., and Reitz, R. D. (2007). Unsteady turbulent round jets and vortex motion. *Phys. Fluids.* 19 (12), 125102. doi:10.1063/1.2821910

Abdelaal, M. M., and Hegab, A. H. (2012). Combustion and emission characteristics of a natural gas-fueled diesel engine with EGR. *Energy Convers. Manag.* 64, 301–312. doi:10.1016/j.enconman.2012.05.021

Amsden, A. (1997). LA Report, LA-13313-MS. KIVA-3V: a block-structured KIVA program for engines with vertical or canted valves. doi:10.1016/0375-6505(82)90028-1

ANSYS, Inc. (2019). *ANSYS 2019R1 Forte best practises*. Canonsburg, PA:ANSYS Inc.

Cheenkachorn, K., Poompipatpong, C., and Ho, C. G. (2013). Performance and emissions of a heavy-duty diesel engine fuelled with diesel and LNG (liquid natural gas). *Energy* 53, 52–57. doi:10.1016/j.energy.2013.02.027

Ciezki, H. K., and Adomeit, G. (1993). Shock-tube investigation of self-ignition of N-heptane-air mixtures under engine relevant conditions. *Combust. Flame.* 93 (4), 421–433. doi:10.1016/0010-2180(93)90142-p

Dimitriou, P., and Javaid, R. (2020). A review of ammonia as a compression ignition engine fuel. *Int. J. Hydrog. Energy.* 45, 7098–7118. doi:10.1016/j.ijhydene.2019.12.209.

Dimitriou, P., and Tsujimura, T. (2017). A review of hydrogen as a compression ignition engine fuel. *Int. J. Hydrog. Energy.* 42 (38), 24470–24486. doi:10.1016/j.ijhydene.2017.07.232

IRENA (2019). *Hydrogen: a renewable energy Perspective.*Tokyo, Japan: IRENA.

ISO 10054 (1998). *Internal combustion compression ignition engines-apparatus for measurement of smoke from diesel engines operating under steady state conditions—Filter type smoke meter*. Berlin: Beuth Verlag.

Karim, G. A. (2003). Combustion in gas fueled compression: ignition engines of the dual fuel type. *J. Eng. Gas Turbines Power.* 125 (3), 827–836. doi:10.1115/1.1581894

Kojima, H., Yoshida, A., Tsujimura, T., Fujino, T., Kawakita, S., Kondo, W., et al. (2016). A strategy of intake gas control for diesel dual fuel engine with natural gas and diesel fuel. *Trans. Soc. Automot. Eng. Jpn. Inc.* 47 (4), 889–894. doi:10.11351/jsaeronbun.47.889

Kong, S.-C., and Reitz, R. D. (2002). Use of detailed chemical kinetics to study HCCI engine combustion with consideration of turbulent mixing effects. *J. Eng. Gas Turbines Power.* 124 (3), 702–707. doi:10.1115/1.1413766

Kusaka, J., Daisho, Y., Kihara, R., Saito, T., and Nakayama, S. (1998). "Combustion and exhaust gas emissions characteristics of a diesel engine dual-fueled with natural gas," in Fourth international symposium COMODIA. Kyoto, Japan, July 20–23, 1998

Liang, L., Naik, C. V., Puduppakkam, K., Wang, C., Modak, A., Meeks, E., et al. (2010). Efficient simulation of diesel engine combustion using realistic chemical kinetics in CFD. SAE Technical papers. doi:10.4271/2010-01-0178

Liu, J., Yang, F., Wang, H., Ouyang, M., and Hao, S. (2013). Effects of pilot fuel quantity on the emissions characteristics of a CNG/diesel dual fuel engine with optimized pilot injection timing. *Appl. Energy*. 110, 201–206. doi:10.1016/j.apenergy.2013.03.024

Lounici, M. S., Loubar, K., Tarabet, L., Balistrou, M., Niculescu, D.-C., and Tazerout, M. (2014). Towards improvement of natural gas–diesel dual fuel mode: an experimental investigation on performance and exhaust emissions. *Energy* 64: 200–211. doi:10.1016/j.energy.2013.10.091

Maricq, M. M., Chase, R. E., Xu, N., and Laing, P. M. (2002). The effects of the catalytic converter and fuel sulfur level on motor vehicle particulate matter emissions: light duty diesel vehicles. *Environ. Sci. Technol.* 36 (2), 283–289. doi:10.1021/es010962l

Mehl, M., and Curran, H. J. (2009). "Chemical kinetic modeling of component mixtures relevant to gasoline." in European combustion meeting, 1–6. Vienna, Austria, March 2, 2009

Papagiannakis, R. G., Rakopoulos, C. D., Hountalas, D. T., and Rakopoulos, D. C. (2010). Emission characteristics of high speed, dual fuel, compression ignition engine operating in a wide range of natural gas/diesel fuel proportions. *Fuel* 89 (7), 1397–1406. doi:10.1016/j.fuel.2009.11.001

Patel, A., Song, C., and Reitz, R. D. (2004). Development and validation of a reduced reaction mechanism for HCCI engine simulations. SAE Technical papers. doi:10.4271/2004-01-0558.

Paul, A., Bose, P. K., Panua, R. S., and Banerjee, R. (2013). An experimental investigation of performance-emission trade off of a CI engine fueled by diesel-compressed natural gas (CNG) combination and diesel-ethanol blends with CNG enrichment. *Energy* 55, 787–802. doi:10.1016/j.energy.2013.04.002

Reitz, R. D., and Beale, J. C. (1999). Modeling spray atomization with the Kelvin–Helmholtz/Rayleigh–Taylor Hybrid model. *Atom. Spr.* 9 (6), 623–650. doi:10.1615/atomizspr.v9.i6.40

Sahoo, B. B., Sahoo, N., and Saha, U. K. (2009). Effect of engine parameters and type of gaseous fuel on the performance of dual-fuel gas diesel engines—a critical review. *Renew. Sustain. Energy Rev.* 13 (6–7), 1151–1184. doi:10.1016/j.rser.2008.08.003

Selim, M. Y. E. (2001). Pressure-time characteristics in diesel engine fueled with natural gas. *Renew. Energy.* 22 (4), 473–489. doi:10.1016/s0960-1481(00)00115-4

Shenghua, L., Longbao, Z., Ziyan, W., and Jiang, R. (2003). Combustion characteristics of compressed natural gas/diesel dual-fuel turbocharged compressed ignition engine. *Proc. Inst. Mech. Eng. Part D J. Automob. Eng.* 217, 833–838. doi:10.1177/095440700321700909

Srinivasan, K. K., Krishnan, S. R., and Midkiff, K. C. (2006). Improving low load combustion, stability, and emissions in pilot-Ignited natural gas engines. *Proc. Inst. Mech. Eng. Part D J. Automob. Eng.* 220 (2), 229–239. doi:10.1243/09544070jauto104

Tsujimura, T., Aoyagi, K., Kurimoto, N., and Nishijima, Y. (2012). "Combustion analysis for natural gas/diesel dual fuel engine," in Proceedings of the 8th international conference on modeling and diagnostics for advanced engine systems, Fukuoka, Japan, July 23–26, 2012 COMODIA 2012, 380–385.

Tsurushima, T. (2009). A new skeletal PRF kinetic model for HCCI combustion. *Proc. Combust. Inst.* 32 (2), 2835–2841. doi:10.1016/j.proci.2008.06.018

UNFCC (2015). "Adoption of the Paris agreement," in Conference of the parties on its twenty-first session. Paris, France, November 30–December 12, 2015

Wang, Y., Ge, H.-W., and Reitz, R. D. (2010). Validation of mesh- and timestep-independent spray models for multi-dimensional engine CFD simulation. *SAE Int. J. Fuels Lubr.* 3, 277–302. doi:10.4271/2010-01-0626

Wei, L., and Geng, P. (2016). A review on natural gas/diesel dual fuel combustion, emissions and performance. *Fuel Process. Technol.* 142, 264–278. doi:10.1016/j.fuproc.2015.09.018

Yang, B., Xi, C., Wei, X., Zeng, K., and Lai, M.-C. (2015). Parametric investigation of natural gas port injection and diesel pilot injection on the combustion and emissions of a turbocharged common rail dual-fuel engine at low load. *Appl. Energy.* 143, 130–137. doi:10.1016/j.apenergy.2015.01.037

Conflict of Interest: Authors KA, NK, and YN were employed by the company DENSO CORPORATION, who was also a funder of this study. The funder had the following involvement with the study: Involved in the experimental analysis, project design, and management.

frontiers in Mechanical Engineering

ORIGINAL RESEARCH
published: 29 October 2020
doi: 10.3389/fmech.2020.555136

On the Variation of the Effect of Natural Gas Fraction on Dual-Fuel Combustion of Diesel Engine Under Low-to-High Load Conditions

Amin Yousefi[1]*, *Madjid Birouk*[1] and *Hongsheng Guo*[2]

[1]Department of Mechanical Engineering, University of Manitoba, Winnipeg, MB, Canada, [2]Energy, Mining and Environment Center, National Research Council Canada, Ottawa, ON, Canada

Natural gas–diesel dual fuel (NDDF) engine has the potential to significantly reduce carbon dioxide (CO_2) and particulate matter (PM) emissions while retaining the diesel engine's high efficiency and reliability. The operation and performance of the NDDF engine depend on natural gas energy fraction (%NG), which ranges from low %NG, where diesel fuel provides most of the combustion energy, to high %NG, where diesel fuel is used only to initiate combustion. Although pertaining published studies demonstrated that the effect of %NG on the combustion performance and emissions of the NDDF engine depend upon the engine load, none of these studies discussed the reasons behind this dependence. The present study attempts to shed light on this issue by experimentally and numerically investigating the effect of different %NGs on the NDDF engine under different load conditions. Both experimental and numerical results revealed that the peak pressure rise rate (PPRR) first increases and then drops with increasing %NG under all load conditions. The calculated local equivalence ratio and charge temperature contours showed that increasing %NG to a certain limit increases local equivalence ratio inside the ignition kernel, which implies that more premixed natural gas–air mixture participates in reactions during the premixed combustion stage. This results in an increased flame temperature and higher PPRR right after ignition. However, increasing %NG beyond this range decreases local equivalence ratio inside the ignition kernel, which leads to lower PPRR. Increasing %NG retards the combustion phasing at low-to-medium load conditions. However, increasing %NG generally advances the combustion phasing under medium-to-high load conditions due to the fact that the flame propagation speed of natural gas–air mixture increases with %NG at medium-to-high load conditions. Methane emissions grow with increasing %NG under all examined engine

OPEN ACCESS

Edited by:
Mingfa Yao,
Tianjin University, China

Reviewed by:
Kan Zha,
Sandia National Laboratories (SNL), United States

***Correspondence:**
Amin Yousefi
Amin.yousefi@umanitoba.ca

Specialty section:
This article was submitted to Engine and Automotive Engineering, a section of the journal Frontiers in Mechanical Engineering

Received: *24 April 2020*
Accepted: *16 September 2020*
Published: *29 October 2020*

Citation:
Yousefi A, Birouk M and Guo H (2020) On the Variation of the Effect of Natural Gas Fraction on Dual-Fuel Combustion of Diesel Engine Under Low-to-High Load Conditions. Front. Mech. Eng. 6:555136. doi: 10.3389/fmech.2020.555136

Abbreviations: %NG, %NG; AMR, adaptive mesh refinement; ATDC, after top dead center; BMEP, break mean effective pressure; BTE, brake thermal efficiency; CA10, crank angle of 10% heat release; CA50, crank angle of 50% heat release; CA90, crank angle of 90% heat release; CAD, crank angle degree; CFD, computational fluid dynamics; CO, carbon monoxide; CO_2, carbon dioxide; COV, coefficient of variation; EGR, exhaust gas recirculation; EVC, exhaust valve closing; EVO, exhaust valve opening; GHG, greenhouse gas; HRR, heat release rate; IMEP, indicated mean effective pressure; ITE, indicated thermal efficiency; IVC, intake valve closing; IVO, intake valve opening; LHV, lower heating value; NDDF, natural gas/diesel dual-fuel; NOx, nitrogen oxides; PM, particulate matter; PPRR, peak pressure rise rate; RPM, revolution per minute; SODI, start of diesel injection; UHC, unburned hydrocarbon.

load conditions. However, this growth becomes much smaller under medium-to-high engine load conditions. Increasing %NG significantly increases greenhouse gas (GHG) emissions under lower load conditions. However, using advanced diesel injection timing decreases GHG emissions of the NDDF engine under lower load conditions. Increasing % NG decreases GHG emissions by 6%–11% under medium-to-high load conditions.

Keywords: natural gas, gas fraction, engine load, combustion, dual-fuel, diesel engine

INTRODUCTION

Diesel engines have been widely used in many engineering applications such as in transportation and stationary power generation industries due to their higher fuel efficiency and reliability as compared with the spark ignition engines. However, high levels of carbon dioxide (CO_2), nitrogen oxides (NO_x), and particulate matter (PM) emissions are becoming serious problems for the future of conventional diesel engines. In recent years, increased fuel cost and alarming environmental issues have forced the governing bodies of developed countries to implement stringent regulations to lower greenhouse gas (GHG) and pollutant emissions. For example, the Government of Canada has set a new target to reduce GHG emissions by 30% and 80% below the 2005–2006 levels by 2030 and 2050, respectively (Treasury Board of Canada Secretariat" 2017). This has exerted a significant pressure on industries using diesel engines, such as transportation and power generation. Therefore, greater research focus is placed on developing more efficient and greener power generation systems with the aim to alleviate dependency on fossil fuels and abate harmful emissions. Electrification has recently drawn great attention in automotive applications. However, its widespread adoption, especially in the heavy-duty engine market, is still impeded by several problems that include charging time, energy density, cost of materials, durability, and reliability (Guo and Liko, 2019). Therefore, a heavy-duty diesel engine will continue to predominate in private and public transportation at least for the next two to 3 decades (Bataille et al., 2015).

Efficiency improvement and fuel switching play an important role in emission reduction of heavy-duty diesel engines (Yousefi et al., 2015; Yousefi and Birouk, 2016). Natural gas is a promising fuel for transportation owing to its abundance, low carbon, and superior combustion characteristics. Combustion of natural gas reduces CO_2 emissions by up to ~20–30% (or up to ~80–90% with renewable natural gas) and produces lower PM emissions than does diesel (Yousefi et al., 2017; Guo and Liko, 2019). Therefore, replacing diesel fuel by natural gas can substantially reduce CO_2 and PM emissions. Natural gas–diesel dual fuel (NDDF) engine has emerged as a practical and efficient technology to satisfy increasingly stringent emission regulations in the near future (Rochussen and Kirchen, 2018; Yousefi et al., 2018). In the NDDF engine, the premixed natural gas–air mixture is compressed during the compression stroke and then auto-ignites upon the injection of diesel fuel. The NDDF engine can achieve similar (or sometimes higher) thermal efficiency than the diesel engine can (Yousefi and Birouk, 2017; Ahmad et al., 2018; Zheng et al., 2019). The NDDF engine can also be reverted back to diesel operation in the case of intermittent natural gas supply. The main problem of NDDF engine technology is high unburned methane (CH_4) emissions under low-to-medium engine load conditions due to poor flame propagation under lean premixed natural gas–air mixture conditions (Jiaqiang et al., 2018; Shim et al., 2018). It is reported that CH_4 has a global warming potential of ~20–30 times more than CO_2 over a 100-year period (Yousefi et al., 2019) and, therefore, is a critical exhaust species to minimize.

The operation of the NDDF engine is governed by natural gas substitution ratio or natural gas energy fraction, which is defined as the energy content of natural gas divided by the total energy content of both natural gas and diesel fuel. This ranges from lower addition of natural gas, where the diesel fuel shoulders most of the combustion energy burden, to high substitution ratio where natural gas is the main fuel and diesel is used primarily as an ignition source. The operation of the NDDF engine under different %NGs has several strengths and drawbacks. While lower %NG is beneficial for obtaining dual-fuel engine without a costly engine retuning, higher natural gas usage is favored in order to reduce fuel cost and more importantly to reduce GHG and other pollutant emissions. The latter option may need significant engine functional alterations to meet operational and emission standards.

The effect of %NG on the combustion characteristics of the NDDF engine under different load and speed conditions has been extensively studied (e.g., Papagiannakis and Hountalas, 2004; Dahodwala et al., 2014; Lounici et al., 2014; Tablan 2014; Cesar et al., 2015; Guo et al., 2015; Nithyanandan et al., 2016; Guo et al., 2017; Mattson et al., 2018; Song et al., 2018; Guo and Liko, 2019). For instance, Papagiannakis and Hountalas (2004) compared the combustion characteristics of the NDDF engine (%NG = 84%) with those of its diesel engine counterpart at different load conditions. They found that the NDDF engine features longer ignition delay than does the diesel engine at low-to-high load conditions. They also noted that the combustion duration of the NDDF engine is longer than that of the diesel engine at low-to-medium load conditions. However, with the increase of engine load, the combustion duration of NDDF becomes shorter than that of the diesel engine especially at low engine speeds (Papagiannakis and Hountalas, 2004). Lounici et al. (2014) found that the NDDF engine has slightly more retarded start of combustion than has the diesel combustion mode at low-to-high load conditions. They also revealed that the peak pressure of the NDDF engine is lower at low-to-medium load conditions. However, at higher engine loads (e.g., over 50%), the peak pressure and heat release rate (HRR) of the NDDF engine are found higher than those of the diesel engine (Lounici et al., 2014). Cesar et al. (2015) reported similar observations. (Guo et al., 2015; Guo et al., 2017; Guo and Liko, 2019) examined the effect of different natural energy fractions on

the combustion performance and emissions of the NDDF engine at low-to-high load conditions. They showed that increasing %NG retards the combustion phasing and decreases the brake thermal efficiency (BTE) under low-to-medium engine load conditions. However, they found that increasing %NG advances the combustion phasing and increases the BTE at medium-to-high engine load conditions. Nithyanandan et al., (2016) studied the effect of %NG on the NDDF engine at medium-to-high load conditions. They found that peak pressure increases with %NG up to 70% and then declines afterwards. They also observed that the ignition delay progressively increases, whereas the combustion duration becomes shorter up to 70% %NG and then starts increasing with further increase in natural gas substitution (Nithyanandan et al., 2016). Matteson et al. (Mattson et al., 2018) studied the effect of different %NG on the combustion characteristics of the NDDF engine under four different engine load conditions. They showed that, at low-to-medium engine load conditions, increasing %NG decreases the peak pressure and retards the combustion phasing. They reported, however, that increasing %NG up to 60% advances the combustion phasing at medium-to-high load conditions, while further increase in the % NG retards the combustion phasing (Mattson et al., 2018). They concluded that, at low %NG (i.e., 0–18%), the combustion generally mimics that of diesel where, for example, the ignition delay remains unchanged and the unburned hydrocarbon (UHC) emissions worsen under all engine load conditions. They also found that midrange natural gas substitution ratio (40–60%) increases the engine thermal efficiency at medium-to-high load conditions (Mattson et al., 2018).

The briefly reviewed literature above showed that the effect of %NG on the combustion performance (e.g., combustion phasing and efficiency) and emissions of the NDDF engine greatly depends upon the engine load. However, none of these studies discussed the reasons behind this dependence on the engine load. The present study is an attempt to shed light on this issue by experimentally investigating the effect of different %NGs on the NDDF engine under different load conditions [brake mean effective pressures (BMEPs) of 4.05, 8.10, 12.15, and 17.60 bar] including testing at different %NGs (i.e., 0%–90%) in order to comprehensively investigate the different phenomena observed at each operational regime. Measured cylinder pressure, HRR, combustion timings, thermal efficiency, and engine out emissions (i.e., methane and CO_2 equivalent) are also considered. Moreover, a computational fluid dynamics (CFD) model based on CONVERGE 2.4 software is developed to help understand the experimental observations in the engine combustion chamber. Specifically, local equivalence ratio, cylinder charge temperature, size of ignition kernels, and flame propagation speed during premixed combustion and flame propagation stages are all investigated to aid in interpreting the experimental observations.

EXPERIMENTAL SETUP AND CONDITIONS

A brief summary of the engine test setup is presented here since more detailed description is reported elsewhere (Guo et al., 2015; Guo et al., 2017; Yousefi et al., 2017). **Figure 1** shows a schematic of the experimental setup, and **Table 1** lists the basic engine specifications. Experiments were conducted using a modified single cylinder Caterpillar's 3400-series heavy-duty diesel engine. The engine was equipped with a high-pressure common-rail direct diesel injection system. The diesel fuel injection was controlled using a data acquisition hardware (National Instruments, model PXI-1031chassis) and LabVIEW-based software (Drivven, Inc.). A natural gas injector manufactured by Alternative Fuel Systems, Inc. (Calgary, Alberta, Canada) was mounted on the intake manifold to create the premixed charge of natural gas–air mixture. The quantity of diesel and natural gas mass flows were measured by Bronkhorst mass flowmeters. Intake and exhaust surge tanks were used to reduce pressure pulsation and simulate the turbocharging system. The intake air mass flow was measured by a turbine mass flow meter.

Natural gas energy fraction is calculated and calibrated by the mass flow rates and lower heating values of diesel and natural gas.

$$\%NG = \frac{\dot{m}_{NG} LHV_{NG}}{\dot{m}_{NG} LHV_{NG} + \dot{m}_{D} LHV_{D}} \quad (1)$$

where $\dot{m}$ represents mass flow rate and LHV represents low heating value. Subscripts NG and D represent natural gas and diesel, respectively.

The engine speed and load were controlled by the engine's electronic control module and an AVL Digalog Testmate. Cylinder pressure was captured by a water-cooled pressure transducer (Kistler model 6041A) coupled with an AVL real-time combustion analysis system, which samples 100 consecutive cycles with a resolution of 0.2 crank angle degree (CAD). California Analytical Instruments' series 600 gas analyzer was used to measure CO_2, carbon monoxide (CO), NO_x, and CH_4 emissions. Soot measurement was performed by an AVL smoke meter (415S).

A maximum peak pressure rise rate (PPRR) of 13 bar/CAD, a maximum cylinder pressure of 150 MPa, and a coefficient of variation of indicated mean effective pressure (IMEP) (COV_{IMEP}) of 5% were used as the engine operating limits during testing. Experiments were carried out at four different engine load conditions including low-to-medium load (BMEPs = 4.05 and 8.10 bar) and medium-to-high load (BMEPs = 12.15 and 17.60 bar). A sweep of %NG and diesel injection timing tests were conducted when investigating each case. For all cases, the intake temperature and diesel injection rail pressure were kept constant at 40°C and 525 bar during the experiments. Exhaust gas recirculation (EGR) was not used in this study. **Tables 2, 3** give the varied and fixed experimental test conditions, respectively. It can be observed, from **Table 2**, that increasing natural gas energy fraction slightly reduces the air mass flow rate at each engine load condition. However, this does not significantly change the density of air at the timing of diesel injection since the density of air is mainly affected by the intake pressure and temperature. Testing was accomplished at steady-state conditions when the engine oil and exhaust gas temperature varied by less than 1% over a 180-s period. Engine performance data, particularly the flow rates of both gaseous and liquid fuels and engine out emissions, were collected over the course of 180 s.

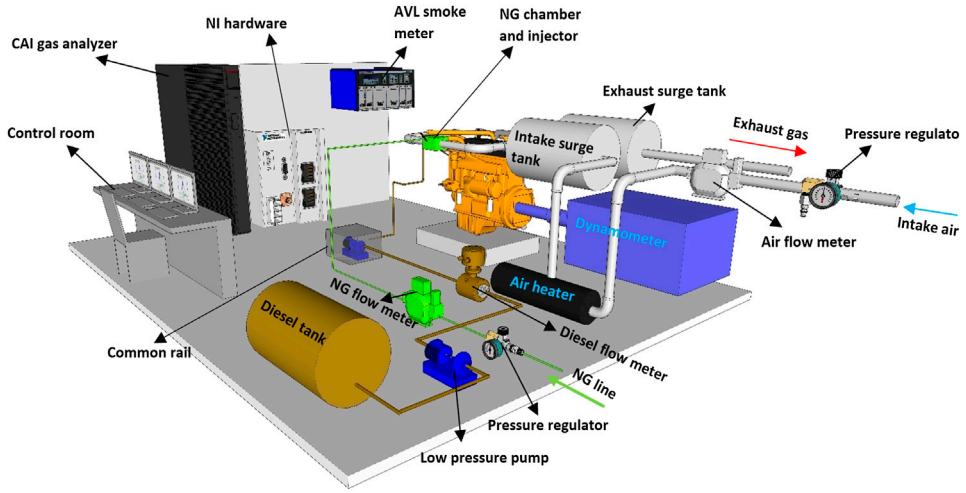

Figure 1 | Schematic of the experimental setup.

NUMERICAL MODELING AND VALIDATION

A three-dimensional model was built in CONVERGE 2.4 software (Richards et al., 2017), which is a CFD solver for modeling complex geometries and complicated phenomena such as engine combustion. Details of the developed CFD model can be found in Yousefi et al. (Yousefi et al., 2018; Yousefi et al., 2019). A transient chemistry solver, named as SAGE (Richards et al., 2017), was used to implement the chemistry calculation. SAGE calculates the reaction rates for each elementary reaction, while the CFD solver solves the governing transport equations. Diesel fuel was represented by *n*-heptane, and natural gas oxidation was represented by methane in the reaction mechanism that consisted of 76 species and 464 reactions (Rahimi et al., 2010). This mechanism, which was validated under different natural gas/diesel dual-fuel engine operating conditions, has also been adopted by CONVERGE software for NDDF combustion simulation (Richards et al., 2017). Kelvin Helmholtz–Rayleigh Taylor and O'Rourke models were applied to model the diesel spray breakup process and droplet collision, respectively (Senecal et al., 2007).

The simulation started from the intake valve closing (IVC) and terminated at the exhaust valve opening (EVO). Since the test engine is a heavy-duty engine, there is a low swirl ratio at IVC, which is estimated to be 0.5. As the diesel injector was located in the central axis of the cylinder and the six nozzle holes were distributed symmetrically, only 1/6th of the combustion chamber was simulated. The baseline grid size was set to be 2 mm, and an adaptive mesh refinement (AMR) was then employed on the velocity and temperature gradients with a maximum embedding level of 3. **Figure 2** displays the piston bowl, squish dimensions, and grid refinements using CONVERGE AMR tool. The upper limit of the total cells in the computational domain is two million. The AMR enables the simulation to efficiently resolve details in the regions of the turbulent flame front and higher species concentration gradients (fine enough cell sizes of 0.25–0.5 mm), while a relatively coarse mesh was used in regions where no reactions or spray dispersion occur (Wijeyakulasuriya 2015; Jupudi et al., 2016).

The simulated pressure and HRR of different cases [under different loads, %NGs, and start of diesel injection (SODI)] are validated against the experimental data and presented in **Figure 3A–C**. Further validation cases can be found elsewhere (Yousefi et al., 2018; Yousefi et al., 2019). It can be observed that, in all these cases, the simulated and experimental pressures and HRR are in agreement. Moreover, it is observed that the agreement between the measured and simulated results of combustion characteristics (e.g., CA10-90 and CA50), thermal efficiency, and emissions is also satisfactory (all these results are presented in Section Result and Discussion).

TABLE 1 | Engine specifications.

Engine type	Single cylinder-caterpillar 3,400
Bore × stroke	137.2 mm × 165.1 mm
Conn. rod length	261.62 mm
Displacement vol.	2.44 L
Compression ratio	16.25
Diesel fuel injector-type	Common rail injector-direct injection
Number of nozzle hole	6
Nozzle hole diameter	0.23 mm
Spray umbrella angle	130°
Natural gas injection timing	−355° ATDC
Number of intake valve	2
Number of exhaust valve	2
IVO	−358.3° ATDC
IVC	−169.7° ATDC
EVO	145.3° ATDC
EVC	348.3° ATDC

ATDC, after top dead center; EVO, exhaust valve opening; EVC, exhaust valve closing; IVO, intake valve opening.

TABLE 2 | Varied experimental test conditions.

Engine load	NG (%)	Air flow (kg/h)	Diesel flow (kg/h)	NG flow (kg/h)	Diesel injection timing (ATDC)
25% load (BMEP = 4.05 bar)	0	66.89–68.82	1.79–1.91	0	−10 to −22
	25	67.53–68.13	1.31–1.40	0.41–0.44	−10 to −19
	50	66.87–68.01	0.89–0.97	0.85–0.94	−10 to −17
	75	66.59–67.69	0.42–0.50	1.24–1.47	−10 to −26
50% load (BMEP = 8.10 bar)	0	90.27–92.53	3.08–3.20	0	−14 to −28
	50	88.91–90.06	1.50–1.63	1.41–1.51	−14 to −26
	75	88.73–89.52	0.74–0.78	2.09–2.26	−14 to −25
	90	87.06–90.02	0.30–0.31	2.49–2.73	−14 to −26.5
75% load (BMEP = 12.15 bar)	0	111.93–112.45	4.50–4.73	0	−14 to −25
	25	109.81–110.82	3.26–3.64	1.01–1.12	−10 to −22
	75	108.19–106.48	1.09–1.13	3.05–3.15	−12 to −16
	90	107.27–107.92	0.42–0.48	3.69–3.83	−10.5 to −15
100% load (BMEP = 17.6 bar)	0	192.85–192.91	7.92–8.13	0	−20 to −22.5
	25	190.12–190.83	5.93–6.19	1.84–1.92	−17 to −20
	50	188.69–189.53	3.91–4.16	3.64–3.83	−14.5 to −18
	65	187.67–188.27	2.71–2.85	4.67–4.92	−12 to −16

ATDC, after top dead center; BMEP, brake mean effective pressure.

RESULTS AND DISCUSSION

In addition to the experimental data, numerical simulation results (i.e., local equivalence ratio, temperature, and CH_4 distribution contours) are also presented for some cases to help better understand the combustion process. Note that CA10, CA50, and CA90 refer to the crank angle position, which corresponds to 10%, 50%, and 90% of cumulative heat release, respectively. The CA50 and the interval from CA10 to CA90 are defined as the combustion phasing and combustion duration, respectively. The average cylinder pressure of 100 consecutive cycles is used as a primary input for calculating HRR using **Eq. 2**.

$$HRR = \frac{\gamma}{\gamma - 1} P \frac{dV}{d\theta} + \frac{1}{\gamma - 1} V \frac{dP}{d\theta} \tag{2}$$

where γ is the ratio of specific heat at constant pressure to that at constant volume, P is the measured cylinder pressure, V is the cylinder volume, and θ is the crank angle in degrees.

Figure 4 presents the measured cylinder pressure and HRR traces for different %NGs at BMEPs of 4.05 bar (**Figure 4A**) and 12.15 bar (**Figure 4B**). For brevity, the cylinder pressure and HRR plots shown herein are only taken for the test case of SODI = −14° after top dead center (ATDC) at BMEPs of 4.05 bar (**Figure 4A**) and 12.15 bar (**Figure 4B**). It can be observed, from **Figure 4A**, that increasing %NG from 0% to 50% yields a consistent growth in the HRR peak at BMEP = 4.05 bar. This is attributed to the fact that more premixed natural gas–air mixture is burnt under premixed combustion regime. However, beyond this point (i.e., 50%), peak HRR falls dramatically. The reason behind this will be explained in **Figure 5A**. The HRR profile of the NDDF engine at BMEP = 4.05 bar indicates that there are only two stages of combustion, namely, premixed followed by diffusion, similar to diesel engine. It can be seen that after premixed and diffusion combustion, there is no flame propagation of natural gas since the premixed natural gas–air mixture is very lean. **Figure 4A** also indicates that adding small amount of natural gas (e.g., 25%) yields a relatively minor change in the cylinder pressure profile, with the most significant difference being its lower cylinder peak pressure compared with 0% NG. Further increase in %NG (i.e., 50% and 75%) continuously lowers the peak cylinder pressure, indicating the struggle of the engine to combust large amount of natural gas. This is also reflected in the PPRR for 75% NG under low load conditions, as it will be discussed later (**Figure 5A**).

A different combustion behavior occurs under higher engine load conditions. As shown in **Figure 4B**, increasing %NG from 0% to 75% slightly increases the first peak of HRR similar to the case at lower engine load (**Figure 4A**). This is due to the fact that a higher portion of natural gas–air mixture participates in reactions in the premixed combustion stage when increasing %NG from 0% to 75% at BMEP = 12.15 bar. **Figure 4B** also shows that the second peak of HRR significantly increases when increasing %NG from 0% to 75%, implying a shift from diffusion to flame propagation of natural gas–air mixture combustion. It can be seen in **Figure 4B** that further increase in %NG from 75% to 90% slightly decreases the first peak while significantly decreases the

TABLE 3 | Fixed experimental test conditions.

Engine load	Intake temperature (°C)	Intake pressure (bar)	Speed (RPM)	Injection pressure (bar)	Engine oil temperature (°C)	Coolant water temperature (°C)
25% load	40	1.05	910	525	85	85
50% load	40	1.50	910	525	85	85
75% load	40	1.80	910	525	85	85
100% load	40	2.20	1,120	525	85	85

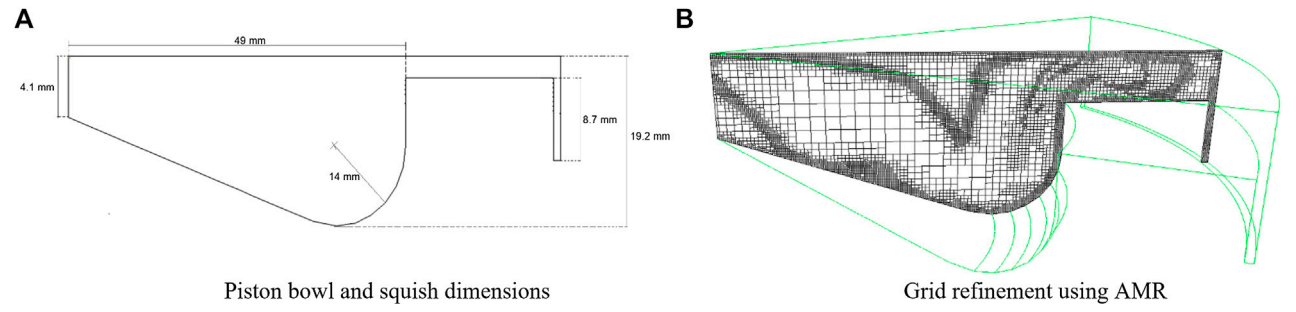

Figure 2 | Piston bowl and squish dimensions and grid refinement using CONVERGE AMR tool.

second peak of the HRR profile. The former is attributed to the fact that the overall equivalence ratio in the flame kernel in the premixed combustion becomes lower, and the latter is due to lower flame propagation speed of natural gas–air mixture. Further related discussion is provided later on. The cylinder pressure profile (**Figure 4B**) indicates that the addition of a small amount of natural gas (i.e., 25% NG) has only a slight effect (slight increase in cylinder peak pressure) on the cylinder pressure compared with that of diesel combustion (i.e., 0% NG). However, a higher increase in %NG (i.e., 75%–90%) results in a significant increase in the peak pressure.

Figure 5 displays the measured and calculated PPRR for different %NGs and SODIs at BMEPs of 4.05 and 12.15 bar. The simulation was only conducted for one SODI at each load condition to minimize the computation cost. It can be observed from the measured results that advancing SODI increases the PPRR under all examined engine load conditions. This is mainly due to the fact that advancing SODI lengthens the ignition delay, which allows more time for diesel fuel to mix with the premixed natural gas–air mixture before the start of combustion. It is observed that PPRR jumps under advanced SODI and high % NGs of 75 and 90% at BMEP of 12.15 bar. Both measured and calculated results showed that at a given SODI, PPRR first increases and then starts declining with increasing %NG under both low and high load conditions. For example, at BMEP of 4.05 bar (**Figure 5A**), PPRR increases with increasing %NG from 0% to 50% and then drops with further increase in %NG. Also, at BMEP of 12.15 bar (**Figure 5B**), PPRR first increases with increasing %NG from 0% to 75% and then starts decreasing with further increase in %NG up to 90%. In order to understand the causes behind this behavior, the concentration contours of local equivalence ratio (at CA10), cylinder temperature (at 2° after CA10), and CH_4 (at 2° after CA10) under different %NGs and a fixed SODI of −14° ATDC are presented in **Figure 6**. As shown in **Figure 6A** (BMEP = 4.05 bar), increasing %NG from 0% to 50% increases the local equivalence ratio in the ignition kernel zone. This implies that more natural gas–air mixture burns under premixed combustion stage, which results in increased temperature, intense HRR (**Figure 4A**), and higher PPRR right after the onset of ignition (**Figure 5A**). However, with further increase in %NG from 50% to 75%, the local equivalence ratio in the ignition kernel zone decreases as more lean natural gas–air mixture mixes with diesel before ignition. This results in a slower heat release and lower PPRR. A similar behavior is observed under higher engine load conditions (at BMEP of 12.15 bar) (**Figure 6B**).

Figure 7 shows the variation of combustion phasing (CA50) at four different engine load conditions. It can be seen that advancing diesel injection timing (in the range of conventional diesel engine) advances the combustion phasing of the NDDF engine at all load conditions. This is expected since diesel and natural gas–air mixture starts mixing earlier with advancing diesel injection timing. At a given SODI, the effect of %NG on combustion phasing varies with the engine load. Under BMEPs of 4.05 and 8.10 bar (**Figure 7A,B**), increasing %NG retards the combustion phasing. However, at BMEPs of 12.15 and 17.60 bar (**Figure 7C,D**), the combustion phasing generally advances when increasing %NG except in the case when increasing natural gas fraction from 75% to 90% at BMEP of 12.15 bar where the combustion phasing slightly retards. To understand the reason behind this observation, the temperature distribution contours under BMEPs of 4.05 and 12.15 are presented in **Figure 8A,B**, respectively.

As previously mentioned, increasing %NG from 0% to 50% increases the local equivalence ratio, whereas further increase up to 75% decreases the local equivalence ratio in the ignition kernel zone at the onset of combustion under BMEP = 4.05 bar. After the premixed combustion stage, the equivalence ratio of natural gas–air mixture around the ignition kernel zone (**Figure 6A**) is very low and hence cannot sustain further burning of the mixture. In addition, the temperature inside the combustion chamber (**Figure 8A**) is not high enough to support the burning of the remainder of the mixture. For example, for 50% NG, the local equivalence ratio and temperature of natural gas–air mixture surrounding the ignited zone is approximately 0.25 and 1,000°C at an engine crank angle of CA10. Increasing %NG to 75% slightly increases the local equivalence ratio around the ignition pocket ($\phi \cong 0.34$), while the temperature in the flame kernels drops as shown in **Figure 8A**. These conditions in the cylinder make it more difficult for the pilot diesel to completely combust the premixed natural gas–air mixture, and hence, the flame quenches after the elapse of the premixed and diffusion combustion stages. Therefore, more heat is released at a crank angle farther away from the TDC, which causes combustion phasing to retard when increasing %NG from 0% to 75% at BMEP = 4.05 bar.

However, increasing %NG, generally, advances the combustion phasing under BMEPs of 12.15 and 17.60 bar. **Figure 8B** shows the high temperature regions inside the combustion chamber. The expansion of high temperature zone at a specific duration of the engine crank angle after the elapse of diffusion combustion is a result of flame propagation of the premixed natural gas–air mixture. Hence, temperature distribution will be used here as a representation of flame propagation to qualitatively compare the results at different % NGs. As shown in **Figure 8B**, at 25% NG, a high temperature region occurs only in the central region of the combustion chamber where the local equivalence ratio is also high. However, the flame does not propagate into the regions near the cylinder wall and squish regions. This is due mainly to the low equivalence ratio around the ignition pocket (**Figure 6B**). With further increase in %NG to 75%, the high temperature zone

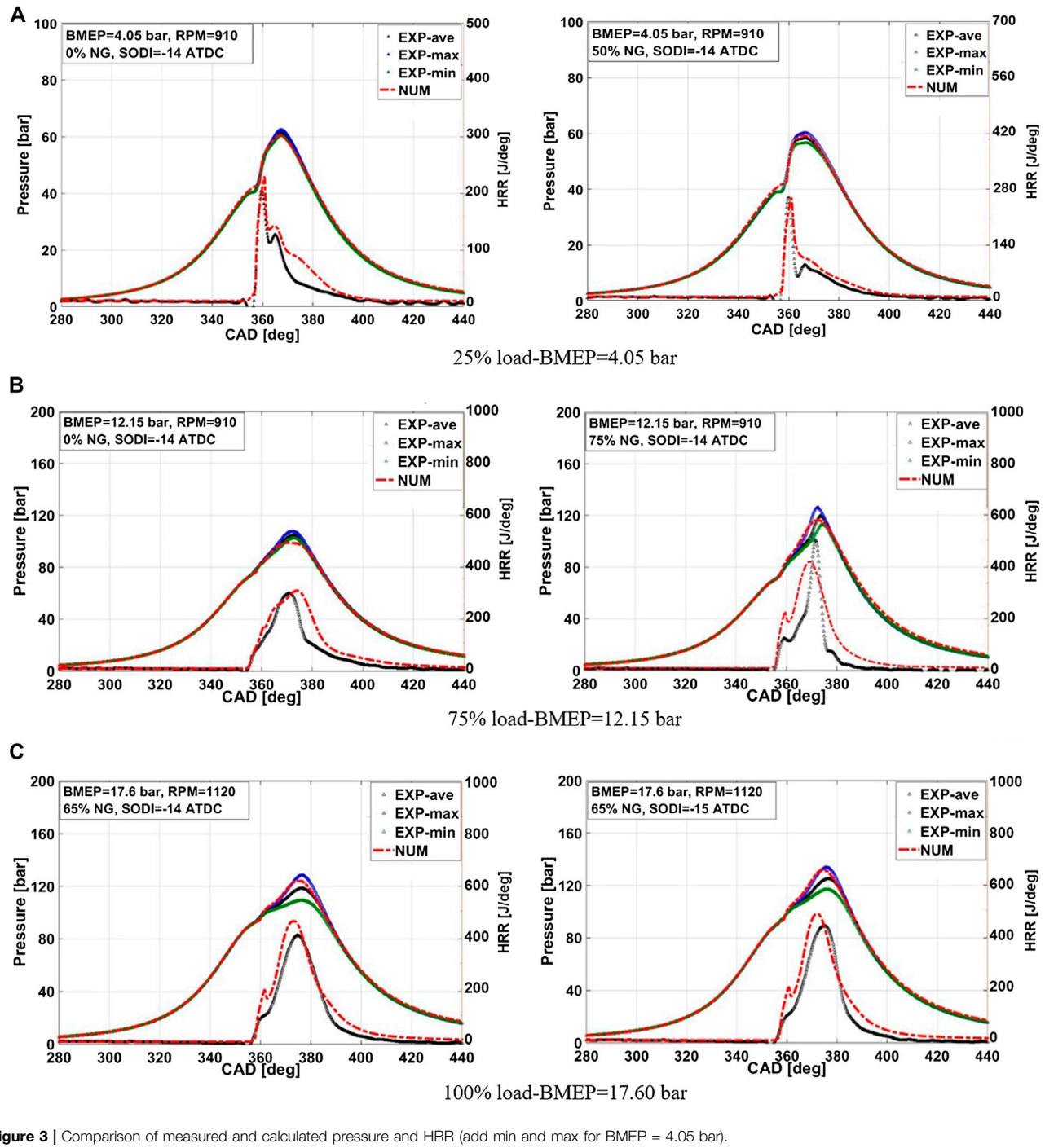

Figure 3 | Comparison of measured and calculated pressure and HRR (add min and max for BMEP = 4.05 bar).

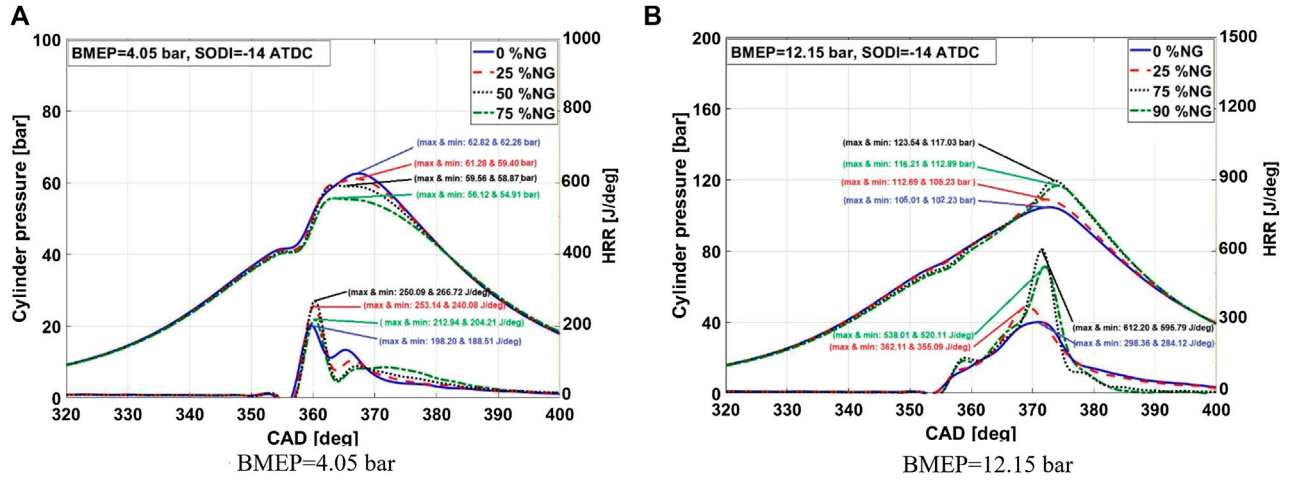

Figure 4 | Measured cylinder pressure and HRR of NDDF engine at BMEPs of 4.05 and 12.15 bar.

occupies almost the entire combustion chamber (i.e., piston bowl, wall, and squish regions at engine crank angle of 12° after CA10) within the same crank angle duration (from 4° to 12° after CA10) similar to the case of 25% NG. This is an indication of higher flame propagation speed of natural gas–air mixture. Under this condition, both the equivalence ratio of the premixed natural gas–air mixture ($\phi_{NG} \cong 0.65$) and the charge temperature (T ≅ 1,150°C) are higher inside the cylinder, which significantly enhance the flame propagation speed of the premixed natural gas–air mixture. With further increase in %NG to 90%, the high temperature zone (**Figure 8B**) does not completely fill the combustion chamber at engine crank angle of 12° after CA10 compared with 75% NG. This indicates that the flame propagation speed slightly decreases compared with that of 75% NG. Under this condition (90% NG), the equivalence ratio of the premixed natural gas–air mixture is $\phi \cong 0.75$, which is higher than that of the 75% NG and is expected to improve the flame propagation speed. However, at 90% NG, the charge temperature at the beginning of the combustion is lower than that of 75% NG (shown in **Figure 6B**), which reduces the flame propagation speed of natural gas–air mixture. Moreover, it can be seen, from **Figure 6B**, that at engine crank angle of 2° after

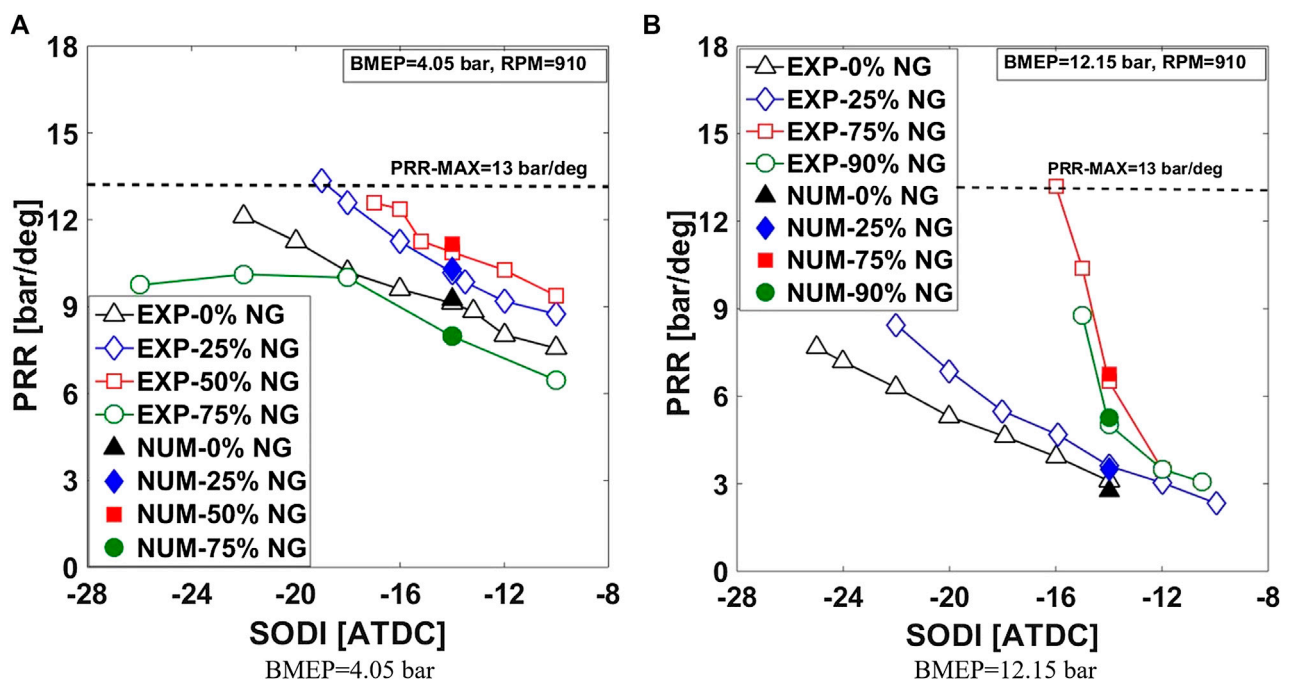

Figure 5 | PPRR of NDDF engine at BMEPs of 4.05 and 12.15.

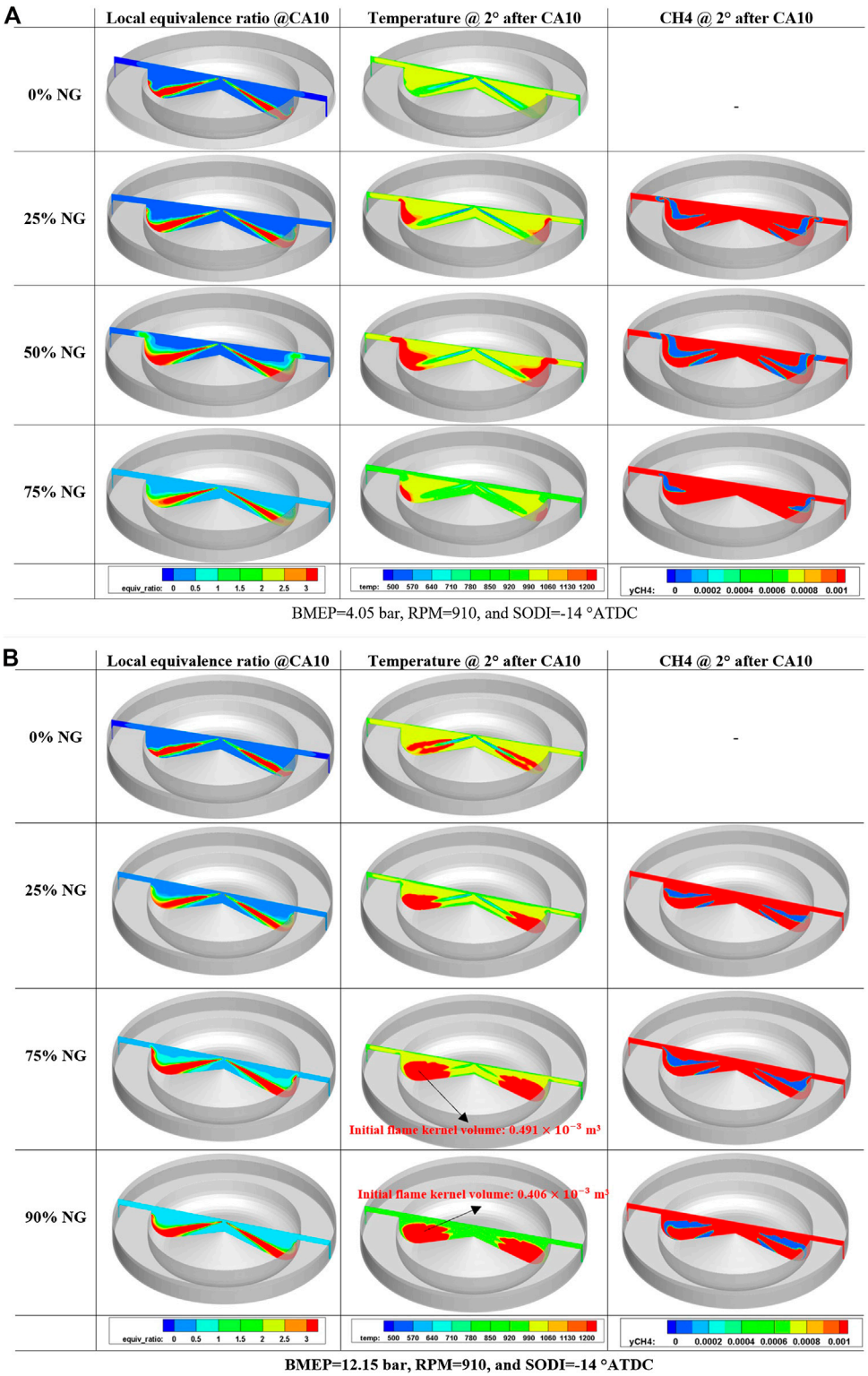

Figure 6 | Local equivalence ratio, temperature, and CH4 distributions of NDDF engine under BMEPs of 4.05 and 12.15 bar.

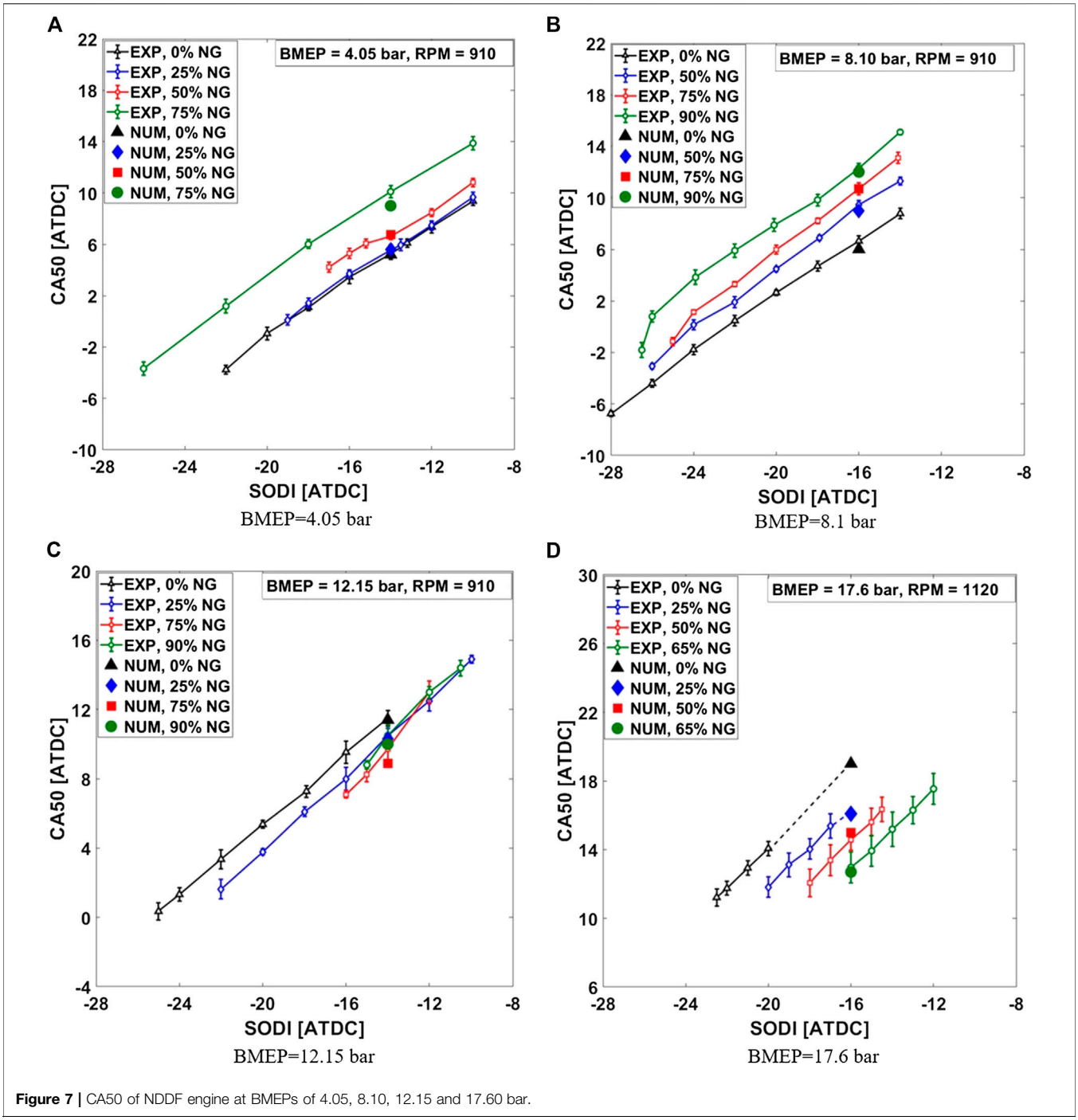

Figure 7 | CA50 of NDDF engine at BMEPs of 4.05, 8.10, 12.15 and 17.60 bar.

CA10, the size of the initial flame kernel at 90% NG (i.e., volume of initial flame kernel at 90% NG = 0.406×10^{-3} m^3) is smaller than that at 75% NG (i.e., volume of initial flame kernel at 75% NG = 0.491×10^{-3} m^3), which is due to the lower amount of injected diesel fuel (lower equivalence ratio inside the flame kernel). This could reduce the flame propagation speed of natural gas–air mixture. The effect of lower cylinder temperature and smaller initial flame kernel on flame propagation speed of natural gas–air mixture is more significant than that of higher premixed equivalence ratio, which results in lower flame propagation speed and slightly retarded combustion phasing when %NG increases from 75% to 90%.

Figure 9 shows the combustion duration of the NDDF engine at BMEPs of 4.05 and 12.15 bar. It can be seen that the combustion duration increases with increasing natural energy fraction from 0% to 75% at BMEP of 4.05 bar (**Figure 9A**). As shown in **Figure 7**, increasing %NG retards the combustion

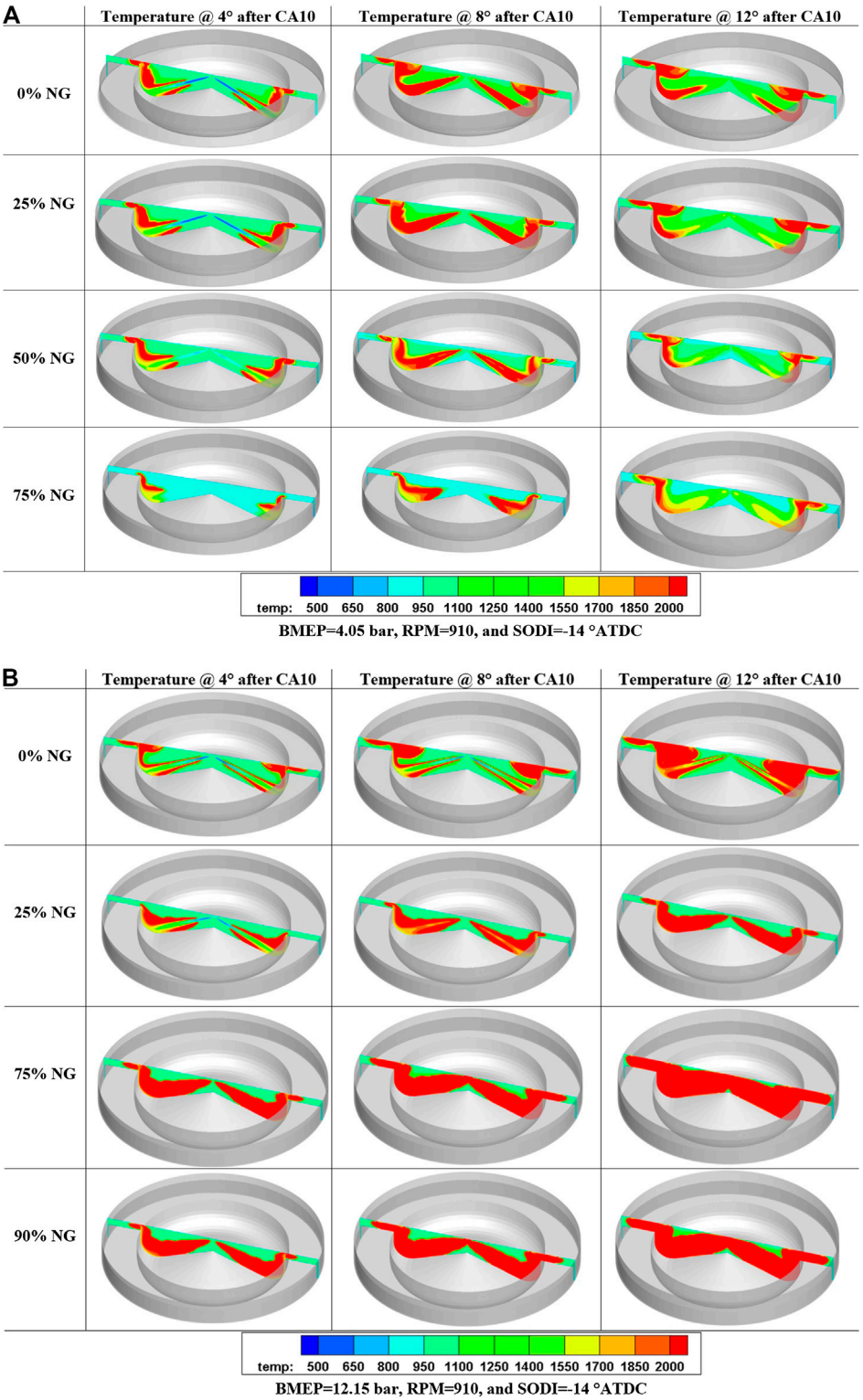

Figure 8 | Temperature distributions of NDDF engine at different engine crank angles under BMEP = 12.15 bar, SODI = −14 ATDC.

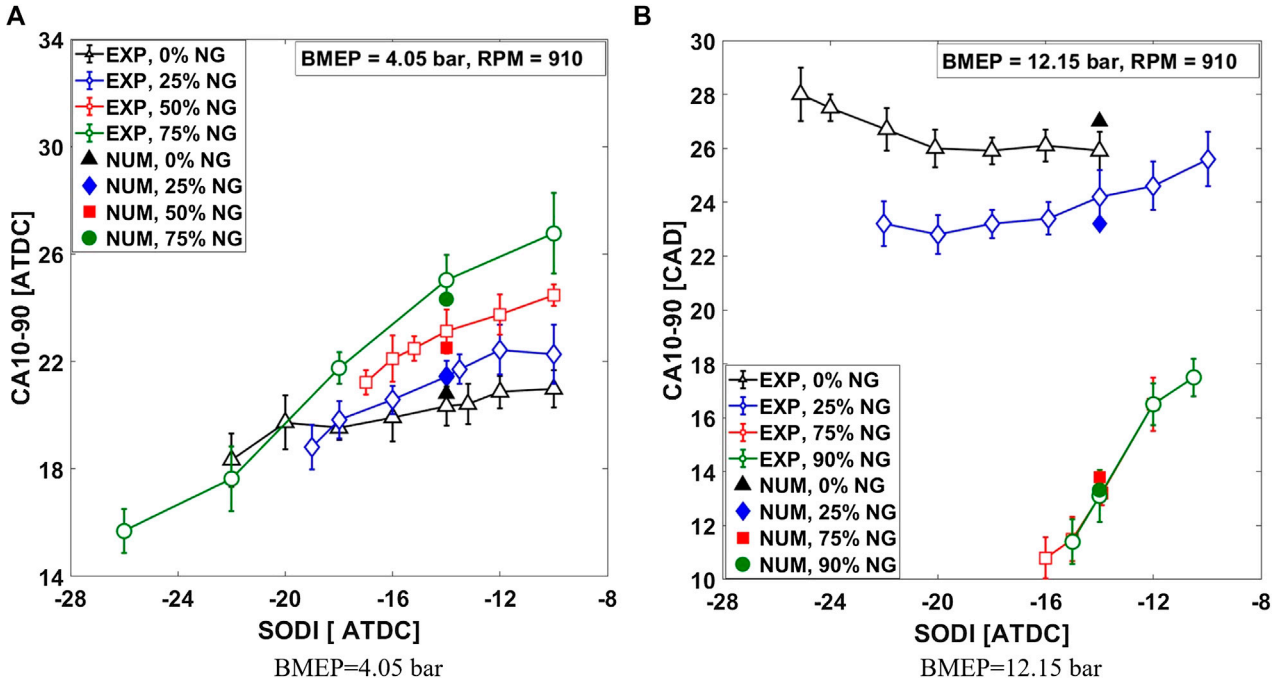

Figure 9 | Combustion duration of NDDF engine under BMEPs of **(A)** 4.05 and **(B)** 12.15 bar.

phasing and therefore lengthens the combustion duration. However, at BMEP of 12.15 bar, the combustion duration significantly decreases with increasing %NG from 0% to 75%. This is due mainly to the increase in the flame propagation speed of natural gas–air mixture as indicated by the flame temperature distribution contours in **Figure 8B**. The combustion duration slightly increases with further increase in %NG from 75% to 90%, which is due mainly to the lower charge temperature and smaller flame kernel size at the onset of combustion.

Figure 10 depicts the variation of indicated thermal efficiency (ITE) of the NDDF engine for four different load conditions. ITE is calculated as (Yousefi et al., 2019)

$$\mathrm{ITE} = \frac{\text{Indicated power}}{(\dot{m}_{NG}\mathrm{LHV}_{NG}) + (\dot{m}_{D}\mathrm{LHV}_{D})} \times 100 \qquad (3)$$

where $\dot{m}_{NG}$ and $\dot{m}_{D}$ are the mass flow rates of natural gas and diesel, respectively, and LHV_{NG} and LHV_{D} are the lower heating value of natural gas and diesel, respectively.

ITE shows a different behavior with %NG, diesel injection timing, and engine load. As shown in **Figure 10A**, at BMEP of 4.05 bar, increasing %NG at a retarded SODI (i.e., −14° ATDC) significantly decreases thermal efficiency. This is due to the failure of flame propagation of the premixed natural gas–air mixture, which causes a very late combustion phasing (**Figure 7A**) and consequently low thermal efficiency. However, advancing SODI significantly improves the combustion of premixed charge and increases thermal efficiency of the NDDF engine, especially at higher %NGs (i.e., 75% NG). Under BMEP = 4.05 bar and dual-fuel mode, the highest thermal efficiency (35.8%) is achieved at 75% NG and SODI = −26 ATDC, which is comparable with that of diesel engine.

A similar behavior occurs at BMEP = 8.10 bar (**Figure 10B**) where advancing SODI significantly improves the premixed natural gas–air mixture combustion and consequently increases thermal efficiency of the NDDF engine, especially at 90% NG. However, due to very advanced combustion phasing (**Figure 7B**), thermal efficiency starts dropping when SODI is earlier than −22° ATDC. At BMEP = 8.1 bar, the highest thermal efficiency in dual-fuel mode is 39.9%, which is obtained at 90% NG and SODI = −22° ATDC. However, the highest thermal efficiency of the diesel engine at similar conditions is only 38.6%.

Interestingly, at BMEPs of 12.15 and 17.60 bar (**Figure 10C,D**), increasing %NG significantly increases thermal efficiency of the NDDF engine at a given SODI. This is due mainly to a combination of advanced combustion phasing (**Figure 7C,D**), improved flame propagation speed of natural gas–air mixture, and shorter combustion duration. However, it can be observed, from **Figure 10C**, that increasing %NG from 75% to 90% slightly decreases thermal efficiency of the NDDF engine. This is due to the fact that the combustion phasing slightly retards and flame propagation speed slightly decreases. Advancing SODI significantly enhances thermal efficiency of the NDDF engine under medium-to-high load conditions. This is primarily attributed to better combustion phasing when advancing diesel injection timing. At BMEP = 12.15 bar, the highest thermal efficiency in dual-fuel mode is 41.4%, which is obtained at 25% NG and SODI = −22° ATDC. However, the highest thermal efficiency of its counterpart's diesel engine is 40.1%, which occurs at SODI = −24° ATDC. Moreover, at

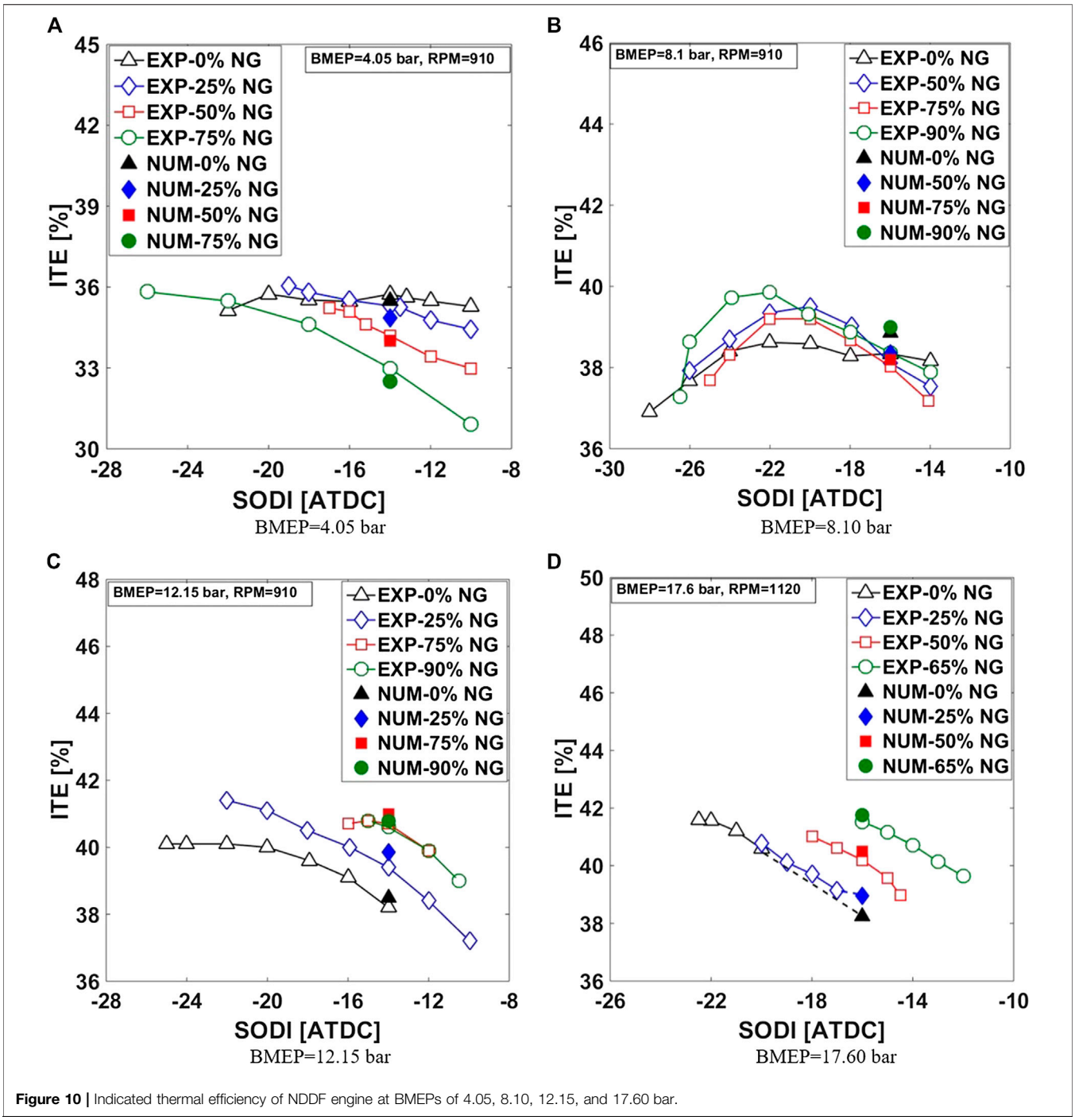

Figure 10 | Indicated thermal efficiency of NDDF engine at BMEPs of 4.05, 8.10, 12.15, and 17.60 bar.

BMEP = 17.60, the highest thermal efficiency (41.5%) of NDDF is achieved at 65% NG and SODI = −16° ATDC, which is comparable with that of the diesel (i.e., 41.6%). It can be concluded from the above discussion that, by tuning diesel injection timing and %NG, a thermal efficiency of the NDDF engine similar that of diesel can be achieved under low-to-high load conditions.

Figure 11 shows the variation of combustion efficiency of the NDDF engine at four different load conditions. Combustion efficiency is calculated using **Eq. 4**.

$$CE = \left[100 - \frac{(ISCO.LHV_{CO} + ISHC.LHV_{DF})}{(\dot{m}_{NG}.LHV_{NG} + \dot{m}_{D}.LHV_{D})}\right] \times indicated\ power \times 100 \quad (4)$$

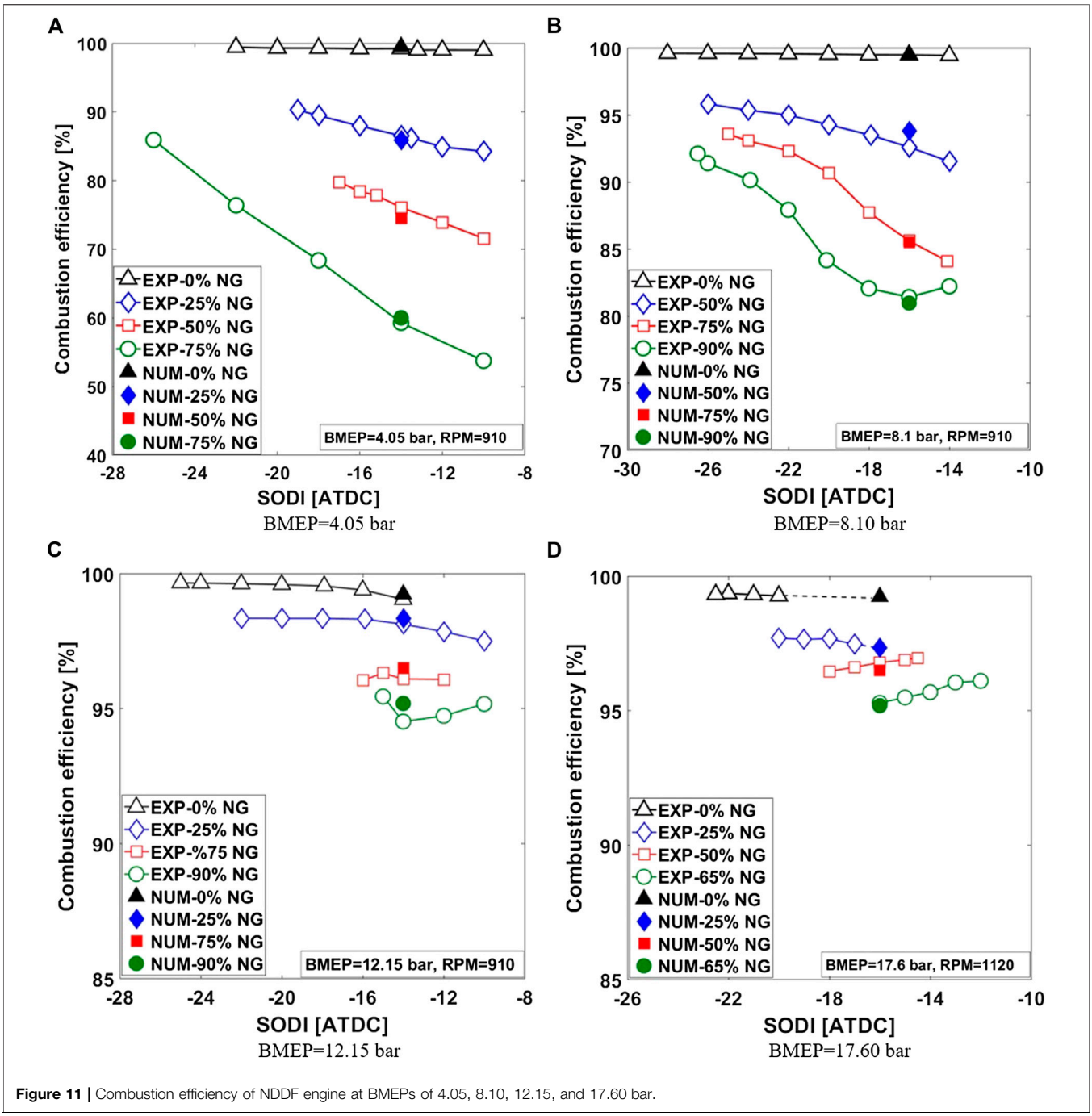

Figure 11 | Combustion efficiency of NDDF engine at BMEPs of 4.05, 8.10, 12.15, and 17.60 bar.

where ISCO and ISHC are, respectively, the indicated specific CO emissions and indicated specific UHC emissions (methane and non-methane emissions). LHV_{DF} is the lower heating value of dual-fuel mode, which is calculated using **Eq. 5**.

$$LHV_{DF} = \frac{\dot{m}_{NG} LHV_{NG} + \dot{m}_{D} LHV_{D}}{\dot{m}_{NG} + \dot{m}_{D}} \quad (5)$$

As shown in **Figure 11**, combustion efficiency decreases with increasing natural gas energy fraction under all examined (low-to-high) load conditions. This is mainly due to the higher amount of unburned fuel in the exhaust, which is caused by the increase in natural gas energy fraction. It can be observed in **Figures 11C,D** that at medium-to-high engine load conditions, combustion efficiency is relatively high and reaches 95% even for high natural gas energy fractions (i.e., NG = 90%). This is mainly due to improved flame propagation speed of premixed natural gas–air mixture under medium-to-high load conditions (shown in **Figure 8B**). It can be seen in **Figure 11A,B** that a decrease in combustion efficiency is more significant under low-to-medium

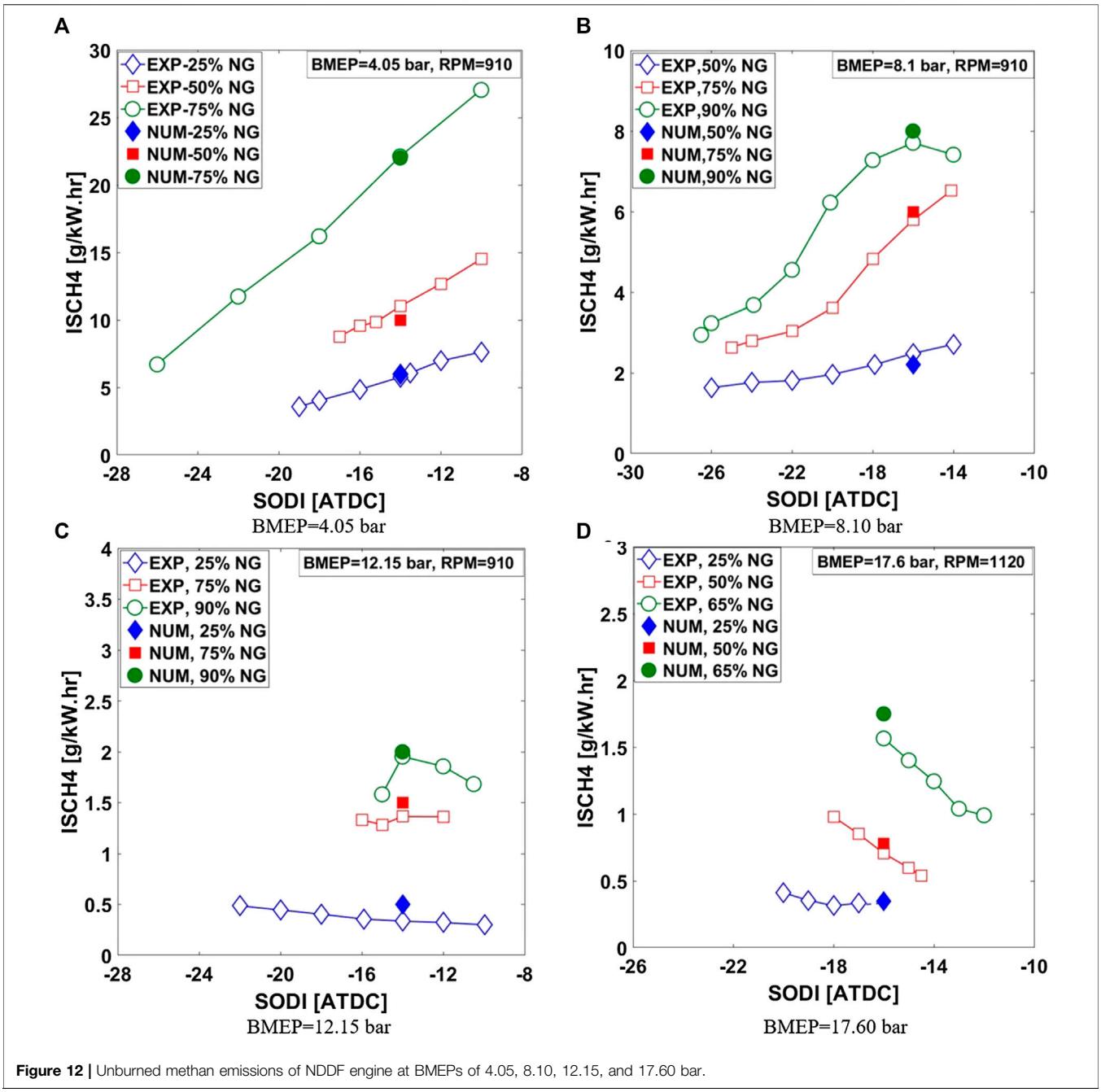

Figure 12 | Unburned methan emissions of NDDF engine at BMEPs of 4.05, 8.10, 12.15, and 17.60 bar.

load conditions, which is due to unsuccessful flame propagation of premixed natural gas–air mixture. However, advancing SODI under low-to-medium load conditions significantly improves combustion efficiency especially at higher natural gas energy fractions. This is due to the fact that advancing SODI allows more time for diesel fuel to mix with premixed natural gas–air mixture before the start of combustion, which results in improved combustion efficiency. However, advancing SODI does not significantly improve combustion efficiency of the NDDF engine at medium-to-high load conditions. This is attributed to a slight increase in unburned methane emissions when advancing SODI under medium-to-high load conditions (**Figure 12C,D**). Further explanation can be found elsewhere (Yousefi et al., 2019).

Figure 12 shows the unburned methane emissions of the NDDF engine under different engine loads. As expected, methane emissions grow significantly with increasing %NGs under all examined engine load conditions. However, this growth becomes much smaller at BMEPs of 12.15 and 17.60 bar (**Figure 12C,D**). It is observed that advancing SODI significantly decreases unburned methane emissions of the NDDF engine at BMEPs of 4.05 and 8.10 bar. However, methane emissions have a different behavior under higher engine load conditions. Advancing

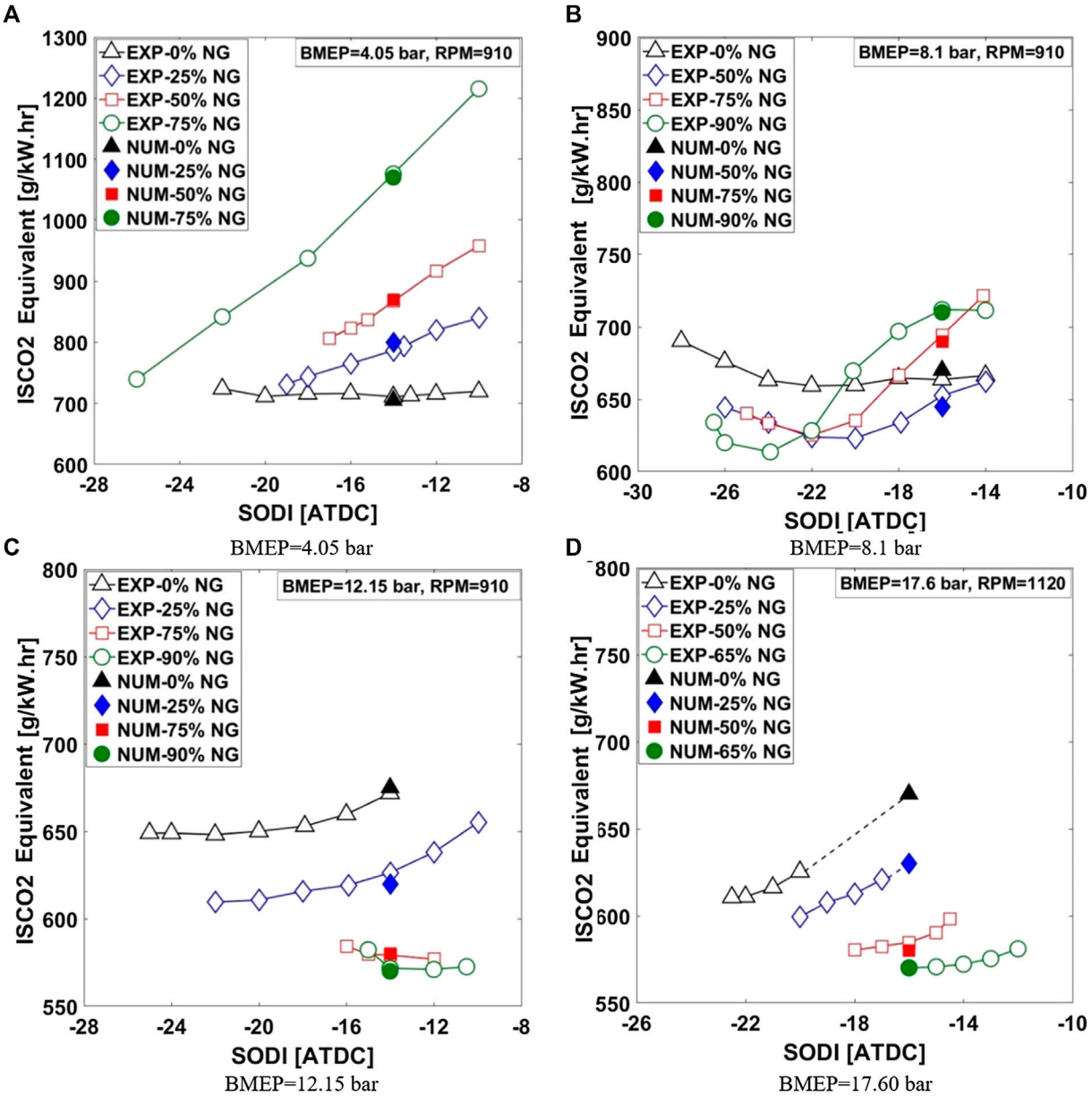

Figure 13 | CO_2 equivalent emissions of NDDF engine at BMEPs of 4.05, 8.10, 12.15, and 17.60 bars.

SODI increases unburned methane emissions at the engine load of 12.15 bar and %NGs of 25% and 90%. Unburned methane emissions drop at SODI of −15° ATDC and 90% NG. Furthermore, unburned methane is relatively flat at engine load of 12.15% and 75% NG. At the highest engine load (BMEP = 17.60 bar), methane emission increase is observed with advancing SODI, especially for 50% and 65% NG. An explanation of this is observation reported in Yousefi et al., (2019).

Figure 13 depicts CO_2 equivalent emissions at different NDDF engine load conditions. As shown in **Figure 13A**, increasing %NG increases CO_2 equivalent emissions at any given SODI for BMEP of 4.05 bar. This is mainly due to a significant amount of unburned methane emissions under low engine load conditions. Advancing SODI significantly reduces CO_2 equivalent emissions of the NDDF engine at BMEP of 4.05 bar. However, advancing SODI does not affect CO_2 equivalent emissions of the diesel engine under a load of 4.05 bar. At this NDDF engine load (BMEP = 4.05 bar), the lowest CO_2 equivalent emissions are 740 g/kW·h, which occur at 75% NG and SODI = −26° ATDC. However, the lowest CO_2 equivalent emissions of the diesel engine are 711 g/kW h.

At an engine load of 8.10 bar (**Figure 13B**) and retarded diesel injection timings, CO_2 equivalent emissions first decrease and then increase with increasing %NG. This is the result of thermal

efficiency and unburned methane emissions. At retarded SODI, thermal efficiency increases when increasing %NG from 0% to 50%, which decreases CO_2 equivalent emissions. However, unburned methane emissions increase with %NG, which leads to an increase in CO_2 equivalent emissions. The effect of the former is more significant, which yields lower CO_2 equivalent emissions with increasing %NG at retarded SODI. However, under advanced SODI, CO_2 equivalent emissions decrease with increasing %NG. This is due to the fact that the SODI timing is very advanced, which allows longer time for natural gas and diesel fuel to mix before the start of combustion, which makes the combustion happen quickly around the TDC and hence significantly decreases unburned methane emissions and increases thermal efficiency. Advancing SODI from a late timing decreases CO_2 equivalent emissions at BMEP of 8.10 bar. However, CO_2 equivalent emissions increase with further advancing diesel injection timing as a result of a decrease in thermal efficiency (**Figure 10B**). At this NDDF engine load (BMEP = 8.10 bar), the lowest CO_2 equivalent emissions are 613 g/kW h, which occur at 90% NG and SODI = −24° ATDC. This is almost 7% lower than the lowest CO_2 equivalent emissions of the diesel engine (659 g/kW h), which occur at SODI = −22° ATDC.

Figures 13C,D show that increasing %NG significantly decreases CO_2 equivalent emissions of the NDDF engine under BMEPs of 12.15 and 17.60 bar. As shown in **Figures 10 and 12**, increasing %NG increases thermal efficiency and unburned methane emissions of the NDDF engine at BMEPs of 12.15 and 17.60 bar. However, its effect on thermal efficiency is more significant than methane emissions, which results in a significant decrease in CO_2 equivalent emissions. At NDDF engine load of 12.15 bar, the lowest CO_2 equivalent emissions are 571 g/kW·h, which occur at 90% NG and SODI = −14° ATDC. This is almost 11.8% lower than the lowest CO_2 equivalent emissions of the diesel engine (648 g/kW·h). Moreover, at BMEP = 17.60 bar, the lowest CO_2 equivalent emissions of the NDDF engine are 571 g/kW·h, which occur at 90% NG and SODI = −16° ATDC. This is almost 6.4% lower than the lowest CO_2 equivalent emissions of the diesel engine (610 g/kW·h).

CONCLUSIONS

An experimental study was conducted to examine the effect of % NG on the combustion performance and GHG emissions of the NDDF engine under low-to-high engine load conditions. A sweep of diesel injection timing was also tested under each operating conditions. A CFD model was also used to further explain the mechanisms behind the phenomena observed in the experiments. The main findings of this study are outlined below.

- The effect of %NG on combustion performance depends on the engine load. The PPRR increases and then drops with increasing %NG under all examined engine load conditions. Increasing %NG from 0% to 50% under low load conditions and from 0% to 75% at high load conditions increases the local equivalence ratio inside the ignition kernel, which indicates that more premixed natural gas–air mixture participates in reactions during the premixed combustion stage. This results in an increased flame temperature, intense HRR, and higher PPRR right after ignition. However, increasing %NG beyond this range decreases local equivalence ratio inside the ignition kernel, which leads to slower heat release and lower PPRR.
- Under low-to-medium load conditions, increasing %NG retards the combustion phasing at a given SODI. Under low-to-medium load conditions, the equivalence ratio of natural gas–air mixture and charge temperature around the ignition pocket is very low. These conditions cause flame quenching after the elapse of premixed and diffusion combustion stages, which, in turn, retards combustion phasing. However, under medium-to-high load conditions, the premixed equivalence ratio and charge temperature are high enough to support flame propagation. Therefore, increasing %NG increases flame propagation speed and generally advances the combustion phasing.
- Increasing %NG at retarded SODI significantly decreases the engine thermal efficiency under low-to-medium load conditions. However, advancing SODI significantly enhances thermal efficiency of the NDDF engine, especially at higher %NGs. Increasing %NG significantly increases thermal efficiency of the NDDF engine at medium-to-high load conditions due to improved flame propagation speed of the premixed natural gas–air mixture.
- Methane emissions grow significantly with increasing %NG under all examined engine load conditions. However, this growth becomes much weaker under medium-to-high engine load conditions. Increasing %NG significantly increases CO_2 equivalent emissions under engine low load conditions. This is due mainly to a significant amount of emitted unburned methane at low load conditions. However, increasing %NG significantly decreases CO_2 equivalent emissions of the NDDF engine by 6%–11% under medium-to-high load conditions.

DATA AVAILABILITY STATEMENT

The raw data supporting the conclusions of this article will be made available by the authors, without undue reservation.

AUTHOR CONTRIBUTIONS

AY wrote the manuscript with support from HG and MB. AY performed the numerical simulations and analyzed the experimental and numerical results. HG carried out the experiments. All authors provided critical feedback and helped shape the research, analysis and manuscript. MB supervised the project.

FUNDING

The funding of the experimental work was provided by Natural Resources Canada through the PERD Energy End Use (project

3B03.003) and National Research Council Canada through the internal Bioenergy Program. The numerical simulation was supported by CONVERGENT Science, Inc. and Compute Canada at the University of Manitoba.

REFERENCES

Ahmad, Z., Aryal, J., Ranta, O., Kaario, O., Vuorinen, V., and Larmi, M. (2018). An optical characterization of dual-fuel combustion in a heavy-duty diesel engine. SAE International, Technical Paper 2018-01–0252. https://doi.org/10.4271/2018-01-0252. Abstract.

Bataille, C., Sawyer, D., and Melton, N. (2015). Pathways to deep decarbonization in Canada. Carbon Management Canada, Low Carbon Pathways Group, SDSN-IDDRI.

Cesar, J., Egúsquiza, C., and Braga, S. L. (2015). Experimental investigation of a diesel cycle engine operating on natural gas/diesel dual-fuel mode. SAE International, Technical Paper 2011-36-0351. https://doi.org/10.4271/2011-36-0351.

Dahodwala, M., Joshi, S., Koehler, E. W., and Frank, M. (2014). Investigation of diesel and CNG combustion in a dual fuel regime and as an enabler to achieve RCCI combustion. SAE International, Technical Paper 2014-01-1308. https://doi.org/10.4271/2014-01-1308.

Guo, H., and Liko, B. (2019). "Injector tip temperature and combustion performance of a natural gas-diesel dual fuel engine at medium and high load conditions," in Proceeding of ASME 2018, V001T03A021. Available at: https://doi.org/10.1115/icef2018-9664.

Guo, H., Liko, B., Luque, L., and Littlejohns, J. (2017). "Combustion performance and unburned hydrocarbon emissions of a natural gas-diesel dual fuel engine at a low load condition," in Proceedings of the ASME 2017 internal combustion engine division fall technical conference ICEF2017, Seattle, WA, October 15–18, 2017, 1–9.

Guo, H., Neill, W. S., and Liko, B. (2015). "An experimental investigation on the combustion and emissions performance of a natural gas - diesel dual fuel engine at low and medium loads," in Proceedings of the ASME 2015 internal combustion engine division fall technical conference ICEF2015, Houston, TX, November 8–11, 2015, 130–137. https://doi.org/10.1115/ICEF2015-1041.

Jiaqiang, E., Pham, M. H., Deng, Y., Nguyen, T., Duy, V. N., Le, D. H., et al. (2018). Effects of injection timing and injection pressure on performance and exhaust emissions of a common rail diesel engine fueled by various concentrations of fish-oil biodiesel blends. *Energy*. 149, 979–989. doi:10.1016/j.energy.2018.02.053

Jupudi, R. S., Finney, C. E. A., Primus, R., Wijeyakulasuriya, S., Klingbeil, A. E., Tamma, B., et al. (2016). Application of high performance computing for simulating cycle-to-cycle variation in dual-fuel combustion engines. SAE International, Technical Paper 2016-01-0798. https://doi.org/10.4271/2016-01-0798.

Lounici, M. S., Loubar, K., Tarabet, L., Balistrou, M., Niculescu, D. C., and Tazerout, M. (2014). Towards improvement of natural gas-diesel dual fuel mode: an experimental investigation on performance and exhaust emissions. *Energy*. 64, 200–211. doi:10.1016/j.energy.2013.10.091

Mattson, J. M. S., Langness, C., and Depcik, C. (2018). An analysis of dual-fuel combustion of diesel with compressed natural gas in a single-cylinder engine. SAE International, Technical Paper 2018-01-0248. https://doi.org/10.4271/2018-01-0248.

Nithyanandan, K., Zhang, J., Li, Y., Meng, X., Donahue, R., Lee, C.-F., et al. (2016). Diesel-like efficiency using compressed natural gas/diesel dual-fuel combustion. *J. Energy Resour. Technol.* 138 (5), 052201. doi:10.1115/1.4032621

Papagiannakis, R. G., and Hountalas, D. T. (2004). Combustion and exhaust emission characteristics of a dual fuel compression ignition engine operated with pilot diesel fuel and natural gas. *Energy Convers. Manag.* 45 (18–19), 2971–2987. doi:10.1016/j.enconman.2004.01.013

Rahimi, A, Fatehifar, E., and Khoshbakhti Saray, R. (2010). Development of an optimized chemical kinetic mechanism for homogeneous charge compression ignition combustion of a fuel blend of *n*-heptane and natural gas using a genetic algorithm. *Proc. Inst. Mech. Eng. Part D J. Automob. Eng.* 224, 1141–1159. doi:10.1243/09544070JAUTO1343.

Richards, K. J., Senecal, P. K., and Pomraning, E. (2017). *Converge 2.4 Manual,* Madison, WI: Convergent Science, Inc.

Rochussen, J., and Kirchen, P. (2018). Characterization of reaction zone growth in an optically accessible heavy-duty diesel/methane dual-fuel engine. *Int. J. Engine Res.* 20, 483–500. doi:10.1177/1468087418756538.

Senecal, P. K., Richards, K. J., Pomraning, E., Yang, T., Dai, M. Z., McDavid, R. M., et al. (2007). A new parallel cut-cell cartesian CFD code for rapid grid generation applied to in-cylinder diesel engine simulations. SAE International, Technical Paper 2007-01-0159. doi:10.4271/2007-01-0159

Shim, E., Park, H., and Bae, C. (2018). Intake air strategy for low HC and CO emissions in dual-fuel (CNG-Diesel) premixed charge compression ignition engine. *Appl. Energy*. 225, 1068–1077. doi:10.1016/j.apenergy.2018.05.060

Song, H., Liu, C., Li, Y., Wang, Z., Chen, L., He, X., et al. (2018). An exploration of utilizing low-pressure diesel injection for natural gas dual-fuel low-temperature combustion. *Energy*. 153, 248–255. doi:10.1016/j.energy.2018.04.041

Tablan, A. D. (2014). "Diesel and compressed natural gas dual fuel engine operating envelope for heavy duty application andrew," in Proceedings of the ASME 2014 internal combustion engine division fall technical conference ICEF2014, Columbus, IN, October 19–22, 2014, 1–10.

Treasury Board of Canada Secretariat" (2017). *Goverment of Canada.* Https://Www.Canada.ca.

Wijeyakulasuriya, S. (2015). "Multidimensional modeling and validation of dual-fuel combustion in a large bore medium speed diesel engine," in Proceedings of the ASME 2015 internal combustion engine division fall technical conference ICEF2015, Houston, TX, November 8–11, 2015, 1–14.

Yousefi, A., and Birouk, M. (2016). Fuel suitability for homogeneous charge compression ignition combustion. *Energy Convers. Manag.* 119, 304–315. doi:10.1016/j.enconman.2016.04.056

Yousefi, A., and Birouk, M. (2017). Investigation of natural gas energy fraction and injection timing on the performance and emissions of a dual-fuel engine with pre-combustion chamber under low engine load. *Appl. Energy*. 189, 492–505. doi:10.1016/j.apenergy.2016.12.046

Yousefi, A., Birouk, M., and Guo, H. (2017). An experimental and numerical study of the effect of diesel injection timing on natural gas/diesel dual-fuel combustion at low load. *Fuel.* 203, 642–657. doi:10.1016/j.fuel.2017.05.009

Yousefi, A., Birouk, M., and Guo, H. (2019). Effect of diesel injection timing on the combustion of natural gas/diesel dual-fuel engine at low-high load and low-high speed conditions. *Fuel.* 235, 838–846. doi:10.1016/j.fuel.2017.05.009

Yousefi, A., Birouk, M., Lawler, B., and Gharehghani, A. (2015). Performance and emissions of a dual-fuel pilot diesel ignition engine operating on various premixed fuels. *Energy Convers. Manag.* 106, 322–336. doi:10.1016/j.enconman.2015.09.056

Yousefi, A., Guo, H., and Birouk, M. (2018). Effect of swirl ratio on NG/diesel dual-fuel combustion at low to high engine load conditions *Appl. Energy*. 229, 375–388. doi:10.1016/j.apenergy.2018.08.017

Yousefi, A., Guo, H., Birouk, M., and Liko, B. (2019). On greenhouse gas emissions and thermal efficiency of natural gas/diesel dual-fuel engine at low load conditions: coupled effect of injector rail pressure and split injection. *Appl. Energy*. 242, 216–231. doi:10.1016/j.apenergy.2019.03.093

Zheng, J., Wang, J., Zhao, Z., Wang, D., and Huang, Z. (2019). Effect of equivalence ratio on combustion and emissions of a dual-fuel natural gas engine ignited with diesel. *Appl. Therm. Eng.* 146, 738–751. doi:10.1016/j.applthermaleng.2018.10.045

Conflict of Interest: The authors declare that the research was conducted in the absence of any commercial or financial relationships that could be construed as a potential conflict of interest.

frontiers in Mechanical Engineering

ORIGINAL RESEARCH
published: 10 December 2020
doi: 10.3389/fmech.2020.545416

A Study on the High Load Operation of a Natural Gas-Diesel Dual-Fuel Engine

Shouvik Dev, Hongsheng Guo and Brian Liko*

Energy, Mining and Environment Research Center, National Research Council Canada, Ottawa, ON, Canada

Diesel fueled compression ignition engines are widely used in power generation and freight transport owing to their high fuel conversion efficiency and ability to operate reliably for long periods of time at high loads. However, such engines generate significant amounts of carbon dioxide (CO_2), nitrogen oxides (NOx), and particulate matter (PM) emissions. One solution to reduce the CO_2 and particulate matter emissions of diesel engines while maintaining their efficiency and reliability is natural gas (NG)-diesel dual-fuel combustion. In addition to methane emissions, the temperatures of the diesel injector tip and exhaust gas can also be concerns for dual-fuel engines at medium and high load operating conditions. In this study, a single cylinder NG-diesel dual-fuel research engine is operated at two high load conditions (75% and 100% load). NG fraction and diesel direct injection (DI) timing are two of the simplest control parameters for optimization of diesel engines converted to dual-fuel engines. In addition to studying the combined impact of these parameters on combustion and emissions performance, another unique aspect of this research is the measurement of the diesel injector tip temperature which can predict potential coking issues in dual-fuel engines. Results show that increasing NG fraction and advancing diesel direct injection timing can increase the injector tip temperature. With increasing NG fraction, while the methane emissions increase, the equivalent CO_2 emissions (cumulative greenhouse gas effect of CO_2 and CH_4) of the engine decrease. Increasing NG fraction also improves the brake thermal efficiency of the engine though NOx emissions increase. By optimizing the combustion phasing through control of the DI timing, brake thermal efficiencies of the order of ~42% can be achieved. At high loads, advanced diesel DI timings typically correspond to the higher maximum cylinder pressure, maximum pressure rise rate, brake thermal efficiency and NOx emissions, and lower soot, CO, and CO_2-equivalent emissions.

Keywords: natural gas, dual-fuel, compression ignition, high load, greenhouse gas reduction

OPEN ACCESS

Edited by:
Xiaosong Hu,
Chongqing University, China

Reviewed by:
Alpaslan Atmanli,
National Defense University, Turkey
Md Nurun Nabi,
Central Queensland University, Australia
Amin Paykani,
University of Hertfordshire, United Kingdom

****Correspondence:***
Shouvik Dev
shouvik.dev@nrc-cnrc.gc.ca

Specialty section:
This article was submitted to Engine and Automotive Engineering, a section of the journal Frontiers in Mechanical Engineering

Received: *24 March 2020*
Accepted: *17 November 2020*
Published: *10 December 2020*

Citation:
Dev S, Guo H and Liko B (2020) A Study on the High Load Operation of a Natural Gas-Diesel Dual-Fuel Engine. Front. Mech. Eng. 6:545416. doi: 10.3389/fmech.2020.545416

INTRODUCTION

As part of the Paris Agreement on climate change, Canada has committed to 30% abatement of its greenhouse gas (GHG) emissions from the 2005 levels by the year 2030 (Government of Canada, 2016). As means of achieving this target, Canada has also been developing the Clean Fuel Standard since 2016 with the aim to reduce GHG emissions through use of "lower carbon fuels, energy sources and technologies" (Government of Canada, 2019).

Diesel fueled compression ignition (CI) engines are widely used in power generation and freight transport owing to their high fuel conversion efficiency and ability to operate reliably for long periods of time at high loads. Owing to their ubiquity and extent of use, the carbon dioxide (CO_2), nitrogen

oxides (NOx) and particulate matter (PM) emissions from these engines can cause a significant adverse impact on the environment. Natural gas (NG) and renewable natural gas (RNG) are lower carbon and renewable fuels which generate about 20–30% and 80–90%, respectively, lower life-cycle CO_2 emissions per unit of energy compared to diesel (Sharpe, 2019). One solution to reduce the CO_2 and PM emissions of diesel engines while maintaining their efficiency and reliability is to replace diesel by NG using diesel-NG dual-fuel combustion technology. A possible configuration of an NG-diesel dual-fuel engine is intake port injection of compressed NG to form a homogenous air/NG mixture in the cylinder, and ignition of this mixture using a direct injection (DI) of diesel. In addition to offsetting diesel consumption, the potential advantages of such a configuration are lower PM emissions and limited engine modifications (Sahoo et al., 2009). Besides, such dual-fuel engines can operate as conventional diesel engines when NG is not available. One of the main disadvantages of NG-diesel dual-fuel engines is the higher methane emissions in comparison to conventional diesel engines (Liu et al., 2013; Guo et al., 2015). The global warming potential of methane over 100 years is 25 times that of CO_2 (United States Environmental Protection Agency, 2020). Moreover, methane is difficult to oxidize effectively in the exhaust after-treatment (EAT) system (Osman, 2016; Gärtner et al., 2018). Methane emissions can therefore offset the advantage of lower CO_2 emissions of the dual-fuel engines, especially at low load conditions. Advanced combustion strategies have been proposed that can minimize the methane emissions at low loads (Srinivasan et al., 2006; Guo et al., 2017; Yousefi et al., 2018). At medium to high load conditions, owing to the high fueling rate and higher temperatures which result in higher flame propagation speed, methane emissions are much lower than that at low load conditions, but they may still be greater than those of diesel engines (Papagiannakis and Hountalas, 2003). The main sources of these methane emissions at medium to high load conditions are crevice regions (Yousefi et al., 2019).

NG-diesel dual-fuel engines have been studied extensively over the years. There are many examples in literature that have summarized the fundamental performance of such dual-fuel engines (Karim, 1980; Wagemakers and Leermakers, 2012; Wei and Geng, 2016). There have also been researches on the effect of the injection parameters of NG and diesel of dual-fuel engines with the aim to improve engine efficiency and reduce methane emissions (Figer et al., 2014; Yang et al., 2015; Guo et al., 2017). Increasing the NG fraction in the total fuel energy input, especially at low and intermediate loads, can cause the brake thermal efficiency (BTE) to decrease and the carbon monoxide and methane emissions to increase (Papagiannakis et al., 2010; Imran et al., 2014). Increasing the NG fraction also tends to cause higher maximum pressure rise rate and lower maximum combustion pressure (Sahoo et al., 2009). However, at all engine loads and speeds, increasing the NG fraction tends to decrease NOx and soot emissions (Papagiannakis et al., 2010). The reduced NOx emissions with increased NG fraction can be caused by the increase in the higher specific heat capacity of the NG-air gas mixture and the lower maximum combustion pressure (Imran et al., 2014). One way to counter the reduced efficiency associated with higher NG fraction is to advance the timing of the diesel injection and increase the diesel injection pressure (Sahoo et al., 2009; Yang et al., 2015). However, this is accompanied by an increase in the NOx emissions and maximum combustion pressure and pressure rise rate (Sahoo et al., 2009). Therefore, there exists a trade-off between NOx-methane emissions for dual-fuel combustion (Wei and Geng, 2016). Additionally, there is an insignificant effect of NG injection timing on combustion performance and emissions at the advanced diesel injection timings (Yang et al., 2015).

The authors' laboratory has previously studied pollutant emissions from dual-fuel engines including the pollutant formation mechanisms (Guo et al., 2017; Li et al., 2018). The present work builds on the previous research by studying the effect of increasing NG fraction and DI timing (of diesel) on engine performance and exhaust emissions at high load-low speed operating conditions. Potential application of such research is the conversion of existing diesel engines to dual-fuel engines in which the diesel DI timing and NG fraction can be the simplest control parameters for optimization without extensive engine hardware modification. An additional and unique metric deployed in this research is the injector tip temperature. Dual-fuel engines with the capability to operate in diesel-only mode tend to use the stock diesel injectors. When operating in dual-fuel mode, the diesel flow rate through the injector may be significantly reduced. Since the diesel also functions as a coolant to reduce the injector tip temperature, the reduced diesel flow rate may cause over-heating and potential coking inside the injector nozzles. This can disrupt the diesel injection and adversely affect the performance of the engine. Past investigations have found that injector coking problems increased when the injector tip temperature exceeded 300°C (Argueyrolles et al., 2007). Research on injector tip temperature for NG-diesel dual-fuel engines is limited. Königsson et al. found that increasing NG fraction caused the injector tip temperature to increase (Königsson et al., 2012). The authors' laboratory conducted research on injector tip temperature at a constant NG fraction of 75% (Guo and Liko, 2018). This study furthers the analysis of injector tip temperature at different NG fractions with the goal to determine if the 300°C threshold can be reached in high load dual-fuel operation. Based on the authors' search, this reported work is unique in its representation of the correlations between NG fraction, diesel DI timing, and injector tip temperature.

In this paper, two high load conditions—75% and 100% load are investigated. The two main variables are the NG fraction and the diesel DI timing of the diesel injection. Combustion performance, injector tip temperature and exhaust emissions are evaluated. The paper is organized as follows. Experimental setup and procedure as well as test conditions are described in *Experimental Setup and Methods*, followed by the discussion of results in *Results and Discussion* which consists of three sub-sections describing the combustion performance, injector tip temperature and exhaust emissions. The main conclusions of this research are presented in *Conclusions*.

TABLE 1 | Test engine specifications and fuel properties.

Base engine model	Caterpillar 3401 (3400 series)
Number of cylinders	1
Bore X stroke	137.2 × 165.1 mm
Displacement	2.44 L
Compression ratio	16.25:1
Number of valves	4 (2—intake, 2—exhaust)
Maximum power output (stock)	74.6 kW (at 2,100 rpm)
Fuel delivery—diesel	Common rail direct injection
Diesel density	814.8 kg/m^3
Diesel cetane number	44
Diesel lower heating value	44.64 MJ/kg at 15°C and 1 atm
Diesel hydrogen/Carbon ratio	1.90
Fuel delivery—natural gas	Port fuel injection
Natural gas composition (by volume)	Methane (94.951%); ethane (3.318%); propane (0.087%); butane (0.003%); nitrogen (0.929%); carbon dioxide (0.712%)
Natural gas lower heating value	33.77 MJ/m^3 at 15°C and 1 atm

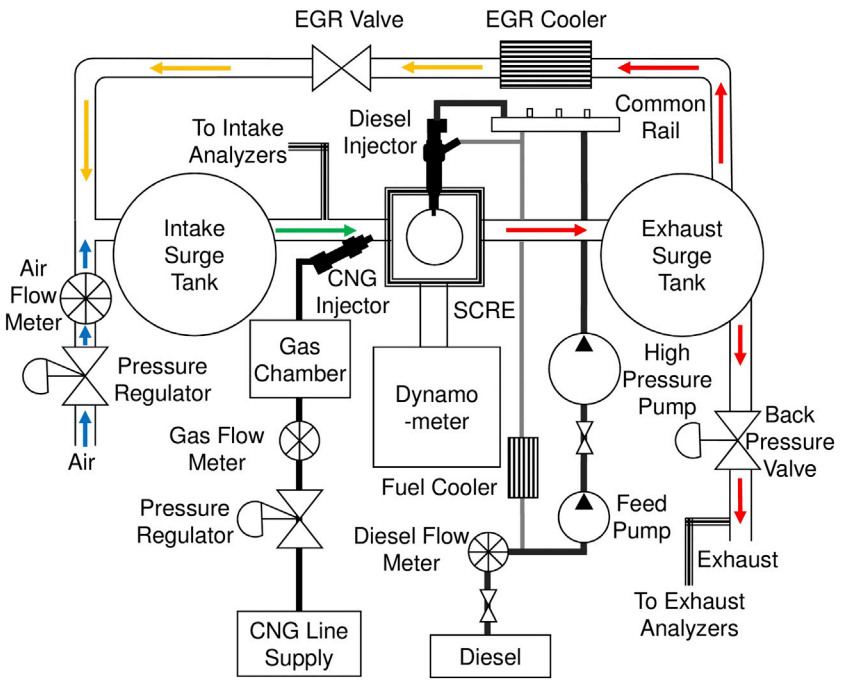

FIGURE 1 | Schematic of experimental setup.

EXPERIMENTAL SETUP AND METHODS

This section is organized into two sub-sections. The first sub-section on experimental setup describes the testing system in detail. The second sub-section describes the experimental procedure and conditions, including calculation methods, test parameters and hardware constraints.

Experimental Setup

The research was performed on a single cylinder research engine. The setup consisted of a Caterpillar 3401 heavy-duty, four-stroke diesel engine coupled with a 131 kW eddy current dynamometer. The specifications of the engine are given in **Table 1** and the schematic of the experimental setup is shown in **Figure 1**. A DC electric motor was used for starting and motoring of the engine.

The test setup also included a gas injection manifold in-line and immediately upstream of the intake port of the engine. Compressed NG was supplied by the local utility provider (Enbridge, Inc.) through their pipeline infrastructure into the test cell directly and a pressure regulator was used to maintain the injection pressure. A Bronkhorst mass flow meter was used to measure the flow rate of NG into the engine. Downstream of the flow meter and upstream of the gas injection manifold, a gas chamber was used to dampen any pressure pulses in the flow. The

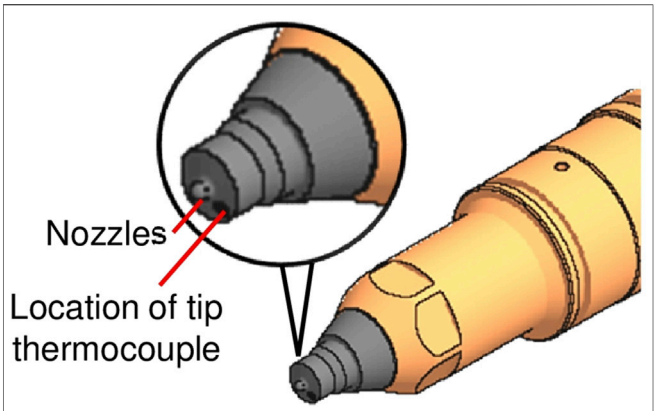

FIGURE 2 | Injector tip temperature measurement.

gas injection manifold consisted of eight gas fuel solenoid injectors (model Gs60 manufactured by Alternative Fuel Systems (AFS) Incorporated) which were individually controlled to inject precise quantities of NG into the intake charge of the engine. Since the composition of NG in the supply line may vary, the NG composition was determined before the tests using an Ametek Model 292B BTU Analyzer. The result is shown in **Table 1**. A custom diesel common rail DI system consisting of a Ganser six-hole solenoid injector and a high pressure fuel pump operated independent of the engine was used to deliver diesel to the engine. The diesel injector had a K-type thermocouple mounted into the sidewall to measure the injector tip temperature. The location of this thermocouple with respect to the nozzle is shown in **Figure 2**. The properties of the Canadian ultra-low-sulphur diesel (ULSD) used in this study are listed in **Table 1**. The diesel flow rate was measured with a Bronkhorst flow meter. The diesel and NG fueling were controlled by National Instruments (NI) hardware and LabVIEW based software (Stand-alone Direct Injector Drive System, Drivven Inc.). The hardware consisted of NI PXI-1031 chassis with NI PXI-8184 embedded controller, NI cRIO-9151 expansion chassis, and NI 7813R RIO injector driver card (for the diesel injector). The PXI-8184 controlled two four-channel AFS Injector Driver modules to drive the eight gas injectors.

The engine was aspirated with a conditioned air supply system with independent control of air pressure (oil-free air compressor and pressure regulators) and in-line intake heating. The air flow rate was measured with a thermal wire-type mass flowmeter manufactured by Sierra Instruments Inc. Intake and exhaust surge tanks were installed in the intake loop and the exhaust loop to dampen pressure waves in the system. An electro-pneumatic back pressure valve was used to simulate back pressure from the turbocharger. The lubricating oil and engine coolant conditioning systems were also operated independent of the engine with both oil and coolant temperatures maintained at 85°C.

CAI 600 series gas analyzers were used to determine the concentrations of CO, CO_2, CH_4, total HC, O_2, and NOx in the engine exhaust. An AVL 415S smoke meter was used to determine the soot emissions. The filter smoke number (FSN) output of the smoke meter was converted to mass concentration (m_{soot} in mg/m^3) using **Eq. 1** (Christian et al., 1993).

$$m_{soot} = \frac{1}{0.405} \times 4.95 \times \mathrm{FSN} \times e^{0.38 \times \mathrm{FSN}}. \quad (1)$$

Additional instrumentation of the engine included the water-cooled, flush-mounted Kistler 6041A pressure transducer for measuring cylinder pressure and an AVL 365 series crank angle encoder. The outputs of the pressure transducer and the encoder were processed using AVL IndiModule combustion analysis system. Engine load and speed were controlled through the AVL Digalog Testmate system. Thermocouples were mounted at multiple locations in the test cell to monitor temperature. The test cell was also equipped with an exhaust gas recirculation (EGR) loop though it was not used in this research. Further details of the test setup are described in Guo and Liko (2018).

TABLE 2 | Experimental conditions.

Parameter	75% full load	100% full load
BMEP (bar)	12.86	17.65
T_{in} (°C)	40	
Diesel $p_{injection}$ (bar)	525	
NG $p_{injection}$ (bar)	4.83	
Engine speed (N) (rpm)	1,010	1,120
Intake pressure (p_{in}) (bar absolute)	1.6	2.2
Exhaust pressure (p_{ex}) (bar absolute)	1.3	1.6
α_{NG} (%)	0–90	0–65

Experimental Procedure and Conditions

In NG-diesel dual-fuel engines, a primary parameter is the NG fraction (denoted by "α_{NG}"). This was calculated using **Eq. 2**. α_{NG} = 0% indicated that all input fuel energy came from diesel.

$$\alpha_{NG} = 100 \times \frac{m_{NG}\mathrm{LHV}_{NG}}{m_{NG}\mathrm{LHV}_{NG} + m_{D}\mathrm{LHV}_{D}}. \quad (2)$$

where, "m" and "LHV" were the mass flow rate (kg/s) and lower heating value (MJ/kg), respectively, and the subscripts "NG" and "D" represented natural gas and diesel, respectively.

The cylinder pressure data was stored for 100 consecutive engine cycles at a resolution of 0.2 crank angle degree (CAD). This data was used to calculate the net heat release rate ("HRR_{net}" in J/CAD) using **Eq. 3**.

$$\mathrm{HRR}_{net} = \frac{1}{\gamma - 1}\left[\gamma p \frac{\mathrm{d}V}{\mathrm{d}\theta} + V\frac{\mathrm{d}p}{\mathrm{d}\theta}\right]. \quad (3)$$

In **Eq. 3**, "γ" was the ratio of the specific heat at constant pressure to the specific heat at constant volume and was calculated as a function of the in-cylinder gas temperature and composition, "p" was the in-cylinder pressure (Pa), "V" was the cylinder volume (m^3) and "θ" was the crank angle (CAD). The heat release analysis was used to calculate the combustion timing values such as start of combustion (denoted by "CA10"),

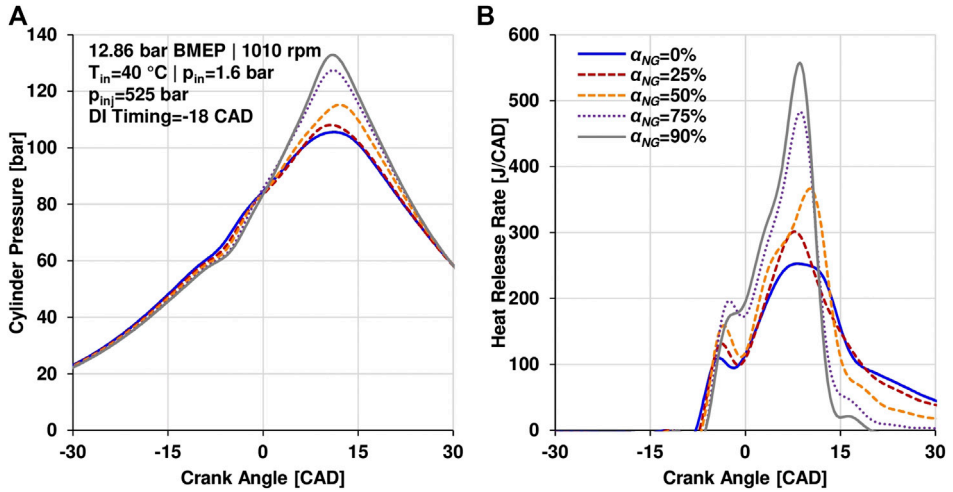

FIGURE 3 | 75% load–**(A)**. Cylinder pressure; **(B)**. Heat release rate.

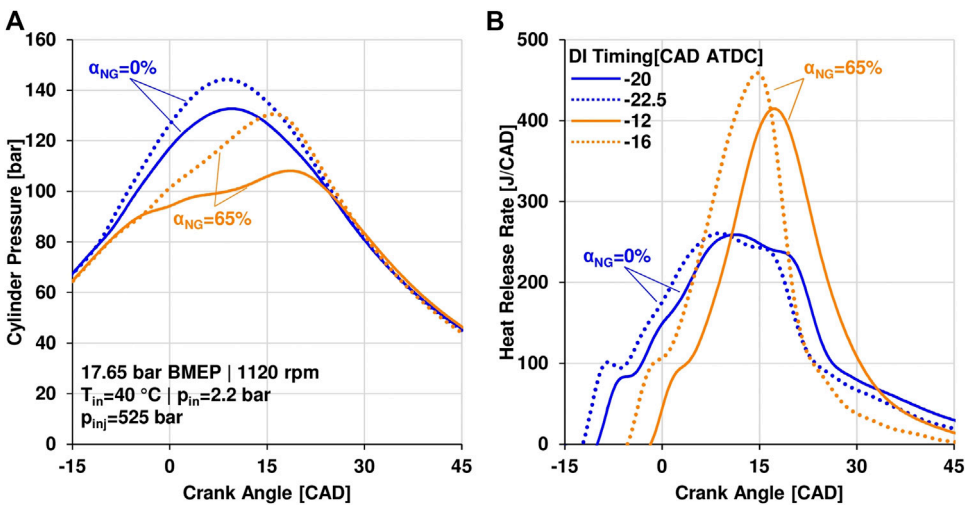

FIGURE 4 | 100% load–**(A)**. Cylinder pressure; **(B)**. Heat release rate.

combustion phasing (denoted by "CA50") and end of combustion (denoted by "CA90"). CA10, CA50, and CA90 corresponded to the specific crank angles at which 10%, 50% and 90%, respectively, of the total heat release occurred. Combustion duration was denoted by CA10-90.

The brake thermal efficiency (BTE) was used as a measure of the engine efficiency. It was expressed as a percentage and calculated using **Eq. 4**. In **Eq. 4**, "$\text{Power}_{\text{brake}}$" was the brake power of the engine measured by the dynamometer (kW), "LHV_f" was the lower heating value of the NG-diesel fuel combination (kJ/kg), and "m_f" was the mass flow rate of the NG-diesel fuel combination (kg/hour).

$$\text{BTE} = 100 \times \frac{3600 \times \text{Power}_{\text{brake}}}{\text{LHV}_f \times m_f}. \quad (4)$$

The experiments consisted of detailed investigation of combustion performance at two typical high load conditions—12.86 and 17.65 bar brake mean effective pressure (BMEP) at engine speeds of 1,010 and 1,120 rpm respectively corresponding to 75% and 100% load respectively. These choices were based on a previous study in which the highest injector tip temperatures had been observed between 75% and 100% load especially at low engine speeds of ~1,000 rpm albeit at a fixed NG fraction of 75% (Guo and Liko, 2018). The lower engine speeds were consistent with the trend of downspeeding of heavy-duty engines especially in transportation applications in the interest of increasing fuel efficiency. While the original intention was to operate the engine at ~1,000 rpm for the 100% load condition as well, in the interest of maintaining the load and stability over varying NG fractions

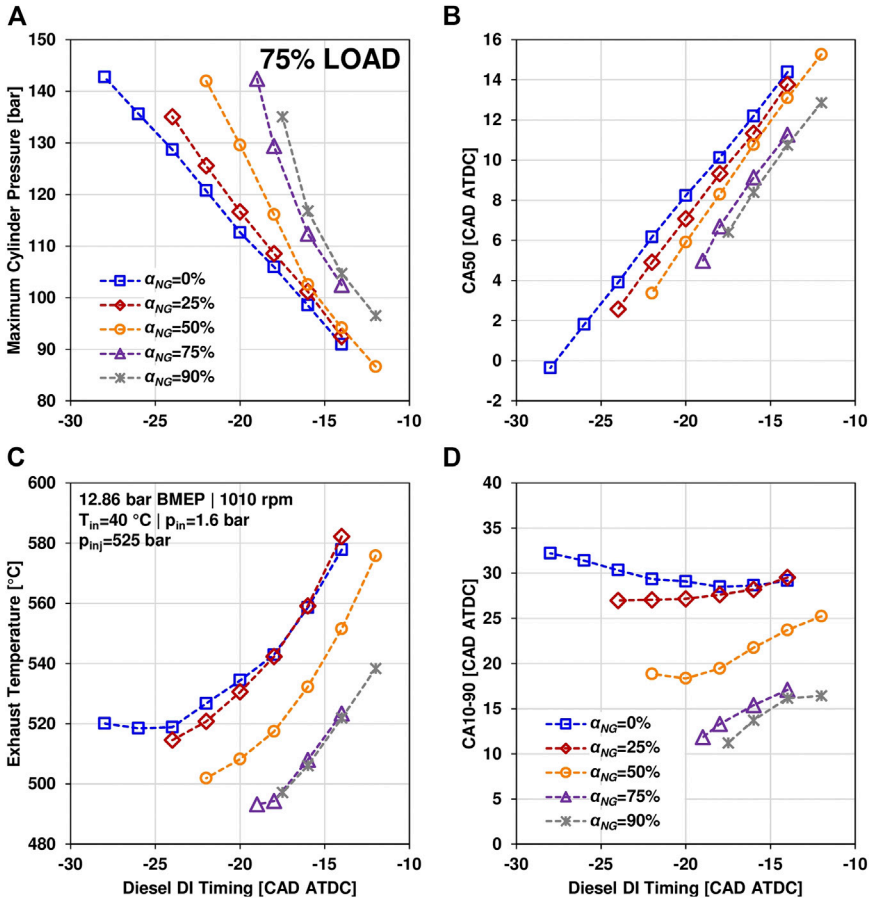

FIGURE 5 | 75% load results–**(A)**: Maximum cylinder pressure; **(B)**: CA50; **(C)**: Exhaust Temperature; **(D)**: CA10–90.

and DI timings, the engine speed had to be increased to 1,120 rpm. The experimental conditions are listed in **Table 2**. The two variables for this stage of experiments were α_{NG} and diesel DI timing (start of diesel injection).

All testing was conducted at steady state conditions without EGR. There are two main reasons for this. First, the purpose of this research was to isolate the effects of NG fraction and diesel DI timing which would be complicated by the profound effects of EGR on the combustion. Second, EGR control would typically be outside the scope of a simple conversion of a diesel engine to operate as an NG-diesel dual-fuel engine. However, the importance of EGR in optimizing NG-diesel combustion cannot be overstated and EGR effects have been evaluated in a separate study (Dev et al., 2020). The test procedure involved the following steps for each load condition. First, the engine motoring was started with the DC motor and a steady motoring speed of 600 rpm was maintained. Next, the diesel DI was initiated to fire the engine. Fueling rate was controlled to maintain the idle speed of 600 rpm and thereafter, the DC motor was disengaged. Subsequently, the engine load and speed were increased gradually to the target value using the dynamometer feedback. The engine was operated at the target load and speed for several minutes to reach steady conditions. Finally, the diesel DI timing was swept over a range. The limits of this range were based on the engine hardware. The timing advance limit was subject to constraints such as the peak pressure rise rate (<12 bar/CAD) and the peak cylinder pressure (<150 bar). The timing retard limit was constrained by the exhaust temperature (<600°C). For dual-fuel conditions, the diesel flow rate was gradually decreased and NG fueling rate was gradually increased to set the α_{NG}. Once the target $\alpha_{NG}$was reached, the diesel DI timing sweep was conducted similar to the diesel only case. The injection pressure of the diesel DI and intake temperature were maintained at 525 bar (denoted by "p_{inj}") and 40°C (denoted by "T_{in}"), respectively. The intake pressure (denoted by "p_{in}") and exhaust pressure (denoted by "p_{ex}") were constant for each load condition (**Table 2**). These values were set with the intention to keep the diesel baseline relative air/fuel ratio in the range of ~1.5–1.7 prevalent in high load operation in conventional diesel engines.

RESULTS AND DISCUSSION

This section is organized into three sub-sections. The combustion performance is described first, followed by the injector tip temperature and the emission results in the second and third sub-sections respectively.

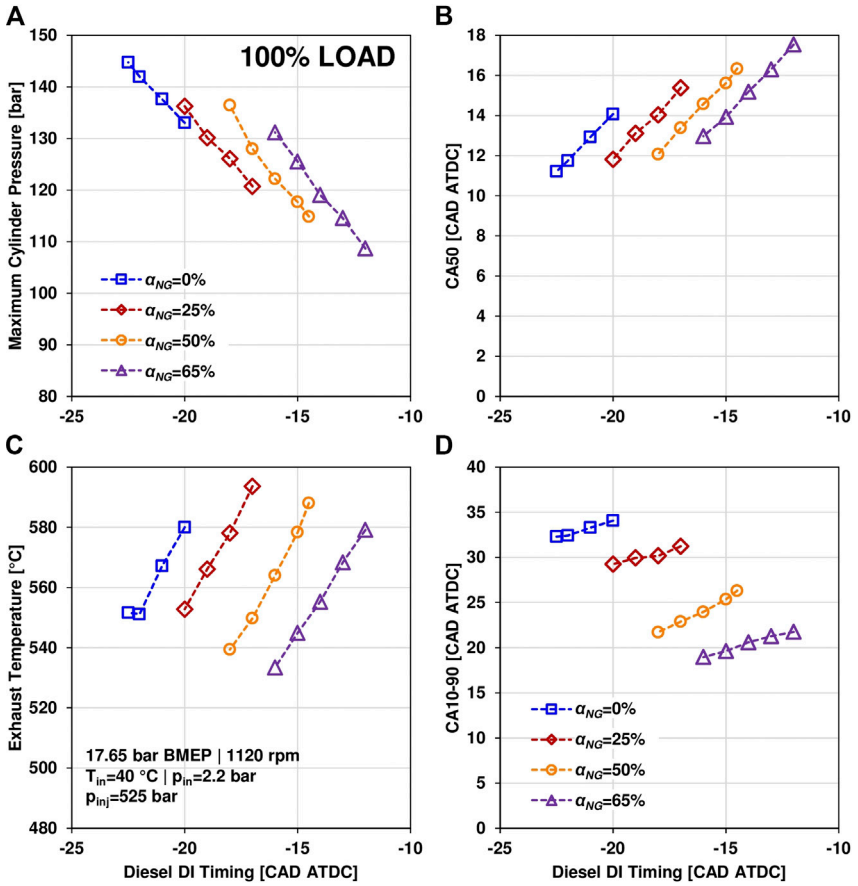

FIGURE 6 | 100% load results–**(A)**: Maximum cylinder pressure; **(B)**: CA50; **(C)**: Exhaust Temperature; **(D)**: CA10–90.

Combustion Performance

The cylinder pressure and heat release rate traces for 75% of full load (BMEP = 12.86 bar) are shown in **Figure 3** at the diesel DI timing of -18 CAD after top dead center (ATDC) and different NG fractions. At each NG fraction, there are two major peaks on the net heat release rate curve. At α_{NG} = 0%, the first peak of heat release corresponds to premixed combustion of air/diesel mixture, followed by the second major peak corresponding to the mixing controlled diffusion combustion. The second peak is followed by the relatively slower diffusion combustion of the remaining combustibles in the cylinder (beyond 15 CAD ATDC). For dual-fuel cases, increasing NG fraction causes the peak cylinder pressure and the peak heat release rate to increase. The first peak on the heat release rate curve of each NG fraction is related to premixed combustion of air/NG/diesel, followed by the diffusion combustion of remaining diesel and subsequent flame propagation of the background air/NG mixture. As the α_{NG} increases, since the intake pressure is constant, the relative air/fuel ratio of the air/NG mixture decreases which in turn increases the flame propagation speed of the air/NG mixture. This can explain the sharp increase in the heat release rate of dual-fuel cases with respect to the diesel only case, and also causes an increase in the peak cylinder pressure. Additionally, as α_{NG} increases, the late combustion (beyond 15 CAD ATDC) is minimized as well probably due to the increased flame propagation speed of the background mixture.

At the full load condition (BMEP = 17.65 bar), owing to the hardware limitations of exhaust temperature and peak pressure, there were limited overlaps in the DI timing sweeps. Therefore, the pressure and heat release traces are shown at α_{NG} = 0% and α_{NG} = 65% at an advanced and a retarded diesel DI timing (**Figure 4**). Advancing timing causes the peak cylinder pressure and peak heat release rate to increase for both diesel and dual-fuel cases. The peak of the heat release rate is advanced as well since the combustion is initiated earlier. Since the dual-fuel DI timing is significantly retarded owing to the higher peak pressure rise rate and maximum cylinder pressure compared to diesel only case, the peak cylinder pressure is lower. Again, similar to the 75% load case, the dual-fuel combustion mechanism can cause the peak heat release rate of α_{NG} = 65% cases to be higher than the diesel cases due to increased flame propagation speed of air/NG mixture.

The maximum cylinder pressure, exhaust temperature, CA50 and CA10–90 at 75% load are shown in **Figure 5**. This figure also highlights the constraints for advancing and retarding the DI timing explained in the previous section. For all α_{NG}, advancing injection timing causes the maximum cylinder pressure to increase, CA50 to advance and the exhaust temperature to

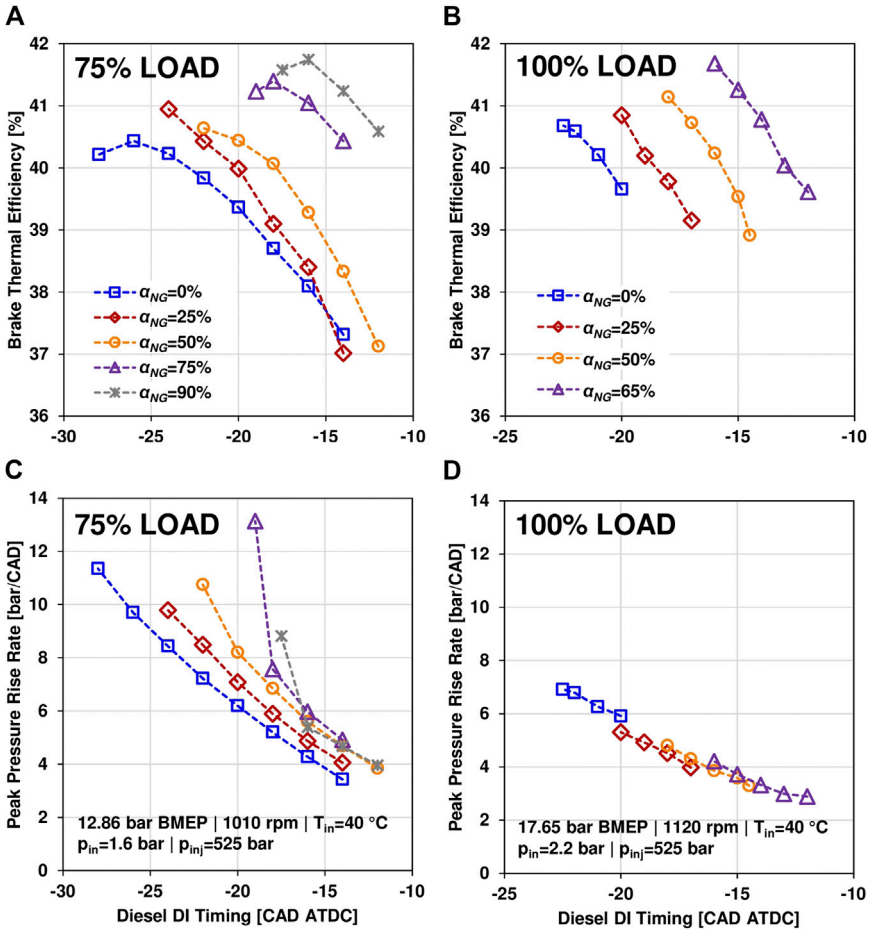

FIGURE 7 | (A). BTE at 75% load; **(B)**. BTE at 100% load; **(C)**. Peak pressure rise rate at 75% load; **(D)**. Peak pressure rise rate at 100% load.

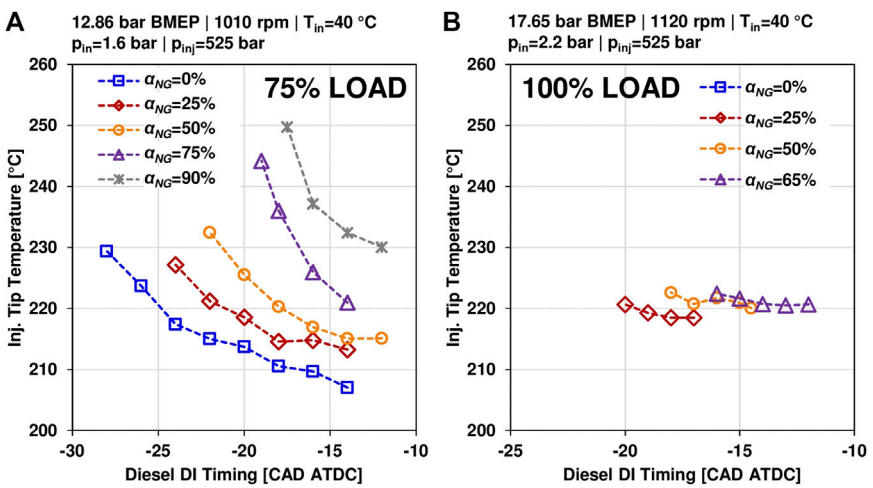

FIGURE 8 | Injector tip temperature–**(A)**. 75% load; **(B)**. 100% load.

decrease. When combustion is initiated earlier during the compression stroke with an advanced DI timing, more heat is released near top dead center, causing the cylinder pressure to be higher. When the injection timing is retarded, a greater portion of fuel energy is released later into the expansion stroke, which causes the exhaust temperature to increase. For α_{NG} = 0%, retarding timing causes the combustion duration (CA10–90) to decrease as more fuel is injected later into the compression stroke when temperature is higher. This can enhance the combustion rate. However, excessive retardation can cause the CA50 to be late (beyond 10 CAD ATDC), which may reduce the combustion efficiency. Consequently, the CA10–90 may start to increase again. For dual-fuel cases, retarding the DI timing tends to increase the combustion duration. An earlier injection timing may allow part of the diesel injection to mix with the air/NG background thereby increasing the reactivity of the background air/NG mixture. This may enhance the rate of the flame propagation that follows.

With increasing α_{NG}, at the same DI timing, the maximum cylinder pressure increases, the exhaust temperature decreases, the CA50 is advanced, and the CA10–90 is shorter. The increase in the maximum cylinder pressure can be correlated with the advance in CA50. As explained previously, this phenomenon can be due to the shift of the combustion from conventional diesel's primarily diffusion combustion to premixed type of combustion with increasing α_{NG}. The lower exhaust temperature with increasing α_{NG} at constant DI timing could be due to the advanced CA50.

At the 100% load condition (**Figure 6**), the overall trends are similar to those at 75% load with one exception. For α_{NG} = 0%, retarding the injection timing increases the combustion duration probably due to the retardation of the combustion phasing (CA50, **Figure 6**) beyond 11 CAD ATDC.

Advancing the DI timing can be advantageous in terms of increasing the BTE at both load levels (**Figure 7**). This is probably due to the optimization of the CA50. When the CA50 is too advanced, the energy release from the fuel combustion could be working against the engine compression. When the CA50 is too retarded, the energy release may be too late to derive useful mechanical work. Therefore, for α_{NG} = 0% at 75% load, the BTE increases with advancing DI timing, but then starts to decrease at the most advanced timing which corresponds to a CA50 that is too close to the TDC. Similar peaks of BTE are observed for other α_{NG} cases as well. Increasing α_{NG} can cause the BTE to increase for both load levels since the CA50 is advanced to a more optimal range, the combustion efficiency is improved with the enhanced reactivity of the background air/NG mixture, and combustion duration is shorter, which causes more heat to be released near the TDC. The highest BTE can be in the range of around 42% at the NG fractions of 90% and 65% for the 75% and 100% load conditions, respectively.

The DI timing advance is subject to an additional hardware constraint of peak pressure rise rate (**Figure 7**). The peak pressure rise rate tends to increase with the advance in the CA50 either through the advance of DI timing or the increase of α_{NG}. Therefore, peak pressure rise rates of 75% load cases are greater than those of 100% load cases because of retarded CA50.

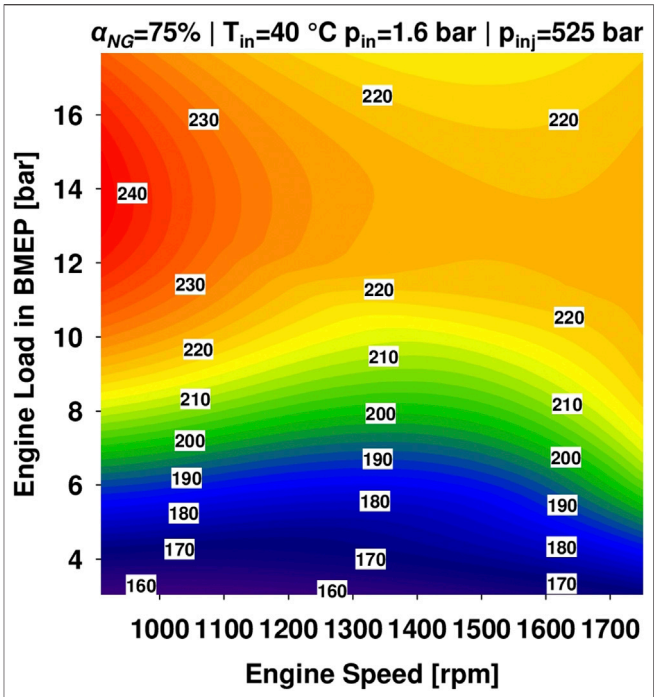

FIGURE 9 | Load-speed map of injection tip temperature at natural gas fraction of 75%.

Injector Tip Temperature

The injector tip temperature at 75% and 100% loads are shown in **Figure 8**. The injector tip temperature is expected to be correlated to the average cylinder temperature during each cycle. However, the range of in-cylinder temperature during a cycle is usually quite wide. At 75% load, as the DI timing is advanced, the injector tip temperature increases probably due to the increased heat release near the TDC and therefore higher cylinder temperature. This is further supported by the fact that the injector tip temperature keeps increasing even though the BTE decreases with advancing DI timing, since the most advanced CA50 approaches the TDC. With increasing α_{NG}, the injector tip temperature keeps increasing. This is because of the decrease in diesel flow rate and increase in the in-cylinder temperature. The decrease in diesel flow rate reduces the cooling effect, and the increase in the peak cylinder pressure (**Figure 5**) increases the cylinder temperature. At 75% load, the maximum observed injector tip temperature is ~250°C.

At 100% load, data of injector tip temperature was not available for α_{NG} = 0%. However, the dual-fuel cases are shown in **Figure 8**. While the general trends for 100% load are similar to those for 75% load, the range of injector tip temperatures is much narrower at ~220°C. This is probably due to the delayed CA50 for the 100% load cases.

For all test conditions, the injector tip temperatures were lower than the critical temperature for coking to occur inside the injector (Argueyrolles et al., 2007). The authors' laboratory has previously conducted a detailed load-speed analysis of the injector tip temperature at α_{NG} = 75% (**Figure 9**). For this test

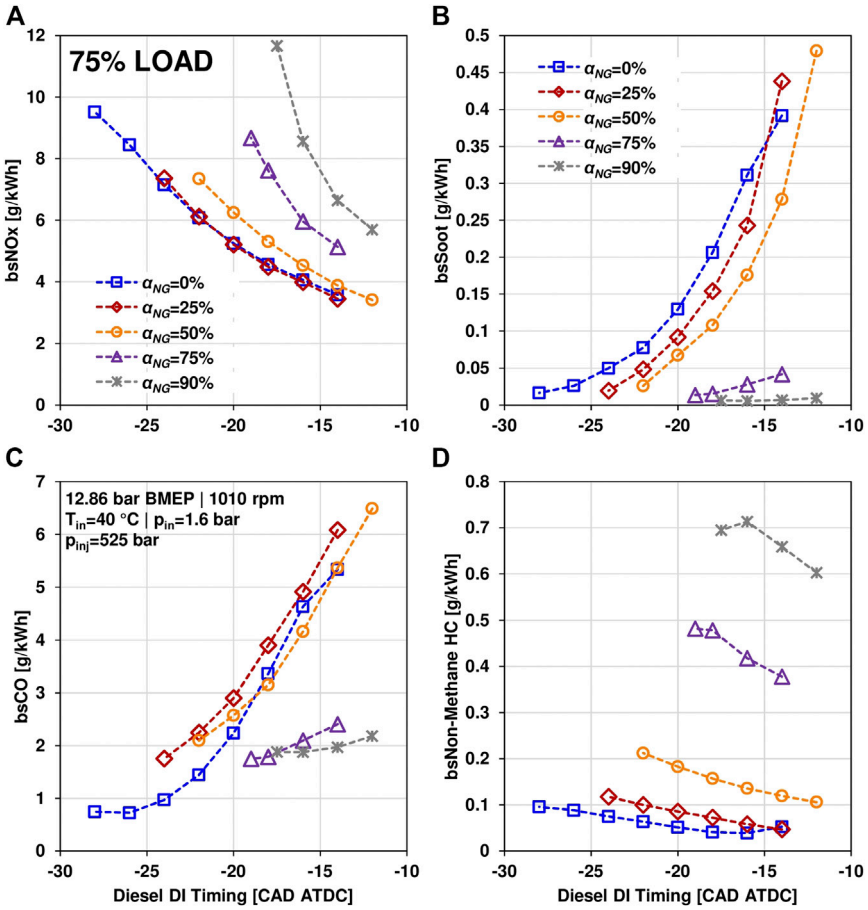

FIGURE 10 | Exhaust emissions at 75% load–**(A)**. NOx; **(B)**. Soot; **(C)**. CO; **(D)**. Non-methane HC.

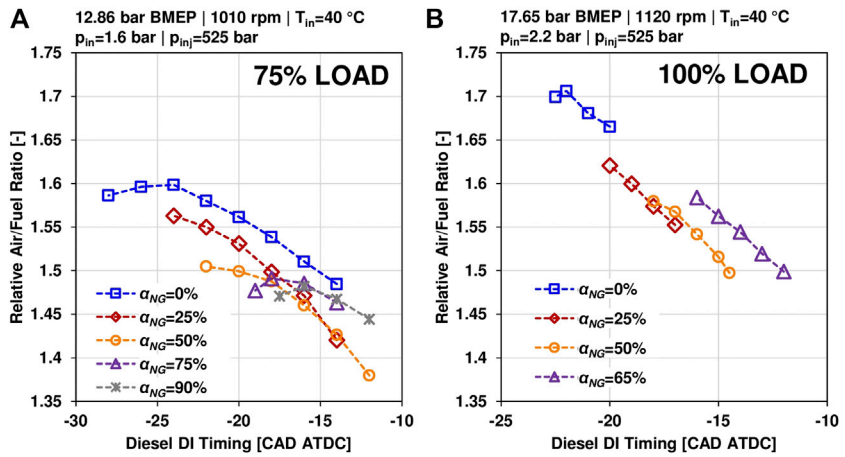

FIGURE 11 | Relative air/fuel ratio–**(A)**. 75% load; **(B)**. 100% load.

setup, the maximum injector tip temperatures are observed in the load range of 12–15 bar BMEP due to the combined effects of high fuel energy input and DI timing (Guo and Liko, 2018).

Emissions

NOx, soot, CO and non-methane total hydrocarbons (HCs) are some of the primary regulated emissions for diesel engines used

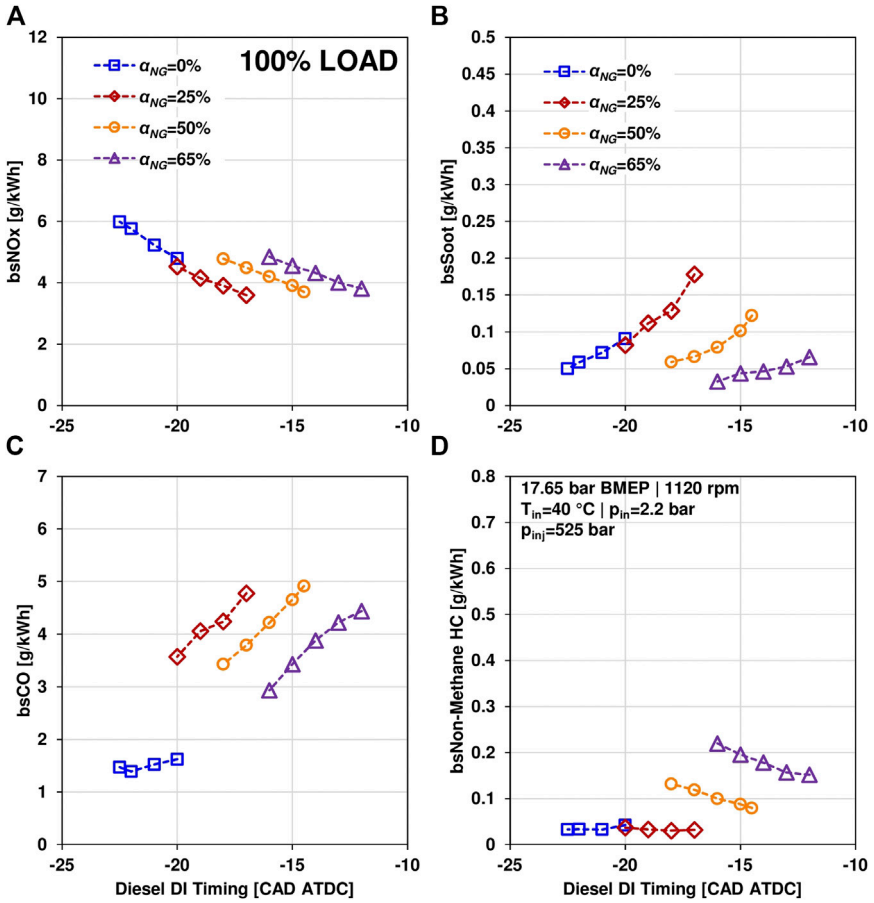

FIGURE 12 | Exhaust emissions at 100% load–**(A)**. NOx; **(B)**. Soot; **(C)**. CO; **(D)**. Non-methane HC.

in the transportation sector. **Figure 10** shows the brake specific emissions of the test cases at 75% load (denoted by "bs" prefix). NOx formation is primarily dependent on the in-cylinder temperature. Generally, at a particular NG fraction and DI timing, the maximum cylinder pressure and the maximum cylinder temperature would be directly correlated. It is noted from **Figure 10** that NOx emissions generally decrease with retarding DI timing. This is because the CA50 is further away from the TDC, which in turn reduces the peak cylinder temperature. The NOx emissions of α_{NG} = 0% and α_{NG} = 25% are similar probably due to combined effects of NOx formation mechanism and in-cylinder temperature. The prompt route and thermal route are the two primary NOx formation mechanisms in most combustion chambers. The prompt route plays a significant role in NOx formation of a diffusion combustion process in which nitric oxide (NO) can be formed due to the initial reactions of hydrocarbon radicals with nitrogen (Miller and Bowman, 1989). The thermal route dominates NOx formation in most premixed combustion processes (Guo et al., 2005) due to the oxidation of nitrogen in high temperature combustion and post combustion zones (Miller and Bowman, 1989). With increasing NG fraction for a dual-fuel engine, the diffusion fraction inside the cylinder decreases, which tends to reduce NOx formation by the prompt route. However, the increase in NG fraction leads to higher cylinder pressure and temperature, as discussed above, which tends to increase NOx formation by the thermal route. The combined variations in NOx formation from the prompt and thermal routes results in the negligible change in NOx emissions when NG fraction increases from zero to 25. For α_{NG} = 50% and higher, the increase in NOx formation due to the thermal route is greater than the decrease in NOx formation by the prompt route, which causes the increase in NOx emissions with increasing NG fraction. This may also reduce the impact of the change in the specific heat capacity of the air-NG mixture with change in the NG fraction as reported in literature (Imran et al., 2014).

Soot tends to form in the in-cylinder regions where the temperature is high and the air-fuel mixture is rich (Dec, 1997; Dec, 2009). When the DI timing is retarded, diesel is injected later in the compression stroke when the temperature is higher and time period available for the diesel to mix with the air/NG background and form a homogenous mixture is limited. This can cause the soot emissions to increase when the DI timing is retarded. With increasing α_{NG}, as the injected diesel quantity decreases, premixed combustion is predominant. Consequently, the soot formation rate can be reduced (**Figure 10**). While the advantage of dual-fuel combustion in terms of soot reduction is

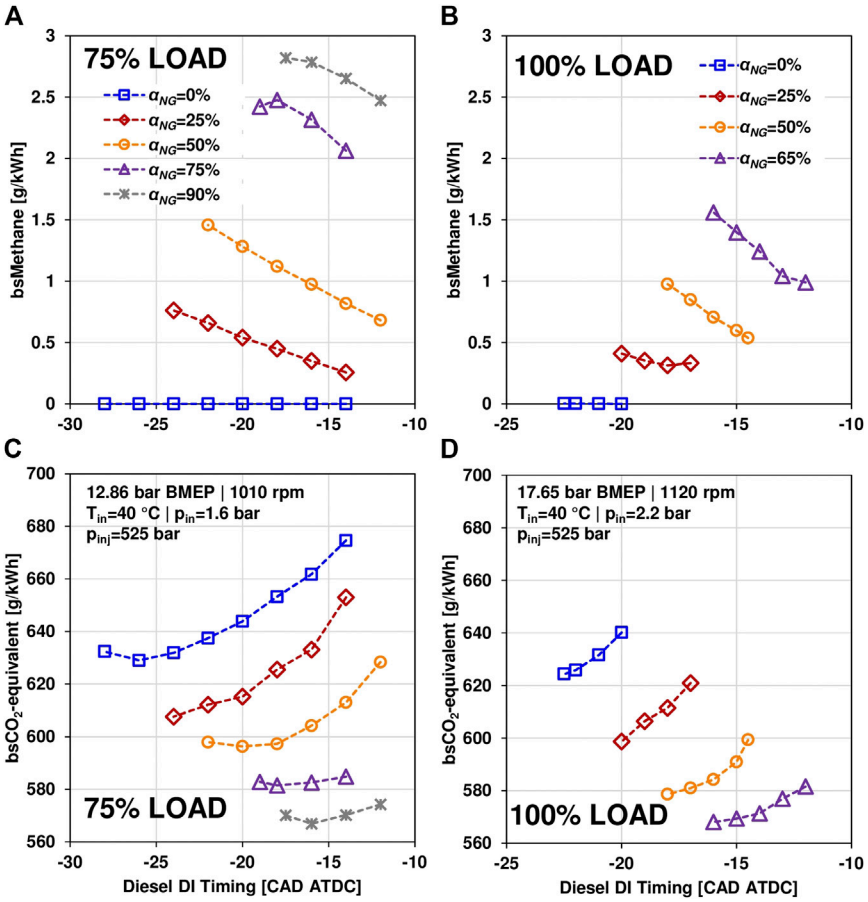

FIGURE 13 | (A). Methane emissions at 75% load; **(B)**. Methane emissions at 100% load; **(C)**. CO_2-equivalent emissions at 75% load; **(D)**. CO_2-equivalent emissions at 100% load.

well established (Wei and Geng, 2016), it is also observed that at very high α_{NG} (75% and above), owing to the reduced diesel injection quantity, the impact of DI timing on the soot emissions is reduced. The lowest soot emissions observed are of the order of 0.01 g/kWh when engine-out NOx emissions are below 6 g/kWh for α_{NG} = 90% at 75% load. Past research on PM speciation of NG-diesel dual-fuel engines has shown that unlike diesel engines, the majority of PM fraction is volatile in nature rather than elemental carbon (Mustafi et al., 2010). Additionally, there are differences in the shape of the PM agglomerates and their fractal dimensions between diesel and dual-fuel operation (Mustafi et al., 2009). The NG fraction can also have an impact on the PM size distribution and volatile mass fraction (Momenimovahed et al., 2019). The present analysis is limited to soot and does not account for the volatile PM. Moreover, these soot emissions tend to originate from the diesel fuel (Graves et al., 2015).

The CO emissions for the 75% load cases are shown in **Figure 10** as well. CO typically originates from the incomplete combustion of hydrocarbons. With DI timing retard, the CO emissions increase. The BTE decreases with DI timing retardation. Therefore, as the fueling rate is increased to maintain the load, the relative air/fuel ratio decreases thereby reducing the oxygen availability (**Figure 11**). Moreover, a delayed DI timing can reduce the time available for diesel to mix with the air/NG background. These two factors can decrease the probability of CO oxidation. With increasing α_{NG}, the CO emissions tend to increase and then decrease. There are two points to consider with increasing α_{NG}. First, the background air/fuel ratio of the air/NG mixture is decreased and second, the flame propagation speed is increased (evidenced by shorter combustion duration (**Figure 5**). The first and second actions can work against each other to increase or decrease CO formation rates respectively. For α_{NG} < 75%, the reduction in the air/fuel ratio may be balanced by the increase in the flame propagation speed which can cause the CO emissions to remain similar. With further increase in α_{NG}, majority of the fuel is NG and the flame propagation speed is higher. NG can form a homogenous mixture with air while the diesel fuel quantity is significantly reduced (diesel flow rate decreases from ~5.7 to ~1.26 kg/h). This may explain the CO trend with change in α_{NG}.

The non-methane HC emissions are also shown in **Figure 10**. When the α_{NG} is increased, the non-methane HC emissions increase. With increasing α_{NG}, while the reactivity of the air/NG background mixture may increase, more HC molecules (from NG) may make their way into the crevice volumes and remain

unburnt. When the DI timing is retarded, the non-methane HC emissions decrease. This may be due to the delayed combustion and higher temperatures during the expansion stroke which may enhance the combustion of the charge trapped in the crevices.

At 100% load, the emission trends are qualitatively similar to those at 75% load (**Figure 12**). There are other exceptions, however. The specific NOx emissions for 100% load cases are lower than the 75% load cases probably due to the retarded CA50 and to a small extent, the higher load. There is slight reduction in the NOx emissions for the dual-fuel cases in comparison to diesel. This could be due to the DI timing retardation necessary to limit the peak cylinder pressure which counters the reduction in CA10–90 as more NG is used. Soot emissions for the diesel case are less than 0.1 g/kWh, and for α_{NG} = 25%, soot emissions tend to increase. The relative air/fuel ratio can decrease from 1.65 for α_{NG} = 0% to 1.55 for α_{NG} = 25% which can cause the increase in the soot emissions (**Figure 11**). Further increase in α_{NG} allows the diesel flow rate to be decreased significantly and premixed combustion is predominant, leading to reduced soot formation.

While non-methane HC trends with increase in α_{NG} are similar for the 75% and 100% load levels, the CO emission trends are different (**Figure 12**). When NG is used, the CO emissions increase. At 100% load, though the diesel flow rate can be decreased with increasing α_{NG}, it is still significant (2.7 kg/h) even at the highest α_{NG} = 65%. Therefore, the richer air/NG background effect explained previously can reduce oxygen availability especially when the DI timing is retarded. At a similar DI timing for instance of −18 CAD ATDC, CO emissions are lower with increasing α_{NG} and the trend is analogous to the 75% load cases.

One of the main objectives of developing diesel-NG dual-fuel engines is the reduction in GHG emissions. **Figure 13** shows the methane emissions and CO_2-equivalent emissions at 75% and 100% load. The trends are similar for both load levels with respect to DI timing and α_{NG}. Methane emissions increase with increasing α_{NG} probably due to higher number of methane molecules trapped in the crevice and boundary regions. With retarding DI timing, the reduced cylinder pressure leads to less methane trapped in crevice and boundary regions.

The CO_2-equivalent emissions are calculated based on the CO_2 and methane emissions (**Figure 13**). Methane is a more potent GHG than CO_2, and a weightage of 25 is included in the CO_2-equivalent calculation. Regardless of the higher methane emissions from dual-fuel cases, it is found that increasing α_{NG} can reduce the CO_2-equivalent emissions at both load conditions. Advanced DI timings which correspond to the highest BTEs typically have the lowest CO_2-equivalent emissions.

CONCLUSIONS

A study on the effects of DI timing and increasing NG fraction on diesel-NG dual-fuel combustion is conducted on a heavy-duty engine setup. Injector tip temperature is measured using a specially modified injector. Combustion performance and exhaust emissions are studied as well. Tests are conducted at 75% and 100% load at the lower range of engine speeds. The main conclusions of this research are

- Combustion phasing (CA50) is a very critical determinant of dual-fuel combustion performance at high engine loads. Increasing NG fraction can advance the CA50 and cause the combustion duration to decrease. Using an optimized CA50 obtained through control of the DI timing, brake thermal efficiencies of the order of ~42% can be achieved.
- At high loads, advanced diesel DI timings typically correspond to the higher maximum cylinder pressure, maximum pressure rise rate, NOx emissions, lower soot and CO emissions, and higher BTE and lower CO_2-equivalent emissions.
- With increasing NG fraction at a given DI timing, injector tip temperature increases. With advancing DI timing at a given NG fraction, injector tip temperature increases as well. At all the test conditions, injector tip temperature does not exceed 250°C. This is lower than the temperature threshold of 300°C beyond which injector coking issues could be exacerbated.
- CO emissions tend to decrease and HC emissions (methane and non-methane) tend to increase with increase in the NG fraction at a given DI timing.
- At high loads, increasing NG fraction can increase the methane emissions. However, the CO_2-equivalent emissions decrease with increasing NG fraction.

DATA AVAILABILITY STATEMENT

The raw data supporting the conclusions of this article will be made available by the authors, without undue reservation.

AUTHOR CONTRIBUTIONS

SD processed the data, made the figures and wrote the manuscript. HG collected and processed the data, and also edited the manuscript. BL conducted the tests and organized the raw data.

FUNDING

Funding for this work was provided by Natural Resources Canada through the PERD Energy End Use (Project 3B03.003) and National Research Council of Canada through the internal Bioenergy program.

SUPPLEMENTARY MATERIAL

The Supplementary Material for this article can be found online at: https://www.frontiersin.org/articles/10.3389/fmech.2020.545416/full#supplementary-material.

REFERENCES

Argueyrolles, B., Dehoux, S., Gastaldi, P., Grosjean, L., Levy, F., Michel, A., et al. (2007). Influence of injector nozzle design and cavitation on coking phenomenon. SAE Technical Paper No. 2007-01-1896.

Christian, V. R., Knopf, F., Jaschek, A., and Schindler, W. (1993). Eine neue Messmethodik der Bosch-Zahl mit erhohter Empfindlichkeit. *Motortech Z.* 54, 16–22.

Dec, J. E. (1997). A conceptual model of DL diesel combustion based on laser-sheet imaging. *SAE Trans.* 1319–1348. doi:10.4271/970873

Dec, J. E. (2009). Advanced compression-ignition engines—understanding the in-cylinder processes. *Proc. Combust. Inst.* 32 (2), 2727–2742. doi:10.1016/j.proci.2008.08.008

Dev, S., Guo, H., Lafrance, S., and Liko, B. (2020). An experimental study on the effect of exhaust gas recirculation on a natural gas-diesel dual-fuel engine. SAE Technical Paper 2020-01-0310.

Figer, G., Seitz, H. F., Graf, G., and Schreier, H. (2014). Commercial vehicle natural gas engines with diesel efficiency. *MTZWorldwide.* 75 (10), 10–15. doi:10.1007/s38313-014-0229-2

Gärtner, U., Rabl, H.-P., and Zink, U. (2018). Exhaust gas aftertreatment of the future. *MTZ Worldwide.* 79, 70–75. doi:10.1007/s38313-018-0060-2

Government of Canada (2019). Clean fuel standard. Available at: https://www.canada.ca/en/environment-climate-change/services/managing-pollution/energy-production/fuel-regulations/clean-fuel-standard.html (Accessed March 07, 2020).

Government of Canada (2016). The Paris agreement. Available at: https://www.canada.ca/en/environment-climate-change/services/climate-change/paris-agreement.html (Accessed March 07, 2020).

Graves, B., Olfert, J., Patychuk, B., Dastanpour, R., and Rogak, S. (2015). Characterization of particulate matter morphology and volatility from a compression-ignition natural-gas direct-injection engine. *Aerosol. Sci. Technol.* 49 (8), 589–598. doi:10.1080/02786826.2015.1050482

Guo, H., and Liko, B. (2018). "Injector tip temperature and combustion performance of a natural gas-diesel dual fuel engine at medium and high load conditions," in Proceedings of the ASME 2018 internal combustion engine division fall technical conference. American Society of Mechanical Engineers Digital Collection, San Diego, CA, November 2018.

Guo, H., Liko, B., and Neill, W. S. (2017). "Effect of diesel injection split on combustion and emissions performance of a natural gas–diesel dual fuel engine at a low load condition," in Proceedings of the ASME 2017 internal combustion engine division fall technical conference. American Society of Mechanical Engineers Digital Collection, Seattle, WC, October 2017.

Guo, H., Liu, F., and Smallwood, G. J. (2005). A numerical study on NOx formation in laminar counterflow CH_4/air triple flames. *Combust. Flame.* 143 (3), 282–298. doi:10.1016/j.combustflame.2005.06.004

Guo, H., Neill, W. S., and Liko, B. (2015). "An experimental investigation on the combustion and emissions performance of a natural gas–diesel dual fuel engine at low and medium loads," in Proceedings of the ASME 2015 internal combustion engine division fall technical conference. American Society of Mechanical Engineers Digital Collection, Houston, TX, November 2015.

Imran, S., Emberson, D. R., Diez, A., Wen, D. S., Crookes, R. J., and Korakianitis, T. (2014). Natural gas fueled compression ignition engine performance and emissions maps with diesel and RME pilot fuels. *Appl. Energy.* 124, 354–365. doi:10.1016/j.apenergy.2014.02.067

Karim, G. A. (1980). A review of combustion processes in the dual fuel engine—the gas diesel engine. *Prog. Energy Combust. Sci.* 6 (3), 277–285. doi:10.1016/0360-1285(80)90019-2

Königsson, F., Stalhammar, P., and Angstrom, H. E. (2012). Controlling the injector tip temperature in a diesel dual fuel engine. SAE Technical Paper No. 2012-01-0826.

Li, Y., Li, H., and Guo, H. (2018). A numerical investigation on NO_2 formation reaction pathway in a natural gas–diesel dual fuel engine. *Combust. Flame.* 190, 337–348. doi:10.1016/j.combustflame.2017.12.006

Liu, J., Yang, F., Wang, H., Ouyang, M., and Hao, S. (2013). Effects of pilot fuel quantity on the emissions characteristics of a CNG/diesel dual fuel engine with optimized pilot injection timing. *Appl. Energy.* 110, 201–206. doi:10.1016/j.apenergy.2013.03.024

Miller, J. A., and Bowman, C. T. (1989). Mechanism and modeling of nitrogen chemistry in combustion. *Prog. Energy Combust. Sci.* 15 (4), 287–338. doi:10.1016/0360-1285(89)90017-8

Momenimovahed, A., Liu, F., Thomson, K. A., Smallwood, G. J., and Guo, H. (2019). Effect of fuel composition on properties of particles emitted from a diesel–natural gas dual fuel engine. *Int. J. Engine Res.* doi:10.1177/1468087419846018

Mustafi, N. N., and Raine, R. R. (2009). Electron microscopy investigation of particulate matter from a dual fuel engine. *Aerosol. Sci. Technol.* 43 (9), 951–960. doi:10.1080/02786820903067210

Mustafi, N. N., Raine, R. R., and James, B. (2010). Characterization of exhaust particulates from a dual fuel engine by TGA, XPS, and Raman techniques. *Aerosol. Sci. Technol.* 44 (11), 954–963. doi:10.1080/02786826.2010.503668

Osman, A. I., Abu-Dahrieh, J. K., Laffir, F., Curtin, T., Thompson, J. M., and Rooney, D. W. (2016). A bimetallic catalyst on a dual component support for low temperature total methane oxidation. *Appl. Catal. B Environ.* 187, 408–418. doi:10.1016/j.apcatb.2016.01.017

Papagiannakis, R. G., and Hountalas, D. T. (2003). Experimental investigation concerning the effect of natural gas percentage on performance and emissions of a DI dual fuel diesel engine. *Appl. Therm. Eng.* 23 (3), 353–365. doi:10.1016/S1359-4311(02)00187-4

Papagiannakis, R. G., Rakopoulos, C. D., Hountalas, D. T., and Rakopoulos, D. C. (2010). Emission characteristics of high speed, dual fuel, compression ignition engine operating in a wide range of natural gas/diesel fuel proportions. *Fuel.* 89 (7), 1397–1406. doi:10.1016/j.fuel.2009.11.001

Sahoo, B. B., Sahoo, N., and Saha, U. K. (2009). Effect of engine parameters and type of gaseous fuel on the performance of dual-fuel gas diesel engines—a critical review. *Renew. Sustain. Energy Rev.* 13 (6-7), 1151–1184. doi:10.1016/j.rser.2008.08.003

Sharpe, B. (2019). Zero-emission tractor-trailers in Canada. ICCT working paper. .

Srinivasan, K. K., Krishnan, S. R., Singh, S., Midkiff, K. C., Bell, S. R., Gong, W., et al. (2006). The advanced injection low pilot ignited natural gas engine: a combustion analysis. *ASME. J. Eng. Gas Turbines Power.* 128 (1), 213–218. doi:10.1115/1.1915428

United States Environmental Protection Agency (2020). Overview of greenhouse gases. Available at: https://www.epa.gov/ghgemissions/overview-greenhouse-gases (Accessed February 15, 2020).

Wagemakers, A. M. L. M., and Leermakers, C. A. J. (2012). Review on the effects of dual-fuel operation, using diesel and gaseous fuels, on emissions and performance. SAE Technical Paper No. 2012-01-0869.

Wei, L., and Geng, P. (2016). A review on natural gas/diesel dual fuel combustion, emissions and performance. *Fuel Process. Technol.* 142, 264–278. doi:10.1016/j.fuproc.2015.09.018

Yang, B., Xi, C., Wei, X., Zeng, K., and Lai, M. C. (2015). Parametric investigation of natural gas port injection and diesel pilot injection on the combustion and emissions of a turbocharged common rail dual-fuel engine at low load. *Appl. Energy.* 143, 130–137. doi:10.1016/j.apenergy.2015.01.037

Yousefi, A., Guo, H., and Birouk, M. (2018). An experimental and numerical study on diesel injection split of a natural gas/diesel dual-fuel engine at a low engine load. *Fuel.* 212, 332–346. doi:10.1016/j.fuel.2017.10.053

Yousefi, A., Guo, H., and Birouk, M. (2019). Effect of diesel injection timing on the combustion of natural gas/diesel dual-fuel engine at low-high load and low-high speed conditions. *Fuel.* 235, 838–846.

Conflict of Interest: The authors declare that the research was conducted in the absence of any commercial or financial relationships that could be construed as a potential conflict of interest.

Advantages of publishing in Frontiers

OPEN ACCESS
Articles are free to read for greatest visibility and readership

FAST PUBLICATION
Around 90 days from submission to decision

HIGH QUALITY PEER-REVIEW
Rigorous, collaborative, and constructive peer-review

TRANSPARENT PEER-REVIEW
Editors and reviewers acknowledged by name on published articles

Frontiers
Avenue du Tribunal-Fédéral 34
1005 Lausanne | Switzerland

Visit us: www.frontiersin.org
Contact us: frontiersin.org/about/contact

REPRODUCIBILITY OF RESEARCH
Support open data and methods to enhance research reproducibility

DIGITAL PUBLISHING
Articles designed for optimal readership across devices

FOLLOW US
@frontiersin

IMPACT METRICS
Advanced article metrics track visibility across digital media

EXTENSIVE PROMOTION
Marketing and promotion of impactful research

LOOP RESEARCH NETWORK
Our network increases your article's readership